# STRUCTURE AND DYNAMICS OF ΛCDM HALOES

A thesis submitted to The University of Manchester for the degree of Doctor of Philosophy in the Faculty of Engineering and Physical Sciences

**2011**

Sarah E. Bryan

School of Physics and Astronomy

# Contents

# List of Figures

# List of Tables

# The University of Manchester

ABSTRACT OF THESIS submitted by Sarah Elizabeth Bryan
for the Degree of Doctor of Philosophy and entitled
Structure and Dynamics of ΛCDM Haloes. January 2011.

In the standard model (ΛCDM) galaxies form and evolve within underlying dark matter structures which are assumed to have grown hierarchically. As such there should be observational signatures of the merging process in the structure and dynamics of the remnant galaxy. State-of-the-art high-resolution cosmological simulations have been used to explore three such signatures: the abundance of substructure, the spin and shape of haloes, and the orbital content of these haloes.

The Millennium Simulation, combined with semi-analytic galaxy catalogues, is used to compare the predicted frequency of bright central satellites to observations of field and lens galaxies. The predicted frequency is largely independent of galaxy type, but is shown to increase with redshift and halo mass. The predicted frequency is found to be lower than that observed in the Compact Lens All Sky Survey, but considerably higher than that observed in the lens sample of the Sloan Lens ACS Survey and in the field galaxies of the Sloan Digital Sky Survey and the Cosmic Evolution Survey.

The distributions of the spin and shape of haloes are explored and the roles of baryons and the physical prescriptions of stellar and black hole feedback are investigated. Baryons act to make the haloes more spherical and are shown to have a significant effect on the shape of the dark matter. The shapes of the simulated haloes are in broad agreement with a wide range of observational estimates of elliptical galaxies.

Results of spectral analyses of the orbital content of simulations with different feedback prescriptions are presented. Dark matter only haloes are dominated by box orbits in the central region, but the fraction of box orbits is found to decrease when baryons are included. The orbits of the stellar particles are found to be remarkably similar to those of dark matter particles.

# Declaration

I declare that no portion of the work referred to in the thesis has been submitted in support of an application for another degree or qualification of this or any other university or other institute of learning.

# Copyright Statement

(i) The author of this thesis (including any appendices and/or schedules to this thesis) owns certain copyright or related rights in it (the "Copyright"), and they have given The University of Manchester certain rights to use such Copyright, including for administrative purposes.

(ii) Copies of this thesis, either in full or in extracts and whether in hard or electronic copy, may be made **only** in accordance with the Copyright, Designs and Patents Act 1988 (as amended) and regulations issued under it or, where appropriate, in accordance with licensing agreements which the University has from time to time. This page must form part of any such copies made.

(iii) The ownership of certain Copyright, patents, designs, trade marks and other intellectual property (the "Intellectual Property") and any reproductions of copyright works in the thesis, for example graphs and tables ("Reproductions"), which may be described in this thesis, may not be owned by the author and may be owned by third parties. Such Intellectual Property and Reproductions cannot and must not be made available for use without the prior written permission of the owner(s) of the relevant Intellectual Property and/or Reproductions.

(iv) Further information on the conditions under which disclosure, publication and commercialisation of this thesis, the Copyright and any Intellectual Property and/or Reproductions described in it may take place is available in the University IP Policy (see http://www.campus.manchester.ac.uk/medialibrary/policies/ intellectualproperty.pdf), in any relevant Thesis restriction declarations deposited in the University Library, The University Library's regulations (see http://www.manchester.ac.uk/library/aboutus/regulations) and in The University's policy on presentation of Theses.

*There are no eternal facts, as there are no absolute truths.*

- Friedrich Nietzsche

*It is the spur of ignorance, the consciousness of not understanding, and the curiosity about that which lies beyond that are essential to our progress.*

- John Pierce

*The one unchangeable certainty is that nothing is certain or unchangeable.*

- John F. Kennedy

*Everything should be made as simple as possible ... but not simpler.*

- Albert Einstein

*non est ad astra mollis e terris via.*

- Seneca

# Dedication

To David, who sparked my interest in science, and Irene, who kept it alight.

To Stephen, Susan and Dion - you made me who I am.

# Acknowledgements

I wish to express my sincerest gratitude to the many people who have been involved in the projects that make up this thesis and the individuals who have made this journey unforgettable; for the support and encouragement they have provided in the preparation of this work.

First and foremost I would like to thank my supervisors, Shude Mao and Scott Kay, for their unending patience, guidance and inspiration, for keeping me motivated and for their integral contribution to my personal and professional growth.

I am also indebted to the many JBCA students and postdocs who have proved to be a lifeline over the last three years. In particular I need to thank Dandan and Alan who shared their time, ideas, enthusiasm and expertise; Mareike for her untiring effort and Richard, Rick, Simon and Rieul for many clarifying conversations. Thanks are also due to Jen for her constant encouragement and empathy. Not forgetting Mark, Gulay, Jenny, Czarek and the many other friends who have made me feel at home.

Special thanks are owed to Neal Jackson for his support and many useful discussions. Also, my appreciation of the technical support provided by Ant Holloway and Bob Dickson should not go unmentioned.

Thanks are also due to Joop Schaye and the OWLS team, especially Craig and Marcel, for their guidance and advice.

Not least, my heartfelt thanks go to my family, once again, for their endless patience, understanding and insight; for their steadfast support, perspective and guidance and for providing a fundamental foundation without which this work would not have been possible. I can't thank you enough. And to Dion whose love, encouragement and inspiration still proves invaluable; for giving me the confidence to achieve my dreams.

Finally I would like to express my appreciation for the support provided by the EU Framework 6 Marie Curie Early Stage Training Programme; and thank Richard Battye and John Magorrian for helpful comments and discussions.

# The Author

The author graduated from the University of Natal in Pietermaritzburg, South Africa, obtaining a degree in Computational Physics, summa cum laude and an Honours degree in Physics, cum laude. She completed her MSc at the University of KwaZulu-Natal, working with Catherine Cress. This degree was awarded with distinction for work on "The figure rotation of dark matter haloes". She then began a PhD at Jodrell Bank Centre For Astrophysics (JBCA) at the University of Manchester in September 2007 working with Shude Mao and Scott Kay. This project has involved collaboration visits to Beijing, Durham, Garching and Leiden.

# Supporting Publications

**Luminous satellite galaxies in gravitational lenses.**

Bryan, S. E., Mao, S. and Kay, S. T, 2008, MNRAS, **391**,Issue 2, pp.959-966.

(This work forms the basis of chapter 4.)

**Satellites in the field and lens galaxies: SDSS/COSMOS versus SLACS/CLASS.**

Jackson, N. , Bryan, S. E., Mao, S. and Li, Cheng. 2010, MNRAS, **403**,Issue 2, pp.826-837.

(This work forms the basis of section 4.5.)

**The effect of baryons on the spin and shape of dark matter haloes.**

Bryan, S. E. et al, to be submitted, 2011.

(This work forms the basis of chapter 5.)

**The impact of feedback on the orbital content of merger remnants.**

Bryan, S. E. et al, to be submitted, 2011.

(This work forms the basis of chapter 6.)

Figure 1: Hubble Space Telescope image of spiral galaxy NGC 4911 located within the Coma Cluster. Credit: NASA, ESA, and the Hubble Heritage Team (STScI/AURA).

# 1

# Introduction

Attempts to understand our own Galaxy, its nature and origin, date back to Greek philosophers such as Democritus and Aristotle in the $4^{\text{th}}$ century BC. Understanding our position in the cosmos, and how things came to be the way they are, are key questions that have naturally piqued the curiosity of mankind over millennia. Even today, the complex nature of galaxy formation and evolution is not completely understood, and is acknowledged as a key research area addressing some of the most fundamental questions in astrophysics and cosmology.

While observations of the present day local Universe indicate an abundance of structure (galaxies, clusters, filaments), measurements of the early Universe from the Cosmic Microwave Background (CMB) paint a very different picture. The early Universe was initially very smooth. Exactly how the objects we see today formed and evolved out of such smooth initial conditions is not an entirely solved problem and is still an active area of research today. Fortunately, the last few decades have provided a rapid increase in the amount of extragalactic data available, and this has contributed towards a marked improvement in our understanding of the processes involved in galaxy formation and evolution. The work presented in this thesis attempts to probe several aspects of the formation process using state-of-the-art cosmological simulations.

As galaxies are thought to form and evolve within underlying dark matter structures, the morphology and kinematics of the dark matter will have important effects on

the development of the galaxies. Clearly a thorough understanding of these properties is fundamentally important in furthering our knowledge of the formation and evolution of galaxies.

Much progress has been made in revealing the nature of dark matter haloes thanks to the rapid progression of computational techniques and advances in computational resources. However, the role of baryons is much more uncertain. A detailed understanding of the role of baryons in galaxy formation and evolution is essential, not only because most observations typically trace baryonic matter but also because of the complex role it may play in the evolution of the dark matter halo itself.

The simulations used in this thesis provide a unique opportunity to analyse the effects of baryons and implemented feedback techniques on a large sample of haloes evolved within a cosmological setting.

The outline of this thesis is as follows. In chapter 2 the current cosmological model is briefly reviewed and conventional views on the structure formation process in the linear regime are introduced. The present status of comparisons of predictions from this model with observations is also outlined. In chapter 3 the non-linear evolution of structure is considered and a brief overview of commonly implemented simulation techniques presented. Chapter 4 discusses lensing as a probe for substructure and compares simulated predictions for the frequency of companion satellites to observations of lens and field galaxies. Chapter 5 investigates the spin and shapes of dark matter haloes in cosmological simulations and how these parameters are affected by baryonic physics. In chapter 6 the results of spectral analyses of the orbital content of these haloes are presented and the effects of different implementations of feedback processes are considered. A summary and discussion of the findings of this thesis can be found in chapter 7.

# 2

# The Standard Model of Cosmology

The standard cosmological model is intrinsically simple, based principally on General Relativity (GR) and the assumptions of isotropy and homogeneity. The current model has strong predictive power and has become well established both due to successful comparison with a wide range of observations and due to the simplicity of the model.

According to this model, the Universe began ∼13 billion years ago in the Big Bang, a point in time and space where the density and temperature of the Universe was extreme. This idea extrapolates from the observation that the Universe is expanding (Lemaître 1927; Hubble 1929) and was based on Hubble's law: that all galaxies appear to be moving away from us and, the further away the galaxy, the faster it appears to be receding. Recent observations based on high precision measurements of type Ia supernovae (SNe Ia) at z ∼ 1 suggest that the expansion of the Universe is currently accelerating (Perlmutter et al. 1999).

Within the standard model, the Universe consists of radiation, baryonic matter, cold dark matter (CDM) and dark energy ($\Lambda$). The existence of dark matter was initially proposed by Zwicky (1937), motivated by the difference in the dynamical virial mass estimates and the observed luminous component of the Coma cluster. While dark matter has not yet been detected directly there is a wealth of evidence now supporting its existence (see section 2.1.1). Dark energy is an unknown force with a negative pressure which is required to explain the current acceleration of the expansion of the

Universe.

The hot dense initial conditions present in the Big Bang allow nucleosynthesis to occur; this provides a prediction for the overall abundances of the elements (Chandrasekhar and Henrich 1942; Gamow 1946) and predicts the existence of a relic thermal radiation field.

The discovery of the Cosmic Microwave Background (CMB) by Penzias and Wilson (1965) lead to general acceptance of the Big Bang model. The CMB radiation is remarkably isotropic on angular scales from $1'$ to $180°$. These regions were not expected to have been in causal contact, and as such there was no proposed mechanism to explain how the temperatures were able to equalise. This is known as the Horizon problem and is solved by inflation – a period of exponential expansion in the early Universe (Guth 1981). All of the visible Universe would have been in causal contact initially before experiencing exponential growth. Inflation provides solutions to several other problems. It provides an origin of the initial density fluctuations (quantum fluctuations). These density perturbations are assumed to grow via gravitational collapse to form the structures we see today, with gas cooling radiatively to the centre of the potentials formed by these structures. Inflation also provides an explanation for the observed flatness of the Universe and predicts that the power spectrum should be nearly scale invariant (these ideas are discussed in sections 2.1.1 and 2.2.2).

While the CMB initially appeared to have a uniform temperature, the tiny fluctuations (of the order $\delta T/T \sim 10^{-5}$) that had been predicted by the standard model, were detected by the COsmic Background Explorer (COBE, Smoot et al. 1992). More recent observations of the CMB with the Wilkinson Microwave Anisotropy Probe (*WMAP*) have led to an era of precision cosmology.

In this chapter a brief review of the current cosmological model and an introduction to linear structure formation is presented. These sections describe the cosmological framework used throughout this thesis. Some of the successes and challenges of this paradigm are discussed. This chapter also describes how the initial conditions for the simulations used in this work are generated and provides a definition for the structures

studied in later chapters.

Note that in this chapter natural units are assumed (in which the speed of light c is set to 1); Greek indices run from 0 to 3; Latin indices from 1 to 3 and the Einstein summation convention is assumed.

## 2.1 The Standard Paradigm

The fundamental framework of the standard model is based on the Cosmological Principle, the Friedmann-Robertson-Walker (FRW) metric and the General Theory of Relativity (GR). The Cosmological Principle – that there are no preferred locations in the Universe (see, for example, Weinberg 1972; Liddle 2003), implies that the properties of the Universe are the same for all observers. Two consequences of this, that are fundamentally important to this model, are the homogeneity and isotropy of the Universe. Current observations (such as: the isotropy of the CMB radiation; estimates of the two-point correlation function and the power spectrum from the Sloan Digital Sky Survey (SDSS) and the Two-degree Field (2dF) galaxy redshift survey; analysis of deep radio surveys and multipoles of the X-ray background) support the assumption that the Universe is homogeneous and isotropic on scales larger than $\sim 100\ h^{-1}$ Mpc (see Yadav et al. 2005 and references therein).

The FRW space-time metric provides a description of the geometry of a homogeneous, isotropic universe. This metric can be expressed as follows:

$$\mathrm{d}s^2 = g_{\mu\nu}\mathrm{d}x^\mu \mathrm{d}x^\nu = \mathrm{d}t^2 - a^2(t)\left\{\frac{\mathrm{d}r^2}{1-kr^2} + r^2\left(\mathrm{d}\theta^2 + \sin^2\theta\, d\phi^2\right)\right\}, \tag{2.1}$$

where $ds$ is the space-time element, $a(t)$ is the scale factor (defined at the present day as $a_0 \equiv a(t_0) = 1$) and $(r, \theta, \phi)$ are the spatial coordinates at an arbitrary time $t$. The trichotomic constant, $k$ (determined by the energy density present), describes the

curvature of space such that (for a suitable choice of the units of $r$)

$$k = \begin{cases} 1 & \text{closed (spherical geometry),} \\ 0 & \text{flat (Euclidean geometry),} \\ -1 & \text{open (hyperbolic geometry).} \end{cases}$$

Consequently, $k = 1$ corresponds to a finite (unbounded) universe, while for $k = -1$ or $k = 0$ space is infinite. The coordinate distance $r$ is related to the comoving distance $\chi$ as follows:

$$r = \begin{cases} \sin\chi & \text{for } k = 1, \\ \chi & \text{for } k = 0, \\ \sinh\chi & \text{for } k = -1. \end{cases}$$

Comoving coordinates provide a convenient choice of coordinate system in which the expansion of the Universe is incorporated, assigning constant spatial coordinates to objects moving with the Hubble flow. The physical (or proper) length $x$ is equal to the comoving length $\chi$ multiplied by the scale factor $a$.

The FRW metric is a general solution of Einstein's field equations that satisfies the Cosmological Principle.

GR provides us with a relationship between mass-energy and geometry (curvature of space-time), where the distribution of energy determines the geometry of space-time.

Defining the Einstein tensor, $G_{\mu\nu} \equiv R_{\mu\nu} - \frac{1}{2}g_{\mu\nu}R$, where $R_{\mu\nu}$ is the Ricci curvature tensor, $g_{\mu\nu}$ the metric tensor and $R$ the scalar curvature, Einstein's field equations can be expressed as

$$G_{\mu\nu} = -8\pi G \underbrace{\left(T_{\mu\nu} - \frac{\Lambda}{8\pi G} g_{\mu\nu}\right)}_{\tilde{T}_{\mu\nu}}, \tag{2.2}$$

where $\tilde{T}_{\mu\nu}$ is the stress-energy tensor, $\Lambda$ is the cosmological constant and $G$ is Newton's gravitational constant. These equations describe the fundamental interaction of gravitation as a result of the curvature of space-time. They are used to determine the

space-time geometry resulting from the presence of mass-energy and linear momentum. $\tilde{T}_{\mu\nu}$ is assumed to have the perfect fluid form

$$\tilde{T}_{\mu\nu} = \tilde{p} g_{\mu\nu} + (\tilde{\rho} + \tilde{p})\, U_\mu U_\nu, \tag{2.3}$$

where $\tilde{\rho}$ denotes the total energy density, $\tilde{p}$ is the total pressure density and $U_\mu$ is a velocity four-vector in which $U_0 = 1$ and $U_i = 0$.

From the energy conservation equation $\nabla^\mu \tilde{T}_{\mu\nu} = 0$, one has

$$\dot{\tilde{\rho}} + 3H(\tilde{\rho} + \tilde{p}) = 0. \tag{2.4}$$

Here the Hubble parameter $H$ describes the rate of expansion of the Universe and is defined as $H \equiv \dot{a}/a$. The Hubble parameter measured at the present day is known as the Hubble constant, and is often expressed as $H_0 = 100\,h\,\mathrm{km\ s^{-1}Mpc^{-1}}$, where $h$ is a dimensionless constant (this convention is adopted for this thesis). Substituting the FRW metric and the perfect fluid energy momentum tensor $\tilde{T}_{\mu\nu}$ (2.3) into Einstein's equations (2.2) gives

$$\dot{H} + H^2 = -\frac{4\pi G}{3}(\tilde{\rho} + 3\tilde{p}) \qquad (00 - \text{component}), \tag{2.5a}$$

$$\dot{H} + 3H^2 = 4\pi G(\tilde{\rho} - \tilde{p}) \qquad (ii - \text{component}). \tag{2.5b}$$

The density and pressure content of the Universe are expressed as $\tilde{\rho}$ and $\tilde{p}$, respectively. The total density content $\tilde{\rho}$ is given by the sum of the components $\tilde{\rho} = \rho + \rho_\Lambda + \rho_k = \rho_r + \rho_m + \rho_\Lambda + \rho_k$, where $\rho_r$ and $\rho_m$ refer to the energy density of radiation and matter respectively and contributions from the curvature, $k$, and cosmological constant, $\Lambda$, have also been written in terms of energy density as $\rho_\Lambda = \Lambda/8\pi G$ and $\rho_k = -3k/8\pi G a^2$. The pressure term $\tilde{p}$ is the total pressure density $\tilde{p} = p + p_\Lambda + p_k = p_r + p_m + p_\Lambda + p_k$. Substituting (2.5a) into (2.5b) gives the Friedmann equation

$$H^2 = \left(\frac{\dot{a}}{a}\right)^2 = \frac{8\pi G}{3}\tilde{\rho}. \tag{2.6}$$

The Friedmann equation (2.6) and the energy conservation equation (2.4) govern the dynamics of the Universe which are driven by the energy content $\tilde{\rho}$. In addition, one must specify the equation of state, which relates pressure to density as

$$p_i = \omega_i \rho_i, \tag{2.7}$$

where $i$ refers to the components $r, m, k, \Lambda$. Components are separated according to their equation of state into: radiation and relativistic matter ($\omega_r = 1/3$); non-relativistic matter ($\omega_m = 0$); the contribution of curvature ($\omega_k = -1/3$) and a positive vacuum energy density (assumed to be constant for simplicity) associated with the cosmological constant term in Einstein's Field Equations ($\omega_\Lambda = -1$). The pressure density from each component is then given by: $p_r = \frac{1}{3}\rho_r$; $p_m = 0$; $p_\Lambda = -\rho_\Lambda = -\frac{\Lambda}{8\pi G}$; $p_k = -\frac{1}{3}\rho_k = \frac{k}{8\pi G a^2}$.

The three equations (2.4), (2.6) and (2.7) are the fundamental equations describing the dynamics of an expanding, isotropic and homogeneous universe. The total energy content plays a critical role in deciding the fate of the Universe.

At the present day, the Friedmann equation (2.6) can be rearranged as

$$\rho_0 = \frac{3}{8\pi G}\left(H_0^2 + k\right), \tag{2.8}$$

where the curvature component has been separated from the rest of the mass/energy terms. Defining a critical density

$$\rho_{\rm crit} = \frac{3H^2}{8\pi G}, \tag{2.9}$$

the current energy density (2.8) can be expressed as

$$\rho_0 = \rho_{\rm crit,0} + \frac{3k}{8\pi G}. \tag{2.10}$$

In (2.10), $k = 0$ corresponds to $\rho_0 = \rho_{\rm crit}$ and a flat universe. An open universe ($k < 0$ and $\rho_0 < \rho_{\rm crit}$) expands forever, while in a closed universe ($k > 0$ and $\rho_0 > \rho_{\rm crit}$)

expansion ceases and a general contraction will occur.

Dividing (2.10) by $\rho_{\mathrm{crit},0}$, results in normalised energy densities

$$\Omega_{\mathrm{total}} = \Omega_r + \Omega_m + \Omega_\Lambda = 1 + \frac{k}{H_0^2}. \tag{2.11}$$

In this way the condition for closure can be expressed as $\Omega_{\mathrm{total}} > 1$; a flat universe has $\Omega_{\mathrm{total}} = 1$ and an open universe has $\Omega_{\mathrm{total}} < 1$. The value of $\rho_{\mathrm{crit}}$ is estimated to be $2.78 \times 10^{11}\, h^2\, M_\odot$ Mpc $^{-3}$ or $1.88 \times 10^{-29}\, h^2$ g cm$^{-3}$ (Kolb and Turner 1993).

In order to discuss the scaling behaviour of the energy components with the scale factor, the energy conservation equation (2.4) is re-expressed as

$$\frac{\mathrm{d}}{\mathrm{da}}\left(\tilde{\rho} a^3\right) = -3\tilde{p} a^2. \tag{2.12}$$

Substituting the equation of state (2.7) into (2.12) and integrating gives

$$\rho \propto a^{-3(1+\omega)}. \tag{2.13}$$

Substituting the scaling behaviour of $\rho$ in (2.13) into the Friedmann equation (2.6) and integrating gives the time evolution of the scale factor

$$a \propto t^{2/3(1+w)}. \tag{2.14}$$

It is then trivial to show the time dependence of the scale factor for each of the epochs: $a \propto t^{1/2}$ in the radiation-dominated era and $a \propto t^{2/3}$ in the matter-dominated era. For the cosmological constant, $\rho_\Lambda$ is constant, and the Friedmann equation simplifies to $H = \dot{a}/a =$ constant. Integrating this equation shows that in this era the scale factor grows exponentially as $a \propto e^{Ht}$.

Rewriting (2.5a) as

$$\frac{\ddot{a}}{a} = -\frac{4\pi G}{3}\left(\tilde{\rho} + 3\tilde{p}\right) = -\frac{4\pi G}{3}\left(\rho + 3p\right) + \frac{\Lambda}{3}, \tag{2.15}$$

and assuming $\rho > 0$, $p > 0$ and $\Lambda = 0$ gives $\ddot{a}/a < 0$. Since the observed $\dot{a} > 0$ (redshifts are observed) $a(t)$ is concave. This implies that at some finite point in time the scale factor was zero and, ipso facto, a Big Bang. The time to when $a = 0$ defines a maximum bound for the age of the Universe $t_0$. For $\ddot{a} = 0$, $\dot{a}$ is constant. One can therefore write $a = (a_0/t_0)\, t = (\mathrm{da/dt})\, t$. Consequently $t_0 = (a_0/a)\, t$ and $t_0 = a_0/\dot{a}_0 = 1/H_0$. Early (inaccurate) measurements of the Hubble constant resulted in the age paradox (see, for example, the discussion in Earman 2001) – where predicted values of $t_0$ were much shorter than the age of the earth (as determined by radioactive decay) and the ages of the stars (as determined by stellar evolution theory).

### 2.1.1 Current Parameters in the Standard Model

The previous section describes the theoretical framework of modern cosmology, ΛCDM. This model is fully described by only six parameters, namely: the matter density $\Omega_m h^2$; the baryon density $\Omega_b h^2$; the Hubble constant $H_0$; the root mean squared amplitude of fluctuations $\sigma_8$ (defined within a sphere of $8h^{-1}$Mpc at $z = 0$); the integrated optical depth $\tau$ ($= \int_0^{z_r} \sigma_T n_e(z) \frac{dt}{dz} dz$ where $z_r$ is the redshift of reionisation, $\sigma_T$ is the Thomson scattering cross-section and $n_e$ the number density of free electrons) and the slope of the scalar perturbation spectrum $n_s$. The amplitude of this spectrum is given by $\Delta^2_R$ and is conventionally defined at the pivot scale $k_0 = 0.002\,\mathrm{Mpc}^{-1}$.

Constraints on these cosmological parameters are most commonly derived from observations of the CMB; additional orthogonal constraints are provided by SNe Ia and Baryonic Acoustic Oscillations (BAO). The joint constraints on the $\Omega_m - \Omega_\Lambda$ plane are shown in figure 2.1. These observations are discussed briefly below.

**Supernovae Ia.** SNe Ia are calibratable distance indicators (Riess et al. 1996). Since distance depends on the underlying cosmology, using the observed redshift with luminosity-distance relation places constraints on the cosmological parameters $h, \Omega_m$ and $\Omega_\Lambda$. Observations based on high-precision measurements of SNe Ia (Riess et al. 1998; Garnavich et al. 1998; Perlmutter et al. 1999; Kowalski et al. 2008) at high redshift find

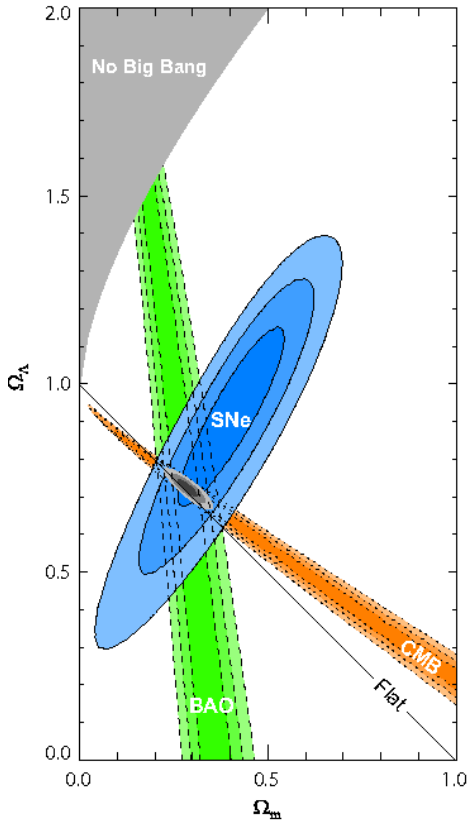


Figure 2.1: Joint constraints on the $\Omega_m - \Omega_\Lambda$ plane from SNe data, BAO and CMB observations (assuming $\omega = -1$), contours show the 1,2 and 3 $\sigma$ confidence levels. Taken from Kowalski et al. (2008).

that these SNe are fainter than expected, implying an accelerating expansion of the Universe at late times. Two possible explanations have been put forward: either GR breaks down at large scales and a modified theory of gravity is required (for example MOdified Newtonian Dynamics or MOND), or there is an unknown energy content with a negative pressure which is driving the expansion. The unknown energy content has been termed *dark energy* and is described by an equation of state $\omega \leq -1/3$. The standard model assumes a cosmological constant $\Lambda$ with $\omega = -1$; however $\omega$ may vary with time.

**Cosmic Microwave Background.** The CMB provides a measure of the surface of last scattering. The detailed pattern of anisotropies observed in the CMB power spec-

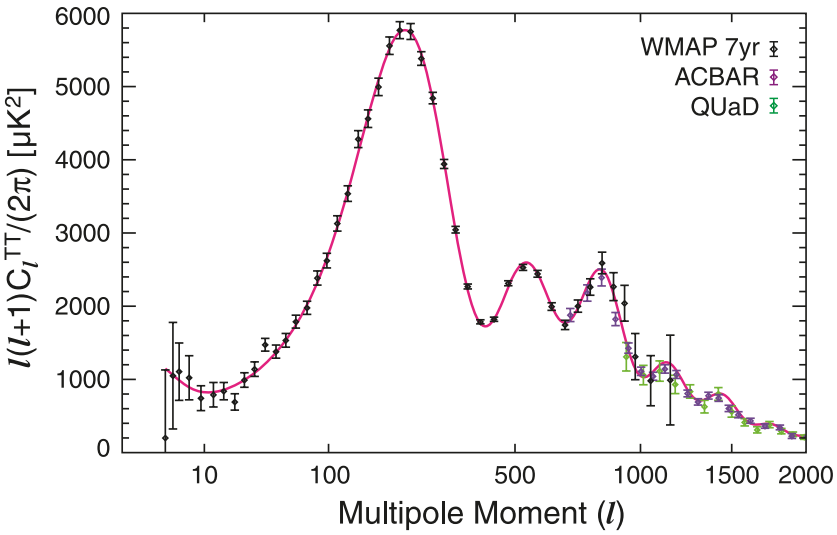


Figure 2.2: The angular power spectrum of CMB temperature anisotropies. Taken from Komatsu et al. (2011) where the *WMAP* 7-year temperature power spectrum (Larson et al. 2010), the ACBAR (Reichardt et al. 2009) and the QUaD (Brown et al. 2009) temperature power spectra are shown and the solid line shows the best-fitting flat ΛCDM model to the *WMAP* 7 year data.

trum places strong constraints on all of the cosmological parameters. The angular power spectrum of CMB temperature anisotropies, taken from Komatsu et al. (2011), is shown in figure 2.2. The power spectrum consists of a series of acoustic peaks which result from oscillations of the photon-baryon fluid within the sound horizon around the time of decoupling. The power spectrum is flat on scales between $10 \lesssim l \lesssim 100$; this is known as the Sachs-Wolfe plateau. The average temperature of the CMB is measured by the multipole moment term $l = 0$ and is directly proportional to $\Omega_r$. The position of the first peak determines the angular-diameter distance of the last scattering surface and places constraints on the spatial geometry, finding it to be consistent with spatial flatness ($\Omega_m + \Omega_\Lambda = 1$). The relative peak heights and positions place constraints on the baryon density. The power spectrum for the standard model can be calculated using linear perturbation theory (discussed in section 2.2) and, as seen in figure 2.2, provides an excellent fit to the overall shape of the CMB data.

**Baryonic Acoustic Oscillations.** The power spectrum of density perturbations (discussed in section 2.2.2) is sensitive to the nature of dark matter and its shape depends

Table 2.1: Current values of the cosmological parameters from Komatsu et al. (2011).

| | *WMAP*7 | *WMAP*7 + SNe + BAO |
|---|---|---|
| $100\Omega_b\, h^2$ | $2.249^{+0.056}_{-0.057}$ | $2.255 \pm 0.054$ |
| $\Omega_{CDM}\, h^2$ | $0.1120 \pm 0.0056$ | $0.1126 \pm 0.0036$ |
| $\Omega_\Lambda\, h^2$ | $0.727^{+0.030}_{-0.029}$ | $0.725 \pm 0.016$ |
| $n_s$ | $0.967 \pm 0.014$ | $0.968 \pm 0.012$ |
| $\tau$ | $0.088 \pm 0.015$ | $0.088 \pm 0.014$ |
| $\Delta^2_R \times 10^9$ | $2.43 \pm 0.11$ | $2.430 \pm 0.091$ |
| $h$ | $0.704 \pm 0.025$ | $0.702 \pm 0.014$ |
| $\sigma_8$ | $0.811^{+0.030}_{-0.031}$ | $0.816 \pm 0.024$ |
| $\Omega_b$ | $0.0455 \pm 0.0028$ | $0.0458 \pm 0.0016$ |
| $\Omega_{CDM}$ | $0.228 \pm 0.0027$ | $0.229 \pm 0.015$ |
| $\Omega_m\, h^2$ | $0.1345^{+0.0056}_{-0.0055}$ | $0.1352 \pm 0.0036$ |
| $t_0$ | $13.77 \pm 0.13$ Gyr | $13.76 \pm 0.11$ Gyr |

on the primordial power spectrum and the horizon scale at matter-radiation equality (determined by $\Omega_m h$). The simplest way to probe the matter distribution is to observe the distribution of galaxies. However galaxies are a biased tracer of the underlying matter distribution; they cluster in regions of high density and different galaxy types show a bias with respect to each other. On large scales the galaxy power spectrum is thought to be a constant multiple $b$ of the dark matter spectrum. On smaller scales coherent infall acts to compress the clustering in the radial direction. The galaxy power spectrum has been measured by 2dF and SDSS and is well-fit by the ΛCDM model. Both of these surveys show evidence for BAOs which can be used as standard rulers.

**Joint Constraints.** Quite remarkably all of these measurements (SNe Ia, BAO and measurements of the CMB) intersect on the $\Omega_m - \Omega_\Lambda$ plane, placing strong constraints on the cosmological parameters, indicating that the Universe is flat and experiencing an epoch of accelerating expansion. The current values for these parameters as derived from these joint constraints (*WMAP*7, SNe Ia and BAOs) are given in Komatsu et al. (2011) and are summarised in table 2.1.

In summary, within the standard model the present day Universe is made up of radiation (negligible contribution), baryonic matter (4%), cold dark matter (CDM ∼ 26%) and dark energy (Λ ∼ 70%). The Universe is modelled as isotropic, homogenous

and flat ($\Omega_m + \Omega_\Lambda = 1$). The model also assumes a nearly scale invariant spectrum of primordial fluctuations ($n_s \sim 1$). Flatness and scale-invariance are both explained by cosmic inflation, a period of exponential expansion in the very early Universe. Dark energy, also known as the cosmological constant, makes up most of the total mass-energy of the present day Universe. This energy has a strong negative pressure and is thought to be responsible for the accelerating expansion of the Universe at late times. Most of the remaining mass of the Universe is made up of cold dark matter, which is non-baryonic and collisionless.

### Dark Matter Candidates

Dark matter interacts primarily through gravity (although weak interactions cannot be ruled out), making direct detection an arduous task. Dark matter is collisionless and assumed to be cold, that is, non-relativistic at the time of decoupling. Hot dark matter models are ruled out through observations of small scale structure, the non-negligible velocities of hot dark matter particles has a dramatic effect on these scales (see section 2.2.2).

Cold dark matter provides an excellent fit to many observations, but some doubt remains on small scales such as the structure of dwarf galaxies and substructure in galaxy haloes. Dark matter plays an important role in structure formation, providing potential wells that enhance the collapse rate of baryons, allowing structure to form on observed time-frames. Further evidence for dark matter is provided by objects such as the Bullet cluster (Clowe et al. 2006) – a merging cluster of galaxies in which the centre of mass determined from the hot gas (observed in X-rays) is displaced from the centre of mass as determined from lensing. A natural explanation arises if collisionless dark matter dominates the potential, while the hot gas interacts during the merging process.

Candidates for dark matter include axions, primordial black holes and weakly interacting massive particles (WIMPs). Dark matter has not yet been directly detected. Direct searches for WIMPs (e.g. light supersymmetric particles) attempt to observe signatures from nuclear recoil. Complementary to the direct detection methods are

indirect methods such as the search for gamma-ray self-annihilation signals.

## 2.2 An Introduction to Linear Structure Formation

Small fluctuations in the temperature of the CMB imply that there are inhomogeneities in the early Universe, the size of which constrain the amplitude of the density perturbations at this time. In order to understand how these tiny fluctuations transform into the structure seen today, a brief introduction to structure formation in the linear regime is given in this section. The details of numerical simulation of structure formation in the non-linear regime can be found in chapter 3.

The standard model assumes that random quantum fluctuations present in the very early Universe grow via gravitational instabilities into the structure observed today. Structure formation began at the time of matter-radiation equality, $t_{eq}$, when matter began to dominate the Universe and baryons are freed from the pressure support of photons.

To study structure formation in the linear regime small, linear, adiabatic perturbations in the FRW metric (2.1) are considered and the growth of these perturbations in a homogeneous background with a mean background density $\bar{\rho}(t) = 3H^2/8\pi G$ is followed. The density perturbations are described as $\rho = \bar{\rho}(t)(1 + \delta(\mathbf{x}, t))$, in terms of their density contrast or amplitude $\delta$ (where, in the linear regime, $\delta \ll 1$). The density contrast $\delta(\mathbf{x})$ can be expressed in terms of the overdensity relative to the background density as

$$\delta(\mathbf{x}) \equiv \frac{\delta\rho(\mathbf{x})}{\bar{\rho}} = \frac{\rho(\mathbf{x}) - \bar{\rho}}{\bar{\rho}}. \tag{2.16}$$

The density contrast $\delta(\mathbf{x})$ can be related to a curvature term (as in Kolb and Turner 1993). Relating the mean background density $\bar{\rho}$ to the density of a flat FRW model gives

$$H^2 = \frac{8\pi G}{3}\bar{\rho} \Rightarrow \bar{\rho} = \frac{3}{8\pi G}H^2. \tag{2.17}$$

Considering a perturbation to this model (without changing the Hubble constant $H$) where the density $\rho > \bar{\rho}$ implies $k > 0$ and gives

$$H^2 = \frac{8\pi G}{3}\rho - \frac{k}{a^2} \Rightarrow \rho = \frac{3}{8\pi G}\left(H^2 + \frac{k}{a^2}\right). \tag{2.18}$$

The density contrast can then be written as

$$\delta = \frac{\rho - \bar{\rho}}{\bar{\rho}} = \frac{k}{a^2 H^2} = \frac{k/a^2}{8\pi G\bar{\rho}/3} \propto \frac{k/a^2}{\bar{\rho}} \propto k a^{1+3\omega}. \tag{2.19}$$

Where the scaling relation (2.14) has been used in the last step. Consequently, an overdensity can be thought of as a closed universe which will collapse, becoming increasingly overdense. Whereas an underdensity, like an open universe, will keep expanding and become increasingly underdense.

The density contrast can also be written in terms of a Fourier expansion (valid in spatially flat models) as

$$\delta_k = \frac{1}{V}\int_{\mathrm{V}} \delta(\mathbf{x}) \exp(-i\mathbf{k}\cdot\mathbf{x})\, \mathrm{d}^3\mathbf{x}, \tag{2.20}$$

where periodic boundary conditions have been imposed and $V$ is the volume of the fundamental cube. The Fourier components are completely characterised by their amplitudes $|\delta_k|$, and the comoving wavenumber $k$. The comoving wavelength of a perturbation is related to the wavenumber as $\lambda \equiv 2\pi/k$, where the physical wavelength $\lambda_{\mathrm{phys}} = a(t)\,\lambda$ describes the physical length scale of perturbations. In curved space-time, the plane wave solutions are replaced by the generalised solution to the Helmholtz equation.

Structures form via the collapse of perturbations under gravity. This can only occur in regions that are in causal contact. This region is described by the horizon scale, $r_H$. If one considers light emitted at the horizon ($r_H$) at $t = 0$ and observed at $r = 0$ at time $t$, then a photon travelling along a null radial geodesic (where $\mathrm{d}s^2 = 0$ and $\mathrm{d}\theta =$

$\mathrm{d}\phi = 0$) in the FRW metric (2.1) gives

$$\mathrm{d}t^2 = a\,(t)^2\,\frac{\mathrm{d}r^2}{1-kr^2}. \tag{2.21}$$

This can be rewritten as

$$\int_0^t \frac{\mathrm{d}t}{a\,(t)} = \int_0^{r_H} \frac{\mathrm{d}r}{\sqrt{1-kr^2}}, \tag{2.22}$$

and the comoving horizon $r_H$ in a flat universe (with $k = 0$) can be expressed as

$$r_H = \int_0^t \frac{\mathrm{d}t}{a\,(t)} = \int \frac{\mathrm{d}t}{\mathrm{d}a}\frac{\mathrm{d}a}{a\,(t)} = \int \frac{\mathrm{d}a}{a^2 H} = \int \frac{\mathrm{d}a}{a^2\sqrt{(a^{-3(1+\omega)})}} \propto a^{1/2(1+3w)}. \tag{2.23}$$

In the radiation-dominated era the comoving horizon grows as $r_H \propto a$, while in the matter-dominated era it grows as $r_H \propto a^{1/2}$. When the energy density is dominated by the cosmological constant the comoving horizon scales as $r_H \propto a^{-1}$. The proper horizon is given by $d_H = a\,(t)\,r_H$. From this it can be seen that fluctuations which are expanded out of the horizon during inflation can re-enter the horizon during the radiation- and matter-dominated eras. The smallest-scale fluctuations will re-enter and collapse before larger-scale fluctuations. During the $\Lambda$-dominated era the comoving horizon size decreases and ever smaller scales remain causally connected. Using $\rho \propto a^{-3(1+w)}$ and $H^2 \propto \rho$, one can easily show that $d_H \propto H^{-1}$. It is worth noting that the proper horizon does not grow in the $\Lambda$-dominated era.

There are two characteristic regimes divided, depending on the size of the perturbations, into either super- or sub-horizon scales. In the early regime, density perturbations are super-horizon-sized. Here the gauge invariance of $\delta\rho/\rho$ needs to be considered and the distinction between isocurvature and adiabatic density perturbations is important. Adiabatic perturbations correspond to fluctuations in the spatial curvature, while isocurvature perturbations correspond to spatial variations in the equation of state. Isocurvature perturbations correspond to perturbations of the relative amounts of the different components while the total energy density remains constant. In the early regime a full general relativistic treatment is required. In the later regime, where

modes are well within the horizon and gravitational collapse is possible, Newtonian analysis is sufficient (Newtonian analysis becomes exact as $\lambda_{\rm phys}/H^{-1} \rightarrow 0$).

### 2.2.1 Linear Perturbation Growth in the Newtonian Regime

The first recognised theory of galaxy formation was proposed by Jeans (1928) who described the Universe as a non-relativistic perfect fluid with mass density $\rho$, pressure $p$ and velocity $\mathbf{v}$ under the influence of a gravitational field with potential $\phi$. In Jeans' analysis small perturbations to a static uniform fluid were considered. Unfortunately, the assumption of a static medium implies that perturbation growth in an expanding universe cannot be explored. The case for an expanding universe was first considered by Bonnor (1957). In the case of an expanding fluid, structure formation in the Newtonian limit, is governed by the following equations:

$$\frac{\partial \delta}{\partial t} + \nabla \cdot [(1+\delta)\,\mathbf{v}] = 0, \tag{2.24}$$

$$\frac{\partial \mathbf{v}}{\partial t} + \frac{\dot{a}}{a}\mathbf{v} + (\mathbf{v}\cdot\nabla)\,\mathbf{v} + \frac{\nabla p}{\rho} + \nabla\phi = 0, \tag{2.25}$$

$$\nabla^2\phi = 4\pi G\bar{\rho}\delta. \tag{2.26}$$

These equations are the perturbed versions of the continuity equation, the Euler equation and Poisson's equation respectively. Combining the first-order perturbed fluid equations (2.24 - 2.26), one derives the following second-order differential equation for the density fluctuations:

$$\ddot{\delta}_m + 2\frac{\dot{a}}{a}\dot{\delta}_m + \delta_m\left(\frac{c_s^2 k^2}{a^2} - 4\pi G\rho_m\right) = 0, \tag{2.27}$$

where the speed of sound is defined as

$$c_s^2 \equiv \left(\frac{\partial p}{\partial \rho}\right), \tag{2.28}$$

where the differentiation is taken with respect to adiabatic changes.

Solutions to the growth equation (2.27) can be considered within the different epochs of the Universe defined by the dominant energy content.

During the radiation-dominated era fluctuations do not grow as perturbation growth is suppressed by radiation pressure, and the perturbations oscillate as acoustic waves with a constant amplitude. The photon pressure of baryonic fluctuations entering the horizon sets the Jeans length scale $L_J$ (critical scale above which gravitational collapse will occur) to be of the order of the horizon scale. The Jeans stability argument sets the sound crossing time $t_{sc}$ to be less than the dynamical time $t_{dyn}$ or

$$\frac{L_J}{c_s} < \frac{1}{\sqrt{G\rho}} \sim \frac{1}{H} \sim t. \tag{2.29}$$

Before decoupling the speed of sound $c_s$ in the relativistic plasma is $\sim \frac{c}{\sqrt{3}}$ and the Jeans length is of the order of the horizon scale ($L_J \sim c\,t \sim r_H$). Perturbations are unable to collapse. During the radiation era CDM fluctuations are suppressed by the Mészáros Effect (Meszaros 1974): expansion of the universe is so fast that the dark matter does not have enough time to respond and collapse and the density fluctuations $\delta$ are effectively frozen out. Comparing the expansion time-scale $t_{exp} = 1/H$ to the dynamical timescale $t_{dyn}$ expressed in terms of the dark matter density $\rho_{dm}$,

$$\frac{1}{H} \sim \frac{1}{\sqrt{G\rho_r}} < \frac{1}{\sqrt{G\rho_{dm}}}, \tag{2.30}$$

shows that expansion rate in this era prevents the collapse of dark matter perturbations.

In the matter-dominated regime, dark matter fluctuations grow as $\delta \propto a$, while the growth of baryonic fluctuations is delayed as baryons and photons are coupled until recombination, at which point the baryons are free from radiation pressure and fall into the enhanced potentials that have already been created by the dark matter. Once $\Lambda$ begins to dominate, the comoving horizon scale shrinks and ever smaller regions are within causal contact, eventually freezing out structure formation.

### 2.2.2 The Power Spectrum

Predictions for the linear theory of matter distribution at early times are usually expressed in terms of the power spectrum of spatial density fluctuations $P(k)$. This power spectrum is usually written as the product of an initial spectrum generated by the primordial fluctuations and the transfer function $T(k)$ representing the later linear evolution of each mode. The seeds of structure formation are thought to be small-amplitude curvature perturbations originating from quantum fluctuations in an inflationary phase of the very early Universe. The initial density fluctuations are assumed to be Gaussian (with uncorrelated amplitudes) and are completely specified by the power spectrum $P(k) = |\delta_k|^2$ (independent of angle in a statistically isotropic universe).

Inflationary models predict a primordial power spectrum of the form $P(k) \propto k^{n_s}$. In the simplest scenarios $n_s = 1$ corresponding to a Harrison-Zel'dovich power spectrum. Here, the dimensionless power spectrum $k^3 P(k)$ is scale invariant (each fluctuation enters the horizon with the same amplitude). After inflation the initial power spectrum is modified by the growth of structures as described by the transfer function. The power spectrum today can be expressed as $P(k) \propto T_k^2 k^{n_s}$. The form of the transfer function is determined by the assumed cosmological model and can be specified either using a fitting formula (see Carroll et al. 1992) or it can be computed numerically (Bardeen et al. 1986; Seljak and Zaldarriaga 1996; Eisenstein and Hu 1999).

The transfer function is defined as

$$T_k \equiv \frac{\delta_k(z_0)}{D(z)\,\delta_k(z)}, \tag{2.31}$$

where $D(z)$ is the growth factor, and can be thought of as relating the initial density contrast $\delta_k(z_0)$ to its present day value $\delta_k(z)$. The growth of perturbations can be expressed as

$$\delta_k(z) = D(z)\,\delta_k(z_0), \tag{2.32}$$

where $D(z) = 1/(1+z)$ for $\Omega_m = 1$. When $\Lambda \neq 0$ the growth factor can be approximated

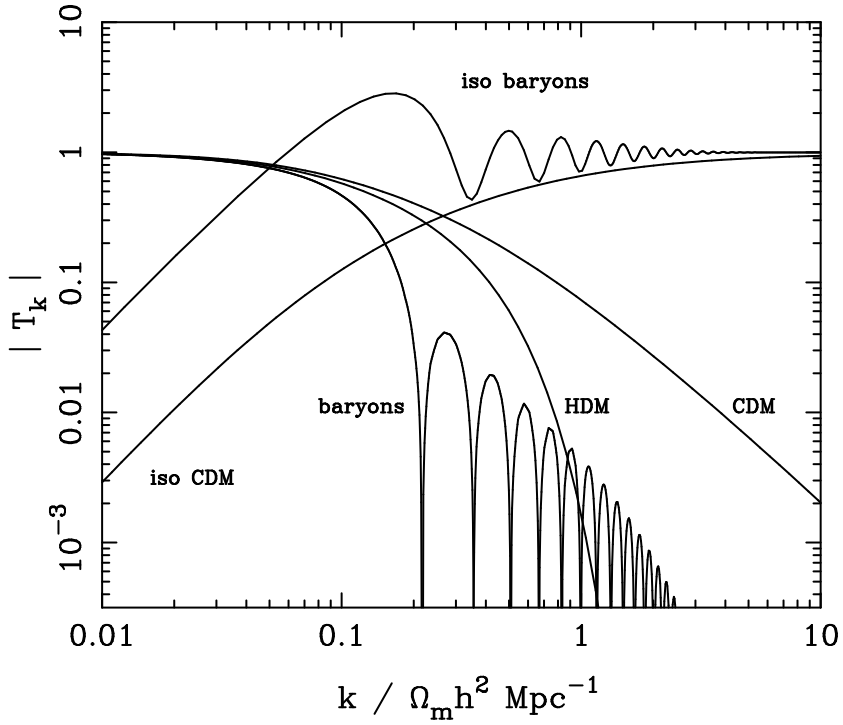


Figure 2.3: The transfer functions of various models taken from Nakamura and Group (2010).

using a fitting formula (for more details see, for example, Peebles 1980; Carroll et al. 1992 or Eisenstein and Hu 1999).

The transfer functions for various models are shown in figure 2.3. Note that after recombination the baryonic Jeans scale drops suddenly to small scales due to the rapid decrease in pressure. CDM fluctuations are also suppressed before equality ($k_{eq} \sim 20\,h$ kpc$^{-1}$) by the Mészáros Effect (see previous discussion). There are also dissipational effects (such as Silk damping in the case of baryons or Landau damping in the case of hot dark matter) that must be considered when the perfect fluid assumption breaks down.

As the Universe cools and recombination is approached, the mean free path of photons increases, photons diffuse out of high density regions into lower density regions smoothing out inhomogeneities. This photon diffusion is known as Silk damping. The Silk damping scale sets a smoothing length for the perturbations, beyond which struc-

ture is not expected to form.

Nearly collisionless components such as neutrinos or hot/warm dark matter particles undergo free streaming or Landau damping. The growth of structures on scales smaller than the free streaming length $\lambda_{FS}$ is strongly suppressed until equality when perturbations become Jeans unstable and begin to grow effectively suppressing the growth of small scale haloes. Following freeze-out of dark matter interactions, dark matter particles will free stream over a distance determined by their thermal velocity. Density fluctuations smaller than this free streaming length are highly suppressed. The smallest haloes which arise are expected to have masses of the order

$$M_{FS} = \frac{4\pi}{3}\bar{\rho}_m \lambda_{FS}^3. \tag{2.33}$$

Smaller haloes could potentially form through non-hierarchical processes such as fragmentation. In warm dark matter models the temperature of dark matter particles is chosen to make free-streaming length correspond to subgalactic scales $\lambda_{FS} \sim 0.1\,h^{-1}$ Mpc (see, for example, the discussion in Bode et al. 2001).

Small $k$ modes enter the horizon and are causally connected later than large $k$ modes; they are therefore less susceptible to damping.

The scaling of the present day power spectrum $P(k) = AT_k^2 k^{n_s}$ can be inferred by considering the evolution of the perturbations as a function of the era in which the perturbation crosses the horizon:

$$P(k) \propto \begin{cases} k^{n_s-4} & k \gg k_{eq}, \\ k^{n_s} & k \ll k_{eq}. \end{cases}$$

The power spectrum is normalised by $\sigma_8$ the root mean square deviation of density fluctuations within an $8\,h^{-1}$ Mpc sphere at $z = 0$. The spectral index $n_s$ and normalisation $\sigma_8$ are key cosmological parameters which fully determine the fluctuation power spectrum. The matter power spectrum (at $z = 0$) for $WMAP7$ cosmological parameters is shown in figure 2.4.

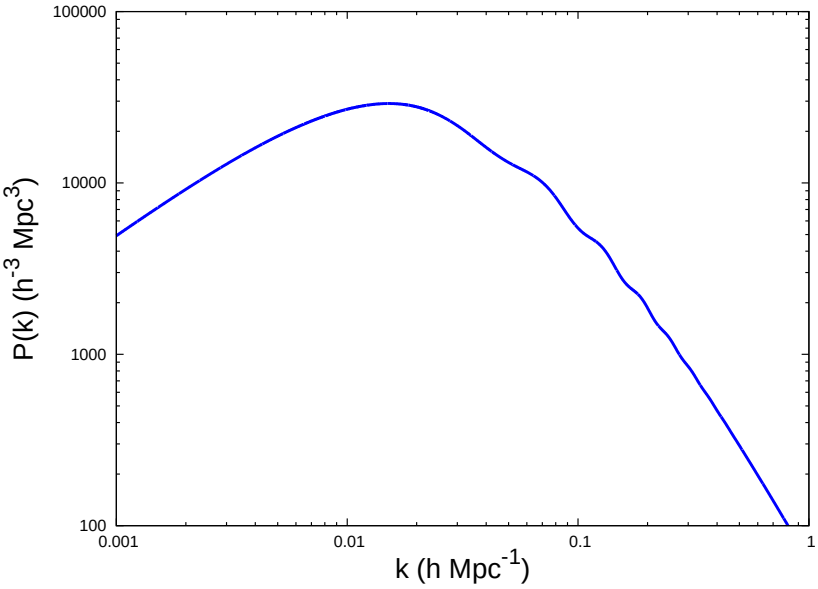


Figure 2.4: The matter power spectrum (at $z = 0$) computed using CAMB (Lewis et al. 2000) for the *WMAP*7 cosmology Komatsu et al. (2011).

If there is significant power at arbitrarily short wavelengths, structure will be present at arbitrarily small scales. Consequently every structure would consist of smaller and smaller substructures. There are several physical processes that act to dampen baryonic fluctuations on small scales. CDM, however, is cold and collisionless and experiences no such damping (or filtering) processes. To treat the formation of structure of a characteristic size, an artificial filter needs to be applied (see section 2.2.5).

Before recombination perturbations do not grow as photon pressure opposes collapse; as baryons are dynamically coupled to photons perturbation growth is suppressed. The perturbations oscillate as acoustic waves. At recombination photons are released but a preferred length scale for both components remains established – the distance propagated by a sound wave since the Big Bang. This is evident, in the case of photons, in the peaks of the temperature anisotropy spectrum. The baryons mix with non-oscillating dark matter and a faint signature of the characteristic length scale is imprinted on the clustering of matter. The preferred length scale depends on the speed of sound in the plasma and the time scales of the early Universe (parameters that can be measured using observations of the acoustic peaks in the CMB) and is thought to be

$\sim 140$ Mpc (Eisenstein 2005). This length scale is apparent as a peak in the two-point correlation function and can be seen as a series of faint wiggles in the power spectrum (BAOs).

### 2.2.3 Zel'dovich Approximation

An efficient method for setting up initial conditions from a given power spectrum is provided by the Zel'dovich (1970) formulation of linear evolution of a general distribution of fluctuations. This formalism provides a first order approximation to Lagrangian perturbation theory (LPT). Formalisms involving second order approximations (2LPT) are also considered for large scale simulations (as in Jenkins 2010). The simulations considered in this work are small enough that the first order approximation will suffice; for this reason only the Zel'dovich approximation is discussed here (following the approach given in White 1996).

The density contrast expressed in terms of the growth factor equation (2.32) implies that density grows self-similarly with time. Substituting equation (2.32) into Poisson's equation (2.26) shows that this is also true for the gravitational acceleration $\nabla\phi$. The gravitational potential $\phi$ scales with the expansion factor $a$ as

$$\phi\left(\mathbf{x}, z\right) = \frac{D(z)}{a}\phi_0\left(\mathbf{x}\right), \tag{2.34}$$

where $\phi_0$ fulfils the perturbed Poisson equation (2.26)

$$\nabla^2\phi_0\left(\mathbf{x}\right) = 4\pi G\bar{\rho}a^3\delta_0\left(\mathbf{x}\right). \tag{2.35}$$

In an Einstein-de Sitter universe (where $\Lambda = P = 0$) $D \propto a$, implying that $\phi$ is independent of the conformal time $\eta$ (where $a\mathrm{d}\eta = \mathrm{d}t$). The linearised version of Euler's equation (2.25) can be integrated with respect to $\eta$ as follows:

$$\mathbf{v} = -\left(a^{-1}\int D\mathrm{d}\eta\right)\nabla\phi_0 = -\left(D^{-1}\int D\mathrm{d}\eta\right)\nabla\phi. \tag{2.36}$$

Note that the peculiar velocity $\mathbf{v}$ is proportional to the current gravitational acceleration $\nabla\phi$. A second integration yields

$$\mathbf{x} = \mathbf{x}_0 - \left( \int \frac{\mathrm{d}\eta}{a} \int D \mathrm{d}\eta \right) \nabla\phi_0. \tag{2.37}$$

Since $D(\eta)$ satisfies the linearised version of the perturbation growth equation (2.27) $a\ddot{\delta} + \dot{a}\dot{\delta} = 4\pi G\bar{\rho}a^3\delta$ the double integral is proportional to $D$ and the above equations can be written as

$$\mathbf{x} = \mathbf{x}_0 - \frac{D(\eta)}{4\pi G\bar{\rho}a^3}\nabla\phi_0, \tag{2.38}$$

$$\mathbf{v} = -\frac{\dot{D}(\eta)}{4\pi G\bar{\rho}a^2}\nabla\phi_0 = -\frac{1}{4\pi G\bar{\rho}a^2}\frac{a\dot{D}}{D}\nabla\phi, \tag{2.39}$$

where the scaling relation (2.34) has been used in the last step.

Given a displacement $\mathbf{x} - \mathbf{x}_0$ and the peculiar velocity $\mathbf{v}$ of every particle, this formalism describes the growth of structure as a function of its initial position $\mathbf{x}_0$. Zel'dovich (1970) proposed that these equations could be extrapolated to describe the evolution of structure when displacements are no longer small. Given the growth of structure (as described by the power spectrum), this approximation can be used to establish the initial positions and velocities of a particle distribution and is used to set up the initial conditions for the simulations used in this thesis.

### 2.2.4 Non-Linear Collapse and the Definition of Haloes

When perturbations grow to the point $\delta\rho/\rho \gtrsim 1$ linear perturbation theory breaks down. While a full treatment of the non-linear regime can only be computed numerically (discussed in the next chapter), simple approximations to this complicated era are considered here in order to define what is meant by a halo.

The simplest approximation for non-linear growth is given by the spherical top-hat collapse model (discussed in many texts including Kolb and Turner 1993). The spherical top-hat model considers a spherical region with uniform overdensity $\bar{\delta}$ and

radius $r$ in an otherwise uniform background described by a flat homogeneous matter dominated FRW model.

The spherical region will decouple from the expansion at 'turn-around' and will begin to collapse. Taylor expanding the parametric solutions of the energy equation

$$E = \frac{1}{2}\dot{r} - \frac{4}{3}\pi G\rho r^2, \tag{2.40}$$

shows that the overdensity $\delta\rho/\rho = 9\pi^2/16$ at 'turn-around'. After reaching this maximum size, the region will collapse and virialise. Such virialised structures are known as *haloes*. After virialisation the kinetic energy is equal to half the gravitational potential energy. Equating the total energy before and after virialisation (assuming no dissipative forces) one finds that $r_{vir} = r_{max}/2$. Since 'turn-around' the region has halved its size, correspondingly its density has increased by a factor of 8. In the time since 'turn-around' the universe has expanded by $2^{2/3}$ and is therefore less dense by a factor of 4. Hence, in an Einstein-de Sitter model virialised haloes have overdensities of $\Delta_c = \rho/\rho_{\rm crit} = 18\pi^2 \approx 200$.

Spherical collapse within open, low mass-density universes with $\Omega_\Lambda = 0$ is considered in Lacey and Cole (1993a) and in a flat ΛCDM universe with $\Omega_r = 0$ in Eke et al. (1996). Bryan and Norman (1998) provide a simple quadratic fit for the overdensity, normalising from simulations. They find

$$\Delta_c = 18\pi^2 + 82x - 39x^2, \tag{2.41}$$

where $x = \Omega(z) - 1$, $\Omega(z) = \Omega_m (1+z)^3 / E(z)^2$ and

$$E^2 = \Omega_m (1+z)^3 + \Omega_r (1+z)^2 + \Omega_\Lambda. \tag{2.42}$$

In the standard cosmology $\Delta_c \sim 92.5$ at $z = 0$ and $\Delta_c \sim 168$ at $z = 2$.

Haloes and their boundaries can be defined by an overdensity $\Delta$ and the radius $r_\Delta$ at which the overdensity is reached. The mass contained within the radius of this sphere

is $M_\Delta = \frac{4}{3}\pi r_\Delta^3 \Delta \rho_{crit}(z)$, where the mean internal density is $\Delta$ times the critical density at that redshift. The virial radius $r_\Delta = r_{vir}$ and associated virial mass, $M_\Delta = M_{vir}$ are defined by setting $\Delta = \Delta_c$ from the spherical top-hat collapse model. Extensions to this model such as the ellipsoid top-hat model will not be considered here.

### 2.2.5 Statistics of Hierarchical Clustering

In order to follow the evolution of dark matter haloes one requires an understanding of hierarchical clustering. As discussed in White (1996), this allows one to address fundamental issues such as the the origin of the mass function of galaxies and galaxy clusters, the differences between galaxies and clusters despite the fact they both form via gravitational collapse, rates of mergers and the relationship between a galaxy and its large-scale environment. There are two general approaches which have been used to this effect: the peak-formalism and Press-Schechter theory (Press and Schechter 1974). Both of these approaches assume Gaussian random field initial conditions.

The peak formalism assumes that the matter that will eventually collapse to form a halo can be identified by locating peaks in the initial density field after smoothing with a filter of an appropriate scale. Haloes are defined as regions where high density peaks have risen above a fixed collapse threshold. This naturally introduces a bias in that haloes will be tend to cluster in high density regions. This approach is detailed in Bardeen et al. (1986) where statistical peak properties (such as height and shape) are used to calculate the abundance and clustering properties of objects.

The second approach is based on the theory developed by Press and Schechter (1974) and extended by Sheth and Tormen (2004). In this approach, the density field is smoothed by a top-hat filter function; density perturbations that grow above a critical overdensity $\Delta_c$ collapse to form virialised haloes (as in the spherical top-hat model). This method provides an analytic form for mass distribution of non-linear objects and has been used extensively in the literature. The excursion set formalism is used to follow the evolution of the abundance of bound haloes.

More accurate versions of the mass function of dark matter haloes are measured from large sets of cosmological simulations (see Jenkins et al. 2001; Tinker et al. 2008.)

## 2.3 Successes of the ΛCDM Model

The standard cosmological model provides many testable predictions that may be compared to observations; some of these comparisons are briefly highlighted here.

GR itself has proved remarkably accurate in providing testable predictions including the gravitational redshift of spectra, deflection of light by the sun and the precession of perihelia of the orbits of inner planets. The Big Bang model predicts the expansion of the Universe as described by Hubble's law, the homogeneity of the galaxy distribution on large scales observed in deep redshift surveys and the isotropy of the radio-galaxy distribution. The age of the Universe as determined from globular clusters appears in agreement with the expansion time-scale of the Universe. The strongest evidence for this model is provided by the existence of CMB seen at redshift $\sim 1100$ (Spergel et al. 2003), the $\sim$3K blackbody spectrum with a high degree of isotropy ($10^{-5}$ apart from the dipole). Furthermore predictions of Big Bang nucleosynthesis and primordial abundances are consistent with observations (Olive et al. 2000). The abundance of light elements agree with the predictions of a $\Omega_b \sim 0.05$ universe containing three neutrino species.

The ΛCDM model also successfully explains the power spectrum of low redshift galaxy distribution (Percival et al. 2002; Tegmark et al. 2004), the non-linear mass distribution at low redshift as characterised by cosmic shear (Van Waerbeke et al. 2002) and the structure seen in the Lyman alpha forest (Mandelbaum et al. 2003). It is consistent with the mass budget for the present Universe inferred from dynamics of large-scale structure (Peacock et al. 2001) and is successful in explaining the baryon fraction in rich clusters (White et al. 1993). ΛCDM also provides an explanation for the present acceleration of the cosmic expansion inferred from supernovae observations (Riess et al. 1998; Perlmutter et al. 1999).

## 2.4 Some Outstanding Issues

While ΛCDM simulations agree well with observations at cluster scales, on smaller scales simulations predict far more substructure than observed. In the Milky Way, hundreds of subhaloes are predicted starting from earlier semi-analytical studies (Kauffmann et al. 1993), to more recent high-resolution simulations (Klypin et al. 1999; Moore et al. 1999; Ghigna et al. 2000; Gao et al. 2004b,a; Diemand et al. 2007b). A few years ago, there were only a dozen or so satellites known, much smaller than the predicted number. However, very recently, a new population of satellites in the SDSS (Belokurov et al. 2007) has been discovered. It should be noticed though that these satellites are compact, and in general much fainter than the previously known ones, thus it is not clear whether the new population of satellite galaxies can completely remove the discrepancy. It is also possible that many of the subhaloes are dark due to inefficient star formation (Efstathiou 1992), for example, due to the suppression of star formation by the UV-background radiation (Kravtsov et al. 2004).

Numerical simulations of dark matter haloes predict that the dark matter density distribution follows an NFW profile (Navarro et al. 1995, 1996) which diverges towards the centre as $\rho \propto r^{-1}$. However rotation curves of dwarf and low surface brightness galaxies indicate a constant matter distribution within the central regions. This is known as the 'cusp/core' problem. Recent hydrodynamical simulations such as Oh et al. (2010) suggest that baryonic feedback processes play a role in reconciling these results.

Another challenge identified by numerical simulations is the formation of realistic disc galaxies, termed the *angular momentum catastrophe* (Navarro and Benz 1991). Angular momentum loss in the simulations results in small, highly concentrated discs. Dynamical friction from the interaction of merging subhaloes is thought to contribute significantly to this angular momentum loss. Piontek and Steinmetz (2010) propose that feedback is fundamentally important in creating more realistic disc galaxies models.

There are many other outstanding issues that will not be discussed here, including, but not limited to, inflationary cosmology, baryogenesis and the nature of dark energy.

# 3

# Numerical Simulations

Due to the non-linear nature of the small-scale mass distribution and the complexity of the hydrodynamical processes, simple, analytic solutions are generally not applicable to the description of the evolution of density fluctuations in the Universe. Supercomputer simulations are thus essential for the construction of realistic models of galaxy formation. Advances in computing power and the efficiency of implemented algorithms have resulted in a rapid increase in the applicability of such simulations. Galaxy formation and evolution studies have benefited greatly from these rapid advances.

In this chapter commonly implemented simulation techniques are reviewed, starting from the approaches used in $N$-body methods to the applications of smoothed particle hydrodynamics (SPH). The $N$-body/SPH code most commonly used in cosmological simulations, GADGET, is also discussed; this code was used to perform the simulations analysed in this thesis. A brief discussion on how haloes are identified within these simulations and how their evolution may be tracked over time is also presented, and the basic foundations of semi-analytic models of galaxy formation reviewed. This chapter is concluded with a discussion of the cosmological simulations that form the basis of the work presented in this thesis: the Millennium Simulation (one of the largest $N$-body cosmological simulations run to date) and the OverWhelmingly Large Simulations OWLS (a set of state-of-the-art, high-resolution cosmological simulations run with SPH). These simulations are used, in the following chapters, to

explore the structure and dynamics of ΛCDM haloes.

## 3.1 Overview

Rapid advances in computational power have been key to the development of cosmological simulations. The first freely programmable computer was the Zuse Z1, a binary, electrically driven mechanical calculator named after its creator Konrad Zuse. The Z1, developed in 1938, had limited programmability and performed approximately 1 floating point operation per second (flop/s). The ASTRON-LOFAR Blue Gene P supercomputer used for the OWLS simulations consists of 3072 4-core compute nodes, each with 2 Gbytes of memory. This 12288 core system is installed at the University of Groningen and performs at 27.45 Tflop/s. It was placed $6^{\text{th}}$ in the top 500 list in 2005, and was, in May 2010, ranked at number 407. In this listing the current fastest supercomputer is the Jaguar Cray XT5-HE Opteron, a six core 2.6 Ghz 1759 Tflop/s machine. Sequoia, a 20 Pflop/s machine with 1.6 million cores and 1.6 Pbytes of memory is expected to be deployed in 2011.

In initial attempts to simulate galaxy formation, galaxy collisions were first modelled using a system of 37 light bulbs (Holmberg 1941). The light intensity was used as a proxy for the gravitational force, since both are proportional to the inverse-square of the distance from the source. Photocells were used to measure the direction and magnitude of the 'gravitational force'. In this way, planar encounters between disc galaxies were first modelled. Early computer simulations such as those of von Hoerner (1963) and Aarseth (1963) evolved systems of 25 to 100 particles. Much progress was made during the 1980s with the development of particle-mesh codes and the tree method (discussed below). These algorithmic advances were coupled with the exponential growth of CPU speed. Codes were parallelised and specialised hardware such as GRAPE (GRavityPipE) boards (Makino et al. 1997) were developed. Currently, cosmological $N$-body simulations are performed with more than $10^{11}$ particles as in the Millennium XXL simulation run by the Virgo Consortium.

The rapid advances in computational power are expected to continue, especially with the introduction of double precision graphics processing units (GPUs), General-Purpose Computing on Graphics Processing units (GPGPU) and multi-GPU machines. Also, distributed computing projects such as MilkyWay@home (which achieves approximately 1.4 Pflop/s using 30000 personal computers) are now becoming viable options.

## 3.2 *N*-body Methods

An $N$-body problem is characterised as a system of $N$ point-like tracer particles. Particles are assigned a finite mass, and can be thought of as representing the mass distribution within a region of space. Each particle experiences a gravitational force due to its interaction with surrounding particles, and the evolution of the system can be tracked by using these forces to update the particles' positions and velocities. The $N$-body method is particularly suited to the evolution of matter that behaves as a self-gravitating collisionless fluid, and can be considered as a good approximation for dark matter and stars.

Gravitating systems that are effectively collisionless satisfy the coupled Vlasov and Poisson equations. Given a distribution function $f_i(\mathbf{r}, \mathbf{v})$ for any component $i$, with particles of mass $m_i$, position $\mathbf{r}_i$ and velocity $\mathbf{v}_i$ these equations are given by

$$\frac{\partial f_i}{\partial t} + \mathbf{v} \cdot \nabla f_i - (\nabla \phi \cdot \nabla_{\mathbf{v}}) f_i = 0, \tag{3.1}$$

$$\nabla^2 \phi = 4\pi G \rho(\mathbf{r}) = 4\pi G \bar{m}(\mathbf{r}) n(\mathbf{r}), \tag{3.2}$$

respectively, where $\nabla_{\mathbf{v}}$ is used to denote a gradient with respect to velocity $\mathbf{v}$ and the mean particle mass $\bar{m}(\mathbf{r})$ is defined to be

$$\bar{m}(\mathbf{r}) = \frac{1}{n(\mathbf{r})} \sum_{i=1}^{N} m_i \int f_i(\mathbf{r}, \mathbf{v}) \, \mathrm{d}^3\mathbf{v}. \tag{3.3}$$

The number density of particles is given by

$$n(\mathbf{r}) = \sum_{i=1}^{N} n_i(\mathbf{r}), \tag{3.4}$$

$$\text{where } n_i(\mathbf{r}) = \int f_i(\mathbf{r}, \mathbf{v})\, \mathrm{d}^3\mathbf{v}. \tag{3.5}$$

The acceleration is given by $\mathbf{a} = -\nabla\phi$. The essence of the problem lies in solving Poisson's equation (3.2). The main constraints on algorithms arise from balancing the computational cost of the simulation with the required resolution. Resolution and discreteness effects need to be considered carefully. In an $N$-body approach the potential consists of discrete particles and, as such, can be regarded as 'grainy'. Two-body encounters may alter the distribution function, causing the acceleration to deviate from the smoothed gravitational force (Binney and Spergel 1982). This would result in the violation of equation (3.1).

### 3.2.1 Direct-Summation Method

The simplest of the $N$-body approaches to calculating the forces on a system of particles is known as the Direct-Summation or Particle-Particle method. This technique was employed in early simulations such as those by Aarseth (1963). It involves calculating the force experienced by each particle by adding the contributions of every other simulated particle. The force is calculated as

$$\mathbf{F}_i = \sum_{\substack{j=1 \\ i \neq j}}^{N} \frac{G m_i m_j \left(\mathbf{r}_i - \mathbf{r}_j\right)}{\left(|\mathbf{r}_i - \mathbf{r}_j|^2 + \epsilon^2\right)^{3/2}}. \tag{3.6}$$

Force softening $\epsilon$ is added to prevent numerical instability and prevent two-body collisions from driving the simulation. Without force softening, particles are able to approach arbitrarily close to one another, in this case the denominator in (3.6) tends to zero and the force (and acceleration) will tend to infinity. Following the trajectory of a particle with an infinite acceleration would require an infinitely small time step.

Such a close physical interaction is unphysical as each particle represents a significant amount of mass. The underlying potential is the well-known Plummer potential $\phi_P \propto \left(r^2 + \epsilon^2\right)^{1/2}$ where $r = |\mathbf{r}|$. While accurate, this method scales as $N^2$ in computation time and quickly becomes unfeasible as particle numbers increase. The direct method is suited to situations where particle numbers do not exceed $\sim 1000$. However, purpose-built hardware, such as the GRAPE boards, have been designed to allow the computationally intensive force calculations to be done in hardware. The chip architecture is optimised to calculate gravitational interactions using the $1/r^2$ law and deliver Tflop/s performance (Sugimoto et al. 1990). GRAPE-6 boards have been used to simulate the evolution of 3–5 $\times 10^5$ particles within a month of computing time (Baumgardt and Makino 2003). GPUs are now also being used, they significantly improve computing power and provide a suitable alternative to GRAPE hardware.

### 3.2.2 Tree Method

A number of algorithmic approaches have been suggested to improve the efficiency of the force calculations. One such approach is the tree algorithm. This method involves grouping the particles of a simulation in a hierarchical manner which can reduce the computational cost to an $N \log N$ scheme. Construction of particle groups can be achieved by various means; a commonly used approach is described in Barnes and Hut (1986). Here each cubic region of space is divided into eight smaller cubes (or nodes), each with a length of half that of the original or parent cube. These eight smaller cubes are known as sibling nodes and are referred to as children of the parent node. This partitioning continues until the leaf nodes (nodes with no children) contain at most one particle. Every cube that is not a leaf node contains the multipole moments of all particles within that cube.

In order to compute the gravitational field at any point in the simulation, the tree is traversed and the force contributions from each cube (node) are summed. Depending on the required accuracy, the multipole expansion of the node may be used or the walk

along the tree may be continued. The accuracy of the simulation is controlled in this way by the 'cell opening criterion'. A maximum opening angle is defined and at each step in traversing the tree – the angle $\theta = l/x$, where $l$ is the branch length and $x$ the distance between the current particle and the centre of mass of the branch, is compared to the maximum opening angle. If the opening angle is larger than the maximum angle then the walk is continued. For small angles, since the force contributions of particles over long distances do not require high accuracy, the multipole expansion is used. Typically potentials are expanded to quadrupole order and a hierarchy of particles is constructed using a recursive binary splitting algorithm. Tree codes are particularly well suited to situations with a high level of clustering and are suitable for any geometry.

### 3.2.3 Particle-Mesh Methods

An alternative approach to circumvent the computational cost of the direct method is to use mesh-based codes which make use of Fourier techniques. Using Fourier transforms is particularly useful in reducing the computational cost of calculating the potential. In Fourier space the solution of Poisson's equation requires multiplication operations rather than more computationally expensive convolutions. Mesh-based codes are particularly well suited to nearly homogeneous mass distributions since the spatial resolution is uniform throughout the domain.

The Particle-Mesh (PM) method uses a grid implementation, where each particle is associated with a grid point (the association is done using particle-cell interpolation methods such as Cloud-In-Cell, Triangular Shaped Cloud etc.). Using these positions, the density at each grid point can be determined. Poisson's equation is solved using Fast Fourier Transform (FFT) methods to compute the potential at each grid point. The force for each grid point is simply the derivative of this potential. The force is then interpolated between grid points in order to establish the force on each particle. This method results in a considerable reduction in the computational cost, allowing a

computation time of the order $N \log N$. However, the required grid size (resolution) is an important factor to consider. Increasing the size of the grid improves the accuracy of the computation, but comes at a computational cost. The mesh size is analogous to the softening length, and increased resolution is achieved by using a finer mesh.

### 3.2.4 Hybrid Methods

The Particle-Particle-Particle-Mesh or $P^3M$ approach was developed by Efstathiou and Eastwood (1981); Efstathiou et al. (1985). This technique employs a hybrid approach of the methods described above in order to optimise the efficiency and resolution of a simulation. In this approach, short-range components (forces attributed to nearby particles – those within a specified radius $r_s$) are computed using the direct method, while long-range components are computed using the Particle-Mesh technique. This method combines the advantages of the direct method with those of the Particle-Mesh approach, allowing computations of large particle numbers with high resolution.

## 3.3 Self-Consistent Field Methods

A number of techniques that can be used to compute the gravitational potential of a system have been discussed above. However, most of these techniques are $N$-body methods, treating the particles as softened point masses. As galaxies are often regarded as collisionless systems, an estimate of the smooth mean gravitational field of the system is appropriate, allowing for the minimisation of the effects of discrete particle representations on the halo potential. One such approach is to expand the density and potential into a set of basis functions. If the first few terms of the basis are sufficient to provide a good representation of the system, then higher-order terms may be neglected, minimising the effects of discreteness (this is analogous to the softening introduced into the direct method).

The self-consistent field method was first applied by Clutton-Brock (1973) to stellar

dynamics. New implementations, using different basis functions sets, are described in Hernquist and Ostriker (1992) and Rahmati and Jalali (2009). Provided the set of basis functions is chosen appropriately to reproduce the underlying potential, this method provides higher accuracy at fixed computational cost than either the tree code or the Particle-Mesh approach. This method is not a replacement for $N$-body methods but a way of representing the potential as a continuously differentiable field. This is particularly useful for evaluating dynamics of particles within a smooth potential.

In this discussion only 'pure expansions' are considered, these are expansions of both the radial and angular dependencies of the potential into a set of basis functions. In Clutton-Brock (1973), a Plummer model is taken to be the zeroth-order term about which the expansion is performed, while in Hernquist and Ostriker (1992) a Hernquist profile is used. Both provide simple analytic functions for the density and potential of the system. The density $\rho$ and potential $\phi$ are expanded in terms of an orthogonal set of functions $\rho_{nlm}$ and $\phi_{nlm}$:

$$\rho(\mathbf{r}) = \sum_{nlm} A_{nlm}\, \rho_{nlm}(\mathbf{r}), \tag{3.7}$$

$$\phi(\mathbf{r}) = \sum_{nlm} A_{nlm}\, \phi_{nlm}(\mathbf{r}), \tag{3.8}$$

where $n$ can be thought of as the radial quantum number and $l, m$ the corresponding angular variable quantities. The set of basis functions $\rho_{nlm}$ and $\phi_{nlm}$ are required to satisfy Poisson's equation

$$\nabla^2 \phi_{nlm} = 4\pi \rho_{nlm}. \tag{3.9}$$

The zeroth-order terms in the expansion are taken from the underlying model. In Hernquist and Ostriker (1992) the zeroth-order terms are

$$\rho_{000} = \frac{1}{2\pi r\,(1+r)^3}, \tag{3.10}$$

$$\phi_{000} = -\frac{1}{1+r}, \tag{3.11}$$

derived from the Hernquist profile, where the quantities are defined to be dimensionless, the gravitational constant $G = 1$, mass $M = 1$ and the scale length $a = 1$. The scale length is then related to the half-mass radius of the model: $r_{1/2} = \left(1 + \sqrt{2}\right) a$.

As is standard, the angular dependencies of $\rho_{nlm}$ and $\phi_{nlm}$ are expanded in spherical harmonics $Y_{lm}(\theta, \phi)$. The $n = 0$ terms are defined to be

$$\phi_{0lm} = -\frac{r^l}{(1+r)^{2l+1}} \sqrt{4\pi} Y_{lm}(\theta, \phi), \tag{3.12}$$

$$\rho_{0lm} = \frac{(2l+1)(l+1) r^l}{2\pi r (1+r)^{2l+3}} \sqrt{4\pi} Y_{lm}(\theta, \phi), \tag{3.13}$$

inspired by the multipole expansion where $\phi_{0lm} \sim r^l Y_{lm}(\theta, \phi)$ as $r \to 0$ and $\phi_{0lm} \sim r^{-(l+1)} Y_{lm}(\theta, \phi)$ as $r \to \infty$. Here the factor $\sqrt{4\pi}$ is introduced so that in the spherical limit these equations reduce to the zeroth-order terms (3.10) and (3.11) for $l = m = 0$.

General terms where $n \neq 0$ are expressed as

$$\rho_{nlm}(r) = \frac{r^l}{2\pi r (1+r)^{2l+3}} K_{nl} W_{nl}(\xi) \sqrt{4\pi} Y_{lm}(\theta, \phi), \tag{3.14}$$

$$\phi_{nlm}(r) = -\frac{r^l}{(1+r)^{2l+1}} W_{nl}(\xi) \sqrt{4\pi} Y_{lm}(\theta, \phi), \tag{3.15}$$

where $W(\xi)$ are functions which include the higher-order radial dependence and $\xi$ is a radial transformation set for convenience as $\xi \equiv (r-1)/(r+1)$, transforming $r$ to compact coordinates $\xi$. The normalisation constant $K_{nl}$ is chosen so that the spherical limit given by (3.10) and (3.11) is reproduced. Hence $K_{0l} = (2l+1)(l+1)$ and $W_{0l}(\xi) = 1$.

Substituting the general expansions (3.14) and (3.15) into Poisson's equation (3.2) using compact coordinates $\xi$ one finds an ordinary differential equation which can be

used to constrain $W(\xi)$ and $K_{nl}$ as follows:

$$W_{nl}(\xi) = C_n^{(2l+3/2)}, \tag{3.16}$$

$$K_{nl} = \frac{1}{2} n(n+4l+3) + (l+1)(2l+1), \tag{3.17}$$

where $C_n^{(\alpha)}$ are the ultraspherical or Gegenbauer polynomials. In summary, the full basis sets for density and potential can be expressed as

$$\rho_{nlm}(r) = \frac{K_{nl}\, r^l}{2\pi r (1+r)^{2l+3}} C_n^{(2l+3/2)}(\xi)\ \sqrt{4\pi} Y_{lm}(\theta,\phi), \tag{3.18}$$

$$\phi_{nlm}(r) = -\frac{r^l}{(1+r)^{2l+1}} C_n^{(2l+3/2)}(\xi)\ \sqrt{4\pi} Y_{lm}(\theta,\phi). \tag{3.19}$$

Multiplying equation (3.7) by $\phi^*_{nlm}$ and using the bi-orthogonality of the basis functions (3.18) and (3.19), one can calculate the expansion coefficients $A_{nlm}$ in equations (3.7) and (3.8) as

$$A_{nlm} = \frac{1}{I_{nl}} \int \rho(\mathbf{r}) \left[\phi_{nlm}(\mathbf{r})\right]^* \mathrm{d}^3\mathbf{r}, \tag{3.20}$$

where

$$I_{nl} = -K_{nl} \frac{4\pi}{2^{(8l+6)}} \frac{\Gamma(n+4l+3)}{n!\,(n+2l+3/2)\left[\Gamma(2l+3/2)\right]^2}, \tag{3.21}$$

and

$$\rho(r,\theta,\phi) = \sum_{k=1}^{N} \frac{m_k}{r_k^2} \delta(r-r_k)\,\delta(\phi-\phi_k)\,\delta(\cos\theta - \cos\theta_k). \tag{3.22}$$

## 3.4 Simulating Gas Dynamics

When simulating gas dynamics standard hydrodynamic equations need to be solved in addition to Poisson's equation. There are two commonly-used approaches to dealing with this problem.

One method for simulating gas dynamics is to use mesh-based codes which are based on an Eulerian approach, describing changes as they occur at a fixed point in the field. Adaptive meshes are used to overcome the limitations of the Particle-Mesh

method. Mesh-based codes revolutionised the computational fluid dynamics world during the 1960s and 1970s and have dominated since in that they remain the most widely used approach. Mesh-based techniques can be found in many different applications such as mechanical, civil and aerospace engineering, architecture, chemical reaction modelling and protein folding. Mesh-based codes are well developed, well established, robust and mature (both mathematically and algorithmically).

While these codes are remarkably good for confined computational domains and computations where boundaries are not moving, they do have their limitations. Generating an intricate mesh can be very expensive and time-consuming and requires great experience. Also, mesh codes find highly non-linear deformations of the fluid notoriously difficult to handle. An alternative is offered by smoothed particle hydrodynamics. Gas is discretised into particles and gravitational interactions are computed as for dark matter and stars. In addition to their mass, position and velocity, gas particles also contain additional information about their intrinsic properties (such as internal energy and temperature). As this technique has been used to perform the simulations used in this thesis it is discussed in more detail below.

### 3.4.1 Smoothed Particle Hydrodynamics

SPH describes a fluid by replacing its continuum properties with locally smoothed particles at discrete Lagrangian locations. It does not consider fixed spatial positions but evolves the fluid equations in a comoving frame. SPH was invented by Lucy (1977) and Gingold and Monaghan (1977) in order to simulate non-axisymmetric events in astrophysical systems and is now implemented in many different fields. The SPH method is a meshless particle method which uses analytic differentiation of interpolation formulae to calculate spatial derivatives. The equations of momentum and energy become sets of ordinary differential equations which are intuitively simple to understand in terms of mechanical and thermodynamical terms. SPH was designed to be easy to utilise and to provide reasonable accuracy. SPH is robust and easily extendable

to complicated physical problems, and is well suited to the complicated conditions which tend to limit mesh-based codes.

The fundamental framework of SPH relies on an interpolation method, allowing any function to be expressed in terms of the values of a set of particles. The value of a function $A(\mathbf{r})$ at a point $\mathbf{r}$ in space can trivially be expressed as

$$A(\mathbf{r}) = \int_V \delta(\mathbf{r} - \mathbf{r}') A(\mathbf{r}') \, \mathrm{d}^3\mathbf{r}', \tag{3.23}$$

where $V$ defines the interpolation volume and $\delta(\mathbf{r} - \mathbf{r}')$ is the Dirac delta function which fulfils the identity $\int \delta(\mathbf{r} - \mathbf{r}') \, \mathrm{d}^3\mathbf{r}' = 1$. Unfortunately a delta function is not computationally useful as it is infinitesimally narrow; instead SPH uses an interpolation procedure in which the delta function is approximated with a weighting function $W$ called the smoothing kernel (which is usually spherically symmetric). The integral SPH averaged quantity $\langle A(\mathbf{r}) \rangle$ can be written as

$$\langle A(\mathbf{r}) \rangle = \int_V W(|\mathbf{r} - \mathbf{r}'|, h) A(\mathbf{r}') \, \mathrm{d}^3\mathbf{r}', \tag{3.24}$$

where the kernel $W$ is subject to the following constraints: the normalisation condition; that it tends towards the delta function and that it is $k$-times differentiable (with a continuous first derivative). These can be expressed as follows:

$$\int_V W(|\mathbf{r} - \mathbf{r}'|, h) \, d^3\mathbf{r}' = 1, \tag{3.25a}$$

$$\lim_{h \to 0} W(|\mathbf{r} - \mathbf{r}'|, h) = \delta(\mathbf{r} - \mathbf{r}'), \tag{3.25b}$$

$$W(|\mathbf{r} - \mathbf{r}'|, h) \in C_0^k. \tag{3.25c}$$

The kernel $W$ depends on the interpolation distance $|\mathbf{r} - \mathbf{r}'|$ between particles and the characteristic smoothing length $h$. This smoothing length defines the extent of the kernel and can either be kept constant or evolved during the simulation.

The discretised version of equation (3.24) is given by

$$A(\mathbf{r}) \approx \sum_{j=1}^{N} A\left(\mathbf{r}_j\right) W\left(|\mathbf{r}-\mathbf{r}_j|, h\right) \frac{m_j}{\rho_j}, \tag{3.26}$$

where $\mathrm{d}^3\mathbf{r}'$ in (3.24) becomes the volume of the $j^{th}$ particle $V_j = m_j/\rho_j$. The sphere of influence is defined as $W(|\mathbf{r}-\mathbf{r}'| \geq h) = 0$. The summations are formally over all particles, but a suitable choice of $W$ will result in a rapid fall-off in the contributions from particles beyond $|\mathbf{r}-\mathbf{r}_j| \geq h$, and only particles within the sphere of influence need to be considered when computing the function. The density is estimated as

$$\rho(\mathbf{r}) = \sum_j m_j W\left(|\mathbf{r}-\mathbf{r}_j|, h\right). \tag{3.27}$$

A key advantage of the SPH method is that the smoothing kernel $W$ can be chosen to suit the problem, providing the accuracy required within the given computational constraints. Common choices for the smoothing kernel include: Gaussian, cubic spline, quadratic as well as higher order kernels. In terms of physical interpretations of the SPH equations, a Gaussian kernel is the best choice. However, spline kernels have proven more computationally efficient. For the sake of brevity, only the cubic spline kernel used in GADGET will be described here. This is a third-order smoothing kernel defined as

$$W(q,h) = \alpha_D \begin{cases} 1-6q^2+6q^3 & 0 \leq q \leq 0.5, \\ 2(1-q)^3 & 0.5 \leq q \leq 1, \\ 0 & q \geq 1, \end{cases}$$

where $q = |\mathbf{r}-\mathbf{r}'|/h$ and $\alpha_D \equiv 8/\left(\pi h^3\right)$. This kernel approximates the Gaussian closely and is computationally cheap.

The spline-softened gravitational potential $\phi_{cubic}$ resulting from the smoothed density distribution $\rho(q) = MW(q,h)$ is given by

$$\phi(q) = G\frac{M}{h} W_2(q,h), \tag{3.28}$$

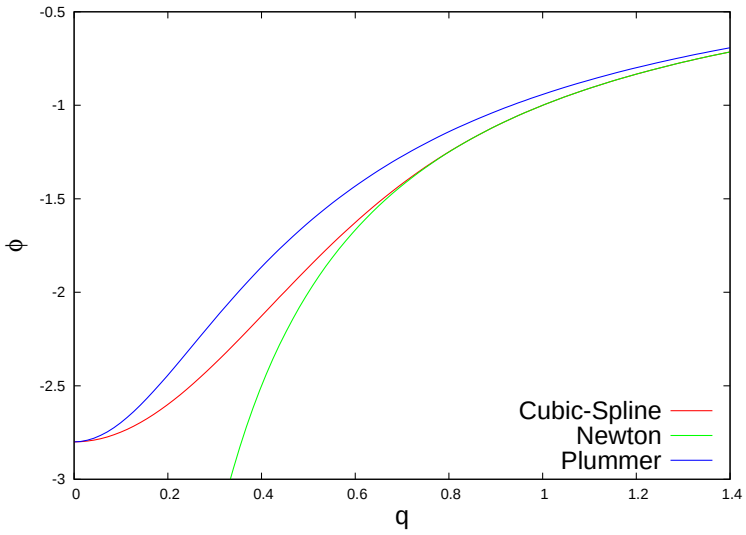


Figure 3.1: As in Springel et al. (2001b), a comparison between the cubic-spline softened potential $\phi_{cubic} = GM/hW_2(q,h)$, the Plummer softened potential $\phi_P = -GM/q$ and the Newtonian potential $\phi_N = -GM/qh$. Here $G = M = h = 1$, the force softening $\epsilon = h/2.8$ and $W_2(q,h)$ is defined in equation (71) of Springel et al. (2001b).

where the kernel $W_2(q,h)$ is defined in equation (71) of Springel et al. (2001b). Figure 3.1 illustrates this potential and compares it with the Newtonian potential $\phi_N$ and a Plummer potential $\phi_P$. The spline-softened potential $\phi_{cubic}$ approaches the Newtonian limit rapidly, converging beyond $2.8\epsilon$, where $\epsilon$ is the force softening described in section 3.2. The Plummer potential converges more slowly becoming Newtonian at large distances. Using a smoothed potential ensures that the potential is well-defined at the origin, avoiding numerical instabilities.

Since the kernel is known a priori, its gradient is known and the gradient of any scattered data can be calculated with ease. One can write

$$\nabla A(\mathbf{r}) = \sum_{j=1}^{N} m_j \frac{A_j}{\rho_j} \nabla W\left(|\mathbf{r} - \mathbf{r}_j|, h\right). \tag{3.29}$$

In SPH, operators $\mathbf{A}$ are written (for convenience and accuracy) using the following identity:

$$\nabla \cdot (\rho \mathbf{A}) = \rho (\nabla \cdot \mathbf{A}) + \mathbf{A} \cdot \nabla \rho. \tag{3.30}$$

For example, to express the divergence of $\mathbf{A}$ one can write

$$\nabla \cdot \mathbf{A} = \left[\nabla \cdot (\rho \mathbf{A}) - \mathbf{A} \cdot \nabla \rho\right] / \rho, \tag{3.31}$$

then the divergence of $\mathbf{A}$ at particle $i$ can be written as

$$\rho_i \left(\nabla \cdot \mathbf{A}\right)_i = \sum_j \left(\mathbf{A}_j - \mathbf{A}_i\right) \cdot \nabla_i W_{ij}, \tag{3.32}$$

where $\nabla_i W_{ij}$ denotes the gradient of $W\left(|\mathbf{r}_i - \mathbf{r}_j|, h\right)$ with respect to the coordinates of particle $i$. The computational cost of this approach is in the interpolation procedure. Typically each particle interacts with $\sim 50$ particles (its nearest neighbours).

The basic equations of motion, the continuity, momentum and thermal energy equations, can be formulated as follows:

$$\left\langle \frac{\mathrm{d}\rho_\mathrm{i}}{\mathrm{dt}} \right\rangle = \sum_j m_j \left(\mathbf{v}_i - \mathbf{v}_j\right) \cdot \nabla_i W_{ij}, \tag{3.33}$$

$$\left\langle \frac{\mathrm{d}\mathbf{v}_\mathrm{i}}{\mathrm{dt}} \right\rangle = \sum_j m_j \left(\frac{p_j}{\rho_j^2} + \frac{p_i}{\rho_i^2}\right) \nabla_i W_{ij}, \tag{3.34}$$

$$\left\langle \frac{\mathrm{dE_i}}{\mathrm{dt}} \right\rangle = \frac{1}{2} \sum_j m_j \left(\frac{p_j}{\rho_j^2} + \frac{p_i}{\rho_i^2}\right) \mathbf{v}_{ij} \cdot \nabla_i W_{ij}, \tag{3.35}$$

where $E_i$ denotes the energy of the particle $i$. The pressure gradient term $\nabla p / \rho$ has been symmetrised and rewritten as

$$\frac{\nabla p}{\rho} = \nabla \left(\frac{p}{\rho}\right) + \frac{p}{\rho^2} \nabla \rho, \tag{3.36}$$

to ensure conservation of linear and angular momenta.

Due to the fact that the smooth nature of SPH notoriously struggles to track shocks, an artificial viscosity term is added to the momentum and energy equations. Positions

$\mathbf{r}_i$ and velocities $\mathbf{v}_i$ of the particle $i$ are evolved using

$$\frac{\mathrm{d}\mathbf{r}_i}{\mathrm{d}t} = \mathbf{v}_i. \tag{3.37}$$

The momentum equation (3.34) rewritten with an artificial viscosity term $\Pi_{ij}$ reads as follows (Monaghan 1992):

$$\frac{\mathrm{d}\mathbf{v}_i}{\mathrm{d}t} = -\sum_j m_j \left( \frac{p_j}{\rho_j^2} + \frac{p_i}{\rho_i^2} + \Pi_{ij} \right) \nabla_i W_{ij}, \tag{3.38}$$

where

$$\Pi_{ij} = \begin{cases} \dfrac{-\alpha \bar{c}_{ij} \mu_{ij} + \beta \mu_{ij}^2}{\bar{\rho}_{ij}} & \text{for } \mathbf{v}_{ij} \cdot \mathbf{r}_{ij} < 0, \\ 0 & \text{for } \mathbf{v}_{ij} \cdot \mathbf{r}_{ij} > 0. \end{cases}$$

and $\mathbf{r}_{ij} = \mathbf{r}_i - \mathbf{r}_j$ ($\mathbf{v}_{ij}$ is defined analogously). The mean sound speed is denoted as $\bar{c}_{ij}$ and

$$\mu_{ij} = \frac{h \mathbf{v}_{ij} \cdot \mathbf{r}_{ij}}{\mathbf{r}_{ij}^2 + \eta^2}. \tag{3.39}$$

The constants $\alpha$, $\beta$ and $\eta$ are introduced to prevent over-smoothing of the viscous term $\Pi_{ij}$ in high-density regions. Values of $\alpha = 1, \beta = 2$ and $\eta^2 = 0.01h^2$ have been shown to provide good results (Monaghan 1992). The expression for the artificial viscosity consists of a linear velocity difference term which produces a shear and bulk viscosity (Monaghan and Lattanzio 1985), and a quadratic term to cope with high Mach number shocks. Tests show that, with this viscosity term, the shock fronts are spread over $\sim 3h$.

## 3.5 GADGET

The most commonly used $N$-body code is GADGET (GAlaxies with Dark matter and Gas intEracT). All of the simulations that were used in this thesis employed the GADGET code to evolve the simulations. GADGET is a tree-SPH code in which the gravitational interactions are computed using a tree method (section 3.2.2) and the baryonic

component is followed using SPH (section 3.4.1). For a full description of the code the reader is referred to Springel et al. (2001b) and Springel (2005). In this section the basic formalism of the code is discussed, and a description of how the dynamics of collisionless and baryonic particles evolve under gravity within an expanding space (section 2.1) is given.

### 3.5.1 Collisionless Particles and Hydrodynamics

Stars and dark matter are treated as collisionless particles. The single particle density distribution function $\tilde{\delta}(\mathbf{x})$ is given by the convolution of the Dirac function with a normalised gravitational softening kernel of comoving scale $\epsilon$. As in SPH a cubic spline kernel is used and $\tilde{\delta}(\mathbf{x}) = W(|\mathbf{x}|, 2.8\epsilon)$. Spline softening becomes exactly Newtonian for $|\mathbf{x}| > h$. For collisionless $N$-body simulations, low force accuracy is required. Provided the intrinsic force errors are random, errors of up to a few percent only increase numerical relaxation slightly (Hernquist et al. 1993).

Particle smoothing lengths $h_i$ are adaptive and defined so that the kernel volume contains a constant mass for the estimated density i.e.

$$\frac{4\pi}{3} h_i^3 \rho_i = N_{\mathrm{SPH}} \bar{m}, \tag{3.40}$$

where $N_{\mathrm{SPH}}$ is the typical number of smoothing neighbours, and $\bar{m}$ the average particle mass.

GADGET optionally allows the user to replace the pure tree method with a TreePM method in which the long-range forces are computed using mesh-based Fourier techniques and the short-range forces are computed using a tree code. For the PM method GADGET uses a clouds-in-cells method (Hockney and Eastwood 1981) to assign particles to grid points.

Baryons are initially described as an ideal gas where particles can be thought of as fluid element tracers and are treated using SPH with a cubic spline kernel. Their evolution is governed by the Euler equation. The particle pressure $P_i$ is given by the

ideal gas equation of state

$$P_i = A_i \rho_i^{\gamma} = (\gamma - 1)\rho u_i, \tag{3.41}$$

where $\gamma$ is the specific heat (equal to 5/3 for an ideal monatomic gas) and $u$ is the thermal energy per unit mass. GADGET uses an entropic function $A \equiv p/\rho^{\gamma}$ instead of the thermal energy per unit mass to define the thermodynamic state of each particle. The density of each particle $\rho$ is estimated at each step using (3.27).

The entropy formulation of the SPH equations, which conserves both energy and entropy (when required) by construction, was derived by Springel and Hernquist (2002). Smoothing lengths are adaptive and the smoothing volume is required to contain a fixed mass ($M_{SPH} = \bar{m} N_{SPH}$). In this formalism the equations of motion governing the evolution of the gas particles are derived from a Lagrangian subject to these constraints. They are given by

$$\frac{\mathrm{d}\mathbf{v}_i}{\mathrm{d}t} = -\sum_{j=1}^{N} m_j \left[ f_i \frac{p_i}{\rho_i^2}(h_i) + f_j \frac{p_j}{\rho_j^2}\left(h_j\right) + \Pi_{ij} \right] \nabla_i W_{ij}, \tag{3.42}$$

where

$$f_i = \left(1 + \frac{h_i}{3\rho_i}\frac{\partial \rho_i}{\partial h_i}\right)^{-1}, \tag{3.43}$$

and $\Pi_{ij}$ is the artificial viscosity term added to treat shocks as discussed in section 3.4.1. GADGET adopts a modified version of the artificial viscosity term

$$\Pi_{ij} = -\frac{\alpha\left(c_i + c_j - 3w_{ij}\right) w_{ij}}{2\rho_{ij}}, \tag{3.44}$$

where $w_{ij} = \mathbf{v}_{ij} \cdot \mathbf{r}_{ij}/|\mathbf{r}_{ij}|$, when particles approach each other $\left(\mathbf{v}_{ij} \cdot \mathbf{r}_{ij} < 0\right)$ and zero otherwise. In the absence of external heat sources (3.42) fully defines reversible fluid dynamics for small changes in state and the entropy $A_i$ remains constant. Entropy increases in the presence of external energy sources such as feedback or shocks. A decrease in entropy can be caused by radiative cooling. The thermal energy $u$ per unit

mass evolves according to the first law of thermodynamics as

$$\frac{\mathrm{d}u}{\mathrm{d}t} = -\frac{p}{\rho}\left(\nabla \cdot \mathbf{v}\right) - \frac{\Lambda\left(u,\rho\right)}{\rho}, \tag{3.45}$$

where $\Lambda\left(u,\rho\right)$ is a cooling function added to describe external sources (or sinks) of heat and the entropy $A_i$ is related to the thermal energy $u_i$ by $A_i = \left(\gamma - 1\right)/\rho^{\gamma-1}\rho u_i$. Even in the absence of shocks the added artificial viscosity term will irreversibly change the kinetic energy of gas into heat and raise the entropy $A$ as

$$\frac{\mathrm{d}A_i}{\mathrm{d}t} = \frac{\gamma - 1}{2\rho_i^{\gamma-1}} \sum_{j=1}^{N} m_j \Pi_{ij} \left(\mathbf{v}_i - \mathbf{v}_j\right) \cdot \nabla \bar{W}_{ij}, \tag{3.46}$$

where the symmetrised kernel $\bar{W}_{ij}$ (Hernquist and Katz 1989) is

$$\bar{W}_{ij} = \frac{1}{2}\left[W\left(|\mathbf{r}_{ij}|, h_i\right) + W\left(|\mathbf{r}_{ij}|, h_j\right)\right]. \tag{3.47}$$

### 3.5.2 Force Computation

The simulations follow the collapse of structure on sub-horizon scales and the Newtonian limit is sufficient. As shown in section 2.2.1 the growth of structure in this regime is governed by equation 2.27. Using comoving coordinates, Newton's equation of motion can be written as

$$\ddot{\mathbf{r}} + 2\frac{\dot{a}}{a}\dot{\mathbf{r}} = -\frac{G}{a^3}\int \frac{\delta\rho\left(\mathbf{r}'\right)\left(\mathbf{r} - \mathbf{r}'\right)}{|\mathbf{r} - \mathbf{r}'|^3}\mathrm{d}^3\mathbf{r}'. \tag{3.48}$$

In an $N$-body simulation with periodic boundary conditions the equation of motion for particle $i$ can be expressed as

$$\ddot{\mathbf{r}}_i + 2\frac{\dot{a}}{a}\dot{\mathbf{r}}_i = -\frac{G}{a^3}\sum_{\substack{j \neq i \\ \text{periodic}}} \frac{m_j\left(\mathbf{r}_i - \mathbf{r}_j\right)}{|\mathbf{r}_i - \mathbf{r}_j|^3}, \tag{3.49}$$

where the sum is computed over all periodic images of $j$.

Forces are computed using a tree code, in which only the monopole of the multipole expansion is considered. While this means that a smaller cell opening angle needs to be used (more interactions need to be computed), the evaluations are simple and the tree construction and storage is low.

Periodic boundary conditions are usually employed for cosmological simulations. To include force contributions from periodic images the tree walk is modified. Each mode is mapped to the position of the nearest periodic image with respect to the considered coordinate. The additional force exerted by all other periodic images is a slowly converging sum which is evaluated using an Ewald summation technique (Ewald 1921).

## 3.6 Identifying and Tracking Haloes

In this thesis virialised dark matter haloes are extracted from cosmological simulations and their properties analysed. Several different methods are available for the identification of such haloes. The simplest group-finder is the friends-of-friends (FOF) method (Davis et al. 1985) which links all particles closer than a predetermined linking length. Selecting the correct linking length is critical – choosing a value for the linking length that is too large will result in all particles being associated with a single group and a value which is too small will not identify any haloes. The common convention is to use a linking length of 0.2 times the mean interparticle spacing corresponding to a value of $\Delta = 178$ (section 2.2.4). One problem with this method is that it can occasionally link haloes which should be separated.

An alternate approach for selecting distinct haloes is to use the spherical overdensity algorithm (Lacey and Cole 1994). A sphere is grown around the minimum potential position of a halo until a specified mean internal density is reached, i.e. the radius of the sphere is chosen so that the enclosed density drops below a threshold value. The centre of the group is redefined as the centre of mass of the sphere and the process is repeated until the group centre and group membership converge. A spherical

overdensity (SO) halo consists of all particles within this sphere. The mass contained within the radius of the sphere ($r_\Delta$) is

$$M_\Delta = \frac{4}{3}\pi r_\Delta^3 \Delta\rho_{crit}(z), \tag{3.50}$$

where the mean internal density is $\Delta\rho_{crit}$. The virial mass $M_\Delta = M_{vir}$ and virial radius $r_\Delta = r_{vir}$ are defined by computing $\Delta$ from the spherical top-hat collapse model (section 2.2.4). In the standard cosmology $\Delta = 92.5$ at $z = 0$. Each ungrouped particle is selected as a group centre and the process is repeated. Groups selected in this manner that overlap or exist within other larger groups are combined into a larger group. This algorithm selects spherical regions.

Another common group-finder, used extensively in the literature, is SUBFIND. The algorithm identifies locally overdense, self-bound particle groups within a larger halo (previously identified using, for example, FOF). An example of the kind of substructure identified by SUBFIND is given in Figure 3.2. The SUBFIND algorithm (Springel et al. 2001a; Dolag et al. 2009) is then used to separate the FOF group into self-bound structures. The main halo itself is considered as the main SUBFIND structure and substructures associated with the main halo are recorded as subhaloes.

To follow the evolution of halo properties with redshift, a method is required to associate each halo with its progenitor haloes at previous timesteps in the simulation. Merger trees provide a way to track a particular halo back in time, and provide a description for the way in which structure builds up over time. The construction of merger trees is essential in tracing the evolution of structure, and is an important factor in semi-analytic modelling (discussed below).

There are two common methods for their construction. The first is based on Monte-Carlo realisations of mergers for individual objects by sampling the predicted masses of progenitors using the Press-Schechter formalism (see section 2.2.5), and is used by, for example Bond et al. (1991) and Lacey and Cole (1993b). The second uses merger trees drawn from $N$-body simulations and is discussed in detail in papers such

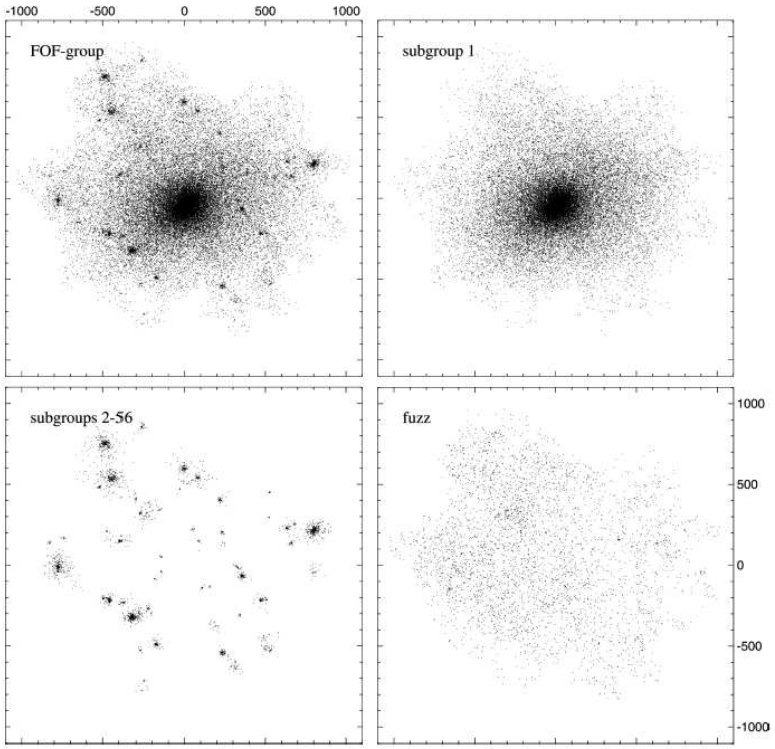


Figure 3.2: The top left image shows the FOF group identified at $z = 0$. Top right shows the largest substructure identified, this is taken to be the background halo. Lower left shows the 55 subhaloes identified from the FOF group. The subhaloes contribute 8% of the halo mass. Lower right depicts all of the particles which are not bound to any of the subhaloes. (Taken from Springel et al. 2001a). Spatial coordinates are given in units of $h^{-1}$ kpc.

as Kauffmann et al. (1993); Springel et al. (2001a); Baugh (2006); Parkinson et al. (2008). In this method merger trees are constructed as follows: a halo at redshift $z_{i-1}$ is said to be a progenitor of a halo at redshift $z_i$ if the $z_{i-1}$ halo contributes at least half of its particles to the halo at $z_i$, and the central (most bound) particle of the $z_{i-1}$ halo is contained within the halo at $z_i$. As haloes are expected to form hierarchically in ΛCDM, each halo may have several progenitors but only one descendant. It may happen that a halo identified at one redshift cannot be associated with any progenitor halo. In this case, the halo cannot be traced any further back.

## 3.7 Semi-Analytic Modelling

In general, the large volume required to produce a reliable cosmological simulation means that the resolution of the simulation will be limited. For this reason, and because of the complexity of the baryonic physics, most of the details of the baryonic physics involved in galaxy formation cannot be explored directly. Physical processes that cannot be resolved (subgrid physics) are implemented using simple analytic or empirical, physically motivated prescriptions to approximate the complicated physical processes involved in galaxy formation.

When simulating galaxy formation, an alternative to running SPH simulations is to rely solely on semi-analytic modelling for the description of the baryonic physics. Semi-analytic modelling involves the identification of dark matter haloes and the association of certain galactic properties with each. Separating the baryonic physics from the $N$-body simulation has many advantages.

Semi-analytic models provide a means to construct mock galaxy catalogues which can contain all of the spatial and kinematic information that would be present in a real redshift survey, allowing for a more direct comparison of dark matter only simulations with observations. They are, in many ways, equivalent to a full dynamical simulation, whilst avoiding the cost of repeating the computationally intensive $N$-body run every time assumptions about the baryonic physics are modified. This allows for rapid exploration of parameter space meaning that results of one run can be fed back into constraining parameters and influence the simplifying assumptions. Also, the dynamic range of the problems considered is not limited to the resolution of the $N$-body simulation. However, the simplifications will introduce uncertainties.

The modelling of galaxy formation is based on the hierarchical merging scenario described in White (1978). Initial work on this method was done by White and Frenk (1991); Cole (1991) and Lacey and Silk (1991). A comprehensive review on the subject can be found in Baugh (2006). Recent semi-analytic models have been very successful in reproducing a number of observables (De Lucia et al. 2004; Guo et al. 2010).

They are able to faithfully reproduce the luminosity function, the number counts, morphology, colour and size of galaxies, clustering strengths, background radiation contributions from ultraviolet to far-infrared and the observed relations between AGN and their host galaxies. The luminosity function is a fundamental description of a galaxy population and is well constrained by observations (Blanton et al. 2003). Feedback processes are required in order to fit both the faint and high ends of the luminosity function (see Granato et al. 2004; Croton et al. 2006; Bower et al. 2006). The inclusion of AGN feedback in the aforementioned models has allowed them to reproduce the observed luminosity function remarkably well.

Implementing a semi-analytic model requires a number of assumptions to be made. Firstly, it is often assumed that gas will cool radiatively, settling into a rotationally supported disc in the centre of the dark matter halo in which it is embedded. The limited amount of gas available to this cooling process then places limits on the characteristic mass and size of galaxies (White 1978). Assumptions also need to be made about how much of this cooled gas can be transformed into stars, the amount of gas reheated by the subsequent star formation and about black hole growth and active galactic nuclei (AGN) outflows. Common implementations of each of these processes are described briefly below.

**Creating a Galaxy**

Every dark matter halo will have an associated central galaxy; as a dark matter halo collapses a proportional mass of baryons will collapse with it. This central galaxy is fixed onto the most bound (central) particle of the halo and all gas within the halo cools onto this galaxy. A halo may also have several satellite galaxies. The position of these satellites is given to them by the position of one of the particles within the halo. Satellite galaxies will have been central galaxies of a halo at some time in the past but, as the host halo undergoes a merger, the central galaxy may become a satellite of another larger halo. No satellite galaxy can accrete cool gas: star formation can only continue until its supply of cold gas is exhausted. The haloes of satellite galaxies

undergo tidal stripping until the halo can no longer be identified within the simulation, at this point the satellite is classed as an 'orphan galaxy' and it is assumed to merge with the central galaxy within the dynamical friction time scale, given in Binney and Tremaine (1987) as

$$t_f = \frac{1.17 v_{vir} r_{sat}^2}{m_{sat} \ln(1 + M_{vir}/m_{sat})}. \tag{3.51}$$

If a galaxy is somehow ejected from its host halo it is defined as a field galaxy and may later accrete back into a halo.

Galaxies are created at the first simulation output in which haloes are formed, at high redshift and are initialised with zero stellar mass, cold gas mass and luminosity. A merger tree is used to track the evolution of the halo and the properties of each of the galaxies are updated according to simple semi-analytic prescriptions based on the properties of the host halo. Some of the simple physical processes common to many semi-analytic models are described below. For a full discussion of the processes modelled see, for example, Kauffmann et al. (1999); Springel et al. (2001a); De Lucia et al. (2004); Croton et al. (2006) and Guo et al. (2010). In this section only the very basic ideas from these papers are outlined.

**Reionisation**

Photo-heating by the ionising background radiation acts to increase pressure forces in low-density gas and smooths out small-scale baryonic structures, and may be responsible for suppressing star formation in dwarf galaxies (Efstathiou 1992; Thoul and Weinberg 1996; Barkana and Loeb 2006). Photoionisation by the UV background radiation provides not only a source of heat but also reduces the cooling rate for both primordial and metal-enriched plasmas (Efstathiou 1992; Wiersma et al. 2009).

The effect of photoionisation heating is modelled by defining a filtering mass $M_F$, below which the gas fraction $f_b$ is reduced relative to the universal value $f^{univ}$ (Gnedin

et al. 2005):

$$f_b^{halo}(z, M_{vir}) = \frac{f_b^{univ}}{[1 + 0.26M_F(z)/M_{vir}]^3}. \tag{3.52}$$

The choice of filtering mass function adopted by Croton et al. (2006) corresponds to a present day filtering scale of $4 \times 10^9\,\mathrm{M}_\odot$.

### Cooling

One of the main differences between baryons and dark matter is that baryons are able to cool, dissipate their binding energy and collapse to the centre of the potential. In fact gas cooling is incredibly efficient and without a feedback mechanism (such as reionisation, supernovae feedback and feedback from black holes) most of the baryonic matter in the Universe would have collapsed into subgalactic objects at high redshift.

Silk (1977), Rees and Ostriker (1977) and White (1978) suggest that the redshift and depth of the potential well will affect the fate of the infalling gas. The infalling gas is assumed to be shock-heated to the virial temperature of the halo $T_{vir}$. The cooling time $t_{cool}$ is conventionally taken to be the ratio of the thermal energy density to cooling rate per unit volume:

$$t_{cool}(r) = \left(\frac{3}{2}\frac{\rho_g(r)kT_{vir}}{\mu m_H}\right) / \left(\rho_g^2(r)\Lambda(T_{vir}, Z)\right), \tag{3.53}$$

where $\mu$ is the mean molecular mass of the gas, $m_H$ is the mass of a hydrogen atom, $k$ is Boltzmann's constant, $\rho_g(r)$ is the density distribution of the gas and $\Lambda(T_{vir}, Z)$ is the temperature and metallicity dependant cooling rate. The virial temperature of the halo is given by $T_{vir}$=35.9 $(v_{vir}/\mathrm{km\,s^{-1}})^2$K where the virial velocity $v_{vir} = (GM_{vir}/r_{vir})^{1/2}$. The hot gas is often assumed to have an isothermal distribution. The cooling rate $\dot{m}_{cool}$ within a halo with an atmosphere of hot gas is given by

$$\dot{m}_{cool} = 0.5 m_{hot}\frac{r_{cool}v_{vir}}{r_{vir}^2}, \tag{3.54}$$

where $m_{hot}$ is the total mass of hot gas within the halo, assumed to extend out to the virial radius $r_{vir}$. The cooling radius $r_{cool}$ is defined in Croton et al. (2006) as the point at which the local cooling time is equal to the halo dynamical time $t_{dyn}$. By relating the virial mass $M_{vir}$ to the virial radius $r_{vir}$ and the virial velocity $v_{vir}$,

$$M_{vir} = \frac{100}{G} H^2(z)\, r_{vir}^3 = \frac{v_{vir}^3}{10GH(z)}, \tag{3.55}$$

the halo dynamical time can be approximated as $t_{dyn} \approx 0.1H(z)^{-1}$. Equation (3.54) is assumed to be valid as long as $r_{cool} < r_{vir}$. When $r_{cool} > r_{vir}$, such as in low mass or high redshift haloes, all infalling material is immediately accreted onto the central disc. The cooling rate is set equal to the rate at which new diffuse gas is added to the halo.

### Star Formation

There is a critical density for star formation. When gas reaches a critical density it is assumed to form a cold interstellar gas phase. The transition between warm and cold gas phases is responsible for triggering gravitational instabilities. This high-density, multiphase gas fragments and collapses to form stars (Schaye 2004). Unfortunately, since cosmological simulations have neither the resolution nor the physics required to model the cold interstellar medium (ISM) they can certainly not be expected to model the formation of stars within molecular clouds.

Once the mass of cold gas $m_{cold}$ associated with a galaxy (assumed to be evenly distributed over the disc) exceeds the critical value (based on observational work conducted by Kennicutt 1998)

$$m_{crit} = 3.8 \times 10^9 \left(\frac{v_{vir}}{200\, kms^{-1}}\right)\left(\frac{r_{disc}}{10\, kpc}\right) M_\odot, \tag{3.56}$$

the star formation rate $\dot{m}_*$ of the galaxy is given by

$$\dot{m}_* = \alpha \frac{m_{cold} - m_{crit}}{t_{dyn}}, \tag{3.57}$$

where $t_{dyn}$ is the dynamical time of the disc and is set to be $r_{disc}/v_{vir}$. The efficiency of star formation is characterised by $\alpha$, set in Croton et al. (2006) so that between 5 and 15% of the gas is converted into stars in the dynamical time $t_{dyn}$.

**Supernovae Feedback**

With star formation occurring, massive stars form, quickly complete their evolution and result in supernovae. These events result in the injection of metals, gas and energy into their surroundings. These supernovae can be responsible for reheating the cold disc gas or even ejecting mass from the halo. The reheated gas mass is given by

$$\Delta m_{reheat} = \epsilon_{disc} \Delta m_{*}. \tag{3.58}$$

Here $\Delta m_{*}$ is the mass of stars formed in a finite time interval and $\epsilon_{disc}$ is a fixed parameter set to 3.5 based on observational data (see Croton et al. 2006). The mass of gas ejected is taken to be

$$\Delta m_{ejected} = \left( \epsilon_{halo} \frac{v_{SN}^2}{v_{vir}^2} - \epsilon_{disc} \right) \Delta m_{*}, \tag{3.59}$$

where $\epsilon_{halo}$ is the efficiency of the reheating of the disc gas (taken to be 0.35), $v_{SN}^2$ is twice the mean energy in supernovae ejecta per unit mass of stars formed ($v_{SN}$ is taken to be $\sim 630$ km s$^{-1}$). This ejected gas may be reincorporated into the halo at a later time. Energy injections from supernovae and stellar winds are thought to be responsible for the quenching of star formation in low mass haloes. This results in a galaxy luminosity function which is shallower than the halo mass function at the low-mass end. However, this form of feedback does not seem to have a significant effect on massive haloes.

**Black Hole Growth and AGN Outflows**

AGN feedback has been shown to be a critical factor in correctly reproducing a number of observable properties such as the colours, stellar masses and luminosities of galaxies

on the bright end of the galaxy luminosity function. Without AGN feedback massive haloes convert large fractions of gas into stars and produce too many bright galaxies. The model for black hole growth implemented in Croton et al. (2006) separates the growth into two modes. In the 'quasar mode' supermassive black holes grow during gas-rich mergers both by the accretion of cold disc gas and by merging with each other. In the 'radio mode' growth results from continuous and quiescent hot gas accretion. Mechanical heating energy is generated by the black hole accretion in the 'radio mode' and is deposited as heat in the hot gas halo.

For the details involved in the implementation of AGN feedback see Croton et al. (2006).

## 3.8 Simulations Used in this Thesis

In this section the simulations used throughout this thesis are presented. The $N$-body Millennium Simulation and the associated semi-analytic galaxy catalogue as well as the set of SPH simulations known as the Overwhelmingly Large Simulations are described.

### 3.8.1 The Millennium Simulation

The Millennium Simulation, run by the Virgo Consortium, follows the evolution of $2160^3$ dark matter particles within a comoving box of length 500 $h^{-1}$ Mpc using GADGET-2 code. The simulation was run on the Max Planck Institute for Astrophysics (Garching, Germany) cluster of 512 processors for 343 000 CPU hours. A force softening length of 5 $h^{-1}$ kpc was used. A $\Lambda$CDM cosmology was assumed, using parameters consistent with the results obtained from the first year *WMAP* data: $\Omega_m = 0.25$, $\Omega_\Lambda = 0.75$, $h = 0.73$, $n_s = 1$ and $\sigma_8 = 0.9$ (Spergel et al. 2003). The parameters of the simulation are summarised in Table 3.1.

Haloes are identified using a simple FOF algorithm (Davis et al. 1985) with the con-

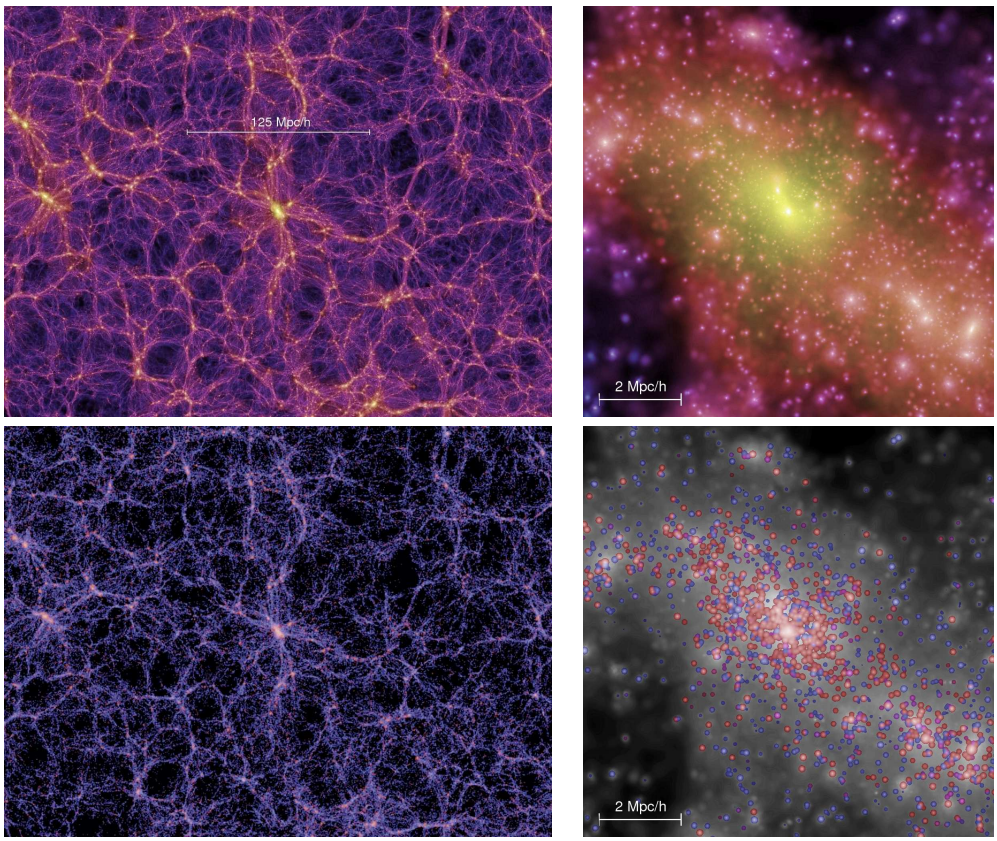


Figure 3.3: Images from the Millennium Simulation. Top row shows the distribution of dark matter on large scales (left) and within a simulated cluster (right). Lower images depict the corresponding luminous matter, bottom left shows the large-scale light distribution, while the bottom right shows the galaxy distribution within the rich cluster (taken from Springel et al. 2005b).

ventional linking length of 0.2 times the mean interparticle spacing. The SUBFIND algorithm (Springel et al. 2001a) is then used to identify bound structure within the haloes. Records are kept for all groups containing at least 20 particles. This means that the minimum mass for a detected halo is $1.7 \times 10^{10}\, h^{-1}\ \mathrm{M}_{\odot}$, corresponding to a baryonic mass of about $3 \times 10^{9}\, h^{-1}\ \mathrm{M}_{\odot}$, if the low mass galaxies have the universal baryon fraction. Data are recorded at 64 time intervals, spaced logarithmically in expansion factor before redshift $z \sim 1$ and in intervals of about 200 Myr thereafter.

Table 3.1: Millennium Simulation parameters.

| Parameter | Parameter Value |
|---|---|
| $N_{particles}$ | $2160^3$ |
| Box Length | $500\,h^{-1}$ Mpc |
| $M_{particle}$ | $8.6 \times 10^8\,h^{-1}\,M_\odot$ |
| Force Softening | $5\,h^{-1}$ kpc |
| Initial Redshift | 127 |

**Millennium Simulation Galaxy Catalogues**

As the Millennium Simulation is a dark matter only simulation, a semi-analytic model is needed to estimate the effects of baryons and determine the properties of galaxies. The publicly available galaxy catalogue created by De Lucia and Blaizot (2007) has been used in chapter 4 to study the predicted frequency of satellite galaxies within the central regions of host haloes. This catalogue uses the Millennium Simulation to trace the underlying dark matter.

The model differentiates between three different types of galaxies – central galaxies, found at the centre of the dark matter halo, satellite galaxies which are associated with a smaller (possibly recently merged) dark matter substructure and 'orphan' satellite galaxies which are no longer associated with a dark matter substructure. In 'orphan' galaxies the dark matter subhalo is assumed to have completely merged with the larger halo. Only these galaxies, which are not associated with any dark matter substructure, are allowed to merge with the central galaxy after a dynamical timescale.

For each halo identified in the simulation, a central galaxy is 'created' with a mass fraction in baryons corresponding to the global ratio $\Omega_b/\Omega_m$. Initially the 'created' galaxy has no stellar mass, no cold gas and zero luminosity. The attributed baryons are in the form of diffuse gas with primordial composition. The semi-analytic model uses merger trees taken from the Millennium Simulation to describe the evolution of haloes that host the galaxies. The formation and evolution of the galaxies is then followed by implementing simple physical prescriptions for the baryonic physics, such as gas cooling, star formation and feedback processes (including AGN feedback) as

discussed in section 3.7. When two haloes merge, the galaxy associated with the larger halo remains the central galaxy while the galaxy attributed to the lower mass progenitor becomes a satellite. Satellite galaxies are stripped of their hot gas and have no new supply of cool gas. They are allowed to form stars until their cool gas reservoir is exhausted. Subhaloes are followed, after merging with a larger system, until the dark matter subhalo is completely disrupted by tidal forces. These tidally stripped 'orphan' galaxies are then assumed to follow the position of the most bound particle in the subhalo before it was disrupted, until it merges with the central galaxy on the dynamical friction timescale. More details on the formation and evolution of the galaxies and their photometric properties can be found in De Lucia et al. (2004) and Croton et al. (2006).

### 3.8.2 The Overwhelmingly Large Simulations

The Overwhelmingly Large Simulations (hereafter OWLS) refers to a set of state-of-the-art, high resolution cosmological hydrodynamical simulations run by Schaye et al. (2010) with varying implementations of the subgrid physics. The simulations were run on Stella (the Bluegene/L supercomputer of the Dutch astronomical institute ASTRON), with additional time on the Cosmology Machine at the Institute for Computational Cosmology in Durham. These simulations were run in order to explore the physics that governs galaxy formation and evolution. While hydrodynamical simulations attempt to model physics from first principles, the limited resolution available requires that subgrid physics models are implemented. These models can be physically or empirically motivated. The simulations are able to address the issue of the sensitivity of simulation predictions to the underlying physics models used in the simulation. More than fifty different simulations were run, with different prescriptions for the physical processes, such as cooling, star formation and feedback from stars and AGN. For full details on OWLS the reader is referred to Schaye et al. (2010).

Periodic boxes of cosmological volumes (typically 25 and 100 $h^{-1}$ Mpc, although

this was varied) were used. Most of the simulations contained $512^3$ dark matter particles and $512^3$ gas particles, although many resolution runs were done.

The cosmological parameters used for the simulations were taken from the third year *WMAP* data (Spergel et al. 2007), with $\Omega_m = 0.238$, $\Omega_\Lambda = 0.762$, $\Omega_b = 0.0418$, $h = 0.73$, $n_s = 0.95$ and $\sigma_8 = 0.74$ (Spergel et al. 2007). The primordial baryonic mass fraction of helium was assumed to be 0.248. For all runs, cosmological initial conditions were generated with CMBFAST (Seljak and Zaldarriaga 1996) and evolved to $z = 127$. Initial positions and velocities were computed using the Zel'dovich (1970) approximation from an initial glass-like state (White 1996). The simulations were run using a modified version GADGET-3 (a private version of the GADGET code) to follow the evolution of $512^3$ dark matter particles and $512^3$ gas particles in cubes of comoving length 100 $h^{-1}$ Mpc at $z = 0$ and 25 $h^{-1}$ Mpc at $z = 2$. The baryon runs follow the baryonic component with smooth particle hydrodynamics, where the number of neighbours $N_{\rm ngb}$ for the SPH interpolation was set to 48. In the dark matter only run the particle masses were $7.7 \times 10^6$ and $4.9 \times 10^8$ $h^{-1}\,{\rm M}_\odot$ in the 25 and 100 $h^{-1}$ Mpc boxes respectively. The mass of the particles in the baryon runs is divided between the gas and dark matter particles according to the universal baryon fraction $f_b^{univ} = \Omega_b/\Omega_m = 0.176$, such that the dark matter (gas) mass in the $100\,h^{-1}$ Mpc run is $4.06\ (0.87) \times 10^8\,h^{-1}\,{\rm M}_\odot$ and $6.34\ (1.35) \times 10^6\,h^{-1}{\rm M}_\odot$ for the $25\,h^{-1}$ Mpc box. Baryonic particle masses were allowed to change during the simulation due to mass transfer from gas to star particles. The comoving gravitational force softening was set to 1/25 of the initial mean interparticle spacing but was limited to a maximum physical scale of $2\,(0.5)\,h^{-1}$kpc for the 100 (25) $h^{-1}$ Mpc boxes. For a given box size the same initial conditions were used in each run. This allows us to follow the same haloes with different implementations of the subgrid physics.

### Gas Physics

The simulations used in this thesis and their implemented subgrid physics are summarised in table 3.2. The baryon runs consider gas cooling and star formation as well

Table 3.2: A list of the OWLS simulations used in this thesis. The names of the simulations are listed (as in Schaye et al. 2010) and comments on the implemented subgrid physics are made.

| | |
|---|---|
| DMONLY | Dark matter only run. |
| NOFB_ZCOOL0 | No feedback with primordial element line cooling. |
| REF | Weak stellar feedback with metal cooling. |
| WDENS | Strong stellar feedback run with metal cooling. |
| AGN | Weak stellar feedback and AGN feedback with metal cooling. |

as feedback from stars and AGN. The implementation of the baryonic processes included in these simulations is briefly discussed below.

**Cooling.** Wiersma et al. (2009) show the importance of photoionisation by the ionising background and of heavy elements, as well as considering the variations in relative abundances of the elements on cooling rates. They provide cooling tables generated with the publicly available CLOUDY radiative transfer code (Ferland et al. 1998) that have been used in implementing the radiative cooling in these simulations. The cooling rates are computed element-by-element in the presence of the cosmic microwave background and an evolving UV/X-ray background radiation from quasars and galaxies (Haardt and Madau 2001). Contributions from hydrogen, helium, carbon, nitrogen, oxygen, neon, magnesium, silicon, sulphur, calcium and iron are considered and the contributions are interpolated as a function of density, temperature and redshift from the precomputed CLOUDY tables, assuming the gas to be optically thin and in photoionisation equilibrium. In the no feedback run, there are no supernovae and no metals are produced so cooling rates are calculated using primordial element abundances. Cooling by both Bremsstrahlung emission and Compton cooling via interactions between the gas and cosmic microwave background is also taken into account. Reionisation is modelled by 'switching on' the Haardt and Madau (2001) background at $z = 9$. Collisional equilibrium is assumed before reionisation, and photoionisation after $z = 9$.

**Star Formation and Evolution.** Star formation is modelled by converting gas particles into collisionless stellar particles, with each stellar particle representing a simple

stellar population. Gas that has a lower density than the critical value is kept warm (and stable) by the UV background. But above this density threshold, the multiphase gas will fragment and collapse to form stars (Schaye 2004). The OWLS simulations impose a star formation density threshold of $n_H > 0.1$ cm$^{-3}$ (where $n_H$ is the hydrogen number density). Above this density an effective equation of state ($P \propto \rho^{\gamma_{\rm eff}}$) is imposed, where $\gamma_{\rm eff}$ is set to 4/3. This acts to suppress spurious fragmentation since neither the Jeans mass, nor the ratio of Jeans length to SPH smoothing length, are density-dependent (Schaye and Dalla Vecchia 2008). Within the simulations, stars form at a rate dependent on their pressure. This pressure-dependent rate is shown to reproduce the Kennicutt-Schmidt law (Kennicutt 1998), $\dot{\Sigma}_* = A\left(\Sigma_g/1{\rm M}_\odot\,{\rm pc}^2\right)^n$ where $\dot{\Sigma}_*$ is the rate of star formation per unit area per unit time and $\Sigma_g$ is the gas surface density in Schaye and Dalla Vecchia (2008). The simulations used in this work employ a Chabrier initial mass function (Chabrier 2003) with a star formation rate normalisation $A$ of $1.515 \times 10^{-4}$ M$_\odot$ yr$^{-1}$ kpc$^{-2}$ and slope $n = 1.4$. Stellar particles are assigned the metallicity of their parent gas particle, and their subsequent evolution is a function of this metallicity.

**Feedback.** The simulations follow the timed release of energy from massive stars (Type II SNe and stellar winds) and intermediate mass stars (Type Ia SNe and asymptotic giant branch (AGB) stars). Massive stars (with initial masses in the range 6 – 100 M$_\odot$) are assumed to end their lives as core-collapse supernovae (SNe), releasing energy into the surrounding environment. Assuming the maximum lifetime of these stars, this energy is added to the surrounding medium after a delay of 30 Myr. Assuming that each of these massive stars injects $10^{51}$ erg of kinetic energy, for the wind models considered here typically 40% of this SNe energy (for the implemented initial mass function) is injected into the surrounding gas. Wind particles are prevented from forming stars for 15 Myr, preventing high velocity stellar particle ejection. In the simulations considered, energy is injected kinetically (stars 'kick' nearby gas particles) using the prescription of Dalla Vecchia and Schaye (2008). This is a variation of

the method described in Springel and Hernquist (2003), however, as discussed in Dalla Vecchia and Schaye (2008), kinetic energy is injected locally, and the winds are not hydrodynamically decoupled. The strength, or efficiency, of the feedback is characterised by the mass-loading parameter $\eta$ and the velocity added to the nearby gas particles $v_w$. The probability for a neighbouring particle $i$ to receive a 'kick' of velocity $v_w$ from a new stellar particle $j$ is given by $\eta\, m_j / \sum_{i=1}^{N_{\rm ngb}} m_i$. Typically each stellar particle 'kicks' $\eta$ times its own mass, and adds a randomly directed velocity $v_w$ to each 'kicked' gas particle.

The REF simulations correspond to a 'weak' feedback run, here $\eta = 2$ and $v_w = 600$ km s$^{-1}$. This implementation of feedback, while referred to as weak, is considerably stronger than many other implementations found in the literature.

The WDENS run provides us with a more efficient form of feedback, where the mass loading depends on the local gas density in the following way: $v_w = 600$ km s$^{-1}$ $\left(n_H/0.1{\rm cm}^{-3}\right)^{1/6}$ and $\eta = 2\left(v_w/600 \text{ km s}^{-1}\right)^{-2}$. While the same amount of the supernovae energy is injected into the surrounding gas particles, the distribution between mass-loading and wind velocity results in a higher feedback efficiency. In this run, winds in the densest regions have the lowest mass-loadings and highest velocities. Winds in the WDENS run are able to remove gas from higher-mass haloes more efficiently than the REF model.

The final feedback run that was considered includes feedback from AGN and is by far the most efficient feedback model discussed here. Feedback from AGN is required in simulations to match the high end of the luminosity function. It is thought to suppress star formation in high-mass galaxies and cooling flows in clusters. In this run, supermassive black holes (BH) are grown at the centre of massive haloes. As matter is accreted onto these BHs, large amounts of high energy radiation are emitted. The AGN run is implemented using the method of Booth and Schaye (2009), a substantially modified version of Springel et al. (2005a). In this model, seed black holes (of mass $9 \times 10^4$ M$_\odot$) are placed in the centre of the haloes with masses above $4 \times 10^{10}$ M$_\odot$. Black holes grow both through gas accretion and merging. The minimum of the

Eddington and Bondi-Hoyle rates is assumed for gas accretion. When a cold gas phase is present, uncertainties in the physics of the multiphase interstellar medium become important and the rate of accretion onto the black hole is uncertain, a naive application of the Bondi-Hoyle formula would strongly underestimate the accretion rate (Booth and Schaye 2009). To compensate for this the Bondi-Hoyle rate, for star forming (high density) gas, is multiplied by $(n_H/10^{-1}\ \mathrm{cm}^{-3})^2$. The BH mass $m_{BH}$ is assumed to grow as $\dot{m}_{BH} = (1 - \epsilon_r)\,\dot{m}_{accr}$ where $\epsilon_r$, the assumed radiative efficiency, is 0.1. It is assumed that 15% of the radiated energy is thermally coupled to the surrounding particles.

# 4

# Luminous Satellites in Lens and Field Galaxies

Substructures, expected in cold dark matter haloes, have been proposed to explain the anomalous flux ratios in gravitational lenses. About 50% of lenses in the Cosmic Lens All-Sky Survey (CLASS) appear to have luminous satellites within $\sim 5\ h^{-1}$ kpc of the main lensing galaxies, which are usually at redshift $z \sim 0.2 - 1$. In this chapter the Millennium Simulation, combined with galaxy catalogues from semi-analytical techniques, is used to study the predicted frequency of such satellites in simulated haloes. The fraction of haloes that host bright satellites within the (projected) central regions is similar for red and blue hosts and is found to increase as a function of host halo mass and redshift. Specifically, at $z = 0$, only $\sim 3\%$ of galaxy-sized haloes (with masses between $10^{12}\ h^{-1}\ \mathrm{M}_{\odot}$ and $10^{13}\ h^{-1}\ \mathrm{M}_{\odot}$) host bright satellite galaxies. The fraction rises to $\sim 6\%\,(10\%)$ if bright (all) satellites of only group-sized haloes (with masses between $10^{13}\ h^{-1}\ \mathrm{M}_{\odot}$ and $10^{14}\ h^{-1}\ \mathrm{M}_{\odot}$) at $z = 0$ are considered. At $z = 1$, about 11% of galaxy-sized haloes host bright satellite galaxies within a projected radius of $5\ h^{-1}$ kpc. This fraction increases to about 17% (25%) if bright (all) satellites of only group-sized haloes are considered. These results are considerably lower than the fraction ($\sim 50\%$) of CLASS lensing galaxies observed to host luminous satellites. However, the pre-

dicted frequency of luminous satellite galaxies is found to be higher than observed in non-lensing galaxies in both the Cosmic Evolution Survey (COSMOS), which has a similar redshift distribution to CLASS, and in the wider but shallower SDSS. The predicted fraction is also higher than that found for lenses in the Sloan Lens ACS Survey (SLACS), which appears to be consistent with the early-type non-lensing galaxies. It is worth noting that most of the simulated satellites found in the inner regions are 'orphan' galaxies where the dark matter haloes have been completely stripped. The fraction predicted by the ΛCDM model crucially depends on the true survival rate of these 'orphan' galaxies.

## 4.1 Introduction

In the standard model larger structures form via the accretion and merging of smaller structures. Dense cores of the smaller structures often survive the merging process and manifest as subhaloes in the primary haloes. If substantial star formation occurs in these subhaloes (or their progenitors), then they will appear as satellite galaxies.

In the Milky Way, hundreds of subhaloes are predicted, starting from earlier semi-analytical studies (Kauffmann et al. 1993), to more recent high-resolution simulations (Klypin et al. 1999; Moore et al. 1999; Gao et al. 2004a,b; Diemand et al. 2007b). A few years ago, there were only a dozen or so satellites known, far fewer than the predicted number of subhaloes. However, very recently, a new population of satellites has been discovered in the SDSS data (e.g. Belokurov et al. 2007). It should be noted though that these satellites are compact and, in general, much fainter than the previously known ones. Thus it is likely that even this new population of satellite galaxies cannot completely remove the discrepancy between simulations and observations (Madau et al. 2008). It is possible that many subhaloes are dark due to inefficient star formation, for example, due to its suppression by the UV-background radiation (e.g. Doroshkevich et al. 1967; Couchman and Rees 1986; Efstathiou 1992; Thoul and Weinberg 1996; Barkana and Loeb 2006) or through gas heating by supernova

feedback (White and Rees 1978) .

Such dark substructure can, potentially, be detected through several means, for example through gamma-ray radiation due to annihilations of dark matter particles (Stoehr et al. 2003; Diemand et al. 2007a). Gravitational lensing is, in principle, another way to detect dark (and luminous) substructure.

Observations of gravitational lens systems, such as image positions (Chen et al. 2007), image fluxes (Mao and Schneider 1998) and time delays (Keeton and Moustakas 2008) provide constraints on the mass profile of the lensing system. Systems with a large number of images provide the most constraints. The simplest approximation, the smooth-mass model, is sometimes able to reproduce the image positions but often fails when attempting to fit the observed flux ratios (Kochanek 1991). Mao and Schneider (1998) suggested that the presence of substructure could be used to explain the anomalous flux ratios. Secure evidence for flux anomalies can be obtained from radio-loud sources, where the image fluxes are not influenced by microlensing and dust extinction. Dalal and Kochanek (2002) showed that a contribution of $\sim 0.6$ to 7% to the surface mass density from substructures would be sufficient to explain the flux anomalies.

If all substructure is equally efficient in affecting the flux ratios, then it is clear that there is more than sufficient mass in subhaloes to explain the flux anomalies. Unfortunately, most subhaloes are in the outer part of the galaxy halo, which means they will have relatively little impact on the flux anomalies occurring in the central parts of lensing galaxies. Curiously, as emphasised by Schneider (2007, private communication), 3 of the 7 radio lenses studied by Dalal and Kochanek (2002) exhibit luminous satellite galaxies close to the primary lensing galaxy, namely MG0414+0534, B1608+656 and B2045+265. A question naturally arises: are such luminous satellite galaxies expected this frequently in the current structure formation theory? This question is addressed here.

The lensing probability depends on the number density of lenses and on the mass profiles of the lensing systems (Schneider et al. 2006). The lensing cross-section (de-

fined by the mass profile) is dominated by elliptical galaxies, thus for lensing applications it is important to divide galaxies into different types and see whether the subhalo populations are different. Furthermore, the evolution of satellite galaxies as a function of redshift $z$ is explored in more detail. If the evolution is slow, one can more conveniently use studies of nearby galaxies to infer the properties of the luminous satellite population of galaxies at intermediate redshifts (between 0.5 and 1, where most lensing galaxies lie). These are the two specific aspects of the subhalo population that will be addressed in this chapter. For this purpose, the Millennium Simulation, one of the largest cosmological simulations run to date, combined with semi-analytical catalogues, has been used to select haloes and study their satellite populations. For a discussion on these simulations please see section 3.8.1. The results are compared to CLASS (Browne et al. 2003; Myers et al. 2003).

## 4.2 Substructure in CLASS Lenses

The CLASS survey has been used as the primary observational data. This survey discovered 22 new gravitational lenses at radio frequencies (Browne et al. 2003; Myers et al. 2003). It included a complete sample of 11 685 flat-spectrum radio sources observed by the Very Large Array (VLA) in the A configuration at 8.46 GHz. Sources satisfying the following criteria were regarded as promising lens candidates: their images contained multiple components with Gaussian full width at half maximum $\leq 170$ milliarcseconds; the image separation was between 0.3 and 15 arcseconds; the total integrated flux density was $\geq 20$ mJy and the component flux-density ratio was greater than 10 to 1. Higher resolution observations with the Multi-Element Radio Linked Interferometer Network (MERLIN) and the Very Long Baseline Array (VLBA) were used to detect compact structures and extended emission in multiple components, thus confirming lens candidates.

Dalal and Kochanek (2002) studied 7 four-image radio lenses, and observed anomalous flux ratios in 6 of them. As discussed in the previous section, 3 of these lens

systems are observed to host luminous companions within the central region. In this work, the whole survey is used to gather statistics; 10 of the 22 CLASS lenses have luminous satellite galaxies within $\sim 5\ h^{-1}$ kpc of the main lensing galaxy: B1608+656, B2045+265, MG 0414+0534, B1127+385, B1359+154, B1030+074, B2108+213, B0445+123, B1152+199 and B0631+519.

For B1608+656, the main lensing galaxy (G1) is at redshift $z_l = 0.63$. In addition, there is a faint galaxy G2 about 0.73 arcseconds away, which is 1.8 magnitudes fainter than G1 both in the HST F160W and F814W (Koopmans et al. 2003) filters. There are also 4 groups along the line of sight, including one at the redshift of the lensing galaxy G1 (Fassnacht et al. 2006). If G2 is at the same redshift as G1, then the projected separation is $3.4\ h^{-1}$ kpc.

For B2045+265, McKean et al. (2007) found a galaxy G2 about 0.66 arcseconds away from the main lensing galaxy G1 (at redshift 0.867), which is between 3.6 and 4.5 magnitudes fainter than the main lensing galaxy G1 in F814W and F160W. The photometric redshift of G2 is consistent with that of G1, although it is also consistent with being at redshift $z \sim 4 - 5$. If the redshifts of G1 and G2 are the same, then the projected separation is $3.5\ h^{-1}$ kpc.

For the quadrupole lens MG 0414+0534, Schechter and Moore (1993) found a fainter companion that is about 1 arcsecond away from the main lensing galaxy (which is at redshift 0.96). The object 'X' is about 2.44 – 2.6 magnitudes fainter than the main lensing galaxy in the HST images of F160W and F814W. If the object 'X' is at redshift $z = 0.96$, then the projected separation is $5.5\ h^{-1}$ kpc.

For B1127+385, there are also two lensing galaxies, G1 and G2 (Koopmans et al. 1999). The fainter one, G2, is about 1 magnitude fainter than G1 in both F814 ($I = 22.5$ for G1) and F555 ($V = 24.4$ for G1). The separation between these two galaxies is about 0.6 arcseconds. If the lensing galaxy's redshift $z_l$ is between 0.5 and 1, then the projected separation is about $2.5 - 3.3\ h^{-1}$ kpc.

B1359+154 is a six-image system produced by a small group of galaxies. Three primary lens galaxies lie on the vertices of a triangle separated by 0.7 arcseconds at

$z \sim 1$ (corresponding to a projected separation of $\sim 3.9\,h^{-1}$ kpc), with magnitudes in $I$ of $22.68 \pm 0.28$ and $23.69 \pm 0.24$ and $23.70 \pm 0.33$ (Rusin et al. 2001).

B1030+074 is a two image system with a secondary emission feature visible 2.45 $h^{-1}$ kpc from the $z_l = 0.6$ lensing galaxy (Fassnacht and Cohen 1998). The $I$-band magnitude difference between the objects is $\sim 2.5$.

McKean et al. (2005) observed B2108+213, finding emission from a secondary galaxy between the two lensed images which are $\sim 4.56$ arcseconds apart. The secondary galaxy is $\sim 1.1$ arcseconds from the $z = 0.36$ primary. The $I$-band flux ratio between the primary and secondary objects was found to be 0.076.

Faint secondaries are found in B0445+123 and B1152+199 (Rusin et al. 2001). In B0445+123, a secondary 4.63 magnitudes fainter than the 20.58 $I$-band magnitude lensing galaxy has been detected. The secondary is $\sim 6.7\,h^{-1}$ kpc from the $z = 0.6$ lens. In B1152+199 the lens has an $I$-band magnitude of 19.26 and is at a redshift of 0.44. A secondary 0.1 magnitudes fainter is observed within $\sim 2.5\,h^{-1}$ kpc.

In B0631+519 a secondary was observed in the original discovery image 2.10 magnitudes fainter than the main lensing galaxy, however this 'companion' was shown to be at a different redshift to the lensing galaxy (McKean et al. 2004; York et al. 2005). This system is included in the statistics that follow.

The top panel of figure 4.1 shows the luminosities $L_I$ of the observed lenses found by the CLASS survey. The patterned histogram shows 18 of the CLASS lenses for which redshifts and $I$-band magnitudes are available (taken from the CASTLES website[1]). Over-plotted (solid histogram) are the 9 of the CLASS lenses which have been shown to host luminous satellites; for B1127+385, its luminosity is unknown due to the uncertain lens redshift.

The bottom panel of figure 4.1 shows the redshift $z_l$ distribution of the CLASS lenses. Most of the lenses with luminous satellites have redshifts higher than the median value of $\sim 0.6$. About 75% of the lenses with $z > 0.8$ have luminous satellites. However, the 4 remaining lenses of the CLASS sample (with unknown redshifts) may

[1] http://www.cfa.harvard.edu/castles/ (Kochanek et al. 2008)

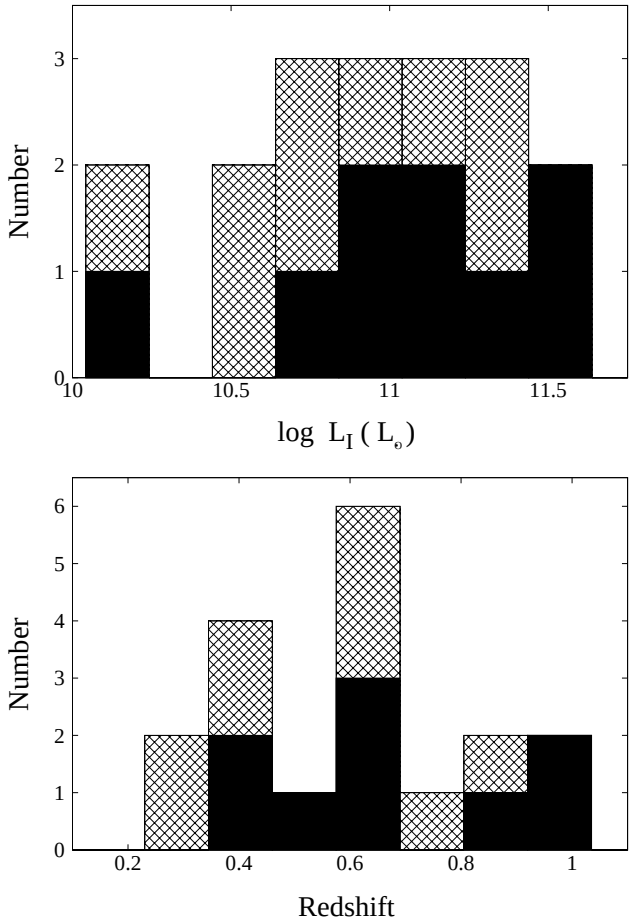


Figure 4.1: Histograms showing the distribution of $I$-band luminosity $L_I$ and redshift $z_l$ of the 18 CLASS lenses with available redshifts and magnitudes. Solid histograms show the distributions of the 9 CLASS lenses with luminous satellites (B1127+385, is not shown due to its uncertain lens redshift). K-correction values have been taken from Poggianti (1997), interpolated using a polynomial fit.

be, on average, at higher $z$. By ignoring these lenses, the redshift distribution may be somewhat skewed. This could mean that the probability of a high redshift lens hosting a luminous satellite may not be as high as implied.

## 4.3 Simulated Galaxy Sample

The De Lucia and Blaizot (2007) semi-analytic galaxy catalogue, based on the Millennium Simulation (discussed in section 3.8.1), has been used to study the satel-

lite population within massive galaxy-sized haloes (haloes with a virial mass $M_{vir}$ between $10^{12}\,h^{-1}\,\mathrm{M}_\odot$ and $10^{13}\,h^{-1}\,\mathrm{M}_\odot$) and group-sized haloes (with $10^{13}\,h^{-1}\,\mathrm{M}_\odot \leq \mathrm{M}_{vir} < 10^{14}\,h^{-1}\,\mathrm{M}_\odot$). Cluster-sized haloes are not considered as none of the CLASS lenses are found in such environments. The number of galaxy-sized host haloes considered in this analysis is around $3 \times 10^5$, varying little between $z = 0$ and $z = 1$. For group-sized haloes, the number is around $3 \times 10^4$ at $z = 0$ decreasing to $\sim 2 \times 10^4$ at $z = 1$. As in Sales et al. (2007), a brightness cutoff of $R$-band magnitude $\mathrm{M}_R < -20.5$ is imposed on the central (host) galaxies to ensure that they have a reasonable chance of hosting detectable satellites. In any case, faint central galaxies have small lensing cross-sections, and will have little effect on the statistics (see section 4.4). All galaxies (within the virial radius $r_{vir}$ of their host) with $\mathrm{M}_R < -17$ are considered to be luminous satellites. This corresponds, approximately, to a 100 particle halo – the morphological resolution limit of the simulation (see Croton et al. 2006). This cut would not exclude any of the observed luminous satellites within the CLASS sample. Furthermore, to aid in direct comparison with observation, bright satellites are required to have $R$-band luminosities between 1% and 50% of that of their host. For completeness, fainter satellites are also considered by dropping the $R$-band magnitude and lower luminosity ratio cuts on the satellite sample.

Since the lensing cross-section is dominated by massive, red elliptical galaxies, it is interesting to divide the sample by galaxy type and determine whether or not there is a significant difference in the subhalo population of red and blue galaxies. To explore this, the sample is divided according to the $B-V$ colour of the host galaxy. The galaxy populations are bimodal as a function of colour, with a well-defined red sequence and a blue cloud (illustrated in figure 4.2 and, for example, figure 9 in Croton et al. 2006). A $B-V$ colour cut of 0.8 at $z = 0$ is adopted, and $B-V$ values of 0.70 and 0.65 are used as colour cuts at $z = 0.5$ and $z = 1.0$ respectively. Using these cuts 67%, 52%, 37% of the galaxy-sized haloes (and 97%, 97%, 94% of the group-sized haloes) are associated with red central galaxies at $z = 0$, 0.5 and 1 respectively.

For nearly all of the observed lensed systems, with which the simulated results

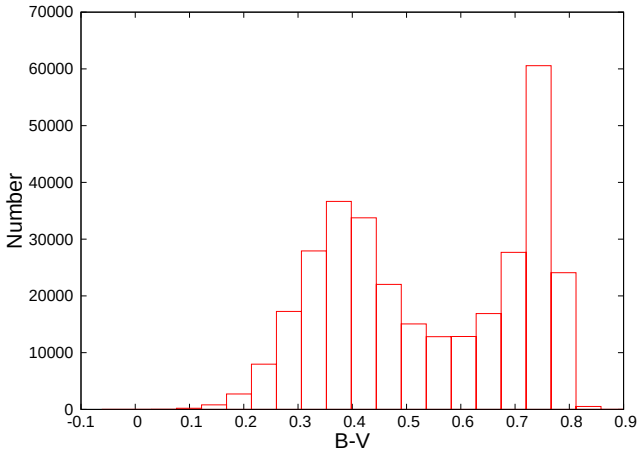


Figure 4.2: Histogram showing the distribution of the colour of simulated host galaxies at $z \sim 1$, to illustrate the bimodality of the population. Similar distributions exist at lower redshift, however the populations are shifted to redder values.

will be compared, the projected (physical) separation between the main lensing galaxy and the luminous satellite galaxy is about 1 arcsecond, corresponding to 4.2 $h^{-1}$ kpc at $z = 0.5$ and 5.5 $h^{-1}$ kpc at $z = 1$. To explore whether current simulations produce enough satellite galaxies in the inner region of a galaxy halo to explain flux anomalies, all satellite galaxies (satisfying the restrictions outlined above) within a 5 $h^{-1}$ kpc projected region from the centre of the host galaxy (defined as the position of the most bound particle) are counted, and these galaxies are referred to as bright central substructures. The effect of increasing this to a 10 $h^{-1}$ kpc projected region is also explored.

## 4.4 Predictions from the Millennium Simulation

In figure 4.3, the fraction of galaxy-sized ($10^{12}\,h^{-1}\,\mathrm{M}_\odot < \mathrm{M}_{vir} < 10^{13}\,h^{-1}\,\mathrm{M}_\odot$) haloes with satellite galaxies, satisfying the magnitude cuts, within the central region (projected) of the halo is shown. The fraction is plotted as a function of the host galaxy's $I$-band luminosity (for ease of comparison with the CLASS data). The fraction shown is the mean value, when averaged over 3 independent projections. The uncertainty

corresponds to the Poisson scatter within each bin. The left column shows the fraction of haloes with bright satellites ($M_R < -17$) within the central 5 $h^{-1}$ kpc (projected) while the right column shows the fraction of haloes which contain any (dark or bright) substructure within the same region. In these plots the red population is depicted using filled red circles, while the blue population is shown using blue squares. The three rows show the fraction of haloes containing substructure for the three different redshifts considered (top: $z = 0$, middle: $z = 0.5$ and bottom: $z = 1$). Note that the most luminous blue hosts are not necessarily the most massive haloes but are likely to have undergone recent star formation.

At $z = 0$, about $3 - 4\%$ of all of the galaxy-sized haloes appear to have bright satellite galaxies within 5 $h^{-1}$ kpc (projected) of the centre of the host. While this fraction is similar in both types of galaxies, it is found to increase with redshift (rising to around $11 - 12\%$ at $z = 1$). Extending the central region to 10 $h^{-1}$ kpc (not shown), about 10% of the galaxy-sized haloes host bright central substructure at $z = 0$, and this is found to increases to almost 27% at $z = 1$. If all substructure within the projected central region is considered, not restricting the search to 'observable' satellite galaxies, the fractions do not change significantly. This is illustrated in the right-hand panels, where the lower magnitude limits and luminosity ratio cuts have been dropped. The fraction of haloes containing any substructure within 5 $h^{-1}$ kpc (projected) of the centre of the host increases only moderately from $\sim 3\%$ to about 5% at $z = 0$. This conclusion remains valid all the way up to $z = 1$, where the fraction increases from $\sim 11\%$ to about 15%.

Since some of the lensing galaxies reside in groups (see section 4.2), the fraction of haloes with bright satellites within a projected 5 $h^{-1}$ kpc region in group-sized haloes (with $10^{13}\, h^{-1}\, M_\odot \leq M_{vir} < 10^{14}\, h^{-1}\, M_\odot$) is explicitly checked. The results are shown in figure 4.4. The fraction of group-sized haloes with bright central substructure is higher than in galaxy-sized haloes, increasing to $\sim 6\%$ at $z = 0$ and to $\sim 16\%$ at $z = 1$ for red galaxies, which dominate the lensing cross-sections; the fraction is slightly higher for blue galaxies.

Table 4.1: Luminosity weighted fraction of galaxy-sized hosts with bright substructure within the central 5 $h^{-1}$ kpc (projected) region. Numbers in brackets correspond to values for group-sized haloes.

| | Redshift | | |
|---|---|---|---|
| | 0.0 | 0.5 | 1.0 |
| All hosts | 3 (6)% | 7 (11)% | 11 (17)% |
| Red hosts | 3 (6)% | 6 (11)% | 11 (16)% |
| Blue hosts | 4 (7)% | 7 (16)% | 11 (24)% |

The lensing cross-section is roughly proportional to $\sigma^4$ (e.g. Turner et al. 1984), where $\sigma$ is the velocity dispersion of the system and, from the Faber-Jackson relation, $L \propto \sigma^4$ for ellipticals (Faber and Jackson 1976). Thus, to compare with observations, the fraction should be weighted by luminosity. The luminosity weighted fraction of hosts with bright central substructure is given in table 4.1. At $z = 0$, the fraction is $\sim 3\%$ for galaxy-sized haloes, increasing to about 6% if only group-sized haloes are considered. At $z = 1$, the fraction for galaxy-sized haloes is about 11%, rising to $\sim 17\%$ for group-sized haloes, still below the observed fraction of galaxies with bright companions (see section 4.2).

Of the systems found to host bright central substructure, most have only one bright central satellite. Only 2% (3%) of galaxy- (group-) sized hosts with bright central substructure host more than one bright central satellite at $z = 0$. At $z = 1$, 5% (7%) of galaxy- (group-) sized hosts have multiple bright central satellites. The largest number of bright central satellites found within any one system is 4.

The force softening of the simulation is 5 $h^{-1}$ kpc (in comoving coordinates); within this region, resolution effects may be significant. For this reason, the fraction of the projected subhaloes within the 3D central region is explicitly checked. The fraction depends strongly on redshift. About 32% of the luminous satellites found within the projected central 5 $h^{-1}$ kpc are found within the 3D central region in galaxy-sized haloes at $z = 0$ (for groups this decreases to $\sim 24\%$). At $z = 1$ this fraction is 11%, dropping to $\sim 6\%$ in group-sized haloes (see table 4.2). All of the satellites within the 3D central region are 'orphan' galaxies (see section 4.4.1).

Figure 4.5 shows the difference in magnitude between the host and satellite galaxy

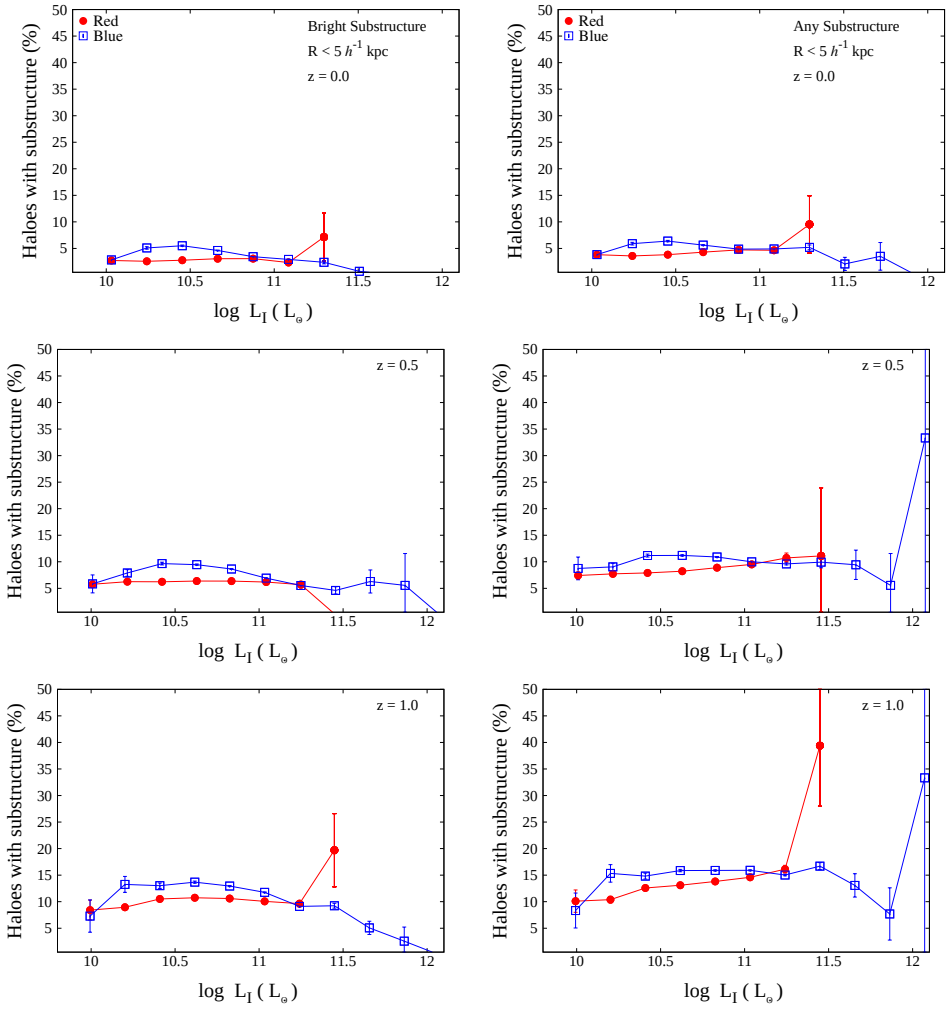


Figure 4.3: The percentage of galaxy-sized haloes ($10^{12}\,h^{-1}$ $M_\odot$ < $M_{vir}$ < $10^{13}\,h^{-1}$ $M_\odot$) which have substructure within the inner region of the halo, as a function of luminosity $L$. The left column shows the fraction of haloes with bright satellites ($M_R < -17$) within the central 5 $h^{-1}$ kpc (projected) region. The right column shows the fraction of haloes which contain any substructure within the central 5 $h^{-1}$ kpc (projected) region. In these plots the red population is depicted using filled red circles, while the blue population is shown using blue squares. The three columns show the fraction of haloes containing substructure for the three different redshifts considered (top: $z = 0.0$, middle: $z = 0.5$ and bottom: $z = 1.0$). The Poisson scatter is shown. Note that the most luminous blue hosts are not necessarily the most massive haloes but are likely to have undergone recent star formation.

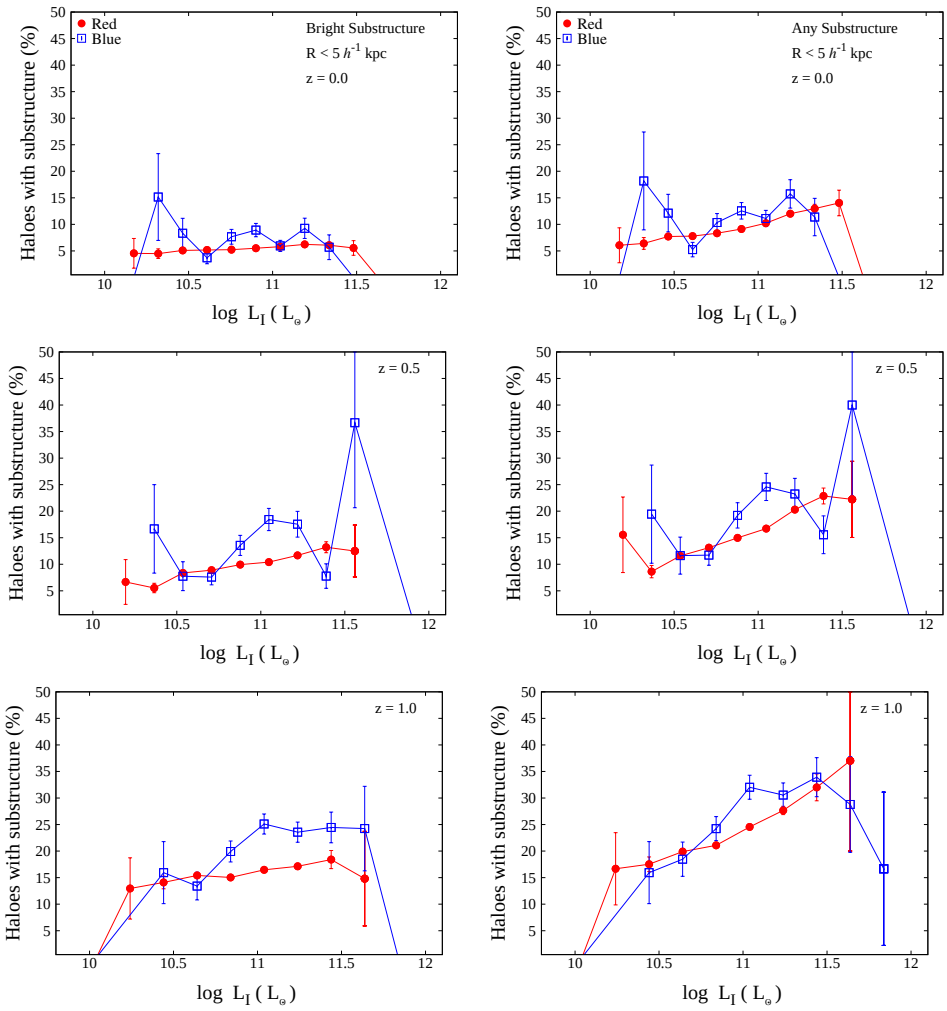


Figure 4.4: As in figure 4.3 but for group-sized haloes ($10^{13}\,h^{-1}\,M_{\odot} \leq M_{vir} < 10^{14}\,h^{-1}\,M_{\odot}$). The left column shows the fraction of haloes with bright satellites ($M_R < -17$) within the central 5 $h^{-1}$ kpc (projected) region. The right column shows the fraction of haloes which contain any substructure within the central 5 $h^{-1}$ kpc (projected) region. In these plots the red population is depicted using filled red circles, while the blue population is shown using blue squares. The three rows show the fraction of haloes containing substructure for the three different redshifts considered (top: $z = 0.0$, middle: $z = 0.5$ and bottom: $z = 1.0$). The Poisson scatter is shown.

versus the projected separation of the satellite galaxy from the host. A random selection of the group-sized haloes with 'dark' substructure (crosses) and bright substructure (circles) from the $z = 1$ sample are shown. The 10 CLASS lenses found to have luminous satellite galaxies are plotted with solid circles; for B1127+385, the horizontal bar shows the range of separations when the lens redshift $z_l$ is varied from 0.5 to

Table 4.2: Fraction of projected central satellites within the 3D central region of galaxy-sized hosts. Numbers in brackets correspond to values for group-sized haloes.

| | $r_{3D}$ < force softening |
|---|---|
| z = 0.0 Bright | 32 (24)% |
| z = 0.0 Total | 26 (17)% |
| z = 0.5 Bright | 17 (11)% |
| z = 0.5 Total | 14 (8)% |
| z = 1.0 Bright | 11 (6)% |
| z = 1.0 Total | 9 (5)% |

Table 4.3: Percentage of bright satellite galaxies without a surviving dark matter subhalo within the virial radius and within the central 5 $h^{-1}$ kpc (projected) region for galaxy-sized hosts. Numbers in brackets correspond to values for group-sized haloes.

| | Redshift | | |
|---|---|---|---|
| | 0.0 | 0.5 | 1.0 |
| Satellites without DM subhalo | 74 (68)% | 81 (76)% | 87 (83)% |
| Projected central satellites without DM subhalo | 98 (98)% | 99 (98)% | 99 (99)% |

1. Selection effects may be complicated and have not been taken into account in this study. While it will be difficult to observe satellites with large magnitude differences at small separations, there are also few simulated satellites found at very small separations. (The increase in number with separation is due to the larger area considered.) As illustrated with the histograms in figure 4.5, the sample of host galaxies and their luminous satellites considered is comparable to the observed galaxies in the (small) CLASS sample.

### 4.4.1 Resolution Effects

As haloes fall into a larger system, they are exposed to tidal forces and are stripped as they orbit the host system. The extent to which a halo is stripped depends on resolution and the inner density profile of the halo (Moore et al. 1996). The simulated subhaloes have artificially low density cores (due to force softening) that make them more susceptible to tidal stripping. Including baryons (and gas cooling) will increase the central density and make the galaxy more resistant to tidal stripping (Moore et al. 1996; Macciò et al. 2006), although the cooling of baryons towards the central host will

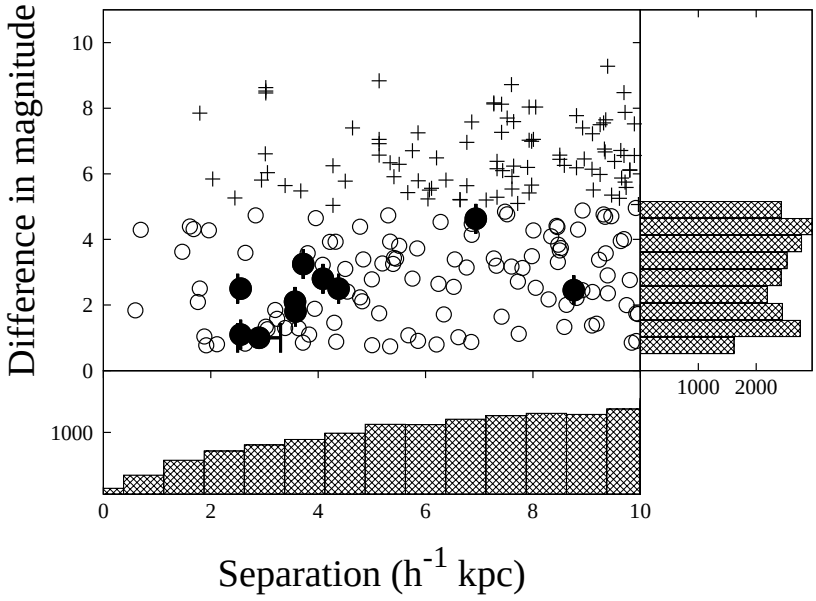


Figure 4.5: Difference in $I$-band magnitude between the host and satellite galaxy versus the projected separation (in $h^{-1}$ kpc) of the satellite galaxy from the host. A random selection of the group-sized haloes (selected at redshift $z = 1.0$) with 'dark' substructure (crosses) and bright substructure (circles) are shown. The 10 CLASS lenses found to have luminous satellite galaxies are plotted with solid circles; for B1127+385, the horizontal bar shows the range of separations when the lens redshift is varied from 0.5 to 1. The histograms show the distribution of bright substructure found within the central 10 $h^{-1}$ kpc (projected) region as a function of separation and magnitude difference.

also increase the tidal forces experienced by subhaloes that come close to the centre.

Nearly all of the satellite galaxies found in the projected central regions are tidally stripped 'orphan' galaxies (see table 4.3). The semi-analytic model used follows the orbits of galaxies which have lost their dark matter subhalo, by assuming that they follow the motion of the most bound particle of the parent subhalo before it was destroyed (this is shown to be a good estimate of the subhalo's position by Springel et al. 2001a). Since the effects of dynamical friction on the orbits of these galaxies are not considered in detail, caution is required when interpreting the results. As noted in Sales et al. (2007), this may affect the overall abundance and radial distribution of these stripped haloes.

Also, it is assumed that the 'orphan' galaxy remains completely undisturbed for a merging time, based on the dynamical friction formula of Binney et al. (1987), until

it merges with the central galaxy. This assumption may result in an over-estimate of the number of 'orphan' galaxies and their associated luminosities. Henriques et al. (2007) take the opposite approach and assume that all 'orphan' galaxies which have not merged with the central galaxy by $z = 0$ are completely disrupted, and are responsible for the diffuse intracluster light. While their results suggest an improved match to the luminosity function in groups and clusters, the model is simplistic. They note that it is more likely that the disruption would happen gradually, and that the dense cores may survive for longer. The extent to which disruption would affect these 'orphan' galaxies remains unclear. However, survival of these 'orphan' galaxies (at least to some extent) has been shown by Wang et al. (2006) to be essential in order to explain the observed correlation signal at small scales. This study used the Millennium Simulation to construct a new model of galaxy clustering. They found that if 'orphan' galaxies were excluded from the analysis, the correlation signal decreased at small scales in contrast to observations.

A related question is: if the numerical resolution of the simulation is increased, would the fraction of luminous satellites rise significantly? Clearly, the number of subhaloes (dark or luminous) must rise further since the subhalo mass function roughly follows a power law with $dn/dM \propto M^{-\alpha}$, $\alpha = 1.7 - 1.9$ (Moore et al. 1999; Ghigna et al. 2000; De Lucia et al. 2004; Gao et al. 2004b; Diemand et al. 2007b). The lowest mass subhaloes which can be resolved have circular velocities $v_c$ at the virial radius of the order $v_c \lesssim 50$ km s$^{-1}$; haloes with $v_c \lesssim 30$ km s$^{-1}$ may be inhibited from star formation by the UV background radiation (for example Rees 1986; Efstathiou 1992; Thoul and Weinberg 1996; Gnedin 2000). Thus many subhaloes may remain dark, and the fraction of bright subhaloes will not increase significantly. Increasing the resolution of the simulation would also mean that some of the 'orphan' galaxies would be resolved. Since only 'orphan' galaxies are allowed to merge with the central galaxy, increasing the resolution may prolong the lifetime of some of the 'orphan' galaxies. To fully understand the impact of this effect a more quantitative analysis is required. Clearly, a firm conclusion can only be reached using higher-resolution

simulations with realistic treatment of the gas processes.

### 4.4.2 The Effect of Cosmology

The Millennium Simulation assumes a power-spectrum normalisation of $\sigma_8 = 0.9$, slightly higher than the latest *WMAP* seven-year result (Komatsu et al. 2011), where $\sigma_8 = 0.8$. A lower value of $\sigma_8$ will mean that haloes are expected to form later and to be less concentrated. However, the impact of this parameter on these results is complicated. The semi-analytic models allow some fine-tuning of parameters to match observations. For example, Wang et al. (2008) found no significant difference in the galaxy populations (at the redshift range relevant here) created from semi-analytic models based on the *WMAP* one-year (Spergel et al. 2003) and *WMAP* three-year (Spergel et al. 2007) $\sigma_8$ values of 0.9 and 0.722, provided suitable galaxy formation parameters were chosen (the difference becomes significant at high redshift). The results are not found to change significantly when based on the *WMAP*3 galaxy catalogue produced by Wang et al. (2008) when the same merger timescale is adopted (as in their model C). However, in their model B (which has the same star formation efficiency but a shorter merger timescale than the De Lucia et al. 2006 catalogue), a factor of $\sim 2$ fewer haloes with central substructure are found.

### 4.4.3 Comparison with CLASS

Approximately half of the 22 primary lensing galaxies in CLASS appear to have a faint companion within the projected central 10 $h^{-1}$ kpc region. The companions have luminosities of about $2 - 40\%$ of the primary galaxy. Simulated host galaxies covering a comparable range of luminosities and host-to-satellite separations to the CLASS lenses have been studied, and the predicted fraction of galaxy- (group-) sized haloes hosting central luminous satellites ($\sim 3\%$ (6%) at $z = 0$; $\sim 11\%$ (17%) at $z = 1$) is found to be lower than the value observed in CLASS. While this fraction is largely independent of galaxy type, it is shown to increase with redshift.

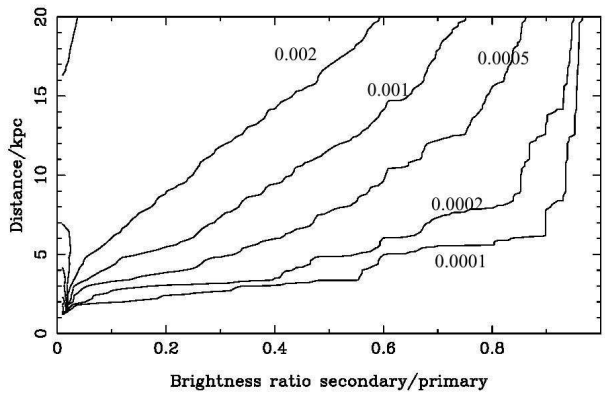


Figure 4.6: Cumulative background-subtracted satellite counts for the COSMOS sample using a colour cut of $B - V > 0.7$ to select elliptical galaxies (figure 6 in Jackson et al. 2010).

The predictions of the redshift and mass dependence appear to be roughly consistent with the data: at least three lenses with luminous satellites are in groups (see section 4.2), and many appear to have redshifts close to $z \sim 1$ , higher than the median redshift ($z \sim 0.6$) of all CLASS lenses (see the bottom panel of figure 4.1).

The comparison so far has not yet considered whether lensing galaxies are biased tracers of substructure; such bias may arise if substructure enhances the lensing cross-sections significantly. Previous studies, on cluster scales, for giant arcs indicate that the bias is small (Hennawi et al. 2007); it remains to be seen whether this holds true for galaxy-scale lenses. Observationally, SLACS seems to indicate that the lensing galaxies at z $\sim$ 0.2 are typical early-type galaxies (Treu et al. 2009).

A natural extension to this study is to compare the predicted frequency with the observed incidence of bright satellites around elliptical galaxies which are not gravitational lens systems. This is addressed in the next section.

## 4.5 Satellites in the Field and Lens Galaxies

In Jackson et al. (2010) elliptical galaxies from the COSMOS survey (Capak et al. 2007; Scoville et al. 2007), a 2-square-degree area observed with the Advanced Camera for Surveys (ACS) on the Hubble Space Telescope (HST) and from the Sloan Digital

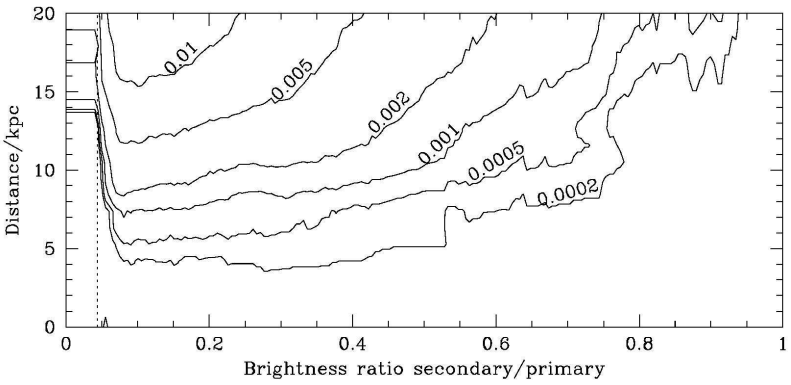


Figure 4.7: Cumulative detection rate of SDSS satellites, as a function of secondary/primary flux ratio and linear distance (figure 9 in Jackson et al. 2010).

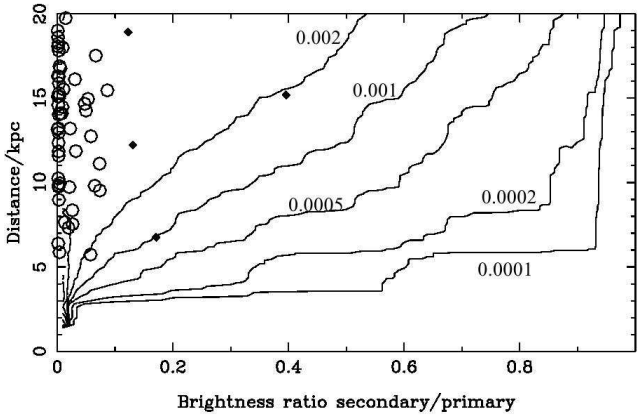


Figure 4.8: Secondary objects identified in SLACS images within 7 arcseconds of the primary lens over-plotted on the background-subtracted COSMOS counts (figure 11 in Jackson et al. 2010).

Sky Survey (SDSS) data release 7 (Adelman-McCarthy et al. 2008) are used to explore the observed frequency of companion galaxies around field ellipticals. The CLASS lenses have also been compared to the SLACS (Bolton et al. 2006, 2008) lens sample, which uses spectroscopic selection of luminous red galaxies from SDSS observed to have more than one redshift in their spectra.

For the COSMOS sample, ACS images in the F814W filter were analysed by Neal Jackson. From this survey 10 974 objects were identified as elliptical galaxies with photometric redshift greater than 0.1 and $I_{814}$ magnitude greater than 24.9. The distri-

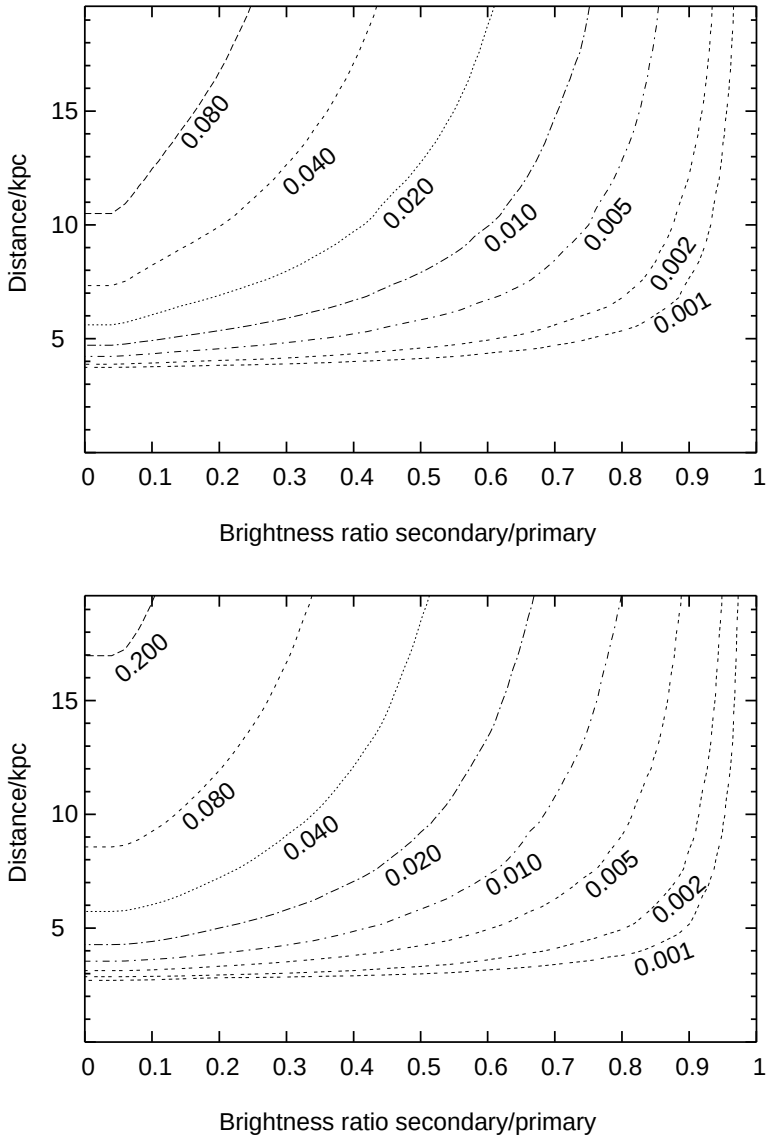


Figure 4.9: The contours show the proportion of galaxies which contain satellites at less than a certain distance $d$ and brighter than a flux ratio $f$, from the primary, using the Millennium Simulation. At each grid point, the contoured quantity represents the proportion of primary galaxies which have secondaries at flux ratio $f$ or brighter, at a distance $d$ or closer. The top plot shows the results for all galaxies with $z \sim 0.5$ and the bottom plot for $z \sim 1$.

butions of redshifts and magnitudes of the COSMOS objects are comparable to those of CLASS. A spherical region of 11.14 arcseconds ($\sim 14\,h^{-1}$ kpc at $z > 0.1$) around the COSMOS objects was searched for secondary objects brighter than $I = 24.9$. To estimate the true frequency of satellites around COSMOS elliptical galaxies, the counts were corrected to account for chance interlopers. Background counts were established using 10 000 random positions within the COSMOS survey area. For full details see Jackson et al. (2010). The background subtracted fraction of elliptical field galaxies with luminous secondaries identified in the COSMOS sample can be seen in figure 4.6.

The SDSS sample was analysed by Cheng Li. For this sample, all galaxies with $r$-band magnitudes $r < 18$ and spectroscopic redshifts less than 0.5 were considered. The sample was trimmed to match the redshift and stellar mass distribution of the SLACS sample, resulting in a sample of 75 839 galaxies. The background subtracted contours of the average correlated neighbour counts around early-type galaxies can be seen in figure 4.7.

It is clear that the observed frequency of satellites around field ellipticals is considerably lower than that seen in the CLASS lens galaxies. In order to increase the lens sample, Neal Jackson analysed the 64 most certain SLACS lenses. Lens candidates are identified by targeting red galaxies in the SDSS data and searching for systems with more than one spectroscopic redshift within the $\sim 0.3$ arcsecond fibre. SLACS lenses typically have redshifts between 0.1 and 0.3. A seven arcsecond radius around each lens galaxy is searched for satellites. A comparison of the COSMOS results with the lens sample of SLACS is shown in figure 4.8.

The frequency of satellites observed in the field elliptical galaxies within the COSMOS sample is consistent with the lower redshift SDSS sample and with that found in the low redshift lens sample obtained from the SLACS survey (although the lens sample is still small).

To compare these observations to theoretical predictions from the standard model, the De Lucia and Blaizot (2007) semi-analytic models run on the Millennium Simulation were used. Haloes were selected from the galaxy catalogue by imposing a

minimum mass cut of $10^{12}\,h^{-1}\,\mathrm{M}_{\odot}$. All galaxies within these haloes satisfying the same cutoffs in brightness and colour selection as the observations were considered (that is, galaxies with magnitudes brighter than $I = 24.9$ and $B - V > 0.7$). The virial radius of each halo was searched for companion galaxies. While previously only central galaxies had been considered, all galaxies satisfying the imposed cuts are included in this analysis. The sample is, however, still dominated by central objects due to the small number of satellites satisfying the mass cuts.

From figure 4.9 it can be seen that, for the mass range considered, the simulations give typical satellite fractions of about 8 times those of the COSMOS values, but even then underpredict the satellite frequency observed in the CLASS samples. The fraction found in simulations does however depend on the lower mass limit imposed when selecting host haloes, as higher mass haloes are more likely to host a companion galaxy. Increasing the mass cut to $10^{13}\,h^{-1}\,\mathrm{M}_{\odot}$ increases the fraction by a factor of $\sim 2$. The number density of the COSMOS sample can be reproduced by imposing a minimum halo mass cut of $\sim 3 \times 10^{11}\,h^{-1}\,\mathrm{M}_{\odot}$ (on non-central galaxies); in doing so the fraction of galaxies found to host a companion is reduced by less than a factor of two (i.e. the fractions are comparable within the level of uncertainty of the observations).

## 4.6 Conclusions

Substructure has been proposed to solve the flux anomaly problem, however it remains unclear as to whether simulations produce enough substructure in the central regions to account for the observed frequency of this phenomenon. In addition, a closer examination of the lensing systems reveals that frequently there is an associated luminous satellite galaxy. The predicted frequency of such luminous satellite galaxies within the ΛCDM model is considered here.

While ~50% of the CLASS lens systems appear to have a bright central companion, the predicted fraction is found to be considerably lower.

Results from the Millennium Simulation combined with semi-analytic galaxy cat-

alogues suggest that ~ 3% (6%) of galaxy- (group-) sized haloes host luminous central satellites. At $z = 1$ this fraction is found to be ~ 11% (17%).

The Poisson probability of detecting luminous substructure in 10 out of 22 lenses, assuming that 3% of haloes host luminous substructure, is $\sim 2\times10^{-9}$. If 17% of haloes host luminous substructure, the probability of such a detection is $\sim 4 \times 10^{-3}$.

Shin and Evans (2008) recently studied the effect of satellite galaxies on gravitational lensing flux ratios using analytic expressions for the host potential and the satellite galaxies. They use a spherically symmetric galaxy distribution, and assume that the three-dimensional number density falls off as $r^{-3.5}$, comparable to the Milky Way. They show that the probability of finding a large dwarf is about 10% within two Einstein radii and about 3% within one Einstein radius. The $z = 0$ simulation results are consistent with this.

The predicted frequency is however found to be higher than that observed in the field galaxies of the COSMOS survey and in the wider, shallower SDSS survey within the depth and resolution limits of the observations. It is also higher than the fraction observed in low redshift ($z \sim 0.2$) SLACS lenses. The high frequency of satellites seen in CLASS is anomalous.

When comparing the lens samples, the main difference lies in the median redshift of the observations. As CLASS lenses are typically at higher redshift than the SLACS lenses, the redshift evolution predicted by the simulations may help to explain this discrepancy. However, the CLASS lenses and COSMOS field galaxies are drawn from a similar redshift range. To explain this discrepancy satellites would need to increase the lensing cross-section enough to bias the lensing statistic. Typically CLASS galaxies are found to be brighter than their COSMOS counterparts by slightly over a magnitude, which could be an indication of higher mass haloes. Simulations show that an increase in halo mass does increase the incidence of close satellites. Increasing the simulated halo mass of a factor of 10 appears to increase the incidence of close satellites by a factor of around 2-3. While this may help to reconcile these results, it is unlikely to increase the fraction sufficiently to completely remove the problem.

The discrepancy may simply be due to the small number of objects within CLASS. Another possibility is that some of the luminous 'satellites' are not associated with lensing galaxies at all, but just happen to be along the line of sight (Metcalf 2005).

What is clear from this work is that studying the very central regions of haloes can provide additional constraints on theoretical models. The central regions are most sensitive to numerical (resolution) and physical (tidal stripping) effects. Models are generally able to reproduce the overall luminosity of satellites, but seem unable to match the small fraction of projected central galaxies.

However, a firm conclusion can only be reached with higher-resolution simulations involving a realistic treatment of the gas processes. At the same time, a larger sample of gravitational lenses will also be beneficial to constrain these models and allow more definitive conclusions on the properties of the substructure to be made.

# 5

# The Impact of Baryons on the Spin and Shape of Haloes

In this chapter the spin and shape of simulated dark matter haloes extracted from OWLS are investigated and the effects of baryons and feedback processes on these properties explored. The spin distributions of the dark matter haloes are well characterised by a log-normal distribution with best-fit values of $\lambda' = 0.035$ and $\sigma = 0.61$ in good agreement with previous studies and the angular momentum appears to be evenly distributed throughout the halo. Dark matter halo shapes are well characterised by Gaussian functions, with best-fit values for the sphericity of $\mu = 0.65$ and triaxiality of $\mu = 0.58$. The radial dependence of the shapes of dark matter haloes is found to be weak – massive haloes show a slight decrease in sphericity between 0.06 and $0.25r_{vir}$. The triaxiality of the dark matter haloes remains almost constant out to the virial radius. The sphericity of the dark matter haloes is shown to decrease as a function of mass while the triaxiality parameter of the halo increases. The overall halo spin parameter is not strongly affected by the addition of baryons nor by the implemented feedback prescription, however the spin parameter of the central region ($r \lesssim 0.12r_{vir}$) of haloes with weak or no feedback is found to be higher than that obtained in the strong feedback runs. The cooling of baryons acts to make the overall halo mass dis-

tribution more spherical, but stronger feedback prescriptions tend to reduce the impact of baryons. The distribution of halo sphericity in the dissipational runs is found to be in broad agreement with observations of elliptical galaxies. The baryonic physics is shown to have a significant effect on the shape of the dark matter distribution. Weak stellar feedback runs are able to produce haloes that are almost oblate within the central regions, while strong stellar and AGN feedback runs result in prolate haloes similar to those found in dark matter only simulations. The effect of baryons is found to be most significant in high mass (cluster-scale) haloes.

## 5.1 Introduction

Dark matter haloes formed in the standard ΛCDM model appear to share a nearly universal internal morphology (see, for example, Navarro et al. 1996, 1997; Bullock et al. 2001 and Duffy et al. 2008) and are typically thought to be triaxial (Frenk et al. 1988; Dubinski and Carlberg 1991; Warren et al. 1992; Cole and Lacey 1996; Jing and Suto 2002; Bailin and Steinmetz 2005b; Allgood et al. 2006; Macciò et al. 2006; Bett et al. 2007). Triaxial dark haloes are a natural consequence of hierarchical structure formation. Smoothed density peaks in the Gaussian random fields that are thought to be the origin of galaxy collapse in hierarchical models are inherently triaxial (Bardeen et al. 1986). Also, mass accretion onto haloes is thought to be directional, with preferential infall from associated filaments. Spherical haloes are extremely unlikely in this formation scenario.

It is also interesting to ask how the shapes of the galaxies embedded within these dark haloes compare with their hosts. Simulations suggest that including baryons and considering dissipational processes acts to make the haloes more spherical. It is therefore likely that galaxies are also more spherical. However, a direct comparison is difficult as galaxy formation is a complicated process and the complex interplay between dissipational cooling and mergers is not fully understood. Disc galaxies are thought to form in undisturbed systems where the gas is able to cool and condense

into a rotationally supported disc, while ellipticals are thought to form via dissipationless mergers (Toomre 1977). The dissipationless nature of elliptical galaxies makes a comparison with dark matter haloes a natural analogy. A comprehensive comparison between theoretical predictions and observations of the angular momentum and the shapes of galaxies and their dark matter haloes may place important constraints on the formation processes and the nature of dark matter, thus providing an additional test of the ΛCDM paradigm.

The angular momentum and shape of a gravitational system are in themselves important quantities in many respects. For example, misalignment of the angular momentum may cause galactic warps (Ostriker and Binney 1989; Debattista and Sellwood 1999; Bailin and Steinmetz 2005a) or may be responsible for the anisotropic distribution of haloes (Holmberg 1969 and Knebe et al. 2004). Asphericity in the dark matter halo will naturally correspond to asphericity in the gas density and will impact on the shape of X-ray isophotes and the Sunyaev-Zel'dovich signal. Deviations from axisymmetry in elliptical galaxies may influence the gas kinematics of the system (de Zeeuw and Franx 1989), and may be responsible for exciting or sustaining warps and stabilising or deforming polar rings (Steiman-Cameron et al. 1992). Axisymmetry may also influence the fuelling efficiency of the central black hole (Franx et al. 1991).

The shapes of dark matter haloes are characterised by the axis ratios $c/a$ and $b/a$ (where $a > b > c$) of either the density or potential distribution of the halo (denoted by a subscript $\rho$ or $\phi$, respectively). The sphericity or amount of flattening is described by $c/a$ while $b/a$ can be used to characterise the elongation of the halo. A spherical halo has $c/a = 1$, prolate haloes have two short axes ($a >> b \sim c$) and oblate haloes are characterised by two long axes ($a \sim b >> c$). A useful measure of the triaxiality of a halo is given by $T = (a^2 - b^2)/(a^2 - c^2)$, where $T = 0$ (1) corresponds to an oblate (prolate) system.

In general, shapes derived from the gravitational potential are more spherical than

those derived from the density distribution . As a general rule of thumb (Sackett 1999):

$$1 - (c/a)_{\rho} \approx 3\left[1 - (c/a)_{\phi}\right]. \tag{5.1}$$

In this chapter the spin and shape of haloes are explored using state-of-the-art high-resolution cosmological hydrodynamical simulations run with different physical prescriptions for the feedback processes. These simulations provide a unique opportunity to explore the effects of baryons and implemented feedback techniques on a large sample of haloes evolved within a cosmological setting. The plan of this chapter is as follows. Section 5.2 reviews current observational estimates of halo shapes and theoretical predictions from the literature are discussed in section 5.3. The simulated haloes used in this analysis are briefly introduced in section 5.4 and the method used to estimate their spin and shape are presented in section 5.5. The spin and shape distributions of the OWLS dark matter haloes are presented in section 5.6. These are compared to the baryon runs in section 5.7. Resolution issues are discussed in section 5.8. The halo shapes are compared to observations of elliptical galaxy shapes in section 5.9 and a summary of the main results is presented in section 5.10.

## 5.2 Observational Constraints

There are several methods used to constrain galaxy and halo shapes observationally. A general review of the techniques used and observational estimates obtained are presented in Sackett (1999) and constraints on the central density distribution and shape of the Milky Way's halo can be found in Merrifield (2004). A useful comparison of the observational constraints on halo flattening is presented in O'Brien et al. (2010). A brief summary of these reviews is given here. This summary is by no means an exhaustive review of the observational constraints but is meant to act as an illustrative introduction to some of the most common techniques used to estimate halo shapes and the range of shape parameters thus obtained. A summary of the constraints on the halo

Table 5.1: Observational constraints on $(b/a)_\rho$ of haloes, updated from Sackett (1999).

| Method | System | Extent | $(b/a)_\rho$ |
|---|---|---|---|
| Scatter in Tully-Fisher relation | | | |
| Franx and de Zeeuw (1992) | Spirals | HI Gas radius | $\gtrsim 0.84$ |
| Elongation of stellar disc | | | |
| Lambas et al. (1992) | APM survey spirals | 1-2 Optical radii | $\gtrsim 0.7$ |
| Fasano et al. (1993) | Unbarred RC3 spirals | 1-2 Optical radii | $\gtrsim 0.8$ |
| K-band imaging of face-on systems | | | |
| Rix and Zaritsky (1995) | Small HI-linewidths | K band radius | $0.77 - 0.93$ |
| Stellar and gas rotation curves | | | |
| Kuijken and Tremaine (1994) | Milky Way | 8 - 16 kpc | $\sim 0.75$ |
| HI gas ring kinematics | | | |
| Franx et al. (1994) | E/SO IC 2006 | $\sim$ 13 kpc | 0.96 |
| Analysis of gas kinematics | | | |
| Franx et al. (1994) | E/SO IC 2006 | $\sim$ 13 kpc | 0.96 |
| Merger remnants | | | |
| Law et al. (2009) | Milky Way | $16 - 60$ kpc | $\approx 0.83$ |

shapes as described by $(b/a)$ and $(c/a)$ can be found in tables 5.1 and 5.2, respectively.

### Elongation

Most observational estimates of the elongation of dark matter density distributions indicate that $(b/a)_\rho > 0.7$ within the central regions of the halo. Lambas et al. (1992) and Fasano et al. (1993) use the intrinsic elongation of the stellar disc to estimate the deviation from axisymmetry of the underlying density distribution. They find that the stellar distribution in elliptical and early-type spirals is typically triaxial, while the distribution in spiral galaxies is more axisymmetric. They determine a lower limit of $(b/a)_\rho \gtrsim 0.7 - 0.8$. Rix and Zaritsky (1995) used K-band imaging of face on systems to minimise the effects of dust and spiral structure from young, bright populations, in an attempt to estimate the non-axisymmetry of the observed potentials. They found an axis ratio estimate of $(b/a)_\phi \approx 0.995$ corresponding to $(b/a)_\rho \approx 0.85$. Kuijken and Tremaine (1994) attempt to resolve the discrepancy between the rotation curve of the Milky Way derived from stellar and gas tracers assuming that the tracers reside in different positions in an intrinsically non-axisymmetric potential. Their models lead to

an estimate of $(b/a)_\rho \approx 0.75$. Observations of the HI gas ring kinematics (Franx et al. 1994) and scatter in the Tully-Fisher relation (Franx and de Zeeuw 1992) also result in similar constraints on the elongation of the dark matter density distribution. Law et al. (2009) modelled properties of the Sagittarius tidal stream and found that $(b/a)_\rho \approx 0.83$ for the Milky Way halo.

**Sphericity**

Observations of dark matter flattening ($c/a$ or the ratio of vertical to radial axes) are less consistent. Estimates of the local surface density from stellar kinematics in the solar neighbourhood result in values of $0.3 < (c/a)_\rho < 0.6$ (van der Marel 1991; Bienaymé et al. 2006). Amendt and Cuddeford (1994) used measurements of RR Lyrae to probe the density distribution of the Milky Way out to 60 kpc, and found $(c/a)_\rho \sim 0.7$. Estimates of the dark matter distribution from the proper motion of a high-velocity star (Gnedin et al. 2005) give $0.5 < (c/a)_\rho \lesssim 1.6$.

**Gas Flaring.** Gas flaring uses the variation of a galaxy's gas layer with radius to provide a constraint on the halo shape. Flattening of the dark matter halo will decrease the tendency for the gas layer to increase with radius. The flaring of HI gas layers is only able to probe scale heights of a few kpc. Olling (1996) first used this technique to show that the halo of NGC 4244 was highly flattened with $(c/a)_\rho \sim 0.2$. A similar flattening is found for NGC 891 by Becquaert and Combes (1997) assuming the gaseous velocity dispersion to be isotropic. Olling and Merrifield (2000) found that flattenings of $0.7 < (c/a)_\rho < 0.9$ were required to fit the observed gas flaring in the Milky Way. Using the same method O'Brien et al. (2010) find that UGC 7321 has a spherical halo density distribution with $(c/a)_\rho \sim 1$.

**Tidal Debris.** Another probe of the Galaxy's shape is provided by the tidal debris of merging satellites. While this approach may extend observational constraints of the dark matter halo to greater scale heights than the previous methods (the apocentre

Table 5.2: Observational constraints on $(c/a)_\rho$ modified and updated from Sackett (1999).

| Method | System | Extent | $(c/a)_\rho$ | Tracer and Comments |
|---|---|---|---|---|
| Stellar kinematics | | | | |
| Binney et al. (1987) | Milky Way | ~ 20 kpc | 0.3 – 0.8 | Pop II stars assumed to trace overall kinematics. |
| van der Marel (1991) | Milky Way | ~ 20 kpc | > 0.34 | Pop II stars. Assumes constant anisotropy locally and approximate hydrostatic equilibrium. |
| Amendt and Cuddeford (1994) | Milky Way | < 60 kpc | ~ 0.7 | RR Lyrae stars. Temperature and anisotropy profiles assumed to vary weakly with radius. |
| Bienaymé et al. (2006) | Milky Way | < 1 kpc | > 0.5 | Red clump stars. Uncertainties on extinction, distances and vertical velocities. Restricted sample size. |
| High velocity stars | | | | |
| Gnedin et al. (2005) | Milky Way | < 80 kpc | 0.5 – 1.6 | SDSS J090745.0+024507. Limited sample size. Assumes axis ratio is constant with radius. |
| Gas flaring | | few kpc | | |
| Olling (1996) | NGC 4244 | | 0.1 – 0.5 | Vertical force balanced by gradients in thermal pressure. Gaseous velocity dispersion ellipsoid round and independent of scale height. |
| Becquaert and Combes (1997) | NGC 891 | | 0.2 – 0.5 | Gaseous velocity assumed to be isotropic. z-isothermality and axisymmetry. Gas and stellar self-gravity ignored. |
| Olling and Merrifield (2000) | Milky Way | | 0.7 – 0.9 | HI emission from gas in hydrostatic equilibrium. Gas thickness does not vary azimuthally. Depends on Galactic constants. |
| Banerjee and Jog (2008) | M 31 | | ~ 0.4 | Bulge and dark matter halo assumed to be rigid and non-responsive. |
| O'Brien et al. (2010) | UGC 7321 | | ~ 1 | Gas velocity dispersion isothermal in z. Pseudo-isothermal halo model assumed. |
| Tidal debris of merging satellites | | | | |
| Law and Majewski (2010) | Milky Way | $16 < R < 60$ kpc | ~ 0.5 | Modelling of the Sagittarius stream. MW modelled as smooth fixed potential, disc assumed to lie on an axis of sym. |
| Polar ring galaxies | | 5 - 20 kpc | | |
| Sackett et al. (1994) | NGC 4650A | | 0.3 – 0.4 | Assumes galaxy is seen edge on. |
| Arnaboldi et al. (1993) | AM2020-50 | | ~ 0.6 | Axisymmetric mass model. |
| X-ray isophotal shapes | | ~ 10 - 20 kpc | | Hydrostatic equilibrium assumed. |
| Buote and Canizares (1996) | NGC 1332 | | 0.28 – 0.53 | |
| Buote and Canizares (1997) | NGC 720 | | 0.37 – 0.60 | |
| Buote and Canizares (1998) | NGC 3923 | | 0.34 – 0.65 | |
| Models of precessing dusty discs | | | | |
| Steiman-Cameron et al. (1992) | NGC 4753 | few kpc | 0.84 - 1.0 | Gas orbits are filled and have completed at least 6 orbits at all radii. |
| Evolution of gaseous warps | | few kpc | | |
| Hofner and Sparke (1994) | 5 spirals | | 0.6 – 0.9 | Assumes gravity is the only acting force, radial mass flow and other dissipative processes ignored. |
| New et al. (1998) | 5 spirals | | > 0.85 | Kinematical viscosity used to simulate effect of dissipative forces. Assumes small warps $\beta \ll 1$. |
| Strong lensing | | | | |
| Oguri et al. (2003) | 38 X-ray clusters | - | ~ 0.5 | Arc statistics. Simulations assume *WMAP*1 cosmological parameters and substructure is ignored. |
| Oguri (2010) | SDSS J1004+4112 | - | ~ 0.76 | Cluster-scale quasar lens system. Model includes perturbations from member galaxies. |
| Kochanek (1995) | MG 1654+134 | - | ~ 0.3 | Assumes an Einstein-De Sitter model. |
| Koopmans et al. (1998) | B1600+434 | - | > 0.4 | Edge on spiral galaxy. |
| Rusin et al. (2002) | multiple quad lens systems | - | > 0.4 | Assumes a smooth halo potential, ignoring substructure. Assumes lens concentration is similar to that of general haloes. |
| Cohn and Kochanek (2004) | multiple quad lens systems | - | ~ 0.7 | Considers the effect of substructure. Lens modelled as singular isothermal sphere. |
| Weak lensing | | | | Ensemble averaged properties. Projected axis ratios. |
| Hoekstra et al. (2004) | Red-Sequence Cluster Survey | - | ~ 0.66 | Assumes halo aligned with galaxy and ellipticity of halo $\propto$ shape of galaxy. Lack of full redshift information. |
| Mandelbaum et al. (2006) | SDSS survey | - | ~ 0.99 | 2 million objects with photometric redshifts. Some dependence on assumed density profile. |

of Sagittarius is thought to be $\sim$ 60 kpc), the results are somewhat uncertain. As a flattened potential would cause the orbit to precess and destroy the observed coherence, the coherence of the Sagittarius dwarf spheroidal stream over a large angle has been used to indicate that the inner halo is nearly spherical (Ibata et al. 2001; Fellhauer et al. 2006). However, Johnston et al. (2005) and Martínez-Delgado et al. (2007) argued for an mildly oblate halo based on a comparison between Sagittarius stream modelling and 2MASS observations of M-stars. Helmi (2004) argued that the data is consistent with both an oblate and a prolate halo. Helmi questioned whether the observed tracers of this stream are dynamically old enough to have been significantly affected by the halo potential. Most recently Law et al. (2009) modelled the Sagittarius stream properties within a triaxial potential and found that the Milky Way halo within $\sim$ 60 kpc is triaxial, with $(c/a)_\rho \approx 0.67$, $(b/a)_\rho \approx 0.83$ and $T \sim 0.56$.

**Polar Ring Galaxies.** Polar ring galaxies probe the flattening of the dark halo perpendicular to the plane of the disc through comparison of two orthogonal rotation curves, those of the disc and the inclined ring. This technique probes the halo on a vertical scale height of between 5 and 20 kpc (Whitmore et al. 1987). Observations of kinematics in polar ring galaxies show a range of shapes varying from $(c/a)_\rho \approx 0.3 - 0.4$ in NGC 4650A (Sackett et al. 1994) to $(c/a)_\rho \approx 0.6$ in AM2020-50 (Arnaboldi et al. 1993). The dark halo flattening appears to be comparable to, and aligned with, the stellar system.

**X-ray Isophotes.** A review of the shapes of elliptical galaxies from X-ray observations is given in Buote and Canizares (1998). The flattening of extended X-ray isophotal shapes is used, under the assumption of hydrostatic equilibrium, to provide a measure of the shape of the gravitational potential in ellipticals, and probes a similar scale height to the polar ring approach. NGC 720 is found to have $0.37 \lesssim (c/a)_\rho \lesssim 0.60$ (Buote and Canizares 1997), a flattening of $0.28 \lesssim (c/a)_\rho \lesssim 0.53$ is observed in NGC 1332 (Buote and Canizares 1996) and NGC 3923 is observed to have $0.34 \lesssim (c/a)_\rho \lesssim$

0.65 (Buote and Canizares 1998). The inferred axis ratios are comparable to, or smaller than, those derived from optical observations of the same systems.

**Dust Lane Modelling.** The complex dust lanes in NGC 4753 were modelled by a precessing dusty disc by Steiman-Cameron et al. (1992) who found that the flattening of the system must be modest with $(c/a)_\rho \geq 0.84$. Estimates of the evolution of warping in the gas layer also tend to favour modest flattening. Hofner and Sparke (1994) and New et al. (1998) apply precessing viscous disc models to fit warps observed in five spiral galaxies (NGC 2841, NGC 3198, NGC 4565, NGC 4013, NGC 4753) finding that the strength of the quadrupole moment of the underlying dark matter potential well must be small, implying that the axis ratios would be small. They found that $0.84 \lesssim (c/a)_\rho \lesssim 1$.

**Gravitational Lensing.** Lensing offers a unique probe of a halo potential in that it provides an estimate of the total mass of the system (baryonic and non-baryonic) and is not limited to luminous matter. It also does not depend on the dynamical state of the system. Lenses may, however, be biased since highly elliptical galaxies may have larger cross-sections. Measuring arc statistics can be used to test the shape of cluster potentials. Intrinsic ellipticity and substructure can contribute significantly to the cluster's ability to form arcs. Oguri et al. (2003) developed a semi-analytic method for measuring arc statistics, using Monte-Carlo ray tracing simulations based on a distribution function for the axial ratios drawn from cosmological simulations. They predicted that triaxial haloes would produce an order of magnitude more arcs than spherical haloes (the exact differences depend on the density profiles). They compare their theoretical predictions to a sample of 38 X-ray selected clusters and note that the triaxial haloes with $(c/a)_\rho \sim 0.5$ drawn from a $\Lambda$CDM cosmology reproduce the observations well. Kochanek (1995) used the radio ring lens galaxy MG 1654+134 to constrain the central mass and structure of this system. The lens models have axis ratios of around 0.3 and are always less elliptical than optical estimates of the inner

regions of the lensing galaxy, where the axis ratio is found to be $\sim 0.7$. The optical estimate is based on the innermost regions of the galaxy and a direct comparison is not possible. A second example of lensing constraints on the shapes of haloes is given by Koopmans et al. (1998), who studied the edge-on spiral lens B1600+434. The lower limit on the oblateness of this halo, based on detailed numerical modelling, was found to be $(c/a)_\rho \geq 0.5$. The dark matter halo around the lensing galaxy is not as flat as the luminous stellar (or gas) component. Oguri (2010) analysed the mass distribution of the cluster-scale quasar lens system SDSS J1004+1422, finding a best-fit axis ratio for the halo of 0.76. Studies of multiple quad lens systems obtain $(c/a)_\rho \geq 0.4$ (Rusin et al. 2002) and $(c/a)_\rho \sim 0.7$ (Cohn and Kochanek 2004). Weak lensing also provides a means to probe the mean projected flattening of the dark matter distribution. Studies by Hoekstra et al. (2004) found $\langle c/a \rangle_\rho \sim 0.66$ and (Mandelbaum et al. 2006) measure $\langle c/a \rangle_\rho \sim 0.99$ (Mandelbaum et al. 2006) from the SDSS survey.

**Concluding Remarks.** The different observational methods yield systematically different results for the shapes of dark matter haloes (Olling and Merrifield 2000; O'Brien et al. 2010). The observations do cover a large range of systems and vary in the extent of the halo probed, making a direct comparison difficult. Whether the discrepancies result from halo-to-halo scatter or systematic errors in the observed estimates is unclear. It is worth noting that Olling and Merrifield (2000) found consistent results for the flattening of the Milky Way halo ($0.7 - 0.9$) using stellar kinematics and the gas flaring technique. With a rapidly accumulating data set and ever increasing sophistication in data analysis tools one can soon expect to have a observational data set which may be more directly compared with theory.

## 5.3 Theoretical Predictions

Theoretical predictions for halo shapes have been studied extensively. Cold dark matter models predict triaxial haloes with $c/a \sim 0.6$. Hot dark matter models predict spher-

ical haloes with $c/a \sim 0.8$ (Peebles 1993), while dark matter candidates such as cold molecular gas and massive decaying neutrinos predict haloes with $c/a \sim 0.2$ (Sciama 1990; Pfenniger et al. 1994). Strongly flattened dark matter haloes indicate that the dark matter is dissipative and possibly baryonic (Sackett et al. 1994). Cosmological $N$-body simulations that use the CDM power spectrum (Frenk et al. 1988; Dubinski and Carlberg 1991) and simulations of an Einstein-de Sitter universe, using a range of spectral indices (Warren et al. 1992), both produce triaxial haloes.

Early studies of haloes drawn from dissipationless simulations found average $(c/a)_\rho$ values of between 0.5 and 0.8 (Dubinski and Carlberg 1991; Warren et al. 1992; Bullock 2002; Jing and Suto 2002). While Dubinski and Carlberg (1991) and Warren et al. (1992) obtained $(b/a)_\rho$ values in the range 0.4 to 0.9, Bullock (2002) estimated halo elongations to lie between 0.7 and 1. In these studies the dark matter haloes were found to be highly flattened and to show a tendency toward prolate shapes ($c/b > b/a$) especially in the inner regions. There is disagreement in the literature regarding the radial dependence of sphericity of simulated haloes. Frenk et al. (1988); Cole and Lacey (1996); Bullock (2002) and Allgood et al. (2006) note that the sphericity of dark matter haloes increases with radius while Dubinski and Carlberg (1991); Warren et al. (1992); Jing and Suto (2002) and Hopkins et al. (2005) suggest that it decreases with radius. Springel et al. (2004) found that the shape of the dark haloes in dissipationless simulations is nearly constant with radius, noting a weak trend for increased elongation in the central region. Bailin and Steinmetz (2005b) identified three distinct regions within a halo; they note that for the most part sphericity increases with radius but that infalling unvirialised structure at the virial radius results in a decrease in sphericity in the outer regions of the halo. They also found that the sphericity rises in the innermost regions ($0.06r_{vir}$) of their haloes, although they note that this may be a numerical artifact. They claim that this complicated non-monotonic radial dependence may help to reconcile the previous results.

Preliminary analyses of galaxy-scale dark matter haloes suggested that they were systematically rounder than the simulated clusters (Bullock 2002). While there is gen-

eral agreement in the literature that the sphericity of a dark matter halo decreases with increasing halo mass, the slope of this relation is debated. Bullock (2002) found that $c/a$ is a strong function of halo mass and decreases from 0.7 for haloes of mass $10^{12}$ $h^{-1}M_{\odot}$ to 0.55 for cluster-sized haloes with masses of around $10^{14}$ $h^{-1}M_{\odot}$. Jing and Suto (2002) found that the sphericity of haloes decreases only slightly with mass. Springel et al. (2004) and Hopkins et al. (2005) noted a mass dependence similar to that claimed by Bullock (2002). Macciò et al. (2006) and Bett et al. (2007) found that the sphericity of the halo ranges from 0.65 to 0.55 over this mass range.

Dissipational simulations predict systematically more spherical haloes than corresponding dissipationless runs (see, for example, Katz and Gunn 1991; Dubinski 1994; Evrard et al. 1994; Barnes and Hernquist 1996a; Tissera and Dominguez-Tenreiro 1998; Springel et al. 2004; Kazantzidis et al. 2004; Debattista et al. 2008). Gas cooling is found to increase the axis ratio $c/a$ by $> 0.2$ in the inner regions; this difference is found to decrease with radius but appears to persist out to the virial radius.

It is clearly established that the condensation of baryons to the centre of dark matter haloes tends to result in the halo becoming more spherical or axisymmetric. This result has been used to explain the discrepancy between the strongly prolate-triaxial shape found in $N$-body simulations with the more spherical systems observed. For example, the distribution of dark matter shapes of haloes drawn from dissipational simulations is shown to provide a good match to the round stellar systems observed in elliptical galaxies (Springel et al. 2004).

Clearly a full picture of galaxy formation and evolution requires realistic treatment of gas processes. However, incorporating baryonic physics in cosmological simulations is a non-trivial task and the computational cost of this process has placed limits on both the parameter space and the size of the sample of haloes explored to date. The role of baryons on galaxy formation therefore remains largely uncertain. By providing identical simulations run with different implementations of the subgrid physics, OWLS offers a unique opportunity to explore the effects of baryons and implemented feedback techniques on the spin and shapes of haloes in high-resolution cosmological

simulations.

## 5.4 Simulations and Halo Sample

The haloes used for this analysis were extracted from OWLS; for detailed information about these simulations the reader is referred to the discussion in section 3.8.2 and to Schaye et al. (2010). Here the relevant aspects of the simulations used in this analysis are briefly reviewed for convenience.

Most of the simulations used in this thesis were run using cosmological parameters taken from the *WMAP*3 data as discussed in chapter 3. However, in this chapter, the effects of cosmology are also considered. This is done by analysing a $512^3$ particle dark matter only simulation run with *WMAP*5 parameters (Komatsu et al. 2009) with: $\Omega_m = 0.258$, $\Omega_\Lambda = 0.742$, $h = 0.719$, $n_s = 0.963$ and $\sigma_8 = 0.796$. For both of these cosmologies the dark matter simulations were run in 100 and 400 $h^{-1}$ Mpc (comoving) boxes. A smaller simulation run with *WMAP*1 parameters (Spergel et al. 2003) with: $\Omega_m = 0.25$, $\Omega_\Lambda = 0.75$, $h = 0.73$, $n_s = 1$ and $\sigma_8 = 0.9$ using $216^3$ particles in a 50 $h^{-1}$ Mpc box was also considered (this run has the same resolution as the Millennium Simulation). In the dark matter only runs the particle mass is $8.6 \times 10^8\, h^{-1}\, \mathrm{M}_\odot$ in the 50 $h^{-1}$ Mpc box, $4.9 \times 10^8\, h^{-1}\, \mathrm{M}_\odot$ in the 100 $h^{-1}$ Mpc box and $3.1 \times 10^{10}\, h^{-1}\, \mathrm{M}_\odot$ in the 400 $h^{-1}$ Mpc box.

To explore the effect of varying levels of feedback on the shapes and spin parameters of haloes extracted from ΛCDM simulations, four baryon runs from the OWLS simulations are considered. These are summarised in table 3.2 and discussed in detail in section 3.8.2. Haloes from dark matter only simulations are compared with haloes in these dissipational hydrodynamic simulations which include gas cooling and star formation as well as various implementations of feedback (no feedback, weak stellar feedback, strong stellar feedback and feedback from stars and AGN).

## 5.5 Methodology

Haloes are defined using the spherical overdensity (SO) approach and all particles (dark matter and baryonic) within the spherical region are selected for analysis. Four definitions for the halo outer radius are used in this chapter. Firstly, all particles within the virial radius $r_{vir}$ are considered, where the mean density is the overdensity $\Delta$ multiplied by the critical density. Here $\Delta$ is based on the spherical collapse model and is assumed to depend on cosmology and redshift as described by Bryan and Norman (1998) (see section 2.2.4). At $z = 0$, the spherical collapse overdensity $\Delta$ is $\sim 95$ for the cosmological parameters considered here. Haloes defined by $r_{200}$, $r_{500}$ and $r_{2500}$ are also considered, where the mean density is 200, 500 and 2500 times the critical density respectively. This range of halo definitions probes increasingly smaller and more central regions of the halo and is chosen to allow for a closer comparison with observations.

Only haloes that contain more than 1000 particles are considered for this analysis, as this ensures that the results are fully converged (for a detailed discussion on the effects of resolution see section 5.8). While estimates of the spin parameter are found to be well resolved for haloes with more than 300 particles (as in Bett et al. 2007) a higher number of particles is required to resolve the halo shape (in particular the triaxiality of the halo). For consistency, the study presented here is therefore limited to haloes with more than 1000 particles; this conservative limit is in agreement with that used in Macciò et al. (2008). Haloes are also required to be in a relaxed state as defined by the centroid shift, that is, the distance between the minimum potential position (halo centre) and the centre of mass of the halo must be less than $0.07 r_{vir}$ (as discussed in Neto et al. 2007).

The spin parameters $\lambda'$ of the simulated haloes are estimated using the expression given by Bullock et al. (2001) as

$$\lambda' = \frac{J}{\sqrt{2} M v_c r}, \tag{5.2}$$

where $J$ is the angular momentum within a sphere of radius $r$ containing mass $M$ and $v_c$ is the halo circular velocity at this radius ($v_c^2 = GM\,(<r)\,/r$). It reduces to the standard spin parameter (Peebles 1969) when measured at the virial radius of a truncated singular isothermal halo. For an isolated virialised system, the spin parameter provides a comparison of the amount of coherent rotation to random motion (Bett et al. 2007). For a spherical object it can be thought of as the ratio of the object's angular velocity to the angular velocity required for rotational support against gravitational collapse.

To characterise the halo shape, the reduced inertia tensor $\mathbf{I}$ (weighting particles by $1/r^2$) is often used such that

$$I_{ij} = \sum_k \frac{m_k \left(r_i^2 \delta_{ij} - r_{k,i} r_{k,j}\right)}{r_k^2}, \tag{5.3}$$

where $I_{ij}$ are the components of the $3 \times 3$ inertia tensor. All $k$ particles, each with mass $m_k$, are summed. The distance of the $k^{th}$ particle from the centre of the halo is denoted as $r_k$ and $r_{k,i}$ is the distance to the $i-$axis. The mass distribution tensor $\boldsymbol{\mathcal{M}}$ (implemented in this work) is also used extensively in the halo shape literature (see, for example, Cole and Lacey 1996; Bailin and Steinmetz 2005b):

$$\mathcal{M}_{ij} = \sum_k \frac{m_k r_{k,i} r_{k,j}}{r_k^2}. \tag{5.4}$$

The square roots of the eigenvalues of the mass distribution tensor, obtained using Jacobi transformations, are defined as $a, b, c$ (where $a > b > c$) and are used to measure the shape of the simulated haloes. Note that the shapes obtained using the inertia tensor $\mathbf{I}$ and the mass distribution tensor $\boldsymbol{\mathcal{M}}$ are equivalent (Bett et al. 2007).

As previously mentioned, the shape parameters are defined as follows: $s = c/a$ is used as a measure of halo sphericity and $T = (a^2 - b^2)/(a^2 - c^2)$ as a measure of the triaxiality of the halo. Computation of the inertia tensor in a spherical region biases the shapes towards higher sphericity; this is corrected for (as in Bailin and Steinmetz 2005b) by adopting the empirically motivated modified axis ratios $(c/a)_{\rm true} \equiv (c/a)_{\rm measured}^{\sqrt{3}}$

and $(b/a)_{\rm true} \equiv (b/a)^{\sqrt{3}}_{\rm measured}$. These corrections were calibrated using constructed haloes with known axis ratios (see Bailin and Steinmetz 2005b).

## 5.6 Results from a Dissipationless Simulation

In this section, the spin and shape of dark matter haloes are discussed and the effect of different cosmological models is assessed. The results obtained are compared with values from the literature.

### 5.6.1 Spin Distributions

The spin distribution $P(\lambda')$ of the 4122 relaxed dark matter haloes (containing more than 1000 particles) extracted from the *WMAP*3 simulation at $z = 0$ is shown in figure 5.1. The left panel shows the distribution of the spin parameter $P(\lambda')$ computed within the virial radius $r_{vir}$ while the right panel shows $P(\lambda')$ of the same haloes calculated using *only* particles within the central region ($0.12r_{vir}$). The spin distributions of the dark matter haloes are well described by a log-normal distribution

$$P(\lambda') = \frac{1}{\lambda' \sqrt{2\pi}\sigma} \exp\left(\frac{-\ln(\lambda'/\lambda'_0)^2}{2\sigma^2}\right). \tag{5.5}$$

with best-fit values of $\lambda'_0 = 0.035$ and $\sigma = 0.61$ when calculated within the virial radius and $\lambda'_0 = 0.038$ and $\sigma = 0.63$ when computed within the central region. The spin distribution drawn from these simulations is in excellent agreement with that found by Bullock et al. (2001) who obtained best-fit values of $\lambda'_0 = 0.035$ and $\sigma = 0.5$, Bailin and Steinmetz (2005b) who measured $\lambda'_0 = 0.035$ and $\sigma = 0.58$ and Macciò et al. (2008) who found a mean value of $\lambda'_0 = 0.031$ and $\sigma = 0.54$.

Note that the best-fit values are not substantially different when limiting the analysis to the most central region. As in Bailin and Steinmetz (2005b) the angular momentum appears to be evenly distributed throughout the halo.

The effects of cosmology on the spin parameter distribution of dark matter haloes

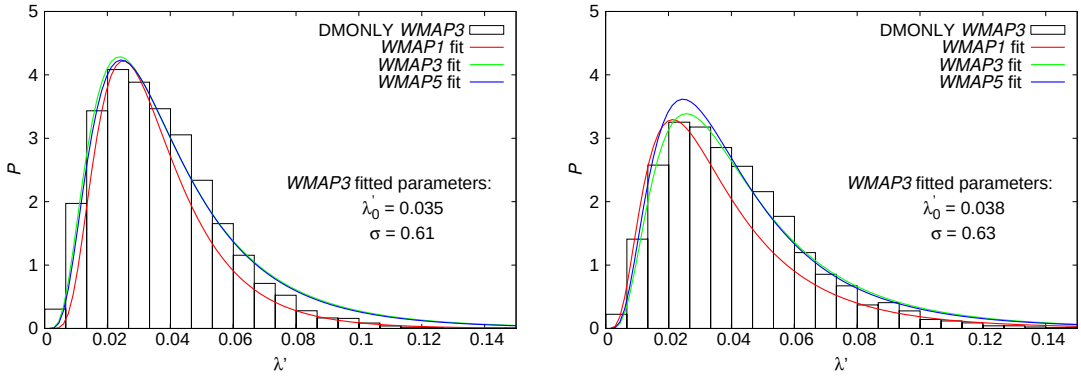


Figure 5.1: Distribution $P$ of the dark matter halo spin parameters $\lambda'$ at $z = 0$ simulation. The histogram depicts the $WMAP3$ halo distribution and the green curve shows the best-fit log-normal function to these haloes. These best-fit values are given within each plot, where $\lambda_0$, $\sigma$ denotes the mean and standard deviation of the distribution, respectively. Also shown are the best-fit curves to the $WMAP1$ (red) and $WMAP5$ (blue) simulations. The left panel shows the spin distribution computed using all particles within the virial radius $r_{vir}$ of the 4122 relaxed haloes (containing at least 1000 particles) while the right panel shows the spin parameter $\lambda'$ computed using particles within the central 12% of $r_{vir}$ of the same haloes.

Table 5.3: Best-fitting parameters for log-normal distribution of spin parameters $\lambda'$ of the relaxed halo sample extracted from the dark matter only simulations. Here $\lambda'_0$ denotes the mean and $\sigma$ the standard deviation.

| | | Within $r_{vir}$ | | Within $0.12r_{vir}$ | |
|---|---|---|---|---|---|
| Cosmology | # haloes | $\lambda'_0$ | $\sigma$ | $\lambda'_0$ | $\sigma$ |
| $WMAP1$ | 415 | 0.032 | 0.50 | 0.032 | 0.64 |
| $WMAP3$ | 4122 | 0.035 | 0.61 | 0.038 | 0.63 |
| $WMAP5$ | 4433 | 0.035 | 0.60 | 0.037 | 0.63 |

are considered by comparing simulations run with the $WMAP1$, $WMAP3$ and $WMAP5$ cosmological parameters. Log-normal curves fit to the spin distribution of each of these simulations are shown in figure 5.1 and the best-fit parameter values are listed in table 5.3. It is evident from this table (as in Macciò et al. 2008) that the spin distribution is not sensitive to the exact choice of cosmological parameters. The largest change in these models is the value of $\sigma_8$, which varies from 0.7 in $WMAP3$ to 0.9 in $WMAP1$. Haloes in a lower $\sigma_8$ cosmology are expected to form later and be less concentrated than those in a higher $\sigma_8$ cosmology. The spin distribution itself remains almost unchanged for the range of parameters explored here.

### 5.6.2 Shape Distributions

The distributions of the dark matter halo shape parameters can be characterised by a Gaussian function and are shown in figure 5.2. Histograms are used to illustrate the shape distribution of haloes from the $WMAP3$ simulation and the best-fit Gaussian is shown as a green curve. The top plot presents the distribution of halo sphericity, which is found to have a best-fit mean value of $\mu = 0.648 \pm 0.002$ and standard deviation $\sigma = 0.098 \pm 0.002$. The halo elongation distribution, displayed in the central panel, is characterised by $\mu = 0.816 \pm 0.005$ and $\sigma = 0.099 \pm 0.005$. The distribution of triaxiality parameters is shown in the bottom plot and is found to have $\mu = 0.58 \pm 0.01$ and $\sigma = 0.26 \pm 0.02$. Also shown are the fits to the $WMAP1$ (red) and $WMAP5$ (blue) haloes.

### 5.6.3 Shape Profiles

The radial distribution of the sphericity and triaxiality of dark matter haloes extracted from the simulations is shown in the left and right panels of figure 5.3, respectively. The shapes have been computed within cumulative bins. Each row represents a different mass range. From top to bottom the mass ranges considered are $M_{vir} < 10^{12} h^{-1} M_{\odot}$ (small galaxies), $10^{12} < M_{vir} < 10^{13}\, h^{-1}\, M_{\odot}$ (large galaxies) and $M_{vir} > 10^{13}\, h^{-1}\, M_{\odot}$ (groups and clusters), respectively. The mass range considered here is comparable to that explored by Bailin and Steinmetz (2005b). The shapes of haloes taken from a $WMAP1$ cosmology are shown as red squares, the shapes of $WMAP3$ haloes are shown as green circles and $WMAP5$ haloes are shown as blue triangles. The error bars show the 25 and 75 percentiles of the halo-to-halo scatter.

There is no significant difference in either the sphericity or the triaxiality of the haloes drawn from these three cosmologies. The radial shape profiles of the low mass haloes are remarkably flat, indicating that the sphericity and triaxiality of these haloes are constant out to the virial radius, although there is large halo-to-halo scatter in the triaxiality parameters. The radial dependence of the more massive objects is weak, but

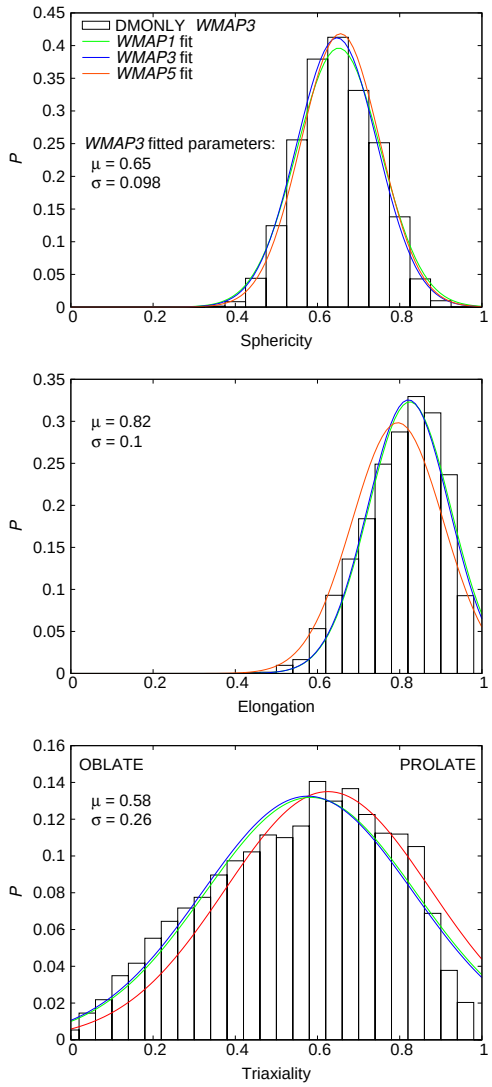


Figure 5.2: Shape distribution $P$ of the dark matter haloes computed within the virial radius $r_{vir}$. The distributions of halo sphericity (top), elongation (central) and triaxiality (bottom) parameters are shown. The best-fit Gaussian to the $WMAP3$ haloes is plotted as a green curve and the best-fit parameters are given in each plot. Here $\mu$ is the mean value and $\sigma$ denotes the standard deviation. Also shown are the fits to the $WMAP1$ (red) and $WMAP5$ (blue) haloes.

suggests that massive haloes become, on average, less spherical, less prolate and more triaxial in the outer regions. While the sphericity of the haloes seems very weakly dependent on mass, the triaxiality parameter increases with mass, showing a tendency for the most massive objects to have prolate shapes.

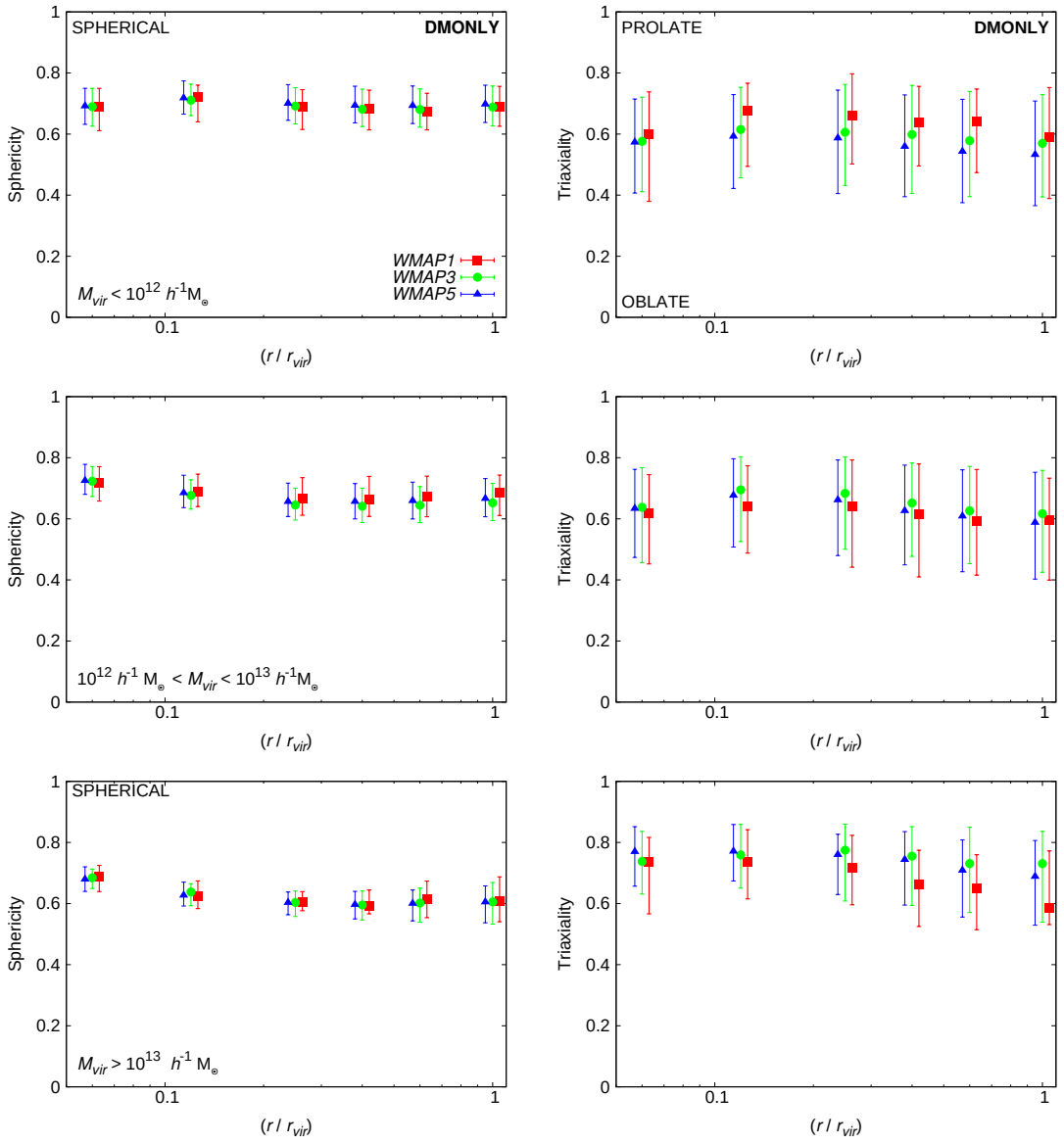


Figure 5.3: The effect of cosmology on the radial shape profiles is explored by comparing dark matter only simulations run with a WMAP1 (red squares), WMAP3 (green circles) and WMAP5 (blue triangles) cosmology. The left panels show the radial distribution of the sphericity of the halo; the right panels show the distribution of the triaxiality of the halo. The distributions are plotted in cumulative bins. Each row represents a different mass range (as denoted in the plot). The error bars show the 25 and 75 percentiles of the halo-to-halo scatter. The positions of the bins have been staggered for clarity. All bins are beyond the softening range $2.8\epsilon$ (defined in section 3.2 and discussed in section 3.4.1).

### 5.6.4 Shape versus Halo Mass

The relationship between halo shape and mass is shown in figures 5.4 and 5.5. These figures show the median halo shape (sphericity and triaxiality) within each mass bin and the error bars show the 25 and 75 percentiles of the halo-to-halo scatter. Haloes are required to contain at least 1000 particles and mass bins at least 5 haloes. Least-squares lines of best-fit to each simulation set are also shown and the best-fit values are listed in table 5.4. This table gives the slope and intercept of the best-fit line, assuming a pivot mass of $M_{pivot} = 1 \times 10^{12}\, h^{-1}\, \mathrm{M}_{\odot}$. The best-fit line to the sphericity-shape relation within $r_{200}$ has a slope of $-0.045^{+0.003}_{-0.007}$ and an intercept of $0.658^{+0.005}_{-0.002}$ in good agreement with the values ($-0.046 \pm 0.016$ and $0.630 \pm 0.018$ ) obtained by Macciò et al. (2008).

Once again, it is clear that there is no significant difference between different cosmologies studied here. There is a trend for more massive haloes to be less spherical. This trend is clear in all cosmologies and for each of the halo definitions considered. Despite the large halo-to-halo scatter in the triaxiality parameter there is a clear trend for more massive haloes to have more prolate shapes. This may be a consequence of their more recent formation time (Springel et al. 2004). The sphericity values computed within $r_{vir}$ vary from 0.66 for haloes of mass $10^{12}\ h^{-1}\, M_{\odot}$ to 0.55 for haloes of mass $10^{14}\ h^{-1}\, M_{\odot}$, in excellent agreement with Macciò et al. (2006) and Bett et al. (2007). The triaxiality parameter varies from $\sim 0.59$ to $\sim 0.73$ over the same mass range. These values are also in agreement with the range of triaxialities ($0.68 - 0.8$) found by Bett et al. (2007).

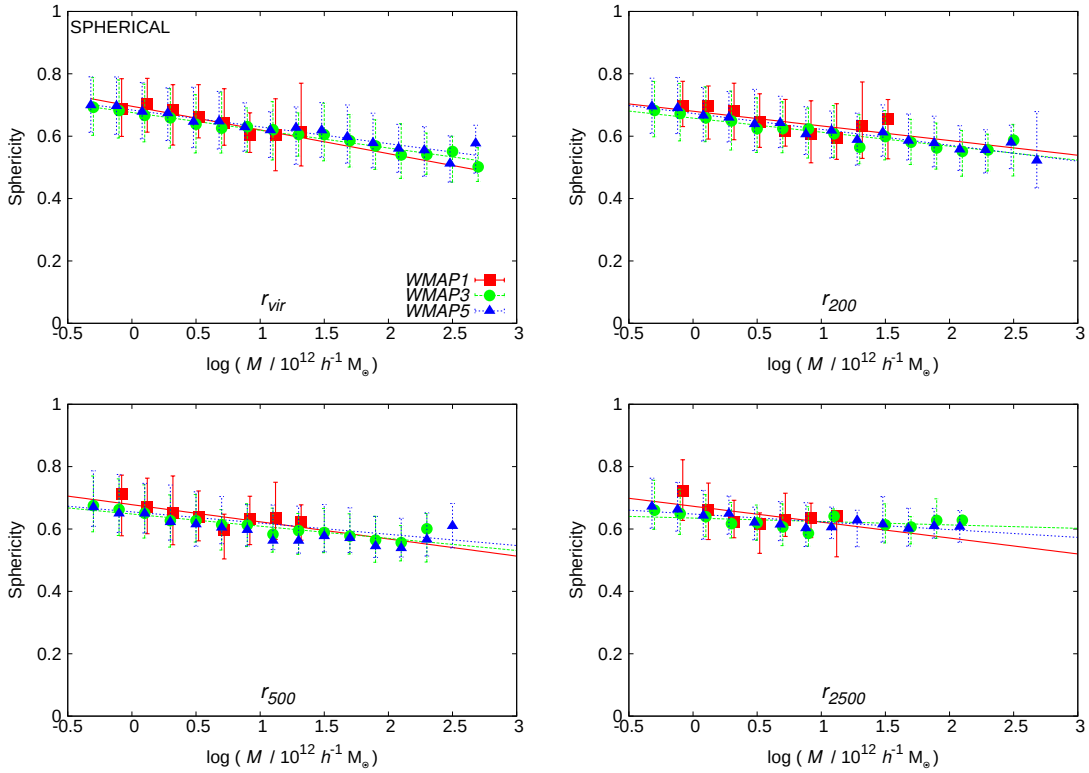


Figure 5.4: Sphericity versus mass $M$ for haloes extracted from dark matter only $WMAP1$ simulation (red squares), $WMAP3$ simulations (green circles) and $WMAP5$ simulations (blue triangles). From left to right, top to bottom the sphericity is measured within $r_{vir}$, $r_{200}$, $r_{500}$ and $r_{2500}$. Least-squares lines of best-fit to each simulation set are shown and the best-fit values are listed in table 5.4. Haloes are required to contain at least 1000 particles and mass bins are required to contain at least 5 haloes.

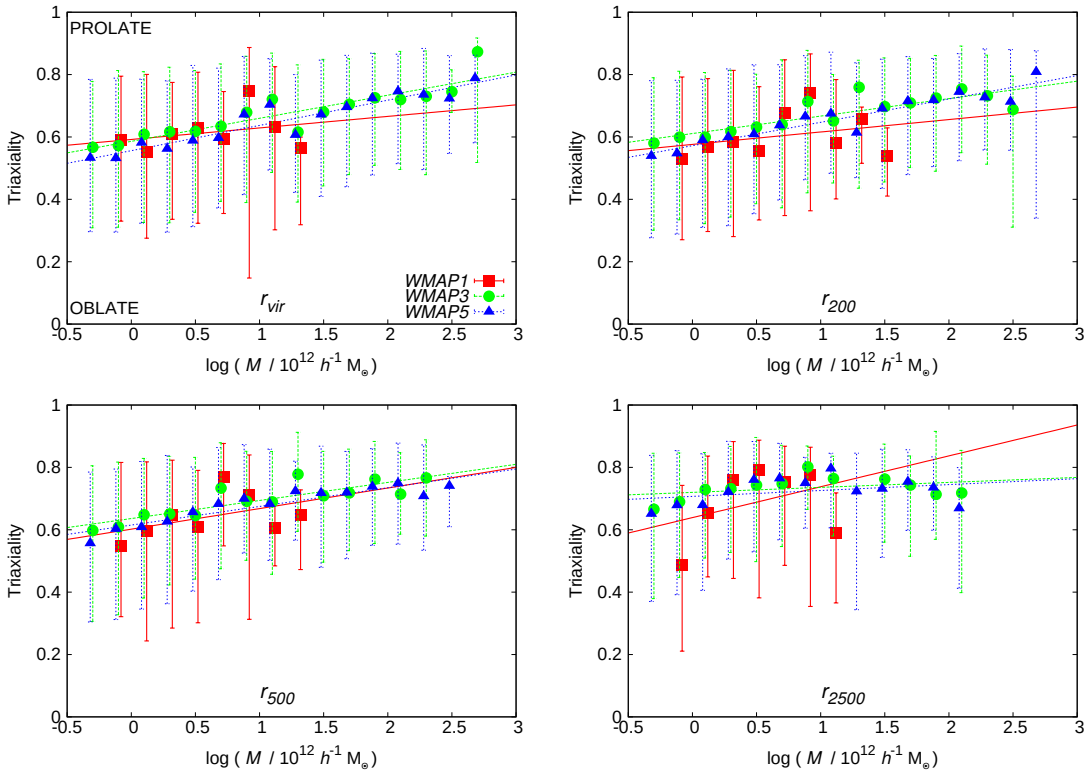


Figure 5.5: As in figure 5.4 but now for triaxiality versus halo mass $M$.

Table 5.4: Best-fit parameters for the median sphericity and triaxiality of the relaxed halo samples extracted from a dark matter only simulation run with the $WMAP1$, $WMAP3$ and $WMAP5$ cosmology. The errors correspond to $1\sigma$ confidence intervals and have been determined by bootstrap resampling (1000 bootstrap samples have been used).

| | Sphericity | | Triaxiality | |
|---|---|---|---|---|
| | Slope | Intercept | Slope | Intercept |
| | | $WMAP1$ | | |
| $r_{vir}$ | $-0.076\ ^{+0.044}_{-0.016}$ | $0.696\ ^{+0.014}_{-0.016}$ | $0.037\ ^{+0.049}_{-0.036}$ | $0.592\ ^{+0.021}_{-0.040}$ |
| $r_{200}$ | $-0.047\ ^{+0.023}_{-0.043}$ | $0.680\ ^{+0.019}_{-0.008}$ | $0.040\ ^{+0.059}_{-0.030}$ | $0.576\ ^{+0.022}_{-0.031}$ |
| $r_{500}$ | $-0.055\ ^{+0.021}_{-0.044}$ | $0.678\ ^{+0.017}_{-0.007}$ | $0.066\ ^{+0.055}_{-0.068}$ | $0.602\ ^{+0.045}_{-0.036}$ |
| $r_{2500}$ | $-0.051\ ^{+0.020}_{-0.065}$ | $0.673\ ^{+0.023}_{-0.016}$ | $0.099\ ^{+0.211}_{-0.068}$ | $0.639\ ^{+0.048}_{-0.073}$ |
| | | WMAP3 | | |
| $r_{vir}$ | $-0.057\ ^{+0.006}_{-0.005}$ | $0.676\ ^{+0.004}_{-0.004}$ | $0.074\ ^{+0.005}_{-0.016}$ | $0.586\ ^{+0.014}_{-0.005}$ |
| $r_{200}$ | $-0.045\ ^{+0.003}_{-0.007}$ | $0.658\ ^{+0.005}_{-0.002}$ | $0.056\ ^{+0.011}_{-0.014}$ | $0.611\ ^{+0.008}_{-0.009}$ |
| $r_{500}$ | $-0.039\ ^{+0.008}_{-0.006}$ | $0.648\ ^{+0.004}_{-0.005}$ | $0.058\ ^{+0.009}_{-0.007}$ | $0.636\ ^{+0.009}_{-0.009}$ |
| $r_{2500}$ | $-0.011\ ^{+0.001}_{-0.008}$ | $0.635\ ^{+0.005}_{-0.002}$ | $0.016\ ^{+0.023}_{-0.012}$ | $0.720\ ^{+0.008}_{-0.012}$ |
| | | WMAP5 | | |
| $r_{vir}$ | $-0.054\ ^{+0.004}_{-0.003}$ | $0.684\ ^{+0.003}_{-0.004}$ | $0.081\ ^{+0.006}_{-0.008}$ | $0.556\ ^{+0.011}_{-0.006}$ |
| $r_{200}$ | $-0.051\ ^{+0.011}_{-0.004}$ | $0.673\ ^{+0.003}_{-0.007}$ | $0.075\ ^{+0.008}_{-0.013}$ | $0.572\ ^{+0.014}_{-0.006}$ |
| $r_{500}$ | $-0.036\ ^{+0.004}_{-0.008}$ | $0.655\ ^{+0.004}_{-0.003}$ | $0.060\ ^{+0.005}_{-0.008}$ | $0.615\ ^{+0.010}_{-0.006}$ |
| $r_{2500}$ | $-0.025\ ^{+0.005}_{-0.004}$ | $0.648\ ^{+0.004}_{-0.004}$ | $0.019\ ^{+0.021}_{-0.025}$ | $0.707\ ^{+0.010}_{-0.014}$ |

## 5.7 The Impact of Baryons and Feedback

This section focuses on the impact of baryons and feedback on the shape and spin of haloes in a fixed *WMAP*3 cosmology.

### 5.7.1 Spin Distributions

The spin distribution of the relaxed haloes (containing more than 1000 particles) extracted from the *WMAP*3 baryonic simulations at $z = 0$ is shown in figure 5.6. The left panel shows the distribution of the spin parameter computed within the virial radius of the haloes, while the right panel shows the spin parameter of the same haloes computed only using particles within the central region (0.12 $r_{vir}$). This central region is likely to be more strongly affected by the influence of baryons and feedback. From top to bottom the spin distribution in the no feedback run (NOFB_ZCOOL0), the weak stellar feedback run (REF), the strong stellar feedback run (WDENS) and the stellar and AGN feedback run (AGN) are shown. The spin distributions are again characterised by a log-normal distribution, shown as a blue curve with best-fit values given in each plot (they are also summarised in table 5.5). While the overall spin parameter within $r_{vir}$ remains unchanged regardless of the type of feedback implemented, the spin parameter computed within the central region of the weak/no feedback runs is found to be higher than that seen in the strong feedback runs. The distribution of spin parameters drawn from the strong feedback runs is comparable to that of the dark matter only haloes. In the weak feedback runs gas is able to cool dissipatively and condenses in the centre of the haloes, increasing the central spin of the systems.

### 5.7.2 Shape Distributions

The distributions of the halo shape parameters are compared to those found in the dark matter only runs in figure 5.7. The top plot shows the distribution of halo sphericity, the middle plot shows the distribution of elongation and the distribution of triaxiality

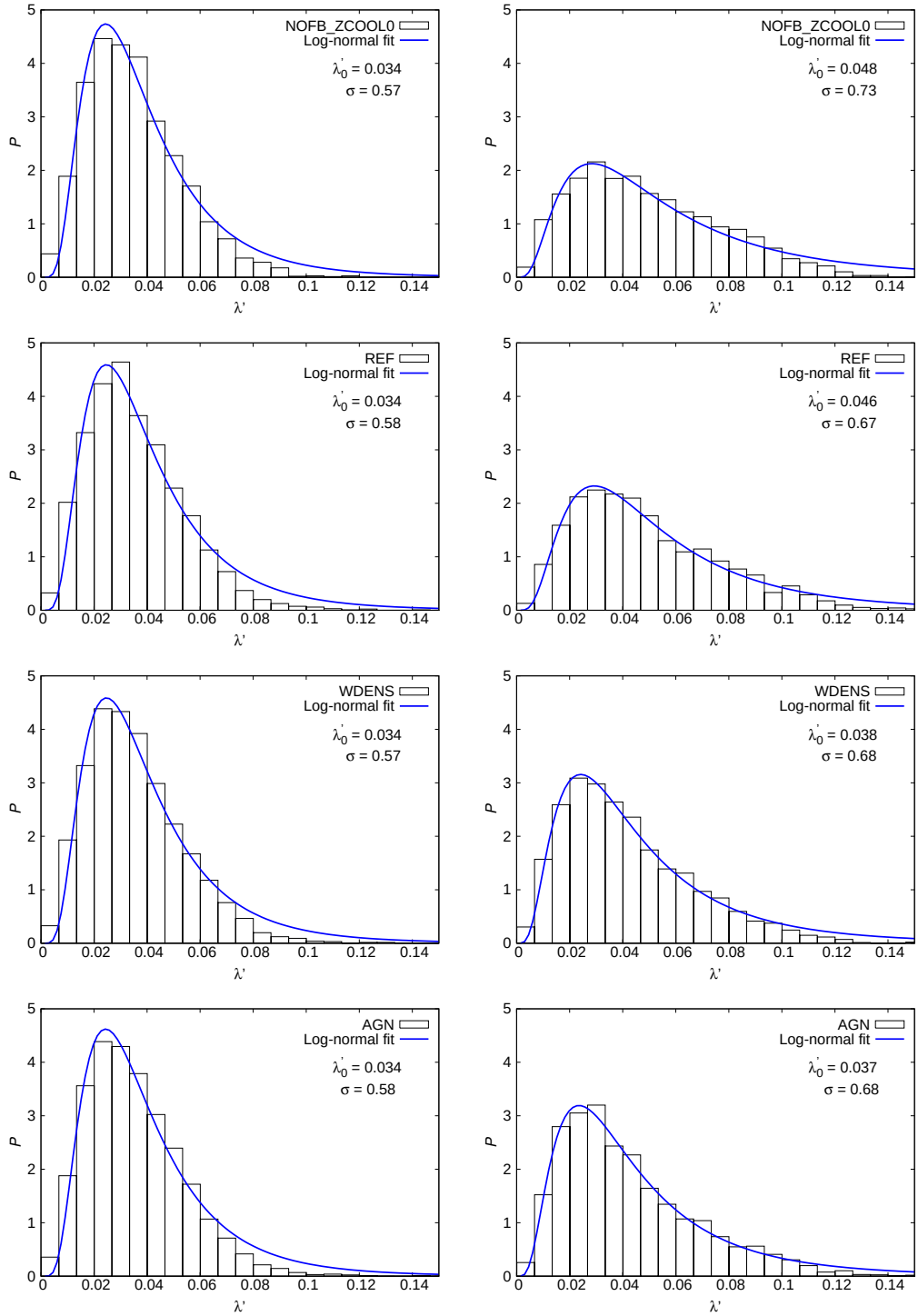


Figure 5.6: The effect of feedback on the distribution $P$ of the halo spin parameters $\lambda'$. From top to bottom the no feedback run (NOFB_ZCOOL0), the weak stellar feedback (REF) run, the strong stellar feedback (WDENS) and the stellar and AGN feedback (AGN) are shown. The curves show the best-fit log-normal distribution, where the best-fit values are given in the top right corner of each plot. Here $\lambda'_0$ denotes the mean and $\sigma$ the standard deviation. The left panel shows the spin distribution computed using all particles within the virial radius of the relaxed halo sample while the right panel shows the spin parameter computed using particles within the central 12% of $r_{vir}$ of the same haloes.

Table 5.5: Best-fit parameters for the log-normal distribution of spin parameters $\lambda'$ of the relaxed halo sample extracted from the simulations. Here $\lambda'_0$ denotes the mean and $\sigma$ the standard deviation.

| | | Within $r_{vir}$ | | Within $0.12r_{vir}$ | |
|---|---|---|---|---|---|
| Cosmology | # haloes | $\lambda'_0$ | $\sigma$ | $\lambda'_0$ | $\sigma$ |
| DMONLY | 4122 | 0.035 | 0.61 | 0.038 | 0.63 |
| NOFB | 4356 | 0.034 | 0.57 | 0.048 | 0.73 |
| REF | 4122 | 0.034 | 0.58 | 0.046 | 0.67 |
| WDENS | 4433 | 0.034 | 0.57 | 0.038 | 0.68 |
| AGN | 4433 | 0.034 | 0.58 | 0.037 | 0.68 |

parameters is shown in the bottom plot. Gaussian best-fit parameters for the shapes of haloes from each simulation are shown and are presented in table 5.6. Haloes from the dissipational simulations are clearly more spherical than their dark matter only counterparts. The axis ratio ($b/a$) is also found to increase significantly when baryons are considered. In the dissipational runs haloes are highly elongated with $b/a > 0.7$, in even better agreement with the observations. Haloes from all of these simulations are predominantly triaxial but baryons act to decrease the triaxiality parameter, i.e. dark matter only haloes are found to be more prolate than haloes from the baryon runs. In all cases increasing the strength of the feedback systematically decreases the impact of the baryons on the shapes of the haloes, making them slightly less spherical and slightly more prolate.

### 5.7.3 Shape Profiles

The radial distributions of the sphericity and triaxiality parameters extracted from the dissipational simulations are shown in figure 5.8, where they are compared to those of the dissipationless haloes. These results are presented in the same manner as in figure 5.3. Here the shapes of haloes extracted from the no feedback simulations are plotted as green squares, those from the weak stellar feedback run as blue circles, the strong stellar feedback run as orange diamonds and the AGN runs as red triangles. For comparison, the results for the dark matter only simulation are shown as black dashed diamonds.

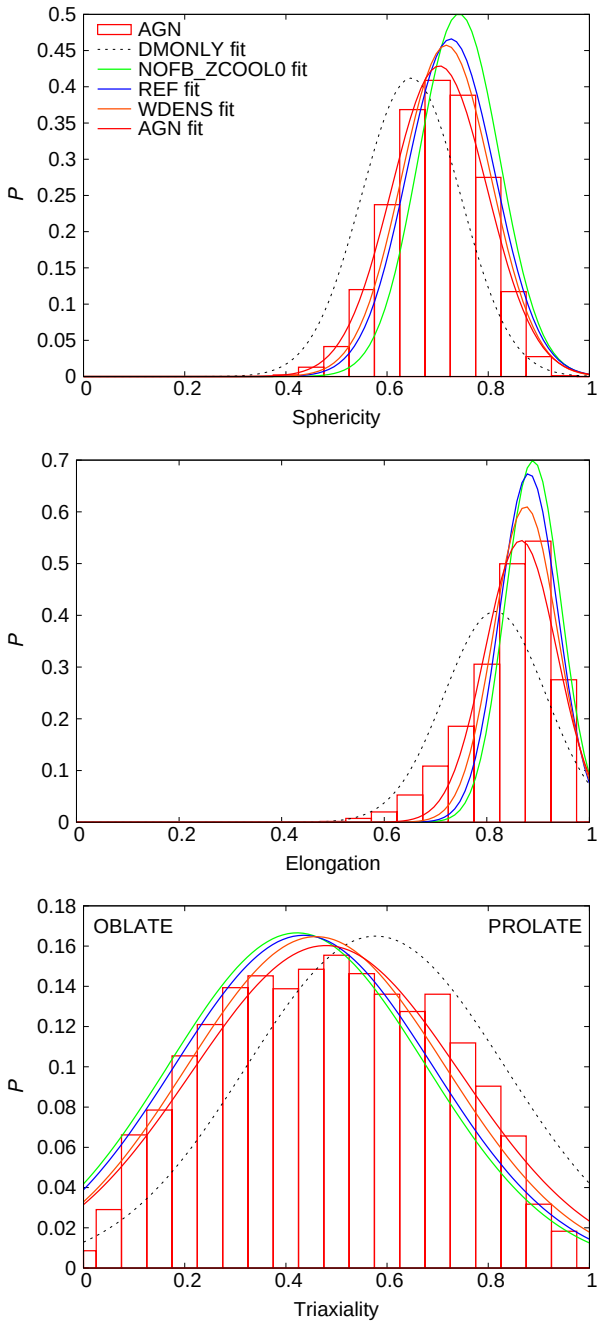


Figure 5.7: The distributions $P$ of dark matter halo shape parameters (measured within $r_{vir}$) are compared to those found in dissipational simulations. The distribution of halo sphericity, elongation and triaxiality are shown in the top, middle and bottom panels, respectively. In each panel, the best-fit Gaussian curve is shown for each of the simulations. The distribution of the AGN halo shapes is shown as a histogram and the distribution of the dark matter only haloes is shown as a dashed black curve.

Table 5.6: Best-fit parameters for the Gaussian distribution of halo shape for each of the baryon runs. Here $\mu$ denotes the mean value of the distribution and $\sigma$ the standard deviation.

| Simulation | $\mu$ | $\sigma$ |
|---|---|---|
| | Sphericity | |
| DMONLY | 0.648 ± 0.002 | 0.098 ± 0.002 |
| NOFB_ZCOOL0 | 0.742 ± 0.001 | 0.080 ± 0.001 |
| REF | 0.726 ± 0.002 | 0.087 ± 0.002 |
| WDENS | 0.717 ± 0.001 | 0.088 ± 0.001 |
| AGN | 0.704 ± 0.002 | 0.094 ± 0.002 |
| | Elongation | |
| DMONLY | 0.816 ± 0.005 | 0.099 ± 0.005 |
| NOFB_ZCOOL0 | 0.890 ± 0.003 | 0.055 ± 0.003 |
| REF | 0.882 ± 0.003 | 0.057 ± 0.003 |
| WDENS | 0.875 ± 0.003 | 0.062 ± 0.003 |
| AGN | 0.876 ± 0.004 | 0.070 ± 0.004 |
| | Triaxiality | |
| DMONLY | 0.577 ± 0.013 | 0.256 ± 0.015 |
| NOFB_ZCOOL0 | 0.422 ± 0.008 | 0.254 ± 0.009 |
| REF | 0.435 ± 0.008 | 0.256 ± 0.009 |
| WDENS | 0.460 ± 0.008 | 0.256 ± 0.009 |
| AGN | 0.479 ± 0.011 | 0.266 ± 0.012 |

The results in figure 5.8 demonstrate that the effect of baryons is significant out to the virial radius. The effects of baryons are felt by haloes of all masses, although it is found to be most significant in the high mass haloes. In the most massive objects there is a weak trend of decreasing sphericity with increasing radius in the strong feedback runs; this trend is reduced for the weak feedback runs. In the low mass haloes there is a slight tendency for haloes to become more spherical at large radii in the weak feedback runs. Similarly, the strongest effects on triaxiality are found in massive haloes from simulations with weak or no feedback, and the baryonic physics is found to influence the halo triaxiality out to the virial radius.

The effects of the dissipational processes on the shape of the *dark matter* distributions are shown in figure 5.9, where the halo shape distributions are determined using *only* dark matter particles. Again, all of the baryonic runs considered show an increase in the sphericity and a decrease in the prolateness of the dark matter distribution; these

effects are significant out to $r_{vir}$ but are particularly important in the central regions of the most massive haloes. Clearly baryons have a significant effect on the shape of haloes, but these modifications can not be explained solely by the baryon distribution itself, as the dark matter distribution is also significantly affected.

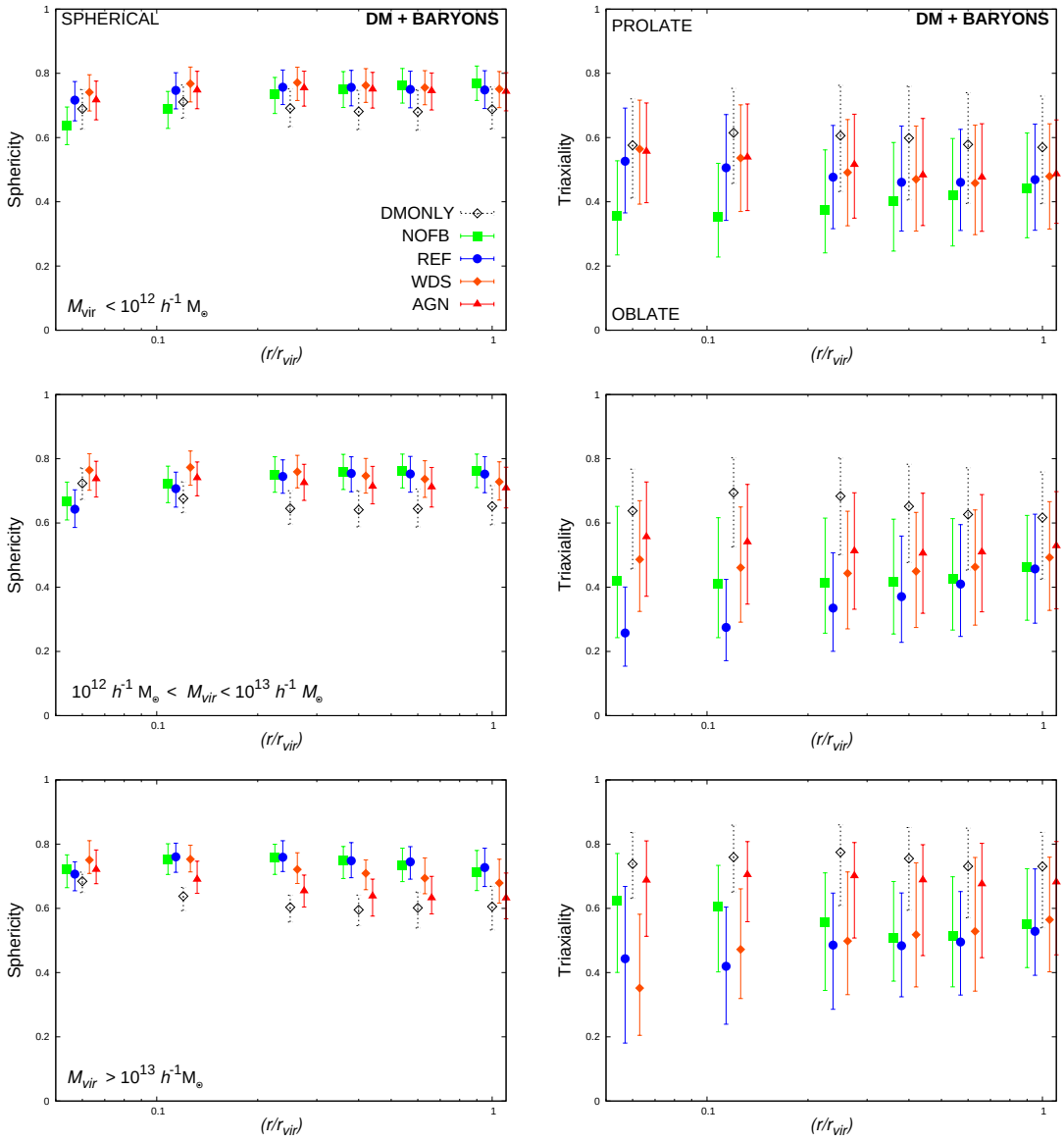


Figure 5.8: Effect of feedback on the radial shape profiles. The shapes of haloes extracted from the no feedback (NOFB_ZCOOL0) simulation are shown as green squares, those from the weak stellar feedback run (REF) as blue circles, the strong stellar feedback run (WDENS) as orange diamonds and the AGN runs as red triangles. For comparison the sphericities of dark matter only haloes are shown as black dashed diamonds. The error bars show the 25 and 75 percentiles of the halo-to-halo scatter. The left panels show the radial distribution of the sphericity of the halo; the right panels show the radial distribution of the triaxiality parameter. The shape parameters are computed in cumulative bins. Each row represents a different mass range. From top to bottom the mass ranges considered are $M_{vir} < 10^{12}\,h^{-1}\,M_\odot$, $10^{12} < M_{vir} < 10^{13}\,h^{-1}\,M_\odot$ and $M_{vir} > 10^{13}\,h^{-1}\,M_\odot$, respectively. All bins are well beyond the softening range $2.8\epsilon$ (defined in section 3.2 and discussed in section 3.4.1).

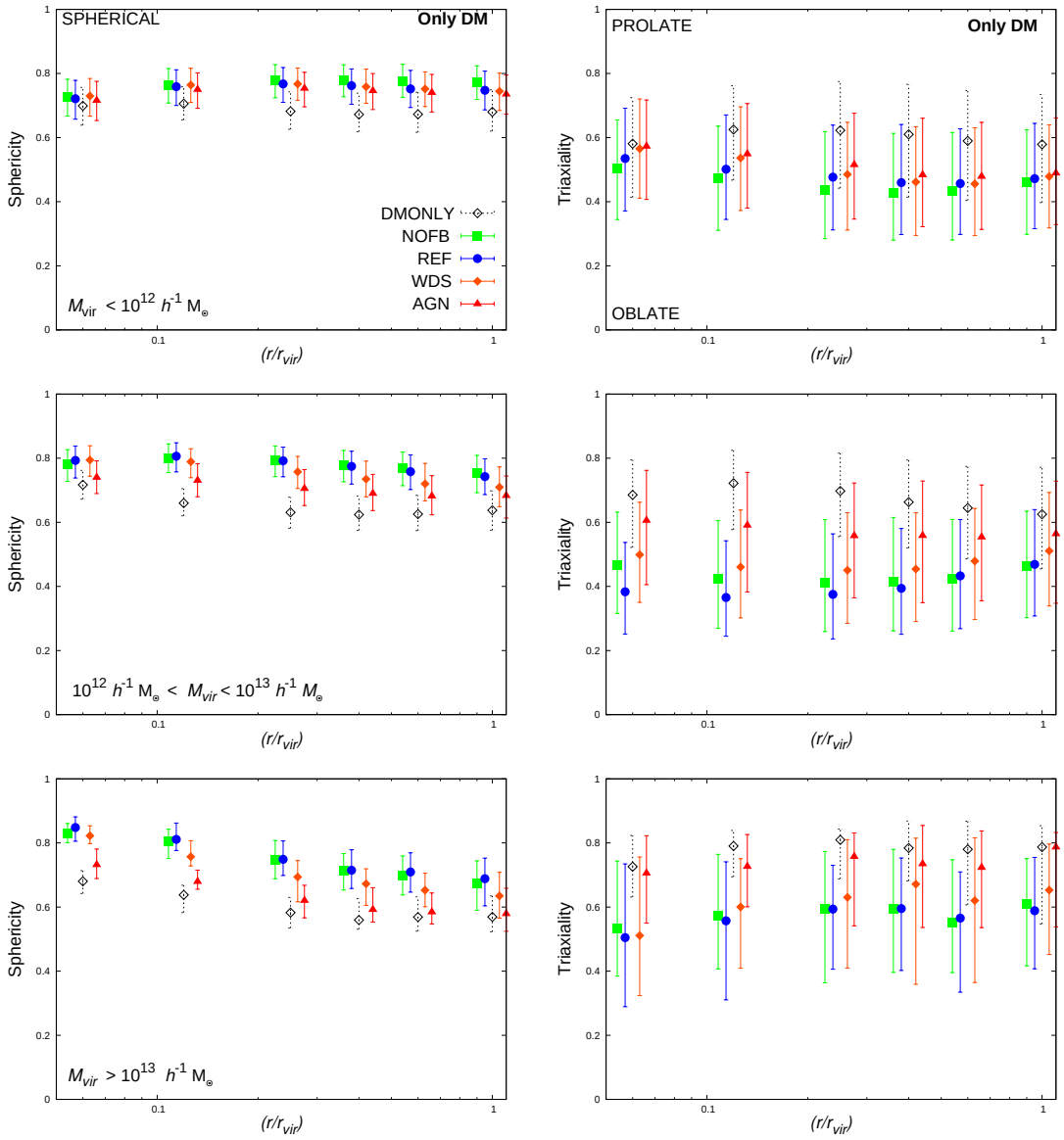


Figure 5.9: As in figure 5.8 but showing the effect of feedback on the radial shape profiles of the *dark matter* distribution.

### 5.7.4 Shape versus Halo Mass

The relationship between halo shape and mass for each of the feedback runs is shown in figures 5.10 and 5.11, and the results are summarised in table 5.7 (as discussed in section 5.6.4).

Again one can clearly see that more massive haloes are less spherical and the differences in halo shape attributed to the implemented feedback processes are most significant in these systems; the smallest haloes do not appear to be significantly affected by the type of feedback implemented. The no feedback and weak feedback runs produce similar halo shape distributions and increasing the strength of the feedback is found to reduce the effect of the baryons for all halo masses. Weak stellar feedback results in the most oblate systems, while stellar and AGN feedback runs produce more prolate systems. For massive haloes the shapes of the haloes extracted from the AGN runs are found to be remarkably similar to the corresponding dark matter only haloes. AGN feedback is thought to be important in suppressing star formation efficiency and is expected to play an important role in high mass haloes, reconciling the mass function with the luminosity function for the most massive haloes.

## 5.8 Resolution Tests

In order to quantify the effects of resolution, the shapes of haloes extracted from a $512^3$ particle run with a force softening length of 2 $h^{-1}$ kpc (used in this analysis) are compared with those from a corresponding lower-resolution run (containing $256^3$ particles with a softening length of 4 $h^{-1}$ kpc). Resolution tests for dark matter only haloes are shown in figures 5.12 and 5.13. These figures show the sphericity and triaxiality, respectively, as a function of halo mass. Similarly, figures 5.14 and figure 5.15 show the sphericity and triaxiality of haloes drawn from the weak stellar feedback run. In each of these plots the shapes of haloes extracted from the $512^3$ particle simulations are shown in red and the lower-resolution run with $256^3$ particles are shown in green. The

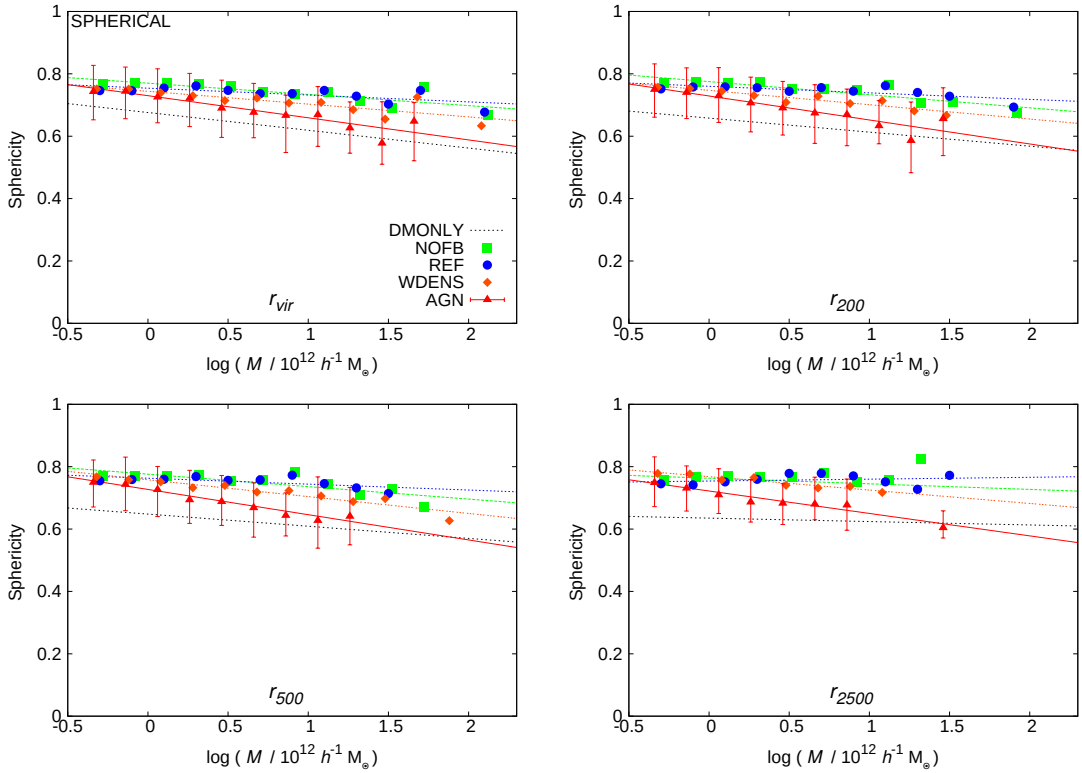


Figure 5.10: Sphericity versus mass $M$ for haloes extracted from the baryon runs. Error bars show the 25 and 75 percentile halo-to-halo scatter for the AGN run (scatter in the other baryon runs is comparable). The shapes of haloes from the no feedback simulation are shown as green squares, the weak stellar feedback simulation as blue circles, the strong stellar feedback simulation as orange diamonds and the stellar and AGN feedback simulation as red triangles. For comparison the shapes of the dark matter only haloes are shown as a dashed black line. From top left to bottom right the sphericity is measured in $r_{vir}$, $r_{200}$, $r_{500}$ and $r_{2500}$. Lines of best-fit to each simulation set are shown and the best-fit values are listed in table 5.7.

error bars are the one-sigma bootstrap resampled median distributions (1000 bootstrap samples have been used). Vertical lines show the 1000-particle cuts that have been used in this analysis. Clearly the shapes are well resolved beyond 1000 particles. This limit is somewhat conservative for the measurement of sphericity but is required for measuring triaxiality (particularly within $r_{2500}$).

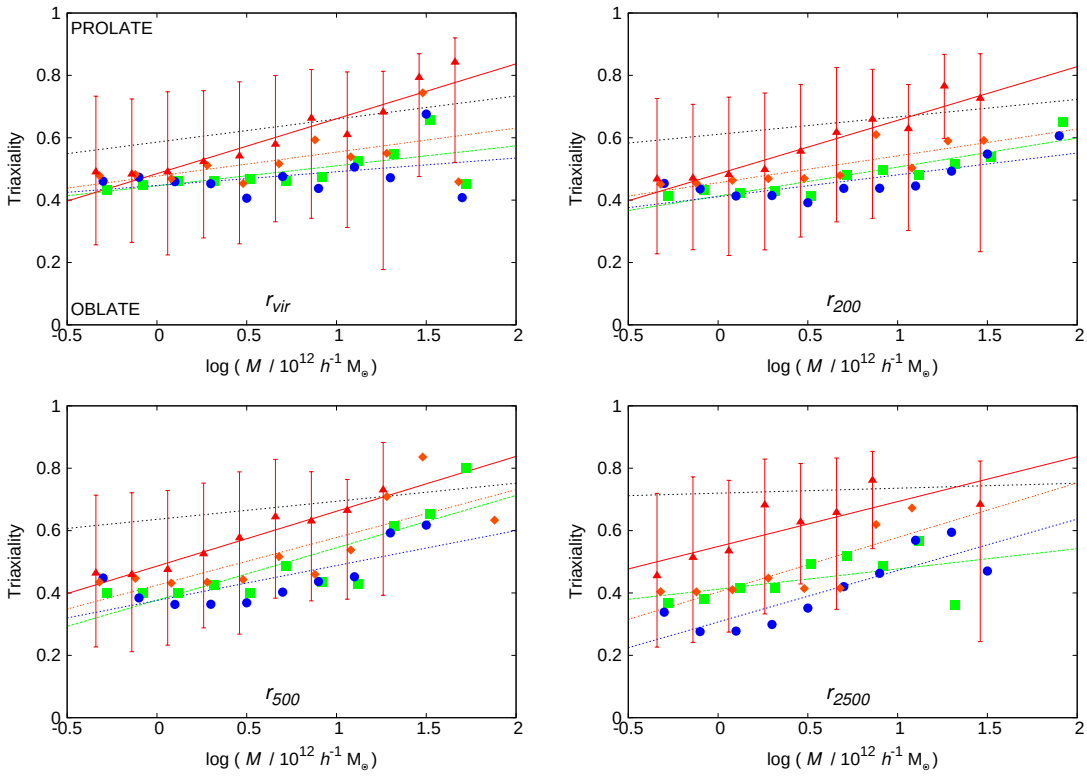


Figure 5.11: As in figure 5.10 but now for triaxiality versus mass of haloes extracted from the baryon runs.

Table 5.7: Best-fit parameters for the median sphericity and triaxiality of the relaxed halo samples extracted from dissipational simulations. The errors correspond to $1\sigma$ confidence intervals and have been determined by bootstrap resampling (1000 bootstrap samples have been used).

| | Sphericity | | Triaxiality | |
|---|---|---|---|---|
| | Slope | Intercept | Slope | Intercept |
| | | NOFB_ZCOOL0 | | |
| $r_{vir}$ | $-0.036\ ^{+0.008}_{-0.026}$ | $0.770\ ^{+0.010}_{-0.003}$ | $0.064\ ^{+0.039}_{-0.028}$ | $0.446\ ^{+0.011}_{-0.016}$ |
| $r_{200}$ | $-0.042\ ^{+0.016}_{-0.010}$ | $0.775\ ^{+0.003}_{-0.006}$ | $0.093\ ^{+0.037}_{-0.032}$ | $0.413\ ^{+0.012}_{-0.013}$ |
| $r_{500}$ | $-0.040\ ^{+0.018}_{-0.008}$ | $0.776\ ^{+0.003}_{-0.005}$ | $0.168\ ^{+0.013}_{-0.069}$ | $0.377\ ^{+0.022}_{-0.006}$ |
| $r_{2500}$ | $0.018\ ^{+0.001}_{-0.030}$ | $0.763\ ^{+0.007}_{-0.001}$ | $0.065\ ^{+0.077}_{-0.016}$ | $0.412\ ^{+0.010}_{-0.015}$ |
| | | REF | | |
| $r_{vir}$ | $-0.022\ ^{+0.010}_{-0.022}$ | $0.754\ ^{+0.008}_{-0.005}$ | $0.044\ ^{+0.039}_{-0.026}$ | $0.447\ ^{+0.014}_{-0.015}$ |
| $r_{200}$ | $-0.021\ ^{+0.009}_{-0.018}$ | $0.760\ ^{+0.007}_{-0.004}$ | $0.070\ ^{+0.038}_{-0.052}$ | $0.411\ ^{+0.018}_{-0.015}$ |
| $r_{500}$ | $-0.019\ ^{+0.010}_{-0.013}$ | $0.763\ ^{+0.004}_{-0.004}$ | $0.112\ ^{+0.063}_{-0.054}$ | $0.376\ ^{+0.013}_{-0.024}$ |
| $r_{2500}$ | $0.006\ ^{+0.021}_{-0.008}$ | $0.754\ ^{+0.003}_{-0.004}$ | $0.165\ ^{+0.033}_{-0.037}$ | $0.307\ ^{+0.007}_{-0.012}$ |
| | | WDENS | | |
| $r_{vir}$ | $-0.041\ ^{+0.011}_{-0.017}$ | $0.744\ ^{+0.006}_{-0.005}$ | $0.077\ ^{+0.027}_{-0.035}$ | $0.477\ ^{+0.014}_{-0.009}$ |
| $r_{200}$ | $-0.046\ ^{+0.018}_{-0.010}$ | $0.747\ ^{+0.004}_{-0.006}$ | $0.086\ ^{+0.042}_{-0.035}$ | $0.456\ ^{+0.012}_{-0.014}$ |
| $r_{500}$ | $-0.054\ ^{+0.020}_{-0.010}$ | $0.758\ ^{+0.004}_{-0.007}$ | $0.153\ ^{+0.037}_{-0.077}$ | $0.425\ ^{+0.015}_{-0.017}$ |
| $r_{2500}$ | $-0.043\ ^{+0.018}_{-0.007}$ | $0.768\ ^{+0.003}_{-0.004}$ | $0.175\ ^{+0.026}_{-0.120}$ | $0.403\ ^{+0.025}_{-0.006}$ |
| | | AGN | | |
| $r_{vir}$ | $-0.071\ ^{+0.013}_{-0.018}$ | $0.730\ ^{+0.006}_{-0.006}$ | $0.176\ ^{+-0.001}_{-0.056}$ | $0.485\ ^{+0.018}_{-0.003}$ |
| $r_{200}$ | $-0.077\ ^{+0.024}_{-0.008}$ | $0.729\ ^{+0.002}_{-0.009}$ | $0.172\ ^{+0.018}_{-0.069}$ | $0.484\ ^{+0.021}_{-0.007}$ |
| $r_{500}$ | $-0.081\ ^{+0.028}_{-0.006}$ | $0.727\ ^{+0.002}_{-0.007}$ | $0.176\ ^{+0.028}_{-0.056}$ | $0.486\ ^{+0.018}_{-0.009}$ |
| $r_{2500}$ | $-0.072\ ^{+0.025}_{-0.000}$ | $0.722\ ^{+0.003}_{-0.004}$ | $0.144\ ^{+0.074}_{-0.067}$ | $0.549\ ^{+0.010}_{-0.019}$ |

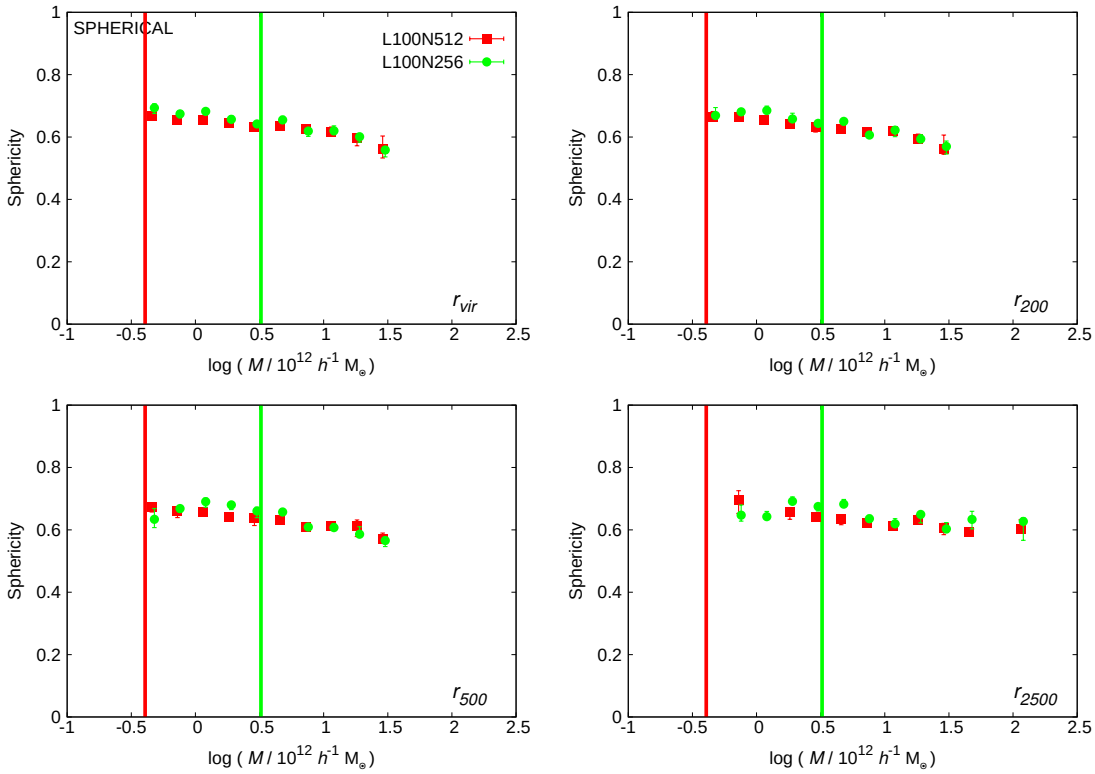


Figure 5.12: The effect of resolution on the sphericity of simulated dark matter only haloes at $z = 0$. The shapes of haloes extracted from the $512^3$ particle simulations are shown in red while those from the lower resolution $256^3$ particle run are shown in green. The errors correspond to $1\sigma$ confidence intervals and have been determined by bootstrap resampling (1000 bootstrap samples have been used). Vertical lines correspond to a 1000-particle cut for each of the simulations considered, only haloes with masses greater than this limit are considered for analysis. From top left to bottom right the sphericity is measured within $r_{vir}$, $r_{200}$, $r_{500}$, $r_{2500}$.

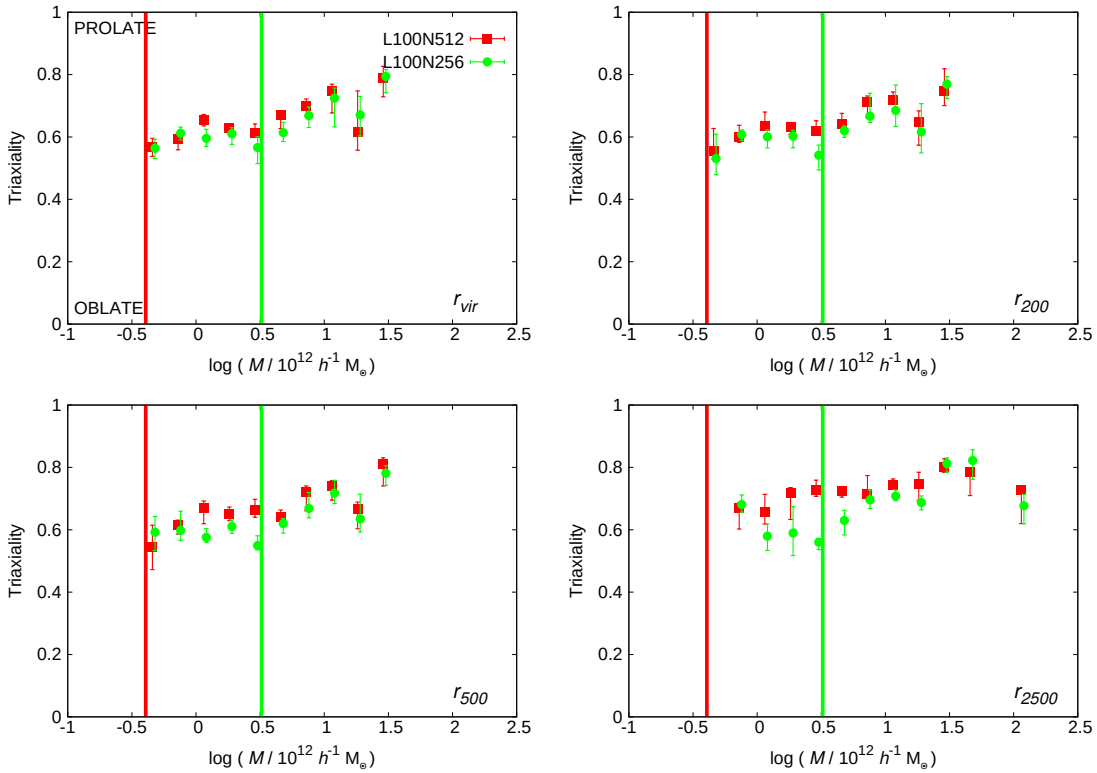


Figure 5.13: As in figure 5.12 but for the triaxiality of the dark matter only haloes.

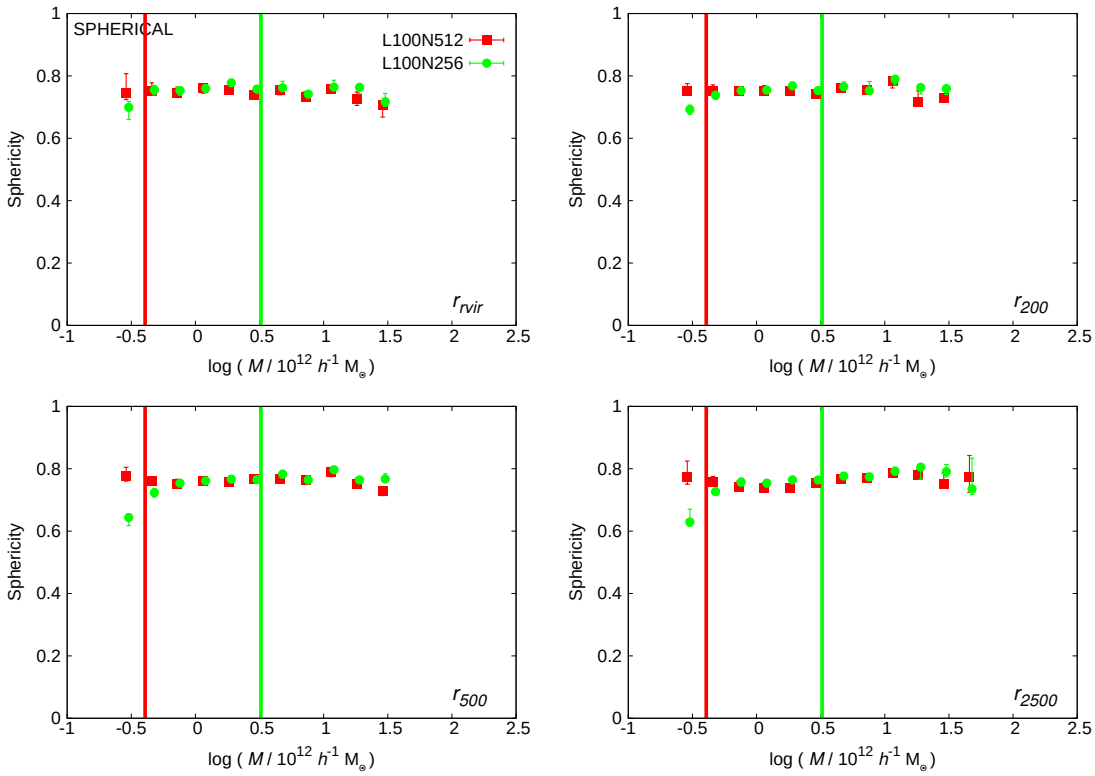


Figure 5.14: The effect of resolution on the sphericity of haloes from a weak stellar feedback simulation (REF) at $z = 0$. The shapes of haloes extracted from the $512^3$ particle simulations are shown in red while the shapes of haloes from the lower resolution $256^3$ particle run are shown in green. The errors correspond to $1\sigma$ confidence intervals and have been determined by bootstrap resampling (1000 bootstrap samples have been used). Vertical lines correspond to a 1000-particle cut for each of the simulations considered, only haloes with masses greater than this limit are considered for analysis. From top left to bottom right the triaxiality is measured within $r_{vir}$, $r_{200}$, $r_{500}$, $r_{2500}$.

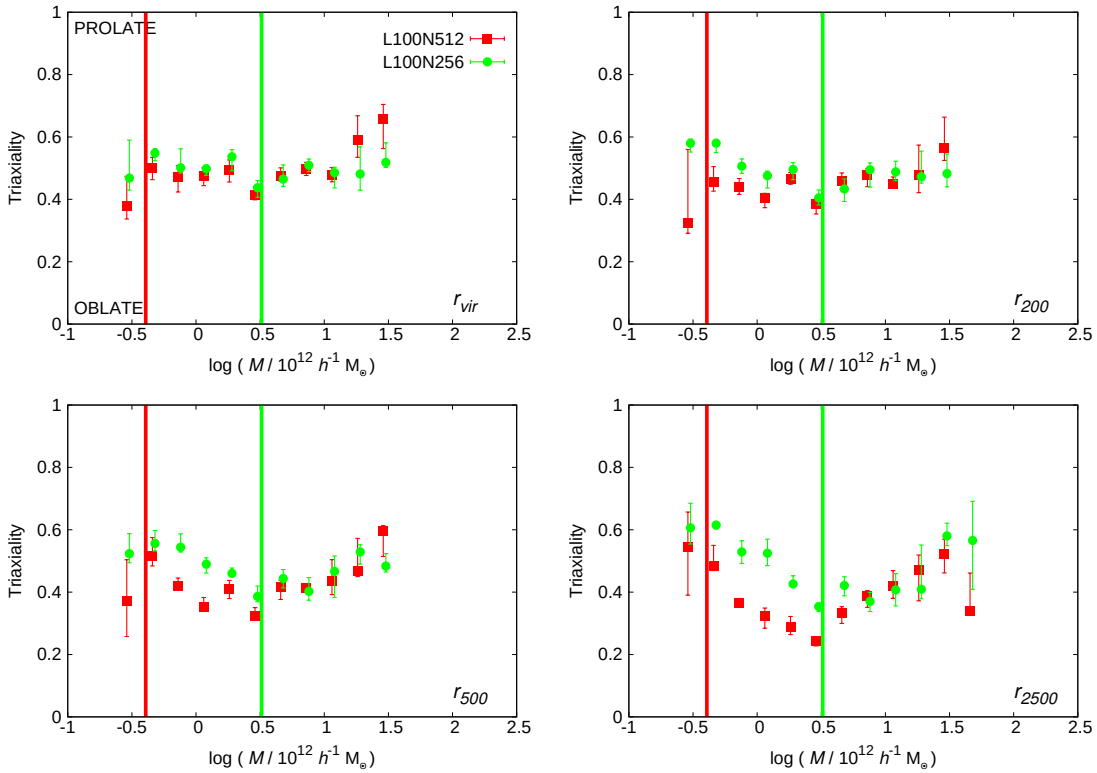


Figure 5.15: As in figure 5.14 but for the triaxiality of the weak feedback (REF) haloes.

## 5.9 Comparison to Shapes of Elliptical Galaxies

In figure 5.16 the $(c/a) \equiv \gamma$ and $(b/a) \equiv \beta$ axis ratios are compared to the observational estimates of Ryden (1992) (shown as a red curve). They used a sample of 171 elliptical galaxies to constrain the intrinsic axis ratios, finding that Gaussian distributions with means $\mu_\gamma = 0.69$, $\mu_\beta = 0.98$ and standard deviations $\sigma_\gamma = 0.11$, $\sigma_\beta = 0.11$ provided good fits to the observations of $(c/a)$ and $(b/a)$ axis ratios, respectively. Similarly, Lambas et al. (1992) studied 3165 elliptical galaxies from the APM Bright Galaxy Survey, finding that the best-fit values for the distribution of axial ratios of the elliptical galaxies were $\mu_\gamma = 0.55$, $\sigma_\gamma = 0.2$ and $\mu_\beta = 0.95$, $\sigma_\beta = 0.35$. Kimm and Yi (2007) use the SDSS data release 5 to estimate the axis ratios of a volume-limited sample of 3922 early-type galaxies at $0.05 \leq z \leq 0.06$. This data is well fit by Gaussian distributions with values of $\mu_\gamma = 0.78$, $\sigma_\gamma = 0.3$ and $\mu_\beta = 0.92$, $\sigma_\beta = 0.1$, in agreement with Ryden (1992).

Figure 5.16 shows the distribution of axis ratios of dark matter haloes in blue and of haloes with baryons, cooling and no feedback, in pink (NOFB_ZCOOL0). These results bracket the range of shapes observed in the simulations. The axis ratios estimated from Ryden (1992) are shown in red. In the left panel the $(c/a)$ axis ratios are compared to the distribution found by Dubinski (1994) for dark matter haloes (in green). The right panel shows the $(b/a)$ axis ratios. Dubinski (1994) found that the $(b/a)$ of dark matter haloes was $\sim 0.5$ but that this increased to $\sim 0.7 - 0.8$ when baryons were included. In this plot the green curve shows the observational estimates of Kimm and Yi (2007). While the distribution of the axis ratios is fairly broad, the distributions predicted by dissipational simulations seem to be in agreement with the observations of elliptical galaxies.

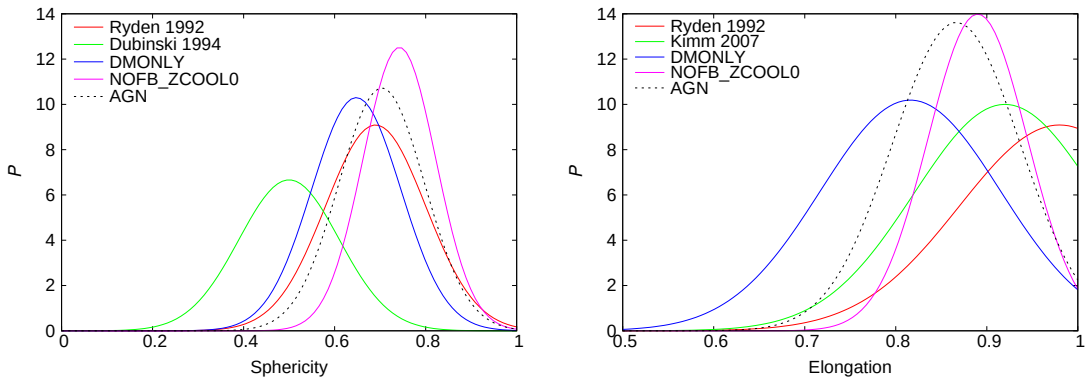


Figure 5.16: Comparison of the shape distributions $P$ with observations. The left panel shows the distribution $(c/a)$ while $(b/a)$ is shown on the right. The shapes simulated haloes from the no feedback (dark matter) run are shown in pink (blue) while those from the AGN simulation are shown as a dashed black curve. The observed samples used for comparison can be seen in the key and are discussed in the text.

## 5.10 Summary

The spin and shape distribution of haloes are characteristic of the paradigm in which they form and evolve. In this chapter the spin distribution and shape of dark matter haloes are explored and compared with simulations which include hydrodynamical treatment of baryonic physics such as gas cooling, star formation and feedback.

The spin parameter of relaxed dark matter haloes is characterised by a log-normal curve with best-fit values of $\lambda_0' = 0.035$ and $\sigma = 0.61$ in excellent agreement with Bullock et al. (2001); Bailin and Steinmetz (2005b) and Macciò et al. (2008). The spin distribution is remarkably similar in a $WMAP1$, $WMAP3$ and $WMAP5$ cosmology. This result suggests that there is no strong redshift dependence as the variation in $\sigma_8$ explored by these simulations results in different halo formation times: haloes in the lower $\sigma_8$ ($WMAP3$) simulation are expected to form later than those in the higher $\sigma_8$ ($WMAP1$) simulation. The angular momentum of dark matter haloes appears to be evenly distributed throughout the halo and the spin parameter remains essentially unchanged if computed using only mass within the central region ($0.12r_{vir}$), as found by Bailin and Steinmetz (2005b).

The spin distribution of haloes extracted from the baryon runs is not significantly

different to that of dark matter only haloes when computed using all mass within $r_{vir}$. However, in the central regions where baryons are expected to dominate, haloes from weak feedback simulations tend to have higher mean spin values than those from strong feedback runs. The spin distribution in the central region of strong feedback simulations is comparable to the distribution found for dark matter only haloes.

Dark matter only haloes extracted from OWLS typically have sphericities of $\sim 0.55$ to 0.7 and triaxialities of between 0.55 and 0.8 (indicating triaxial to prolate shapes). The choice of cosmological parameters does not significantly affect the shape of the simulated haloes (consistent with Macciò et al. 2006). Again, as the halo shape is not particularly sensitive to the choice of $\sigma_8$; this suggests that the redshift evolution of the shape of haloes is weak.

The radial shape profiles of low mass dark matter halo shapes are remarkably flat, indicating that the halo shape is essentially constant out to the virial radius (as found in Springel et al. 2004). There is a weak radial trend in the triaxiality parameters of massive haloes, indicating that these haloes become less prolate and more triaxial towards $r_{vir}$. More massive haloes are found to be less spherical and more prolate than lower mass haloes, in agreement with Macciò et al. (2006) and Bett et al. (2007).

It is well established that dissipational simulations tend to produce more spherical haloes than corresponding dissipationless runs (see, for example, Katz and Gunn 1991; Evrard et al. 1994; Tissera and Dominguez-Tenreiro 1998; Kazantzidis et al. 2004; Springel et al. 2004; Debattista et al. 2008) due to the presence of isotropic gas pressure. It is thought that baryons act to influence the orbital content of the halo, decreasing the fraction of box orbits responsible for supporting the triaxial halo (see chapter 6). In all of the OWLS runs considered, baryons act to make the haloes more spherical, although the stronger the feedback prescription the smaller the impact on the halo shape. Weak stellar feedback runs are able to produce almost oblate haloes, while stellar and AGN feedback runs result in prolate haloes similar to those found in dark matter only simulations. The effect of baryons is found to be most significant in high mass haloes. Baryons are also shown to have a significant effect on the shape of the

dark matter distribution, i.e. the results cannot solely be attributed to the shape of the baryon distribution itself.

Finally, the shapes of the dark matter haloes taken from the OWLS simulations are found to be in agreement with a wide range of observational estimates of the shapes of elliptical galaxies.

# 6

# The Effect of Feedback on the Orbital Content of Haloes

In this chapter, the orbital content of a large sample of haloes extracted from state-of-the-art high-resolution cosmological hydrodynamical simulations has been explored. The effects of the feedback prescriptions on the dynamics and orbits of the dark matter particles, stellar particles and subhaloes are quantified through spectral analyses of their orbits. The inner region ($0.25r_{200}$) of dark matter haloes is found to be dominated by box orbits. However, adding baryons to these simulations results in a decrease in the fraction of central box orbits. Increasing the strength of the feedback implementation is found to reduce the central concentration of baryons, and correspondingly results in an increase in the fraction of box orbits. The orbital content described by the stellar particles is found to be remarkably similar to that drawn from the orbits of dark matter particles. How the orbital content of the haloes depends on several key parameters such as their mass, redshift and dynamical state is also considered. The results presented in this chapter may be used as constraints for dynamical modelling of galaxies using Schwarzschild's or Made-to-Measure methods.

## 6.1 Introduction

Studying the dynamics of a halo provides an unparallelled view of its internal kinematics and affords the opportunity to infer its basic properties. Studying the orbital content of haloes may also provide dynamical information about the halo's formation history. The Gaia satellite, to be launched in 2012, will provide a kinematic census of our Galaxy. In order to fully exploit observational datasets such as this, a comprehensive comparison with simulations is essential.

Stellar systems, such as elliptical galaxies, are fully described by their distribution function or density in 6D phase space. All of the galaxy's photometric and kinematic properties can be thought of as a superposition of the underlying orbits within the galaxy. Approaches such as Schwarzschild's method (Schwarzschild 1979) and Made-to-Measure techniques (Syer and Tremaine 1996; de Lorenzi et al. 2007; Dehnen 2009; Long and Mao 2010) attempt to reproduce observables using a superposition of the orbital density distributions. While in many cases, these techniques are able to reproduce a number of observables, the chosen orbital distribution may not be unique. It is possible that different combinations of orbits with distinctly different shapes may produce the same triaxial density distribution (de Zeeuw and Franx 1991). Studying the orbital content of merger remnants provides a unique insight into the types of orbital distributions expected to be present in galaxies with specified properties, and may help to provide initial conditions for these methods.

Orbits are divided into groups, or families, according to the phase space they cover. Families of regular orbits have similar morphologies because they conserve similar integrals of motion. These isolating integrals restrict the region of phase space available to an orbit. Each lowers, by one, the dimensionality of the region available to the orbit. As such, an orbit is shaped by its isolating integrals. Axisymmetric potentials have two classical integrals of motion: energy $E$ and the $z$-component of the angular momentum $L_z$, it has been shown that a third non-classical integral is required to understand the dynamics of the solar neighbourhood (Lindblad 1933; Contopoulos 1960; Binney

and Spergel 1982). However, it is well-known that many elliptical galaxies are not axisymmetric (Franx et al. 1991). In more relevant triaxial systems, there are two non-classical integral that play a fundamental role in shaping the system (Schwarzschild 1979).

Within simple generic triaxial models, regular orbits can be divided into two main families: box and tube orbits. Tube orbits are further divided according to their orientation into major- and minor-axis tubes (Schwarzschild 1979; Statler 1987). Box orbits are free to pass close to the centre of the potential and their orbit-averaged angular momentum is zero. While box orbits show no sense of rotation, tube orbits tend to rotate around the centre of the system, avoiding the centre. Studying the orbital families allows us to use the orbital structure of the galaxy to infer information about its formation history.

Box orbits are fundamentally important, as they are thought to be responsible for conveying information from the central regions of a halo to the outer parts of the system and are required to support the triaxial halo. It has been proposed that the decrease in triaxiality of dark matter haloes experienced when baryons are included is due to the scattering of these box orbits (see, for example, Debattista et al. 2008). Any central concentration (such as gas cooling and settling to the centre of the potential or massive black hole growth) is likely to affect the box orbits. Altering the distribution of the orbits can modify the shape of the halo. Scattering of the box orbits is likely to make the halo rounder and more oblate (Gerhard and Binney 1985). It is interesting to ask what kind of orbits are possible within a given potential, and how these orbits are modified when the potential is altered. These questions are addressed in this chapter.

Several authors have investigated the orbital content of analytic potentials and remnants of simulated disc mergers. The first attempt to classify the orbital content of simulated merger remnants was conducted by Barnes (1992) who simulated a small sample of merging encounters between equal mass disc galaxies with varying disc orientations and impact parameters. Orbits were classified using a ‘spin classification routine’, based on changes in the sign of the angular momentum vector. The merger

remnants were found to exhibit a wide variety of shapes and orbital structure. The remnants' shapes and kinematic properties were found to be related to the initial disc spin vectors and other encounter parameters. Almost all of the most tightly bound particles were found to be on box orbits and, further out, minor-axis tube orbits dominated the merger remnant. In major mergers (where the masses of the progenitor haloes are comparable) the violent merging process tends to result in a remnant largely dominated by box orbits. During minor mergers, the disc component is not destroyed and tube orbits remain. Barnes (1992) argues that most ellipticals cannot have formed by stellar dynamical mergers of equal-mass galaxies since significant misalignment between the minor and rotation axes was found in many of the merger remnants.

By including gas dynamics in the merging galaxies, Barnes and Hernquist (1996b) showed that gas tends to accelerate the orbital decay slightly, and that it can have a dramatic effect on the structure of the resulting remnant. Torques experienced during the merger act to remove angular momentum from the gas, causing it to flow inwards to form a central mass concentration. The relative orbit and orientation of the discs was found to influence the speed and strength of the gas inflow. They found the depth of the potential well to be highly correlated with the stellar kinematics and that gas acts to destabilise box orbits (as in Dubinski 1994). This causes minor-axis tubes to become dominant and results in a more oblate remnant. The remnants are found to exhibit better alignment between the spin and minor axis than the dark matter only simulations. This is a direct consequence of the orbital content of the remnant.

Removal or destruction of box orbits has important consequences. Box orbits are the backbone of a triaxial potential; without box orbits a system cannot remain triaxial. Since box orbits travel arbitrarily close to the centre of the halo, they can be expected to be strongly affected by the central mass concentration. The presence of a supermassive black hole is likely to have a large effect in this regard. As shown in Merritt and Valluri (1999), a central black hole containing 0.1 – 1% of the total mass is enough to cause box orbits to become stochastic when their closest approach to the central region is less than 0.05 – 0.1 times the half-mass radius of the model. Debattista

et al. (2008) discussed the impact of growing a central disc on the orbital content of a halo. They found that while the central concentration does result in rounder, more radially anisotropic haloes, by artificially 'evaporating' the disc the halo's shape is essentially returned to its original state. This indicates that the character of the orbits is not generally changed by the central mass concentration. The box orbits are not destroyed but simply become rounder in line with the potential. This was also considered in Valluri et al. (2010) who explored the orbital evolution induced by baryonic condensation in triaxial haloes. They found that the evolution depends on the radial distribution of the baryonic component and that a massive compact central mass will result in the scattering of a large fraction of both box and long-axis tube orbits even at fairly large pericentric distances.

Jesseit et al. (2005) studied a statistical sample of disc galaxy mergers using the automated spectral classification of Carpintero and Aguilar (1998) to classify the orbital content of the remnants. They found that the most abundant orbital classes are minor-axis tube and box orbits. The inner regions were found to be dominated by box orbits, while tube orbits become more important at intermediate radii. Jesseit et al. (2005) suggested that the ratio of these two classes may determine the basic properties of the remnant. Minor-axis-tube-dominated haloes were found to be discy, while those dominated by box orbits were boxy. Major-axis tubes were found to be dominant in prolate remnants. Again, it was noted that gas affects the fraction of box orbits, causing an increase in the population of minor-axis tubes. They also varied the mass ratio of merging galaxies and found an increase in the minor-axis tubes and a decrease in the fraction of box orbits when the mass ratio of the progenitor haloes was increased.

A comprehensive study of the orbital structure of 1:1 merger remnants can be found in Hoffman et al. (2010). Mergers between equal mass discs at varying initial gas fractions (ranging from 0 to 40%) were simulated, taking into account both star formation and feedback. They showed that, by varying the fraction of gas in a merger, a wide range of kinematic structures can be produced. The remnants formed in these simulations are typically prolate-triaxial. The central regions are dominated by box orbits,

while tube orbits dominate in the outer parts of the remnant. The inclusion of gas acts to decrease the fraction of box orbits in the central region, replacing them with minor-axis tubes. The remnants were found to become progressively more oblate as the gas fraction is increased. Outside of 1.5 $R_e$ (where $R_e$ is defined to be the $40^{\text{th}}$ percentile in binding energy) the remnants are found to be largely unaffected by the addition of gas.

This work aims to extend the previous work on the effect of baryons on orbital structure by comparing several models for the feedback implementation within realistic cosmological simulations.

The outline of this chapter is as follows. In section 6.2 we briefly review the simulations used for this study. The method used to define the orbital content of a merger remnant is discussed in section 6.3 and the main results are presented in section 6.4. Numerical issues, such as resolution/convergence tests, the effect of halo definition and the choice of basis sets are discussed in section 6.5. Finally, a summary of the conclusions can be found in section 6.6.

## 6.2 Halo Sample

The haloes used for this analysis were extracted from OWLS. For a detailed discussion about OWLS the reader is referred to Schaye et al. (2010) and to the discussion in chapter 3. In this chapter the same subset of five of the OWLS simulations used in the previous chapter is analysed to explore the effect of varying levels of feedback on the orbital content of the haloes: a dark matter only run; a run which includes baryons and primordial element line cooling but no feedback; a weak stellar feedback run; a strong stellar feedback run and a run which includes feedback from stars and supermassive black holes. The simulations used and the type of subgrid physics implemented are summarised in table 3.2 and are discussed in detail in section 3.8.2.

The main SUBFIND halo of each group is used to calculate the potential and to compute the orbital content of the simulated haloes, but the radial dependence of the results is scaled by the spherical overdensity (SO) definition of $r_{200}$. The choice of halo defi-

nition does not influence the results significantly (discussed further in section 6.5).

An example of a single halo extracted from each of the five simulations is shown in Figure 6.1. This figure shows, from left to right, the dark matter only run (DMONLY), the no feedback (NOFB_ZCOOL0), weak stellar feedback (REF), strong stellar feedback (WDENS) and stellar and AGN feedback (AGN) runs. An increase in brightness corresponds to an increase in surface mass density. In each image, $r_{200}$ is shown as a white circle. The top row shows a $z = 0$ cluster with $M_{200}$ of $3.8{\times}10^{14}$ $h^{-1}$ $M_\odot$ and $r_{200}$ of 899 $h^{-1}$ kpc. The bottom row shows a $z = 2$ galaxy with $M_{200}$ of $4.1{\times}10^{12}$ $h^{-1}$ $M_\odot$ and $r_{200}$ of 394 $h^{-1}$ kpc. While these images are meant to be purely illustrative, from the top panel it is clear that the baryons act to make the central regions of the relaxed cluster more spherical and result in an increase in the fraction of substructure. The galaxy at $z = 2$ is less relaxed and the effects of the baryons are less obvious.

Baryon fractions of the OWLS haloes are shown in Figure 6.2. This plot illustrates how the central baryonic mass concentration is affected by the strength of the different feedback models. Left panels correspond to $z = 0$ haloes, while the right panels correspond to haloes at $z = 2$. The top row shows the central baryon fraction (within 0.05 $r_{200}$) versus $M_{200}$ and error bars represent the quartile scatter. As expected, the runs with weak or no feedback have a much higher central baryon concentration than the stronger feedback runs. The AGN run clearly has a significantly lower central baryonic concentration than any of the other runs considered here. The central baryon fraction does not appear to vary significantly as a function of the halo mass at $z = 0$. At $z = 2$, neither of the strong feedback runs are mass dependent, but in the no feedback run low mass haloes have slightly higher central concentrations than their high mass counterparts, while the opposite is true for the weak feedback run.

To explore this further the baryon fraction within $r_{200}$ as a function of the central baryon fraction ($r/r_{200} < 0.05$) is shown in the middle row. Differently sized points for the same runs indicate different mass ranges. (At $z = 0$ the largest points correspond to cluster-scale haloes with masses greater than $10^{14}$ $h^{-1}$ $M_\odot$, medium sized symbols correspond to large group-sized haloes with $5 \times 10^{13} < M_{200} < 10^{14}$ $h^{-1}$ $M_\odot$, while

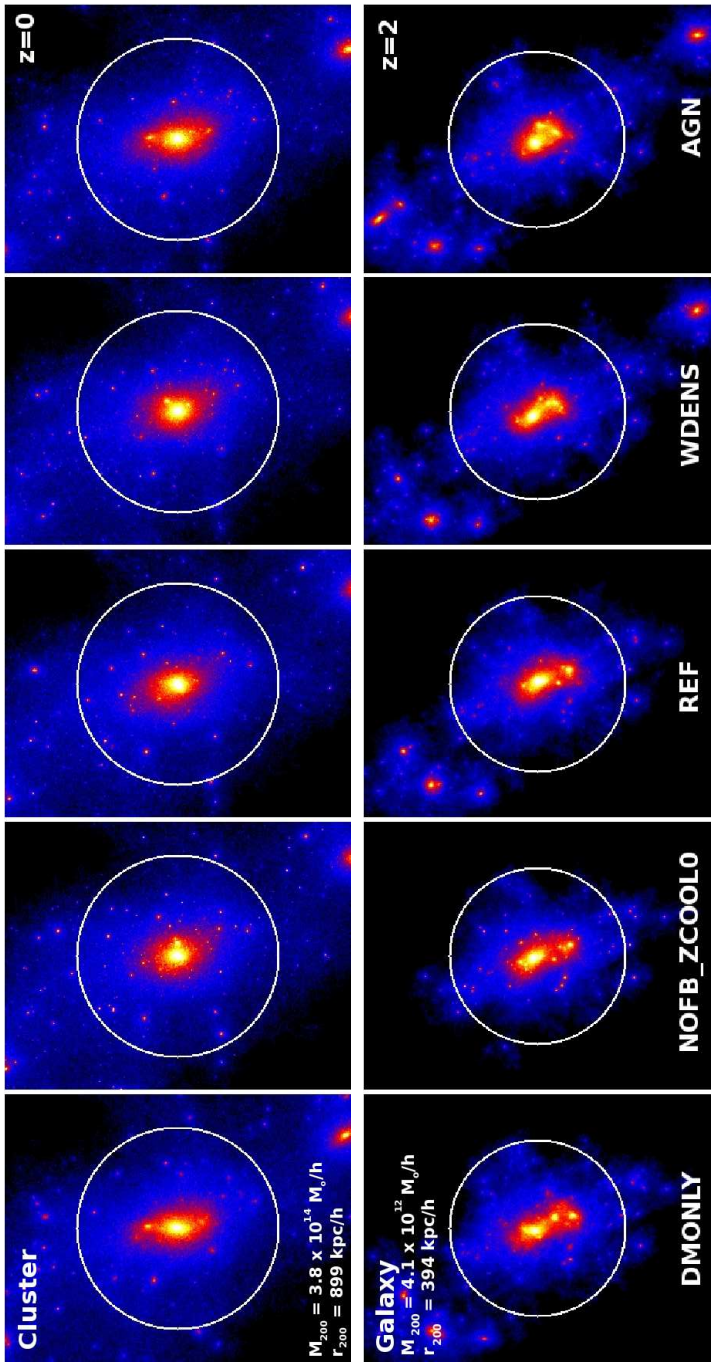


Figure 6.1: An example of a halo extracted from each of the simulation runs considered; an increase in brightness corresponds to an increase in surface mass density. In this figure the halo is extracted from (left to right), the dark matter only run (DMONLY), the no feedback (NOFB_ZCOOL0), weak stellar feedback (REF), strong stellar feedback (WDENS) and stellar and AGN feedback (AGN) runs. In each image, $r_{200}$ is shown as a white circle. Top: a $z = 0$ cluster with $M_{200}$ of $3.8{\times}10^{14}\ h^{-1}\ \mathrm{M}_\odot$ and $r_{200}$ of 899 $h^{-1}$ kpc. Bottom: a $z = 2$ galaxy with $M_{200}$ of $4.1{\times}10^{12}\ h^{-1}\ \mathrm{M}_\odot$ and $r_{200}$ of 394 $h^{-1}$ kpc. While these images are meant to be purely illustrative, it is evident that the baryons act to make the central regions of the relaxed cluster considerably more spherical.

the smallest points represent group-scale haloes with $10^{13} < M_{200} < 5 \times 10^{13}\ h^{-1}\ \mathrm{M}_{\odot}$. At $z = 2$, the largest points correspond to haloes with masses greater than $5 \times 10^{12}\ h^{-1}\ \mathrm{M}_{\odot}$, medium sized symbols correspond to $10^{12} < M_{200} < 5 \times 10^{12}\ h^{-1}\ \mathrm{M}_{\odot}$, while the smallest points represent $5 \times 10^{11} < M_{200} < 10^{12}\ h^{-1}\ \mathrm{M}_{\odot}$.) These plots show the fraction of baryons that are concentrated at the centre. At both redshifts the no-feedback and weak feedback runs clearly contain the highest baryon fraction overall, as well as the highest central concentration. At $z = 0$, the strongest mass dependence is evident in the WDENS run, where the feedback is a function of the local gas density. While the higher mass haloes contain more baryons than the lower mass haloes, the central concentration remains similar for the mass range considered. The feedback in the WDENS run is very effective at removing baryons from the centre of high mass haloes. The same is true for the AGN run, where the haloes have a lower overall baryon fraction. At $z = 2$, neither the total baryon fraction nor the central baryon fraction of the strong feedback runs is strongly dependent on mass. The weak feedback results in the removal of the central baryon concentration of low mass haloes. When no feedback is applied, the low mass haloes have the highest overall baryon fraction as well as the highest central concentration of baryons, as is the case at $z = 0$.

Finally, in the bottom row the fraction of stellar mass within $r_{500}$ is shown against the total mass within the same region. Again no mass dependence is evident for the strong feedback runs. The AGN run has the lowest central stellar fraction. Observations of the stellar mass fractions within $r_{500}$ as a function of total mass within $r_{500}$ tend to favour the strong feedback prescriptions (Duffy et al. 2010). As the strength of the feedback is decreased, more stars are able to form in the central regions. This is evident at $z = 0$ and $z = 2$. However, at $z = 2$ the lowest mass haloes in the weak feedback run are significantly affected by the stellar feedback processes and star formation is prohibited.

The fifty most massive haloes (with masses between $10^{13}$ and $10^{14}\,h^{-1}\ \mathrm{M}_{\odot}$ at $z = 0$ and between $10^{11}$ and $10^{12}\,h^{-1}\ \mathrm{M}_{\odot}$ at $z = 2$) from the five different physics runs (discussed above) were selected for this analysis. For each halo we consider its mass,

dynamical state, spin, concentration, velocity anisotropy parameter, stellar mass and halo shape. A brief discussion of these quantities is given below.

The velocity anisotropy parameter $\beta$ measures the proportion of radial to tangential orbits and is given by

$$\beta = 1 - 0.5\frac{\sigma_t^2}{\sigma_r^2}, \tag{6.1}$$

where $\sigma_t$ is the tangential velocity dispersion, and $\sigma_r$ the radial velocity dispersion. A value of $\beta = 1$ corresponds to radially-dominated orbits. The concentration, $c$ (defined as $r_{200}/r_s$, where $r_s$ is the characteristic scale radius) is positively correlated with the total velocity dispersion of the halo $\sigma_v$. As such, the concentration of each halo is estimated using the formula given in Faltenbacher and White (2010):

$$c = \frac{\sigma_v}{(H(z)M)^{1/3}}, \tag{6.2}$$

where the scaling with mass is introduced to compensate for the intrinsic mass dependence.

The spin parameter, shapes and dynamical state of the halo are defined as discussed in chapter 5. Of the fifty most massive haloes at $z = 0\,(2)$, $27\,(20)$ are found to be relaxed. These haloes contain between $10^3$ and $10^6$ dark matter particles.

## 6.3 Orbital Content Computation

The aim of this chapter is to identify the orbital content of cosmological haloes and to link this with their observable and intrinsic properties. To this end orbits are integrated within the potentials of OWLS haloes and are classified using the spectral classification routine of Carpintero and Aguilar (1998).

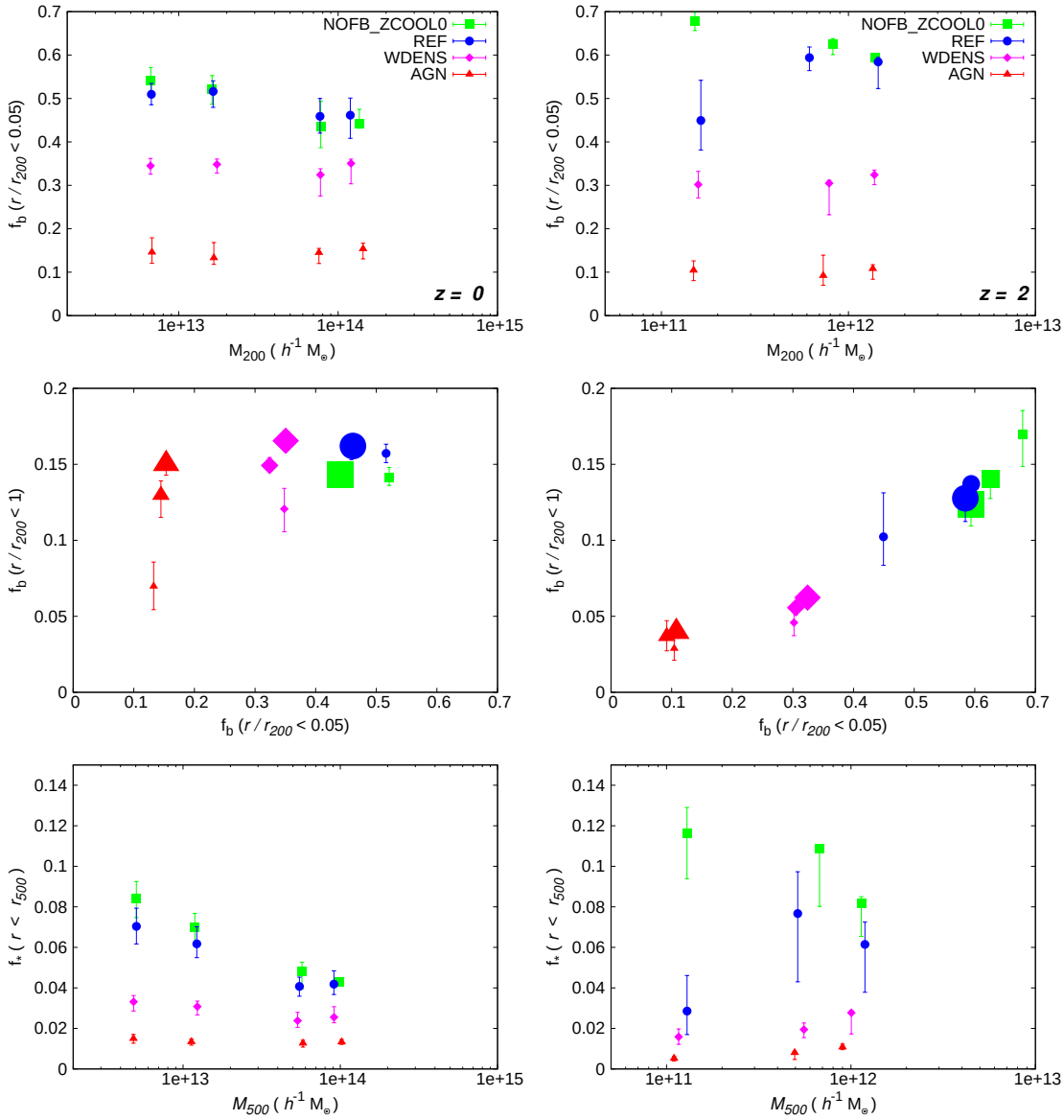


Figure 6.2: The baryon fraction $f_b$ in each of the simulation runs. Left panels correspond to $z = 0$, right panels to $z = 2$. The top panel shows the baryon fraction within 5% of $r_{200}$ versus $M_{200}$ of the halo. Error bars represent the quartile scatter. The middle panel shows $f_b$ within $r_{200}$ as a function of the central baryon fraction. Differently sized points for the same runs indicate different mass ranges with increasing size representing increasing mass (as described in the text). The bottom panel shows the fraction $f_*$ of stellar mass with $r_{500}$ versus the total mass $M_{500}$ within the same region. In all of these plots the strength of the different feedback models is clearly visible.

### 6.3.1 Calculating the Potential

There are a number of techniques that can be used to compute the gravitational potential of a system (see chapter 3). As galaxies are regarded as collisionless systems, an estimate of the smooth mean gravitational field of the system which minimises the effects of discrete particle representations on the halo potential is particularly useful. One such approach is the SCF method (discussed in detail in section 3.3). This method is used to obtain an estimate of the mean gravitational field by expanding the density and potential into a set of basis functions. If the first few terms of the basis are sufficient to provide a good representation of the system, then higher order terms may be neglected, minimising the effects of discreteness. In this work the SCF method described in Hernquist and Ostriker (1992) is used to reconstruct the potential of the haloes extracted from OWLS (code generously provided by the authors). Density and potential are given as

$$\rho(r,\theta,\phi) = \sum_{n,l,m} \mathrm{A}_{nlm}\,\rho_{nl}\,Y_{lm}(\theta,\phi), \tag{6.3}$$

$$\Phi(r,\theta,\phi) = \sum_{n,l,m} \mathrm{B}_{nlm}\,\Phi_{nl}\,Y_{lm}(\theta,\phi), \tag{6.4}$$

where $n$ denotes the radial expansion terms and $l$ and $m$ the angular terms. There are two commonly used basis functions: those suggested by Clutton-Brock (1973) and by Hernquist and Ostriker (1992). The basis set used here is constructed from the latter so that the lowest order terms represent the Hernquist profile (Hernquist 1990). However, the choice of basis set does not seem to affect the reconstruction of the potential significantly (see section 6.5 for further discussion). The density-potential pair is given by

$$\rho\,(r) = \frac{M}{2\pi}\frac{a}{r}\frac{1}{(r+a)^3}, \tag{6.5}$$

$$\phi\,(r) = -\frac{GM}{r+a}, \tag{6.6}$$

where $M$ is the total mass and $a$ is scale-length defined as

$$a = \left( \frac{r_{1/2}}{1 + \sqrt{2}} \right), \tag{6.7}$$

where $r_{1/2}$ is the half mass radius.

Twelve radial terms and six angular terms are used as this has been found to be sufficient to reproduce the potential to within a few percent of the $N$-body potential.

Choosing a reasonable scale-length (in the Hernquist profile) is also important in the potential reconstruction. To optimise the potential reconstruction, particles are divided into two components: a diffuse component consisting of dark matter and hot gas ($T > 10^5$ K), and a compact component consisting of stars, cold gas and black holes. The scale-length, computed separately for each component, is set to be that of the Hernquist profile.

### 6.3.2 Computing the Orbits

For each of the haloes considered, a subsample of 500 dark matter particles is selected, and the orbits of these particles are followed in the underlying potential of the halo. The orbits of stellar particles and subhaloes are also considered and compared to those of the dark matter particles. One hundred particles are chosen at random from each of the 5 radial bins considered. The bins are equally spaced in $\log r$ and cover a range of radii from 4% to 25% of $r_{200}$ (see discussion on convergence testing in section 6.5). The motion of each particle is integrated assuming that the potential remains static. The time interval for each bin is adjusted such that particles in the innermost region are integrated for 100 Gyr; this time interval is then increased with radius. Particles are required to undergo at least forty orbits to ensure that they have clearly defined spectra. As the aim is simply to characterise the orbital content of a halo, assuming a static potential is adequate. The characteristic orbital content of a halo at a given time is of interest, not the evolution of this property. Also, the figure rotation of these haloes is assumed to be slow (Bailin and Steinmetz 2004; Bryan and Cress 2007) and would

probably have a negligible effect on the quantities calculated here. A full investigation of the figure rotation of these haloes is deferred to future work.

### 6.3.3 Classifying the Orbit

To classify the orbits obtained, the spectral classification routine of Carpintero and Aguilar (1998), hereafter CA98, is used. This is a fully automatic classification routine based on the Fourier spectra of the motions of the particles. For a full description of the technique the reader is referred to their paper, but the method behind this routine is discussed briefly here.

CA98 uses the result that, once a frequency spectrum of an orbit is decomposed into its fundamental frequencies, the relationship between these frequencies can be used to classify the orbit in a 3D potential into the major orbital families: box, major($x$)-axis and minor($z$)-axis tubes where orbits are orientated such that the major axis corresponds to the $x$-axis and the minor axis to the $z$-axis. Since regular orbits are quasiperiodic, the Fourier spectra of the time series of each coordinate will consist of discrete peaks (this is not the case for irregular orbits). The Fourier transform of the time series of each coordinate is performed and the dominant peak frequency determined. For each pair of coordinates ($x$-$y$, $y$-$z$ and $x$-$z$) these frequencies are compared, searching for linear combinations (resonances). If the peak frequency in each direction of motion $i$ is represented by $\omega_i$, then a resonance is defined as

$$l\omega_x + m\omega_y + n\omega_z = 0, \tag{6.8}$$

for non-trivial combinations of the integers $n$, $l$ and $m$. If all dominant frequencies are a multiple of a single unit frequency, there is one base frequency. If there is no resonance, all dominant frequencies are irrationally related. Once the dominant frequencies have been compared, the spectra are searched for additional base frequencies. The number of base frequencies specifies whether an orbit is regular (open, closed or thin) or irregular, while the number of resonances specifies the orbital family as box or $x$-tube,

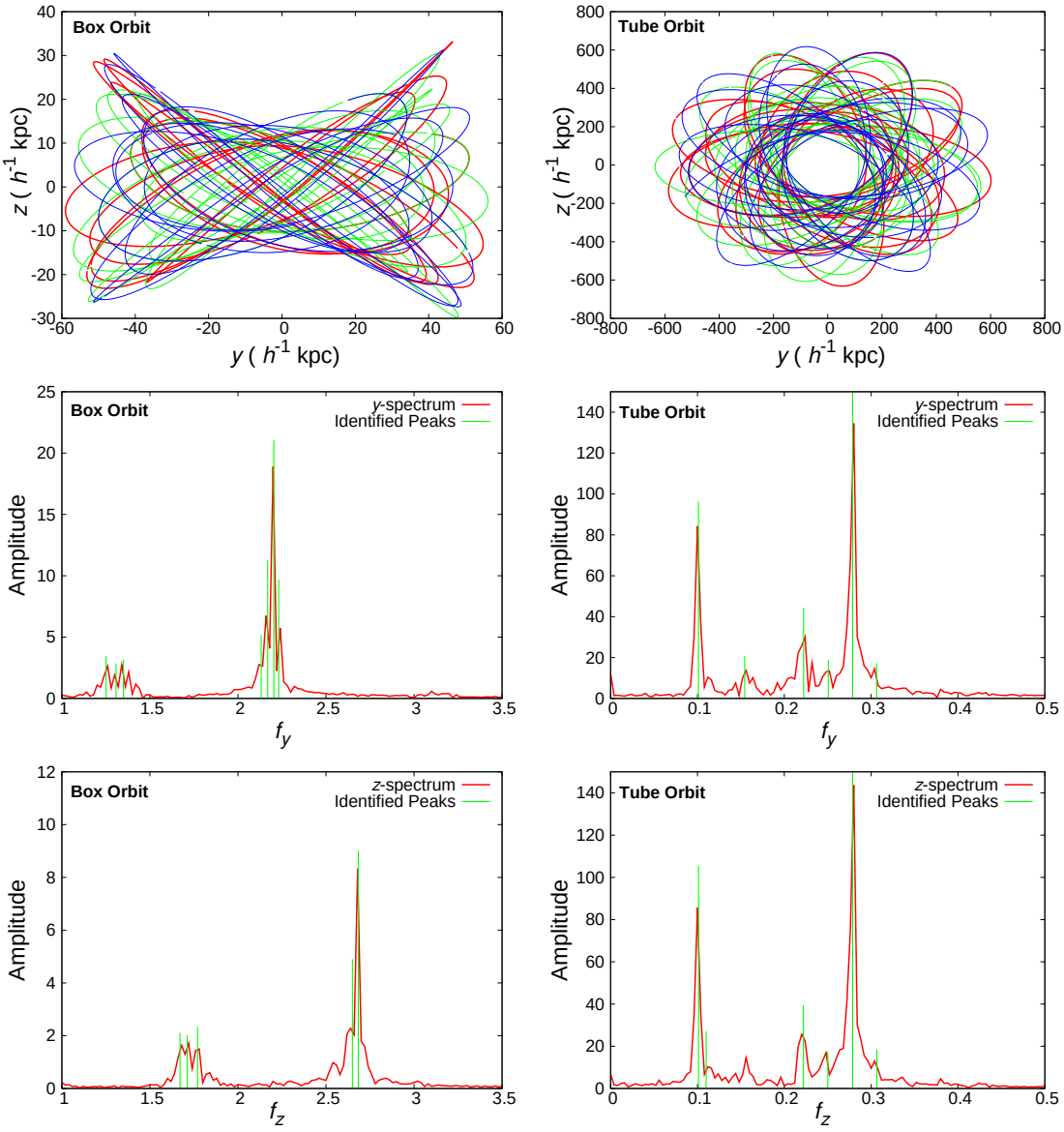


Figure 6.3: Examples of the orbital types extracted from the dark matter only simulations. The left (right) columns show an example of a box ($x$-tube) orbit. The $y$-$z$ projection of the orbit is shown in the top panel; the Fourier spectra of the $y$- and $z$-motion are shown in the middle and bottom panels, respectively. Peaks identified by the routine are depicted as lines. One can clearly see that the dominant peaks in the $y$- and $z$-spectra of the tube orbit show a 1:1 resonance ($f_y/f_z = 1$). Colour indicates the time evolution of the orbit, from red to green to blue indicates progression with time.

$y$-tube or $z$-tube.

A 3D orbit with 4 or more base frequencies is classified as irregular; if it has 3 (or fewer) base frequencies it is classified as regular. Orbits with 3 base frequencies are known as open, 2 base frequencies as thin and 1 base frequency as closed orbits. The base frequencies of a box orbit are incommensurable; this is the only class which does not exhibit resonance between the dominant frequencies. The orbit is classed as a $z$-tube if the $x$- and $y$-spectra show a 1:1 resonance, that is $l = 1$, $m = 1$ and $n$ is arbitrary. If $y$ and $z$ show a 1:1 resonance ($m = 1$ and $n = 1$), then the orbit is classified as an $x$-tube. As orbits around the intermediate axis are unstable it is only in rare cases that $y$-tubes are identified. These show resonances between the $x$- and $z$-base frequencies. A summary of the orbit classifications (taken from Carpintero and Aguilar 1998) is given in table 6.1.

Examples of the orbital types extracted from the dark matter only simulations are shown in Figure 6.3. The left (right) panels show an example of a box ($x$-tube) orbit. The $y$-$z$ projection of the orbit is shown in the top row while the Fourier spectra of the $y$- and $z$-motion are shown in the middle and bottom panels, respectively. Peaks identified by the routine are depicted as lines. One can clearly see that the peaks in the $y$- and $z$-spectra of the tube orbit are linear combinations of each other.

The CA98 algorithm has been tested rigorously using a number of analytic potentials. As it is fully-automated, it allows for the classification of large numbers of orbits, it also distinguishes more orbital classes than classifications based on the sign of a component of the orbits' angular momentum. For comparison, the orbits considered here have also been classified using the spin classification technique (Barnes 1992). In this approach orbits are classified according to changes in the sign of the components of angular momentum vector. Orbits in which a sign change is noted in each of the components are classified as box orbits while those which conserve the sign of a component are classified as tubes. While the fraction of box orbits is in general higher than that obtained using the method of CA98, the same general trends are found using both classification schemes.

Table 6.1: Classifications of orbits (as in Carpintero and Aguilar 1998).

| | | Number of base frequencies | | | |
|---|---|---|---|---|---|
| | | 1 | 2 | 3 | > 4 |
| Number of Resonances | 1 | axial | 2-D box | 3-D box | Irregular |
| | 2 | closed 0 : $m$ : $n$ box<br>closed 0 : 1 : 1 loop | thin $\pi$ : $m$ : $n$ box<br>thin $\pi$ : 1 : 1 tube | open $\pi$ : $m$ : $n$ box<br>open $\pi$ : 1 : 1 tube | |
| | 3 | closed $l$ : $m$ : $n$ box<br>closed $l$ : 1 : 1 tube | thin $l$ : $m$ : $n$ box<br>thin $l$ : 1 : 1 tube | open $l$ : $m$ : $n$ box<br>open $l$ : 1 : 1 tube | |

## 6.4 Results

In this section the results of the spectral analysis of the orbital content of the OWLS haloes are presented. This section begins with a discussion of the orbits of dark matter particles and how these are affected by the addition of baryons and feedback. The effect of basic halo properties (such as concentration, shape and spin) on the dark matter orbits is also considered. These orbits are then compared to those of stellar particles and subhaloes.

As discussed above, orbits are classified as either box, tube or irregular. Tube orbits are subdivided into $x$-, $y$- and $z$-tubes depending on their orientation with respect to the halo axes. Haloes are reorientated so that the $x$-axis corresponds to the major axis, $y$ to the intermediate axis and $z$ to the minor axis. Typically, only a small fraction of particles have not undergone more than 40 periods. These orbits are not classified.

### 6.4.1 Orbits of Dark Matter Particles

In this section the orbital content of dark matter particles is considered; this is shown as a function of radius for dissipationless and dissipational simulations. The effect of halo properties on the orbits is also investigated.

#### Dark Matter Only Simulations

The orbital content of the DMONLY haloes is shown in Figure 6.4. In the top panel the orbital content of the $z = 0$ haloes is shown; the haloes at $z = 2$ are shown in

the bottom panel. The left column shows the 50 most massive haloes selected for this analysis, while the right panel shows only the 27 (20) haloes which are considered to be relaxed at $z = 0$ (2).

The orbital content of the relaxed sample does not appear to be significantly different from that of the whole sample so all 50 haloes are used for the rest of the analysis. At both redshifts, the haloes are dominated by box orbits out to $0.25r_{200}$. The dominance of box orbits is not surprising as these orbits are required to support the triaxial haloes characteristic of dark matter simulations. There is a trend for the fraction of box orbits to decrease with increasing radius, accompanied by an increase in the fraction of tube orbits. While box orbits dominate in the centre of the haloes, tube orbits become more dominant towards $r_{200}$ (as in Jesseit et al. 2005; Hoffman et al. 2010). Resonant box orbits account for approximately half of the box orbits and are also found to decrease with increasing radius. The fraction of $y$-tubes and irregular orbits is negligible and less than 10% of the orbits are not classified. The fractions of both $x$- and $z$-tubes increase with radius. While $x$-tubes dominate the tube contribution at small radii, the fraction of $z$-tubes becomes increasingly important at larger radii.

**Baryon Simulations and the Effect of Feedback**

The central baryonic mass concentration is significantly affected by the strength of the different feedback models, as shown in figure 6.2. In this section the impact of this central concentration on the orbital content of the haloes is discussed. Results for the $z = 0$ sample are shown in Figure 6.5.

All of the baryon runs are found to have a smaller fraction of box orbits at all radii out to $0.25r_{200}$ than the dark matter only haloes, but this decrease is most noticeable in the very central regions where baryon physics is expected to dominate. This is consistent with earlier findings (see, for example, Debattista et al. 2008; Hoffman et al. 2010). The central concentration of baryons seems to transform the box orbits into tube orbits. While the orbital content of haloes extracted from the AGN run is remarkably similar to the dark matter only haloes, the weak feedback (REF) run has the most

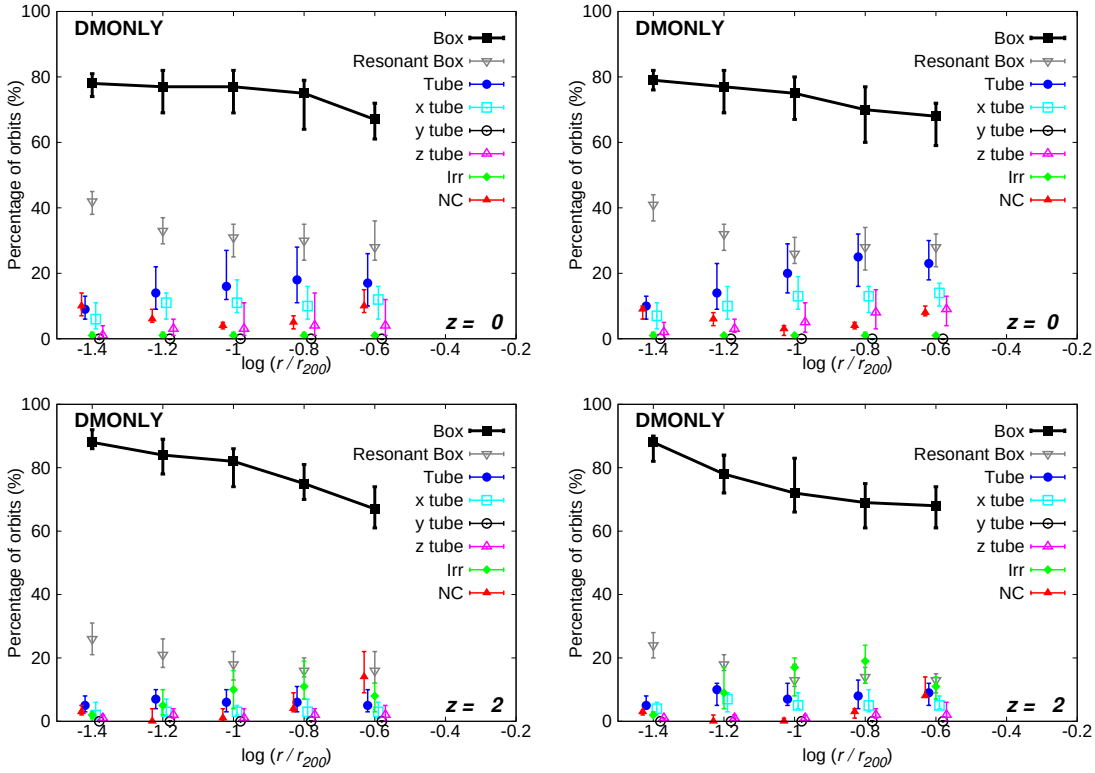


Figure 6.4: The orbital content of the most massive haloes from the DMONLY simulation. The upper panels show the orbital content of the haloes at $z = 0$, while the orbital content at $z = 2$ is shown in the lower panels. The left column shows the 50 most massive haloes while the right column shows the 27 (20) of these that are found to be relaxed at $z = 0\,(2)$. Orbits that do not undergo more than 40 periods are not classified (NC).

significant effect on the fraction of box orbits in the central region. These results are not unexpected. The AGN feedback expels most of the baryonic component from the central regions (as is evident in Figure 6.2) and the orbital content of these haloes is remarkably similar to the dark matter only haloes. The runs with no or weak feedback have a much higher central baryon concentration and hence fewer box orbits than the stronger feedback runs.

Figure 6.6 shows the orbital content of the fifty most massive haloes at $z = 2$ (these will, presumably, evolve into the most massive haloes today). Here the picture is somewhat different. We expect the merger rate at $z = 2$ to be high. The fraction of box orbits in the dark matter only run appears to be higher than that observed at

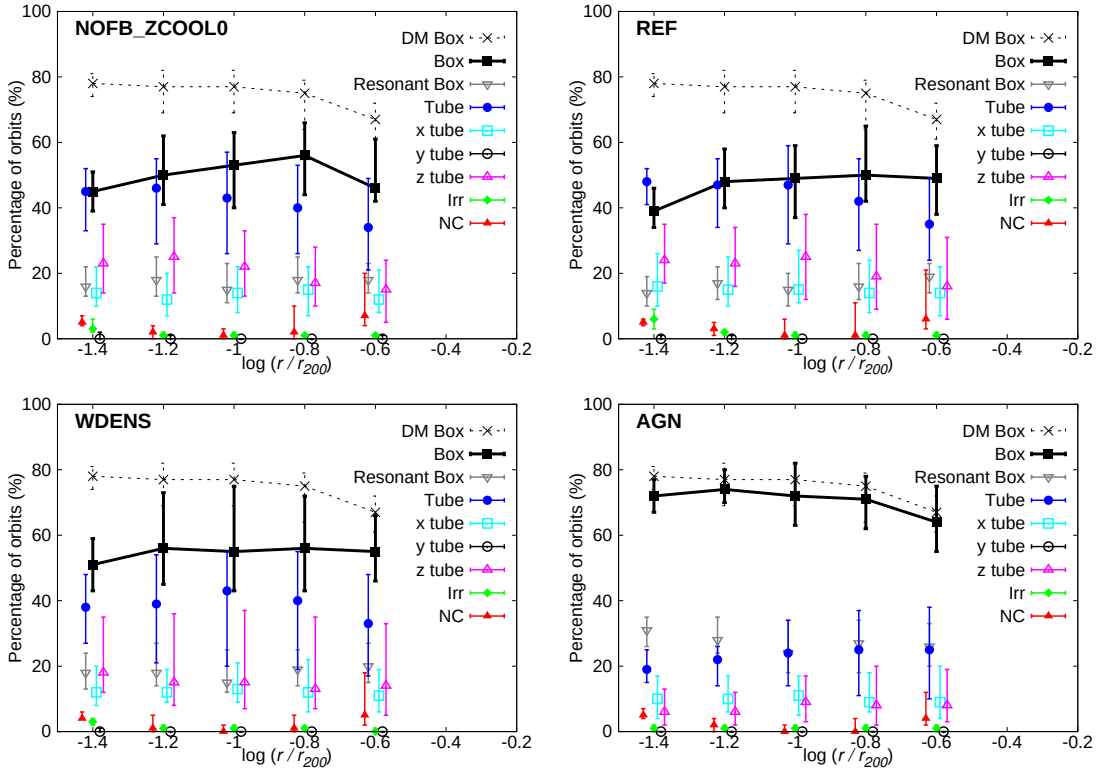


Figure 6.5: The orbits of dark matter particles at $z = 0$ (as in figure 6.4) for runs with different feedback implementations.

$z = 0$, as expected when major mergers dominate the formation process. We also note a significant increase in the fraction of irregular orbits. This is particularly apparent in the weak feedback (REF) and no feedback (NOFB_ZCOOL0). These runs appear very similar in the most central regions; perhaps unsurprising in that they appear to share very similar baryon fractions at $z = 2$. However, the large fraction of irregular orbits extends to larger radii in the weak feedback run than it does in the no feedback case. The orbital content of the strong feedback run (WDENS) does not appear to have changed as significantly between $z = 0$ and $z = 2$. A clear difference can be noted in the AGN runs at $z = 2$; there are many more tube orbits in the $z = 0$ counterparts. It is likely that the AGN have not had time to affect the orbits significantly by $z = 2$.

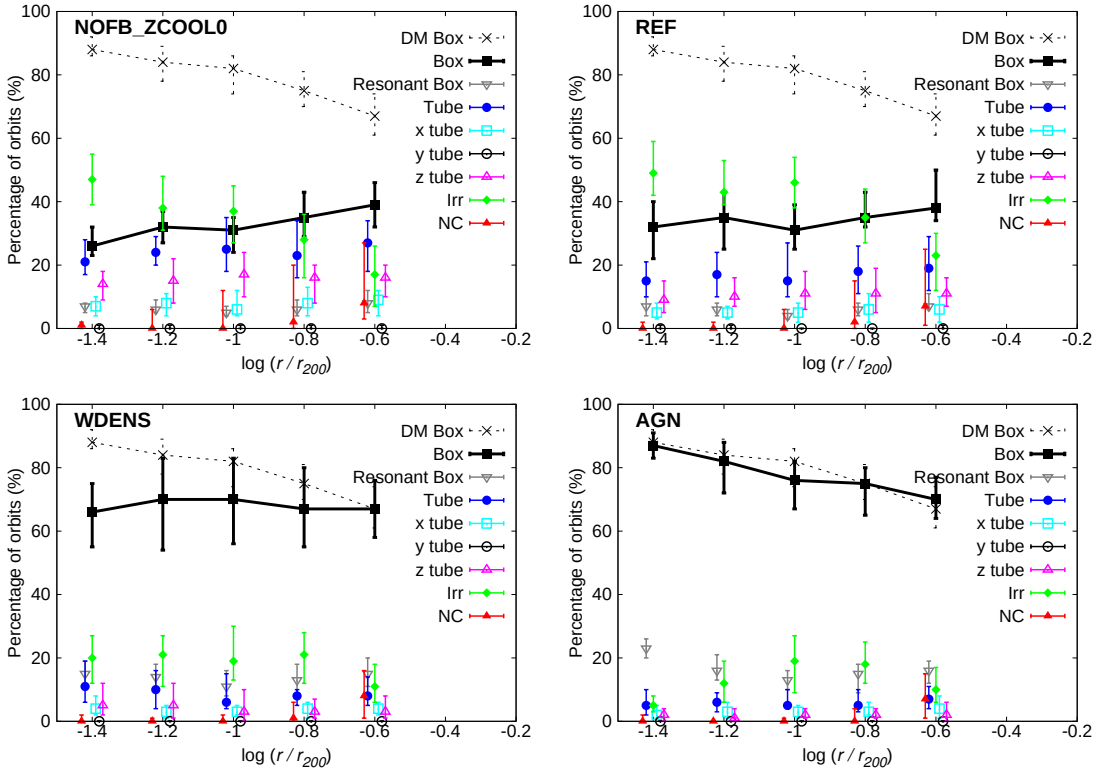


Figure 6.6: As in figure 6.5 for the orbits of dark matter particles at $z = 2$.

### Orbital Content versus Halo Properties

In this section the dependence of the orbital content of the haloes extracted from the cosmological simulations on several key parameters such as their concentration, spin, shape and velocity anisotropy is considered. The effect of basic halo properties on the fraction of box orbits can be seen in Figure 6.7. From the sample of the fifty most massive haloes in the weak stellar feedback (REF) simulation at $z = 0$, the ten haloes with the highest value of a given property (shown in pink) and the ten haloes with the lowest value of that property (in grey) were selected. For the REF run, there is a definite trend for more concentrated haloes to have fewer box orbits, and for haloes with high stellar mass to have more box orbits. Haloes with high velocity anisotropy values (radially dominated haloes) have more box orbits. The fraction of box orbits does not depend on the spin parameter or the shape of the haloes, for the range of

parameters considered here.

For the dark matter only simulations (not shown) the orbital content does not appear to depend significantly on properties such as mass, spin and shape for the range of haloes considered here. There is a weak trend for more concentrated haloes to have fewer box orbits, and for haloes with high triaxiality values to have fewer box orbits. Haloes with high velocity anisotropy values (radially dominated haloes) have few box orbits in the innermost regions. This trend is reversed closer to $0.25r_{200}$. This is mirrored in the fraction of tube orbits. Dark matter haloes with low spin parameters tend to have a slightly higher fraction of resonant box orbits at radii $> 0.06r_{200}$, and haloes with high velocity anisotropy parameters have more resonant box orbits at all radii considered. Haloes with low concentrations have a slightly lower fraction of tube orbits in the central regions, but the fraction of tube orbits (both $x$ and $z$) increases with increasing radius. High concentration haloes appear to experience a drop in the fraction of tube orbits at $\sim 0.10r_{200}$, and appear to have almost no $z$-tubes over the range of radii considered. Also, while there are more $x$-tubes in highly triaxial haloes, there are fewer $z$-tubes.

Figure 6.8 shows the fraction of box orbits (within $0.25r_{200}$) as a function of the halo mass $M_{200}$. The right (left) panels show the haloes extracted from the $z = 0$ (2) simulations. The dark matter is compared to the weak (strong) feedback runs in the top (bottom) panels. Horizontal lines indicate the mean fraction of box orbits within this region. With the exception of the AGN run, all dissipational simulations show a significant decrease in the fraction of box orbits.

The dependence of the fraction of box orbits (within $0.05r_{200}$) on the central baryon fraction $f_b$ is explicitly shown in figure 6.9. Plots are shown for haloes at $z = 0$ (left) and $z = 2$ (right). The grey band indicates the scatter in the fraction of box orbits in the dark matter only run, while the coloured points show the median and scatter of this fraction for the baryon runs. This plot emphasises the effect that baryons have on box orbits. Baryons are able to cool dissipatively to form a central mass concentration that acts to decrease the observed fraction of box orbits.

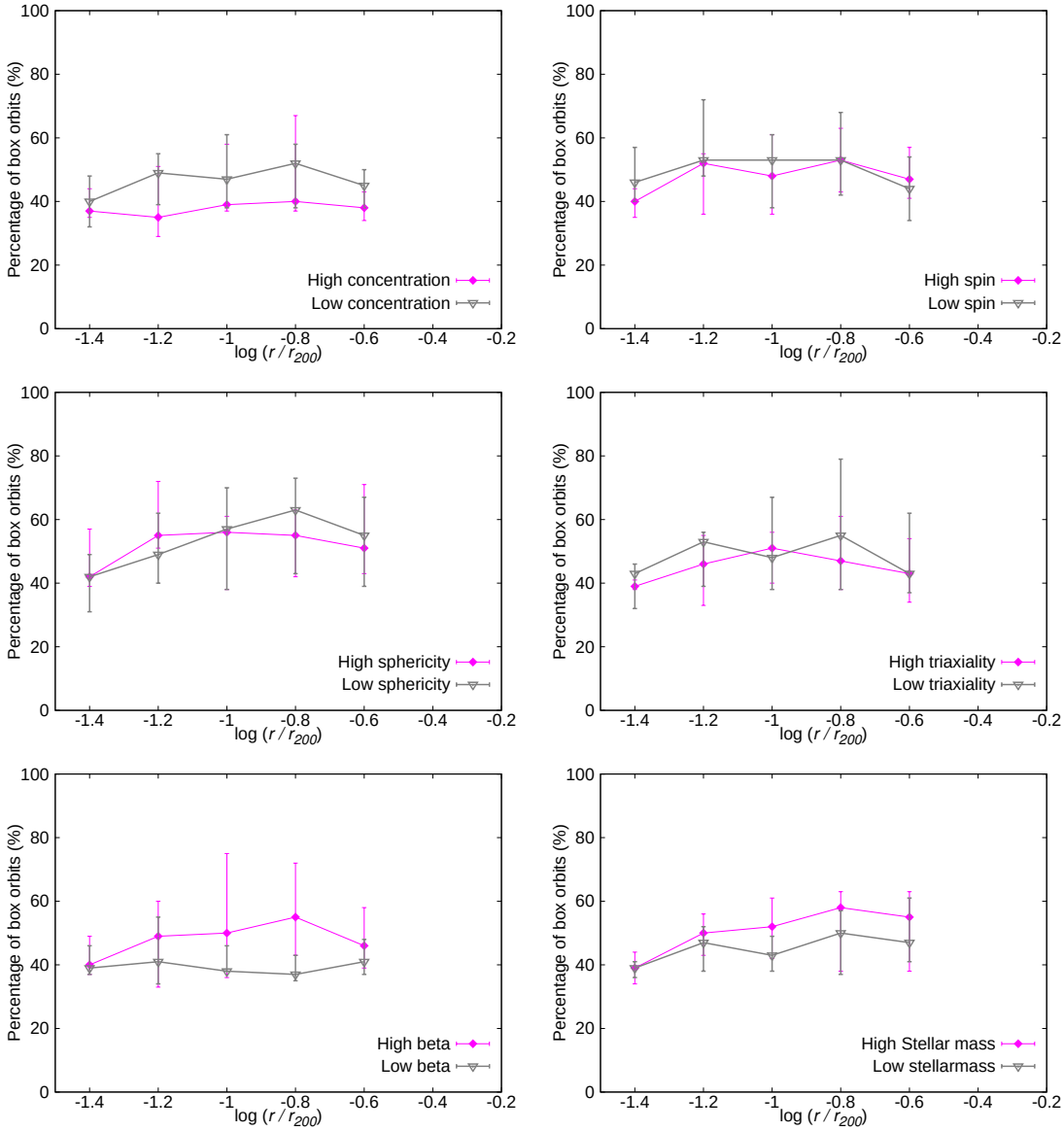


Figure 6.7: Impact of halo properties on box orbits at $z = 0$. Top left to bottom right: concentration, spin, sphericity, triaxiality and velocity anisotropy. The 10 haloes with the largest value of the relevant halo property are shown in pink, while the 10 haloes with the lowest relevant halo property are shown in grey.

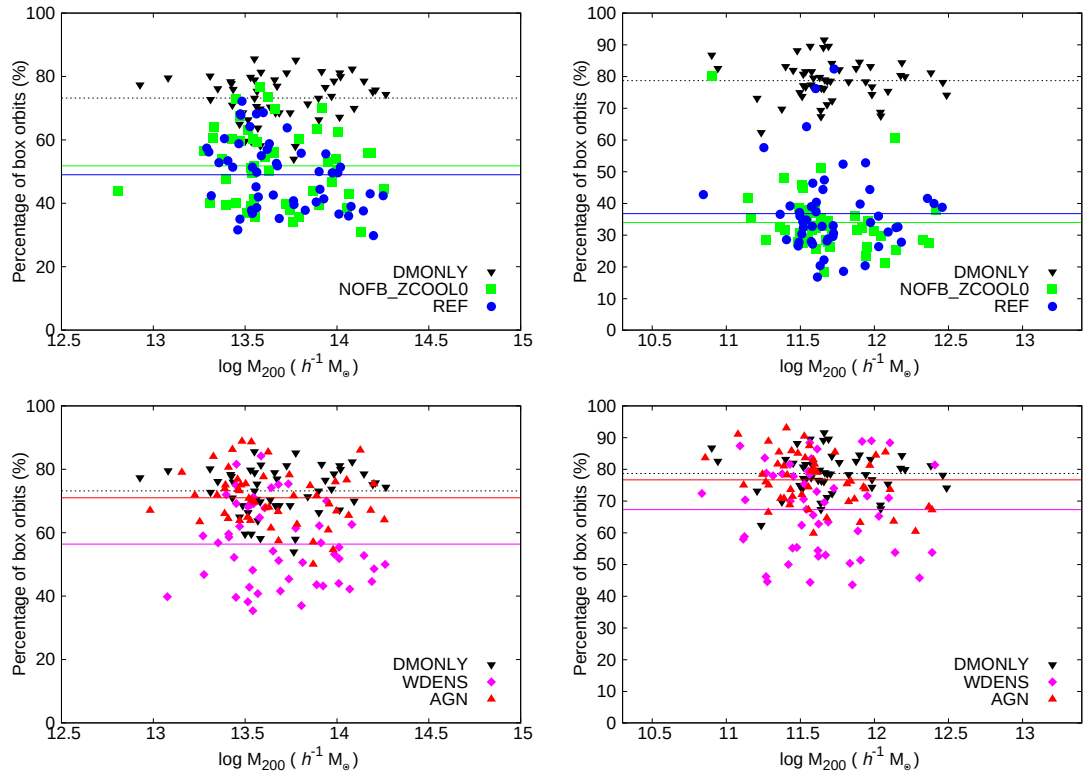


Figure 6.8: The fraction of dark matter particles (within $0.25r_{200}$) on box orbits as a function of halo mass ($M_{200}$) for the different feedback runs considered. Horizontal lines indicate the average fraction of box orbits for each simulation. Left panel: $z = 0$, right panel: $z = 2$. Weak (strong) feedback runs are compared to the dark matter only haloes in the top (bottom) panels.

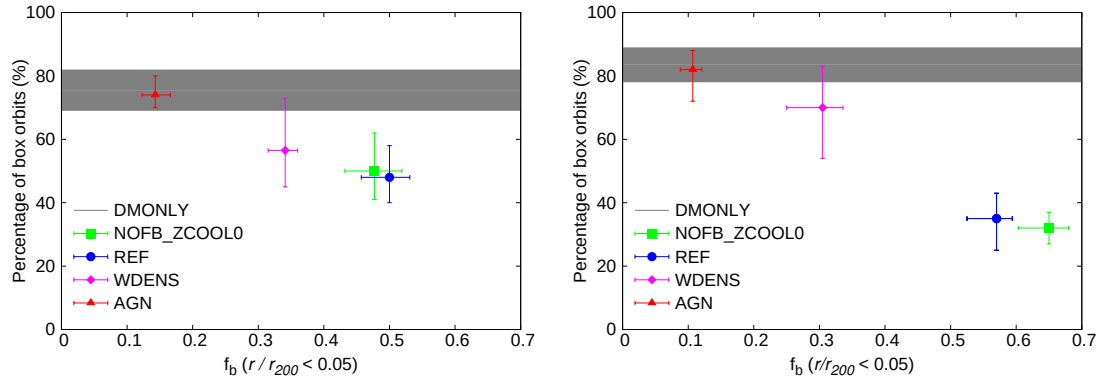


Figure 6.9: The fraction of dark matter particles on box orbits as a function of the baryon fraction $f_b$ within 5% of $r_{200}$ for the different feedback runs considered. Error bars represent the quartile scatter. The grey band indicates the scatter in the fraction of box orbits in the dark matter only run. Left panel: $z = 0$, right panel: $z = 2$.

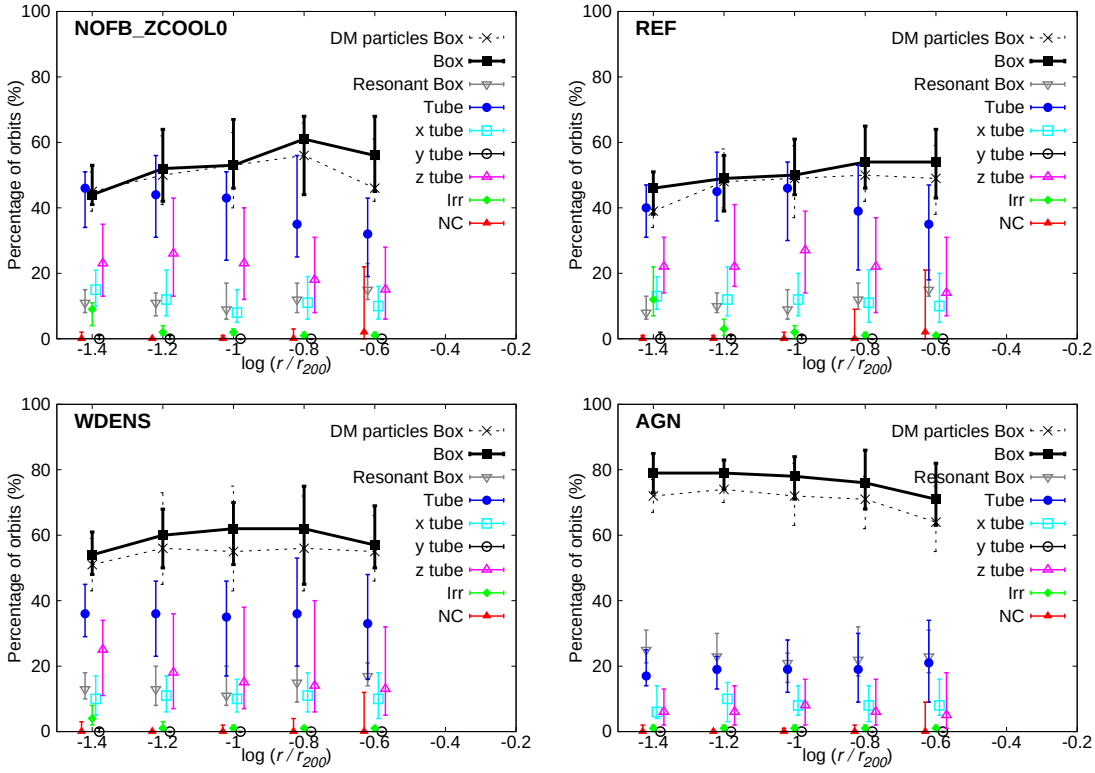


Figure 6.10: As in figure 6.5 for the orbits of stellar particles at $z = 0$. In each plot the grey dashed line shows the percentage of dark matter particles on box orbits from the same simulation (for comparison).

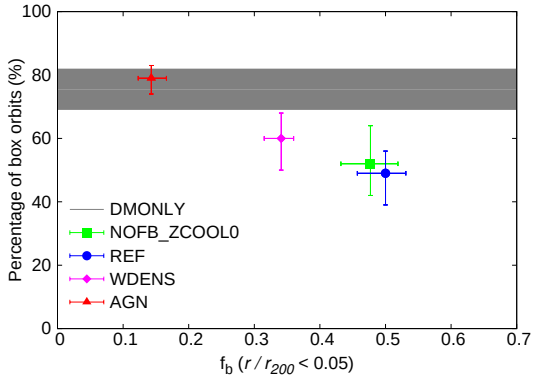


Figure 6.11: As in figure 6.9 but for stellar particles at $z = 0$. The grey band indicates the scatter of dark matter particles on box orbits in the dark matter only run.

### 6.4.2 Orbits of Stellar Particles

In Figure 6.10 the orbital classifications of stellar particles at $z = 0$ are shown. As in figure 6.5 the different feedback implementations are compared. In each plot the grey dashed line shows the percentage of dark matter particles on box orbits from the same simulations (for comparison). As in figure 6.9 the dependence of the fraction of stellar particle box orbits (within $0.05r_{200}$) on the central baryon fraction $f_b$ is shown in figure 6.11.

The orbital content described by the stellar particles is remarkably similar to that drawn from the orbits of dark matter particles. While the dark matter and stellar particles are selected from the same radius, one might expect a different trend due to the formation history of the stellar particles. Since the potential and initial conditions are drawn from the main SUBFIND halo, distinct subhaloes and satellites are not included and the stellar population considered here is associated with the central galaxy and the diffuse intra-halo component. A full analysis of the history of the stellar particles (such as when they were stripped from parent subhaloes) could prove insightful. The results presented here seem to indicate that either they were stripped a long time ago and have forgotten their dynamical history or subhaloes bringing in the stars are not biased significantly with respect to the main distribution - the velocity bias (measured as the ratio of galaxy to dark matter velocity dispersion) is weak (e.g. Springel et al. 2001a).

### 6.4.3 Orbits of Subhaloes

The orbits of the subhaloes associated with each SUBFIND main halo have also been considered. The initial position was taken to be an average over the ten most bound particles and velocity of the subhalo is assumed to be that of the most bound particle. The orbits of the 20 most massive subhaloes within $r_{vir}$ of each of the 50 haloes discussed above are explored. The subhaloes trace a region much further out than discussed previously (mean $r/r_{vir} = 0.6$ compared to a mean value of $r/r_{vir} = 0.12$ for the

dark matter and stellar particles). Subhaloes are also subject to tidal stripping.

The fraction of subhaloes on box orbits as a function of the halo mass $M_{200}$ is shown in figure 6.12. All of the runs indicate a similar fraction of box orbits. The region probed by the subhaloes is less strongly affected by the presence of baryons than the central regions discussed before.

Figure 6.13 emphasises this point, showing the median fraction and scatter of subhaloes on box orbits as a function of the central baryon fraction at $z = 0$. Comparing this plot to figures 6.9 and 6.11 shows that a similar fraction of subhaloes and dark matter (or stellar) particles are on box orbits in the weak or no feedback runs. The main difference observed in this plot is the drop in the fraction of box orbits in the dark matter and AGN runs expected at large radii. The fraction of box orbits is expected to decrease with radius (as observed in the strong feedback and dark matter only cases), but baryons act to flatten the slope in the central regions, giving rise to an almost constant box orbit fraction with radii.

This behaviour is already visible in figure 6.5, where the difference between the fraction of box orbits in dissipational and dissipationless simulations decreases with radius.

The drop in the fraction of dark matter subhaloes on box orbits may also be due to the tidal disruption of the subhaloes as they pass close to the centre of the halo. Cooling would act to increase the central concentration of both the subhalo and the main halo. Strong feedback, such as the AGN run, would be more efficient in the main halo than in the subhalo and it is likely that tidal disruption would be less severe for these runs than in the dark matter only case.

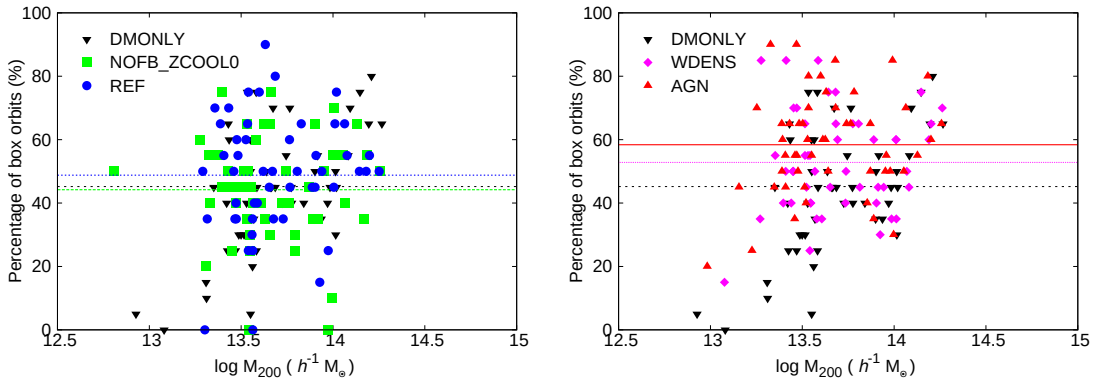


Figure 6.12: The fraction of subhaloes on box orbits as a function of the halo mass $M_{200}$ for the different simulations considered. The left (right) panel compares orbits of subhaloes from the dark matter only simulation to runs with weak (strong) feedback.

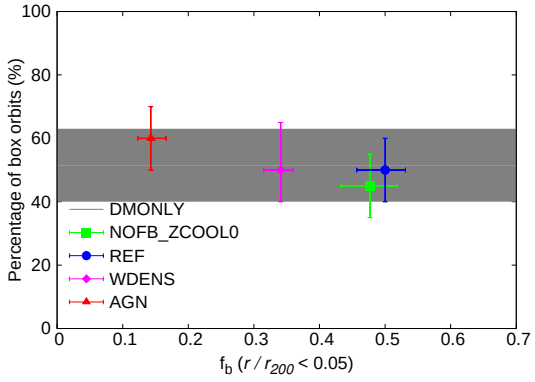


Figure 6.13: As in figure 6.9 but for subhaloes $z = 0$. The grey band indicates the scatter of dark matter subhaloes on box orbits in the dark matter only run.

## 6.5 Numerical Issues

In this section the convergence radius $r_{conv}$ and resolution effects are considered in order to show that the results presented in this chapter are well converged. The choices of halo definition and basis sets are also discussed.

### 6.5.1 Convergence Radius

Power et al. (2003) showed that numerical convergence in inner regions of dark matter haloes was achieved outside of the convergence radius $r_{conv}$. This radius is defined to ensure that the two-body dynamical relaxation time within this radius is comparable to the age of the Universe ($t_{relax} \gtrsim t_0$). Power et al. (2003) define

$$\frac{t_{relax}(r)}{t_{circ}(r_{200})} = \frac{N(r)}{8 \ln N(r)} \frac{r/V_c}{r_{200}/V_{200}} = \frac{\sqrt{200}}{8} \frac{N(r)}{\ln N(r)} \left(\frac{\bar{\rho}}{\rho_{crit}}\right)^{-1/2}, \tag{6.9}$$

where $t_{circ}(r_{200}) \sim t_0$ and $N(r)$ is the number of particles enclosed within radius $r$. Power et al. (2003) show that the density profile converges at radii that enclose a sufficient number of particles to ensure that $t_{relax}(r) \geq 0.6 t_0$.

The convergence radius depends on halo size and the resolution of the simulation and sets a minimum resolved length scale or the analysis. Figure 6.14 shows an estimate of the convergence radius as a fraction of $M_{200}$ for the haloes used in this analysis. From this plot one can see that the innermost radial bin considered in this chapter is beyond the convergence radius (i.e. $r_{conv} < r_{min}$).

### 6.5.2 Resolution Effects

In order to quantify the effects of resolution on the orbital content, the $512^3$ particle run from the DMONLY simulations (with a softening length of 2 $h^{-1}$ kpc) is compared with the corresponding lower resolution runs (containing $256^3$ and $128^3$ particles and with softening lengths of 4 and 8 $h^{-1}$ kpc, respectively). In Figure 6.15 the fraction of box orbits found in the $128^3$ simulation is shown in blue, the $256^3$ simulation in green

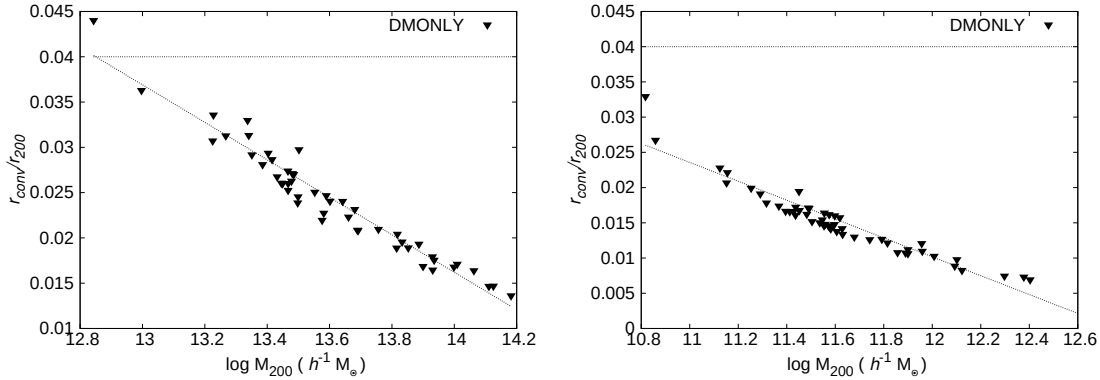


Figure 6.14: Convergence radius $r_{conv}$ for the dark matter only simulation at $z = 0$ (left) and $z = 2$ (right). The horizontal line shows the innermost bin considered in this analysis. Orbits of particles beyond the convergence radius are studied.

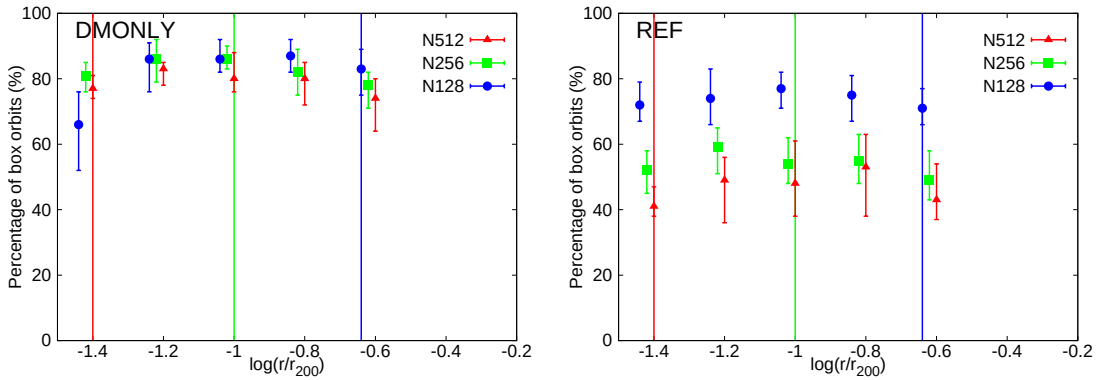


Figure 6.15: The effect of resolution on $z = 0$ results. Results from the $128^3$ simulation are shown in blue, the $256^3$ simulation in green and the $512^3$ simulation used for this analysis in red. The fraction of box orbits found in the dark matter only run is shown in the left plot. The fraction of box orbits found in the weak feedback run (REF) is shown in the right plot. The convergence radius for each simulation is shown as a vertical line.

and the $512^3$ simulation used for this analysis in red. The fraction of box orbits found in the dark matter only run is shown in the left plot while the fraction of box orbits found in the weak feedback run (REF) is shown on the right. Only relaxed haloes that are matched between the different resolution runs are considered.

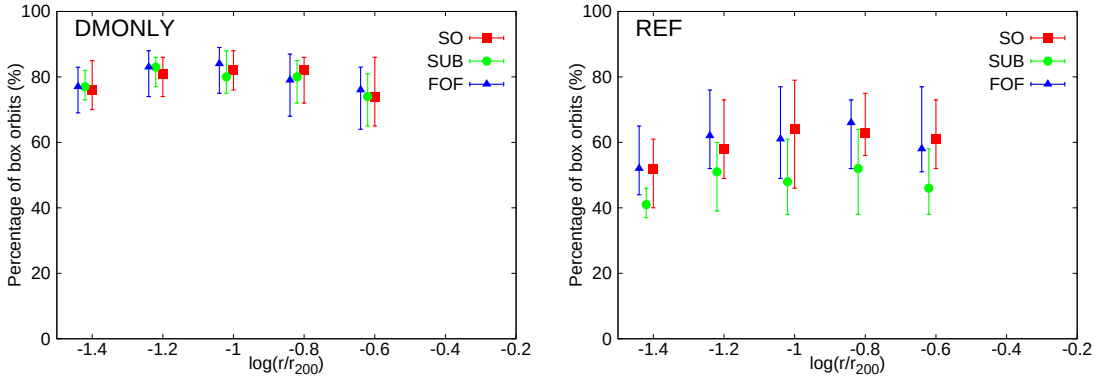


Figure 6.16: The effect of halo definition on the orbital content of haloes, using the $512^3$ particle simulations at $z = 0$. The left plot shows the fraction of box orbits in the dark matter only simulations, while the right plot shows the fraction of box orbits in the weak feedback run (REF). Results obtained if haloes are defined using the FOF algorithm are shown in blue, those using the main SUBFIND halo are shown in green and those obtained using SO are shown in red. The orbital content of a halo is not particularly sensitive to the halo definition.

### 6.5.3 Effect of Halo Definition

To explore the effect of the halo definition on the results presented here, the three common definitions of a group – FOF, main subhalo as identified by SUBFIND and the SO approach – were used. The orbital content of the haloes is not significantly affected by the halo definition, as shown in Figure 6.16. The main subhalo is therefore used throughout this analysis, this has the advantage of providing a smooth potential, unperturbed by substructure. The radial dependence of the orbital content is scaled by the spherical overdensity definition of $r_{200}$. In the dark matter only simulations the fraction of box orbits does not depend on the choice of groupfinder. In the weak feedback run (REF) the SUBFIND haloes show a slightly lower fraction of box orbits, however the trends discussed in this chapter are not significantly affected by the choice of the groupfinder.

### 6.5.4 Choice of Basis Set and Expansion Coefficients

The basis set used in this analysis is constructed so that the lowest order terms represent the Hernquist profile (Hernquist 1990). Twelve radial terms and six angular terms

Table 6.2: Classifications of orbits from the most massive relaxed cluster at $z = 0$. Different numbers of expansion coefficients have been used to reconstruct the potential using the Hernquist basis set (top) and the Clutton-Brock basis set (bottom).

| (n,l) | Box | Tube | Irr | resonant box | $x$-tube | $z$-tube | Not classified |
|---|---|---|---|---|---|---|---|
| 20,6 | 0.510 | 0.386 | 0.014 | 0.194 | 0.056 | 0.326 | 0.090 |
| 20,4 | 0.528 | 0.376 | 0.006 | 0.194 | 0.034 | 0.340 | 0.090 |
| 12,6 | 0.582 | 0.314 | 0.016 | 0.188 | 0.044 | 0.268 | 0.088 |
| 12,4 | 0.532 | 0.370 | 0.009 | 0.162 | 0.042 | 0.328 | 0.088 |
| 8,6 | 0.564 | 0.318 | 0.024 | 0.188 | 0.054 | 0.258 | 0.009 |
| 8,4 | 0.484 | 0.400 | 0.006 | 0.144 | 0.030 | 0.366 | 0.110 |
| 20,6 | 0.582 | 0.337 | 0.008 | 0.238 | 0.038 | 0.298 | 0.080 |
| 20,4 | 0.490 | 0.424 | 0.008 | 0.178 | 0.032 | 0.392 | 0.078 |
| 12,6 | 0.458 | 0.428 | 0.012 | 0.182 | 0.029 | 0.398 | 0.102 |
| 12,4 | 0.430 | 0.476 | 0.008 | 0.144 | 0.034 | 0.438 | 0.086 |
| 8,6 | 0.422 | 0.468 | 0.008 | 0.186 | 0.014 | 0.452 | 0.102 |
| 8,4 | 0.412 | 0.456 | 0.022 | 0.176 | 0.010 | 0.440 | 0.110 |

are used as this has been found to be sufficient to reproduce the potential to within a few percent of the $N$-body potential. Table 6.2 shows the orbital content of the most massive relaxed cluster from the weak feedback simulation at $z = 0$ as determined using both the Hernquist and the Clutton-Brock basis sets. This cluster has a mass of $2 \times 10^{14}\, h^{-1}\, M_{\odot}$. The orbital content does not vary significantly when more terms are used. Varying the number of expansion coefficients affects the orbital classifications on the percent level. The choice of basis set is not found to affect the reconstruction of the potential significantly. Figure 6.17 shows the difference in potential computed using SCF method and the potential computed using the Direct Summation method. Blue points indicates the SCF potential has been computed using the Hernquist basis set, while green points show the SCF potential computed using the Clutton-Brock basis set.

## 6.6 Summary and Discussion

The orbital content of a large sample of haloes extracted from state-of-the-art high-resolution cosmological hydrodynamical simulations has been explored in order to

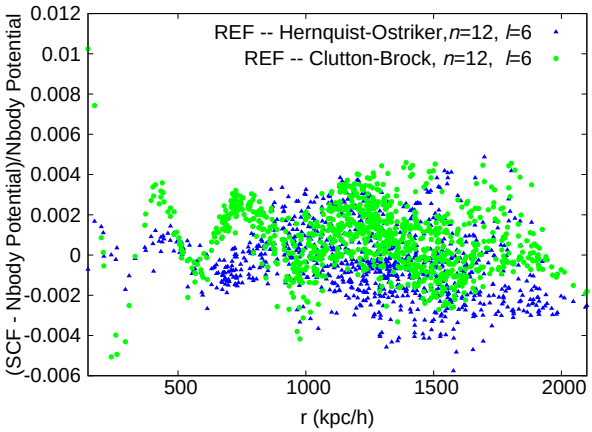


Figure 6.17: Difference in potential as computed by the SCF method and the Direct-Summation approach for the most massive weak feedback (REF) halo. For the blue points the SCF has been computed using the basis set of Hernquist-Ostriker, while for green points the SCF potential is calculated using the Clutton-Brock basis set.

study what observational signatures may result. Dark matter only haloes are dominated by box orbits out to $0.25r_{200}$. This is not surprising as box orbits are known to be required to support the triaxial haloes characteristic of dark matter only haloes. The fraction of box orbits is found to decrease with increasing distance from the halo centre; this is mirrored by an increase in the fraction of tube orbits. Roughly half of the box orbits are found to exhibit resonance. The fraction of resonant box orbits is also found to decrease with radius. Very few of the orbits analysed in the dark matter only simulations were found to be on $y$-tubes and a negligible fraction of the orbits where classified as irregular. The tube orbits are dominated by $x$-tubes in the central region, and the fraction of both $x$- and $z$-tube orbits is found to increase with increasing radius; $z$-tubes dominate the fraction of tube orbits at larger radii.

The orbital content of these dark matter haloes does not appear to be strongly dependent on basic halo properties such as spin, mass, redshift and dynamical state in either the dark matter only or the weak feedback runs for the range of parameters considered here.

By comparing simulations run with no feedback, with stellar feedback and with feedback from AGN, the fraction of box orbits in the central region is found to decrease

when baryonic physics is included. Baryons are able to cool and condense to the centre of the halo, and this central concentration tends to transform box orbits into tube orbits. Increasing the strength of the feedback implementation is found to reduce the central concentration of baryons, and increase the fraction of box orbits. The orbital content described by the stellar particles is found to be remarkably similar to that drawn from the orbits of dark matter particles. Subhaloes probe a more extended region of the halo and are subject to tidal stripping. The different implementations of the baryon physics do not appear to change the fraction of subhaloes on box orbits significantly. Typically $\sim 50\%$ of the subhaloes are found to be on box orbits.

# 7

# Summary and Future Work

Currently, with simulations such as the Millennium Simulation (Springel et al. 2005b), Aquarius (Springel et al. 2008), Via Lactea (Diemand et al. 2008) and Ghalo (Stadel et al. 2009), we have a good understanding of dark matter structure formation. Dark matter haloes formed in a ΛCDM cosmology appear to share many universal properties, such as their internal morphology (see, for example, Navarro et al. 1996; Navarro et al. 1997; Bullock et al. 2001; Duffy et al. 2008) and an abundance of substructure (Klypin et al. 1999; Moore et al. 1999; Gao et al. 2004a,b; Diemand et al. 2007b) and are typically thought to be triaxial (Frenk et al. 1988; Dubinski and Carlberg 1991; Warren et al. 1992; Cole and Lacey 1996; Jing and Suto 2002; Bailin and Steinmetz 2005b; Allgood et al. 2006; Macciò et al. 2006; Bett et al. 2007). These generic predictions are a result of hierarchical structure formation and the dissipationless nature of dark matter. The role of baryons on structure formation is much more uncertain and has become the focus of galaxy formation studies. A thorough understanding of the role of baryons in galaxy formation and evolution is essential, not only because most observations are only able to trace baryonic matter but also because of the complex role it may play in the evolution of the dark matter halo itself.

The merging process will leave imprints on the structure and dynamics of the remnant galaxy. Studying these relic imprints will provide information about the galaxies' formation history. However, the complex interplay between mergers and dissipational

effects needs to be considered. In order to fully optimise the use of such observational signatures, comparisons with simulations such as these are essential. In this thesis state-of-the-art simulations have been used to explore three such observational signatures: the abundance of substructure, the shape of haloes and the orbital content of the haloes.

This work incorporates two different approaches to baryonic and gas physics in the simulations. The first uses simple semi-analytic prescriptions to approximate the complicated physical processes involved in galaxy formation (see section 3.7) and the second implements SPH techniques (see section 3.4.1). These simulations provide a unique opportunity to analyse the effects of baryons and implemented feedback techniques on a large sample of haloes evolved within a cosmological setting.

A generic prediction of CDM models is an abundance of substructure. While this matches well with observations on cluster scales, galactic scales have proven a more stringent test on galaxy formation models. Simulations on galaxy scales predict almost an order of magnitude more satellites than are actually observed in the Milky Way. These results are however reconcilable as fainter and fainter objects are being detected observationally and the suppression of star formation in the smallest objects is modelled. Gravitational lensing is a unique probe of the mass along the line of sight in that it is not sensitive to the type of matter (baryonic or otherwise), but only to the total mass. CDM substructure has been proposed as an explanation of the anomalous flux ratios seen in gravitational lens systems. While there is sufficient mass in simulated substructures, its not clear that substructures are able to survive in the very central regions probed by lensing. Surprisingly, about 50% of lenses in the Cosmic Lens All-Sky Survey (CLASS) appear to have luminous satellites within $\sim 5\ h^{-1}$ kpc of the main lensing galaxies.

In chapter 4 the Millennium Simulation (Springel et al. 2005b), combined with galaxy catalogues from semi-analytical models (De Lucia and Blaizot 2007), is used to study the predicted frequency of such satellites in simulated haloes. The fraction of haloes that host bright satellites within the (projected) central regions is similar for red

and blue hosts and is found to increase as a function of host halo mass and redshift. However, even in group-sized haloes at $z = 1$, the predicted number of haloes found to host a luminous satellite galaxy is lower than that observed in CLASS. It is worth noting that most of the satellites found in the inner regions are 'orphan' galaxies where the dark matter haloes have been completely stripped. Thus the agreement crucially depends on the true survival rate of these 'orphan' galaxies. While the limited number of lenses in CLASS makes it difficult to draw any strong conclusions, the predicted number of haloes found to host a luminous satellite galaxy is significantly lower than that observed in CLASS.

This work was extended to include companions of all elliptical galaxies, in order to compare the fractions of satellites in field and lens galaxies (see Jackson et al. 2010). The frequencies of luminous satellites in the central regions of galaxies selected from SDSS, COSMOS and SLACS were studied, significantly increasing the sample size. No significant difference was found between the populations of field and lens systems. The fractions of systems found to host a luminous companion within the projected central region in the SDSS, COSMOS and SLACS samples are even lower than that observed in the semi-analytic galaxy catalogue and considerably lower than the CLASS lenses. The frequency of luminous satellites in CLASS appears to be anomalously high, however firm conclusions await the acquisition of a large sample of high redshift lenses.

In chapter 5, the predicted distributions of the spin and shape of dark matter haloes are investigated and the roles of baryons and the physical prescriptions of stellar and black hole feedback are examined. The spin distribution of haloes extracted from the baryon runs is not significantly different to that of dark matter only haloes when computed over the whole halo. However, in the central regions where baryons are expected to dominate, haloes from weak feedback simulations tend to have higher median spin values than haloes from high feedback runs. The spin distribution in the central region of strong feedback simulations is comparable to the distribution found for dark matter only haloes. Dark matter only haloes typically have triaxial to prolate

shapes and their radial shape profiles are close to flat. More massive haloes are found to be less spherical and more prolate than lower mass haloes. Baryons act to make the haloes more spherical and weak stellar feedback runs are able to produce almost oblate haloes, while stellar and AGN feedback runs result in prolate haloes similar to those found in dark matter only simulations. Baryons are also shown to have a significant effect on the shape of the dark matter distribution. The shapes of the simulated haloes are shown to be in agreement with a wide range of observational estimates of the shapes of elliptical galaxies.

In chapter 6, the orbital content of simulated haloes is analysed, with particular focus on the role of energy ejected (feedback) from SNe and black holes in shaping the orbital content of haloes. How the orbital content of these haloes depends on several key parameters (such as their mass, redshift and dynamical state) is also considered. Efficient cooling causes the haloes to become centrally concentrated and this results in a decrease in the fraction of orbits passing close to the centre. As the feedback efficiency from stars and black holes increases, the central concentration is reduced and the number of orbits passing close to the centre increases. The Gaia satellite, to be launched in 2012, will provide a kinematic census of our Galaxy. To optimise the use of this data, comparison with simulations will be crucial.

What is clear from this work is that baryons play an important role in the formation and evolution of galaxies and an understanding of these processes is incomplete without careful consideration of gas physics. Studying the central regions of haloes may place strong constraints on formation theories. While studying this region is made complicated by the effects of baryons and limited resolution (both observationally and in simulations) it may yield some of the most useful constraints on galaxy formation models by providing insight into the important physical processes that govern galaxy evolution. Galaxies found in the innermost regions of a halo are likely to be significantly affected by physical processes such as tidal stripping and, in simulations, are the most sensitive to numerical effects. Comparison between observations and simulations in this regime is essential. Fortunately, rapid advances in computational power and in-

creasingly sophisticated treatment of gas physics is now allowing us to probe this in more detail than ever before.

## Proposed Future Directions

The orbital content of dark matter haloes in the Phoenix simulations (Liang Gao[1]) will be analysed using the techniques described in chapter 6. The Phoenix simulations are high-resolution dark matter simulations and consist of 9 clusters simulated at different resolutions, the highest resolution run containing $10^9$ particles within the virial radius. The unprecedented resolution of the Phoenix cluster simulations will make it possible to probe the dynamics of substructure to a unparallelled level, allowing for the study of orbits of subhaloes covering an exceptionally large range in mass. This resolution would be ideal for exploring dynamic mass segregation (massive subhaloes are more centrally concentrated than their lower mass counterparts) in detail. This would provide valuable information about the origin of the mass segregation and the relative importance of the mechanisms present in clusters that drive the evolution of the subhaloes and their associated galaxies.

The force resolution of the simulations would allow us to probe the very central regions of the cluster. Semi-analytic catalogues run on these simulations will allow for a study of the dynamics of satellite galaxies covering a wide range of masses, luminosities, colours, star formation histories and accretion times. The orbital content of the simulated clusters and their subhalo and satellite populations will be assessed.

As haloes are known to rotate (Bailin and Steinmetz 2004; Bryan and Cress 2007), it would also be interesting to investigate the effects of a live halo, considering the time evolution of the potential, on the dynamics of the system. This can be achieved by tracing the halo through time using merger trees. The halo potential can be estimated using the SCF method at the redshifts recorded in the simulation and the SCF coefficients can be interpolated between these time intervals.

[1] private communication

Further applications of this work would be to use the predicted orbits to explore disc heating, angular momentum transfer from satellites and the tidal stripping of satellites in high-resolution simulations such as Phoenix, Aquarius and OWLS. Discs are able to provide strong constraints on the merging history of a system and angular momentum transfer from satellites to the dark matter may play an important role in shaping the density profile of a system.

# References


Aarseth, S. J. *Dynamical evolution of clusters of galaxies, I.* MNRAS, 126:223, 1963.

Adelman-McCarthy, J. K., Agüeros, M. A., Allam, S. S. et al. *The sixth data release of the Sloan Digital Sky Survey*. ApJS, 175:297, 2008.

Allgood, B., Flores, R. A., Primack, J. R. et al. *The shape of dark matter haloes: Dependence on mass, redshift, radius and formation*. MNRAS, 367:1781, 2006.

Amendt, P. and Cuddeford, P. *Pseudomoment stellar dynamics. 1: Spheroidal galactic equilibria*. ApJ, 435:93, 1994.

Arnaboldi, M., Capaccioli, M., Cappellaro, E. et al. *Studies of narrow polar rings around E Galaxies. I - Observations and model of AM 2020-504*. A&A, 267:21, 1993.

Bailin, J. and Steinmetz, M. *Figure rotation of cosmological dark matter halos*. ApJ, 616:27, 2004.

Bailin, J. and Steinmetz, M. *Can satellite dwarfs excite galactic warps?* In H. Jerjen & B. Binggeli, editor, *IAU Colloq. 198: Near-fields cosmology with dwarf elliptical galaxies*, 207–210. 2005a.

Bailin, J. and Steinmetz, M. *Internal and external alignment of the shapes and angular momenta of $\Lambda$CDM halos*. ApJ, 627:647, 2005b.

Banerjee, A. and Jog, C. J. *The flattened dark matter halo of M31 as deduced from the observed H I scale heights*. ApJ, 685:254, 2008.

Bardeen, J. M., Bond, J. R., Kaiser, N. et al. *The statistics of peaks of Gaussian random fields*. ApJ, 304:15, 1986.

Barkana, R. and Loeb, A. *Detecting reionization in the star formation histories of high-redshift galaxies*. MNRAS, 371:395, 2006.

Barnes, J. and Hut, P. *A hierarchical O(N log N) force-calculation algorithm*. Nature,

324:446, 1986.

Barnes, J. E. *Transformations of galaxies. I - Mergers of equal-mass stellar disks*. ApJ, 393:484, 1992.

Barnes, J. E. and Hernquist, L. *Transformations of galaxies. II. Gasdynamics in merging disk galaxies*. ApJ, 471:115, 1996a.

Barnes, J. E. and Hernquist, L. *Transformations of galaxies. II. Gasdynamics in merging disk galaxies*. ApJ, 471:115, 1996b.

Baugh, C. M. *A primer on hierarchical galaxy formation: the semi-analytical approach*. Reports of Progress in Physics, 69:3101, 2006.

Baumgardt, H. and Makino, J. *Dynamical evolution of star clusters in tidal fields*. MNRAS, 340:227, 2003.

Becquaert, J. and Combes, F. *The 3D geometry of dark matter halos.* A&A, 325:41, 1997.

Belokurov, V., Zucker, D. B., Evans, N. W. et al. *Cats and dogs, hair and a hero: A quintet of new Milky Way companions*. ApJ, 654:897, 2007.

Bett, P., Eke, V., Frenk, C. S. et al. *The spin and shape of dark matter haloes in the Millennium simulation of a* $\Lambda$ *cold dark matter universe*. MNRAS, 376:215, 2007.

Bienaymé, O., Soubiran, C., Mishenina, T. V. et al. *Vertical distribution of galactic disk stars*. A&A, 446:933, 2006.

Binney, J., May, A. and Ostriker, J. P. *On the flattening of dark haloes*. MNRAS, 226:149, 1987.

Binney, J. and Spergel, D. *Spectral stellar dynamics*. ApJ, 252:308, 1982.

Binney, J. and Tremaine, S. *Galactic dynamics*. Princeton, NJ, Princeton University Press, 1987, 747 p., 1987.

Blanton, M. R., Hogg, D. W., Bahcall, N. A. et al. *The galaxy luminosity function and luminosity density at redshift z = 0.1*. ApJ, 592:819, 2003.

Bode, P., Ostriker, J. P. and Turok, N. *Halo formation in warm dark matter models*. ApJ, 556:93, 2001.

Bolton, A. S., Burles, S., Koopmans, L. V. E. et al. *The Sloan lens ACS survey. I. A large spectroscopically selected sample of massive early-type lens galaxies*. ApJ, 638:703, 2006.

Bolton, A. S., Burles, S., Koopmans, L. V. E. et al. *The Sloan lens ACS survey. V. The*

*full ACS strong-lens sample*. ApJ, 682:964, 2008.

Bond, J. R., Cole, S., Efstathiou, G. et al. *Excursion set mass functions for hierarchical Gaussian fluctuations*. ApJ, 379:440, 1991.

Bonnor, W. B. *Jeans' formula for gravitational instability*. MNRAS, 117:104, 1957.

Booth, C. M. and Schaye, J. *Cosmological simulations of the growth of supermassive black holes and feedback from active galactic nuclei: Method and tests*. MNRAS, 398:53, 2009.

Bower, R. G., Benson, A. J., Malbon, R. et al. *Breaking the hierarchy of galaxy formation*. MNRAS, 370:645, 2006.

Brown, M. L., Ade, P., Bock, J. et al. *Improved measurements of the temperature and polarization of the cosmic microwave background from QUaD*. ApJ, 705:978, 2009.

Browne, I. W. A., Wilkinson, P. N., Jackson, N. J. F. et al. *The Cosmic Lens All-Sky Survey - II. Gravitational lens candidate selection and follow-up*. MNRAS, 341:13, 2003.

Bryan, G. L. and Norman, M. L. *Statistical properties of x-ray clusters: Analytic and numerical comparisons*. ApJ, 495:80, 1998.

Bryan, S. E. and Cress, C. M. *Figure rotation of dark haloes in cold dark matter simulations*. MNRAS, 380:657, 2007.

Bullock, J. S. *Shapes of dark matter halos*. In P. Natarajan, editor, *The Shapes of Galaxies and their Dark Matter Haloes*, 1099. 2002.

Bullock, J. S., Dekel, A., Kolatt, T. S. et al. *A universal angular momentum profile for galactic halos*. ApJ, 555:240, 2001.

Buote, D. A. and Canizares, C. R. *X-ray constraints on the intrinsic shape of the lenticular galaxy NGC 1332*. ApJ, 457:177, 1996.

Buote, D. A. and Canizares, C. R. *The nature of the X-ray emission and the mass distributions in two early-type galaxies*. ApJ, 474:650, 1997.

Buote, D. A. and Canizares, C. R. *The shapes and sizes of elliptical galaxy halos from x-ray observations*. In D. Zaritsky, editor, *Galactic Halos*, volume 136 of *Astronomical Society of the Pacific Conference Series*, 289. 1998.

Capak, P., Aussel, H., Ajiki, M. et al. *The first release COSMOS optical and near-IR data and Catalog*. ApJS, 172:99, 2007.

Carpintero, D. D. and Aguilar, L. A. *Orbit classification in arbitrary 2D and 3D*

*potentials*. MNRAS, 298:1, 1998.

Carroll, S. M., Press, W. H. and Turner, E. L. *The cosmological constant*. ARA&A, 30:499, 1992.

Chabrier, G. *Galactic stellar and substellar initial mass function*. PASP, 115:763, 2003.

Chandrasekhar, S. and Henrich, L. R. *An attempt to interpret the relative abundances of the elements and their isotopes.* ApJ, 95:288, 1942.

Chen, J., Rozo, E., Dalal, N. et al. *Astrometric perturbations in substructure lensing*. ApJ, 659:52, 2007.

Clowe, D., Bradač, M., Gonzalez, A. H. et al. *A direct empirical proof of the existence of dark matter*. ApJL, 648:L109, 2006.

Clutton-Brock, M. *The gravitational field of three dimensional galaxies*. Astrophysics and Space Science, 23:55, 1973.

Cohn, J. D. and Kochanek, C. S. *The effects of massive substructures on image multiplicities in gravitational lenses*. ApJ, 608:25, 2004.

Cole, S. *Modeling galaxy formation in evolving dark matter halos*. ApJ, 367:45, 1991.

Cole, S. and Lacey, C. *The structure of dark matter haloes in hierarchical clustering models*. MNRAS, 281:716, 1996.

Contopoulos, G. *A third integral of motion in a galaxy*. ZAp, 49:273, 1960.

Couchman, H. M. P. and Rees, M. J. *Pregalactic evolution in cosmologies with cold dark Matter*. MNRAS, 221:53, 1986.

Croton, D. J., Springel, V., White, S. D. M. et al. *The many lives of active galactic nuclei: cooling flows, black holes and the luminosities and colours of galaxies*. MNRAS, 365:11, 2006.

Dalal, N. and Kochanek, C. S. *Direct detection of cold dark matter substructure*. ApJ, 572:25, 2002.

Dalla Vecchia, C. and Schaye, J. *Simulating galactic outflows with kinetic supernova feedback*. MNRAS, 387:1431, 2008.

Davis, M., Efstathiou, G., Frenk, C. S. et al. *The evolution of large-scale structure in a universe dominated by cold dark matter*. ApJ, 292:371, 1985.

de Lorenzi, F., Debattista, V. P., Gerhard, O. et al. *NMAGIC: A fast parallel implementation of a $\chi^2$-made-to-measure algorithm for modelling observational data*.

MNRAS, 376:71, 2007.

De Lucia, G. and Blaizot, J. *The hierarchical formation of the brightest cluster galaxies*. MNRAS, 375:2, 2007.

De Lucia, G., Kauffmann, G. and White, S. D. M. *Chemical enrichment of the intracluster and intergalactic medium in a hierarchical galaxy formation model*. MNRAS, 349:1101, 2004.

De Lucia, G., Springel, V., White, S. D. M. et al. *The formation history of elliptical galaxies*. MNRAS, 366:499, 2006.

de Zeeuw, T. and Franx, M. *Kinematics of gas in a triaxial Galaxy*. ApJ, 343:617, 1989.

de Zeeuw, T. and Franx, M. *Structure and dynamics of elliptical galaxies*. ARA&A, 29:239, 1991.

Debattista, V. P., Moore, B., Quinn, T. et al. *The causes of halo shape changes induced by cooling baryons: Disks versus substructures*. ApJ, 681:1076, 2008.

Debattista, V. P. and Sellwood, J. A. *Warped galaxies from misaligned angular momenta*. ApJL, 513:L107, 1999.

Dehnen, W. *Tailoring triaxial N-body models via a novel made-to-measure method*. MNRAS, 395:1079, 2009.

Diemand, J., Kuhlen, M. and Madau, P. *Dark matter substructure and gamma-ray annihilation in the Milky Way halo*. ApJ, 657:262, 2007a.

Diemand, J., Kuhlen, M. and Madau, P. *Formation and evolution of galaxy dark matter halos and their substructure*. ApJ, 667:859, 2007b.

Diemand, J., Kuhlen, M., Madau, P. et al. *Clumps and streams in the local dark matter distribution*. Nature, 454:735, 2008.

Dolag, K., Borgani, S., Murante, G. et al. *Substructures in hydrodynamical cluster simulations*. MNRAS, 399:497, 2009.

Doroshkevich, A. G., Zel'Dovich, Y. B. and Novikov, I. D. *The origin of galaxies in an expanding universe.* Soviet Astronomy, 11:233, 1967.

Dubinski, J. *The effect of dissipation on the shapes of dark halos*. ApJ, 431:617, 1994.

Dubinski, J. and Carlberg, R. G. *The structure of cold dark matter halos*. ApJ, 378:496, 1991.

Duffy, A. R., Schaye, J., Kay, S. T. et al. *Dark matter halo concentrations in the Wilkin-*

*son Microwave Anisotropy Probe year 5 Cosmology*. MNRAS, 390:L64, 2008.

Duffy, A. R., Schaye, J., Kay, S. T. et al. *Impact of baryon physics on dark matter structures: A detailed simulation study of halo density profiles*. MNRAS, 405:2161, 2010.

Earman, J. *Lambda: The constant that refuses to die*. Archive for History of Exact Sciences, 55:189, 2001. 10.1007/s004070000025.

Efstathiou, G. *Suppressing the formation of dwarf galaxies via photoionization*. MNRAS, 256:43P, 1992.

Efstathiou, G., Davis, M., White, S. D. M. et al. *Numerical techniques for large cosmological N − body simulations*. ApJS, 57:241, 1985.

Efstathiou, G. and Eastwood, J. W. *On the clustering of particles in an expanding universe*. MNRAS, 194:503, 1981.

Eisenstein, D. J. *Dark energy and cosmic sound [review article]*. New Astronomy Reviews, 49:360, 2005.

Eisenstein, D. J. and Hu, W. *Power spectra for cold dark matter and its variants*. ApJ, 511:5, 1999.

Eke, V. R., Cole, S. and Frenk, C. S. *Cluster evolution as a diagnostic for Omega*. MNRAS, 282:263, 1996.

Evrard, A. E., Summers, F. J. and Davis, M. *Two-fluid simulations of galaxy formation*. ApJ, 422:11, 1994.

Ewald, P. P. *Die Berechnung optischer und elektrostatischer Gitterpotentiale*. Annalen der Physik, 369:253, 1921.

Faber, S. M. and Jackson, R. E. *Velocity dispersions and mass-to-light ratios for elliptical galaxies*. ApJ, 204:668, 1976.

Faltenbacher, A. and White, S. D. M. *Assembly bias and the dynamical structure of dark matter halos*. ApJ, 708:469, 2010.

Fasano, G., Amico, P., Bertola, F. et al. *The intrinsic shapes of galactic discs*. MNRAS, 262:109, 1993.

Fassnacht, C. D. and Cohen, J. G. *Keck spectroscopy of three gravitational lens systems discovered in the JVAS and CLASS surveys*. AJ, 115:377, 1998.

Fassnacht, C. D., Gal, R. R., Lubin, L. M. et al. *Mass along the line of sight to the gravitational lens B1608+656: Galaxy groups and implications for $H_0$*. ApJ,

642:30, 2006.

Fellhauer, M., Belokurov, V., Evans, N. W. et al. *The origin of the bifurcation in the Sagittarius stream*. ApJ, 651:167, 2006.

Ferland, G. J., Korista, K. T., Verner, D. A. et al. *CLOUDY 90: Numerical simulation of plasmas and their spectra*. PASP, 110:761, 1998.

Franx, M. and de Zeeuw, T. *Elongated disks and the scatter in the Tully-Fisher relation*. ApJL, 392:L47, 1992.

Franx, M., Illingworth, G. and de Zeeuw, T. *The ordered nature of elliptical galaxies - Implications for their intrinsic angular momenta and shapes*. ApJ, 383:112, 1991.

Franx, M., van Gorkom, J. H. and de Zeeuw, T. *Evidence for axisymmetric halos: The case of IC 2006*. ApJ, 436:642, 1994.

Frenk, C. S., White, S. D. M., Davis, M. et al. *The formation of dark halos in a universe dominated by cold dark matter*. ApJ, 327:507, 1988.

Gamow, G. *Expanding universe and the origin of elements*. Physical Review, 70:572, 1946.

Gao, L., De Lucia, G., White, S. D. M. et al. *Galaxies and subhaloes in ΛCDM galaxy clusters*. MNRAS, 352:L1, 2004a.

Gao, L., White, S. D. M., Jenkins, A. et al. *The subhalo populations of ΛCDM dark haloes*. MNRAS, 355:819, 2004b.

Garnavich, P. M., Jha, S., Challis, P. et al. *Supernova limits on the cosmic equation of state*. ApJ, 509:74, 1998.

Gerhard, O. E. and Binney, J. *Triaxial galaxies containing massive black holes or central density cusps*. MNRAS, 216:467, 1985.

Ghigna, S., Moore, B., Governato, F. et al. *Density profiles and substructure of dark matter halos: Converging results at ultra-high numerical resolution*. ApJ, 544:616, 2000.

Gingold, R. A. and Monaghan, J. J. *Smoothed particle hydrodynamics - Theory and application to non-spherical stars*. MNRAS, 181:375, 1977.

Gnedin, N. Y. *Effect of reionization on structure formation in the universe*. ApJ, 542:535, 2000.

Gnedin, O. Y., Gould, A., Miralda-Escudé, J. et al. *Probing the shape of the galactic halo with hypervelocity stars*. ApJ, 634:344, 2005.

Granato, G. L., De Zotti, G., Silva, L. et al. *A physical model for the coevolution of QSOs and their spheroidal hosts*. ApJ, 600:580, 2004.

Guo, Q., White, S., Boylan-Kolchin, M. et al. *From dwarf spheroidals to cDs: Simulating the galaxy population in a LCDM cosmology*. ArXiv e-prints, 2010.

Guth, A. H. *Inflationary universe: A possible solution to the horizon and flatness problems*. Phys. Rev. D, 23:347, 1981.

Haardt, F. and Madau, P. *Modelling the UV/X-ray cosmic background with CUBA*. In D. M. Neumann & J. T. V. Tran, editor, *Clusters of Galaxies and the High Redshift Universe Observed in X-rays*. 2001.

Helmi, A. *Is the dark halo of our galaxy spherical?* MNRAS, 351:643, 2004.

Hennawi, J. F., Dalal, N., Bode, P. et al. *Characterizing the cluster lens population*. ApJ, 654:714, 2007.

Henriques, B., Bertone, S. and Thomas, P. *Disruption of dwarf galaxies in semi-analytic models*. arXiv:astro-ph/0706.3814, 2007.

Hernquist, L. *An analytical model for spherical galaxies and bulges*. ApJ, 356:359, 1990.

Hernquist, L., Hut, P. and Makino, J. *Discreteness noise versus force errors in $N-Body$ simulations*. ApJL, 402:L85, 1993.

Hernquist, L. and Katz, N. *TREESPH - A unification of SPH with the hierarchical tree method*. ApJS, 70:419, 1989.

Hernquist, L. and Ostriker, J. P. *A self-consistent field method for galactic dynamics*. ApJ, 386:375, 1992.

Hockney, R. W. and Eastwood, J. W. *Computer simulation using particles*. 1981.

Hoekstra, H., Yee, H. K. C. and Gladders, M. D. *Properties of galaxy dark matter halos from weak lensing*. ApJ, 606:67, 2004.

Hoffman, L., Cox, T. J., Dutta, S. et al. *Orbital structure of merger remnants: Trends with gas fraction in 1:1 mergers*. ArXiv e-prints, 2010.

Hofner, P. and Sparke, L. S. *Time evolution of galactic WARPS*. ApJ, 428:466, 1994.

Holmberg, E. *On the clustering tendencies among the nebulae. II. A study of encounters between laboratory models of stellar systems by a new integration procedure.* ApJ, 94:385, 1941.

Holmberg, E. *A study of physical groups of galaxies*. Arkiv for Astronomi, 5:305,

1969.

Hopkins, P. F., Bahcall, N. A. and Bode, P. *Cluster alignments and ellipticities in ΛCDM cosmology*. ApJ, 618:1, 2005.

Hubble, E. *A relation between distance and radial velocity among extra-galactic nebulae*. Proceedings of the National Academy of Science, 15:168, 1929.

Ibata, R., Lewis, G. F., Irwin, M. et al. *Great circle tidal streams: Evidence for a nearly spherical massive dark halo around the Milky Way*. ApJ, 551:294, 2001.

Jackson, N., Bryan, S. E., Mao, S. et al. *Satellites in the field and lens galaxies: SDSS/COSMOS versus SLACS/CLASS*. MNRAS, 403:826, 2010.

Jeans, J. H. *Astronomy and Cosmogony*. 1928.

Jenkins, A. *Second-order Lagrangian perturbation theory initial conditions for resimulations*. MNRAS, 403:1859, 2010.

Jenkins, A., Frenk, C. S., White, S. D. M. et al. *The mass function of dark matter haloes*. MNRAS, 321:372, 2001.

Jesseit, R., Naab, T. and Burkert, A. *Orbital structure of collisionless merger remnants: On the origin of photometric and kinematic properties of elliptical and S0 galaxies*. MNRAS, 360:1185, 2005.

Jing, Y. P. and Suto, Y. *Triaxial modeling of halo density profiles with high-resolution N − body simulations*. ApJ, 574:538, 2002.

Johnston, K. V., Law, D. R. and Majewski, S. R. *A two micron all sky survey view of the Sagittarius dwarf galaxy. III. Constraints on the flattening of the galactic halo*. ApJ, 619:800, 2005.

Katz, N. and Gunn, J. E. *Dissipational galaxy formation. I - Effects of Gasdynamics*. ApJ, 377:365, 1991.

Kauffmann, G., Colberg, J. M., Diaferio, A. et al. *Clustering of galaxies in a hierarchical universe - I. Methods and results at z=0*. MNRAS, 303:188, 1999.

Kauffmann, G., White, S. D. M. and Guiderdoni, B. *The formation and evolution of galaxies within merging dark matter haloes*. MNRAS, 264:201, 1993.

Kazantzidis, S., Kravtsov, A. V., Zentner, A. R. et al. *The effect of gas cooling on the shapes of dark matter halos*. ApJL, 611:L73, 2004.

Keeton, C. R. and Moustakas, L. A. *A new channel for detecting dark matter substructure in galaxies: gravitational lens time delays*. arXiv:astro-ph/0805.0309, 2008.

Kennicutt, R. C., Jr. *The global Schmidt law in star-forming galaxies*. ApJ, 498:541, 1998.

Kimm, T. and Yi, S. K. *Intrinsic axis ratio distribution of early-type galaxies from the Sloan Digital Sky Survey*. ApJ, 670:1048, 2007.

Klypin, A., Kravtsov, A. V., Valenzuela, O. et al. *Where are the missing galactic satellites?* ApJ, 522:82, 1999.

Knebe, A., Gill, S. P. D., Gibson, B. K. et al. *Anisotropy in the distribution of satellite Galaxy orbits*. ApJ, 603:7, 2004.

Kochanek, C., Falco, E., C. Impey, J. L. et al. *http://www.cfa.harvard.edu/castles/*. 2008.

Kochanek, C. S. *The implications of lenses for galaxy structure*. ApJ, 373:354, 1991.

Kochanek, C. S. *Evidence for dark matter in MG 1654+134*. ApJ, 445:559, 1995.

Kolb, E. and Turner, M. *The early universe*. Addison-Wesley Publishing Company, 1993.

Komatsu, E., Dunkley, J., Nolta, M. R. et al. *Five-Year Wilkinson Microwave Anisotropy Probe observations: Cosmological interpretation*. ApJS, 180:330, 2009.

Komatsu, E., Smith, K. M., Dunkley, J. et al. *Seven-year Wilkinson Microwave Anisotropy Probe (WMAP) Observations: Cosmological Interpretation*. ApJS, 192:18, 2011.

Koopmans, L. V. E., de Bruyn, A. G. and Jackson, N. *The edge-on spiral gravitational lens B1600+434*. MNRAS, 295:534, 1998.

Koopmans, L. V. E., de Bruyn, A. G., Marlow, D. R. et al. *A new radio double lens from CLASS: B1127+385*. MNRAS, 303:727, 1999.

Koopmans, L. V. E., Treu, T., Fassnacht, C. D. et al. *The Hubble constant from the gravitational lens B1608+656*. ApJ, 599:70, 2003.

Kowalski, M., Rubin, D., Aldering, G. et al. *Improved cosmological constraints from new, old, and combined supernova data sets*. ApJ, 686:749, 2008.

Kravtsov, A. V., Gnedin, O. Y. and Klypin, A. A. *The tumultuous lives of galactic dwarfs and the missing satellites problem*. ApJ, 609:482, 2004.

Kuijken, K. and Tremaine, S. *On the ellipticity of the galactic disk*. ApJ, 421:178, 1994.

Lacey, C. and Cole, S. *Merger rates in hierarchical models of galaxy formation*. MN-

RAS, 262:627, 1993a.

Lacey, C. and Cole, S. *Merger rates in hierarchical models of galaxy formation*. MNRAS, 262:627, 1993b.

Lacey, C. and Cole, S. *Merger rates in hierarchical models of galaxy formation - Part Two - Comparison with N − body simulations*. MNRAS, 271:676, 1994.

Lacey, C. and Silk, J. *Tidally triggered galaxy formation. I - Evolution of the galaxy luminosity function*. ApJ, 381:14, 1991.

Lambas, D. G., Maddox, S. J. and Loveday, J. *On the true shapes of galaxies*. MNRAS, 258:404, 1992.

Larson, D., Dunkley, J., Hinshaw, G. et al. *Seven-Year Wilkinson Microwave Anisotropy Probe (WMAP) Observations: Power spectra and WMAP-derived parameters*. ArXiv e-prints, 2010.

Law, D. R. and Majewski, S. R. *Assessing the Milky Way satellites associated with the Sagittarius dwarf spheroidal galaxy*. ApJ, 718:1128, 2010.

Law, D. R., Majewski, S. R. and Johnston, K. V. *Evidence for a triaxial Milky Way dark matter halo from the Sagittarius stellar tidal stream*. ApJL, 703:L67, 2009.

Lemaître, G. *Un Univers homogène de masse constante et de rayon croissant rendant compte de la vitesse radiale des nébuleuses extra-galactiques*. Annales de la Societe Scietifique de Bruxelles, 47:49, 1927.

Lewis, A., Challinor, A. and Lasenby, A. *Efficient computation of cosmic microwave background anisotropies in closed Friedmann-Robertson-Walker models*. ApJ, 538:473, 2000.

Liddle, A. *An Introduction to Modern Cosmology, Second Edition*. 2003.

Lindblad, B. *Die Milchstraße*. Handbuch der Astrophysik, 5:937, 1933.

Long, R. J. and Mao, S. *Made-to-measure Galaxy models - I. Methodology*. MNRAS, 405:301, 2010.

Lucy, L. B. *A numerical approach to the testing of the fission hypothesis*. AJ, 82:1013, 1977.

Macciò, A. V., Dutton, A. A. and van den Bosch, F. C. *Concentration, spin and shape of dark matter haloes as a function of the cosmological model: WMAP1, WMAP3 and WMAP5 results*. MNRAS, 391:1940, 2008.

Macciò, A. V., Moore, B., Stadel, J. et al. *Radial distribution and strong lensing*

*statistics of satellite galaxies and substructure using high-resolution ΛCDM hydrodynamical simulations*. MNRAS, 366:1529, 2006.

Madau, P., Diemand, J. and Kuhlen, M. *Dark matter subhalos and the dwarf satellites of the Milky Way*. arXiv:astro-ph/0802.2265, 2008.

Makino, J., Taiji, M., Ebisuzaki, T. et al. *GRAPE-4: A massively parallel special-purpose computer for collisional N-Body simulations*. ApJ, 480:432, 1997.

Mandelbaum, R., Hirata, C. M., Broderick, T. et al. *Ellipticity of dark matter haloes with galaxy-galaxy weak lensing*. MNRAS, 370:1008, 2006.

Mandelbaum, R., McDonald, P., Seljak, U. et al. *Precision cosmology from the Lyman α forest: power spectrum and bispectrum*. MNRAS, 344:776, 2003.

Mao, S. and Schneider, P. *Evidence for substructure in lens galaxies?* MNRAS, 295:587, 1998.

Martínez-Delgado, D., Peñarrubia, J., Jurić, M. et al. *The Virgo stellar overdensity: Mapping the infall of the Sagittarius tidal stream onto the Milky Way disk*. ApJ, 660:1264, 2007.

McKean, J. P., Browne, I. W. A., Jackson, N. J. et al. *CLASS B2108+213: A new wide-separation gravitational lens system*. MNRAS, 356:1009, 2005.

McKean, J. P., Koopmans, L. V. E., Browne, I. W. A. et al. *Keck spectroscopy of Cosmic Lens All-Sky Survey gravitational lenses*. MNRAS, 350:167, 2004.

McKean, J. P., Koopmans, L. V. E., Flack, C. E. et al. *High-resolution imaging of the anomalous flux ratio gravitational lens system CLASS B2045+265: Dark or luminous satellites?* MNRAS, 378:109, 2007.

Merrifield, M. R. *The galactic halo and CDM*. In S. Ryder, D. Pisano, M. Walker, & K. Freeman, editor, *Dark Matter in Galaxies*, volume 220 of *IAU Symposium*, 431. 2004.

Merritt, D. and Valluri, M. *Resonant orbits in triaxial galaxies*. AJ, 118:1177, 1999.

Meszaros, P. *The behaviour of point masses in an expanding cosmological substratum*. A&A, 37:225, 1974.

Metcalf, R. B. *The importance of intergalactic structure to gravitationally lensed quasars*. ApJ, 629:673, 2005.

Monaghan, J. J. *Smoothed particle hydrodynamics*. ARA&A, 30:543, 1992.

Monaghan, J. J. and Lattanzio, J. C. *A refined particle method for astrophysical prob-*

*lems*. A&A, 149:135, 1985.

Moore, B., Ghigna, S., Governato, F. et al. *Dark matter substructure within galactic halos*. ApJL, 524:L19, 1999.

Moore, B., Katz, N. and Lake, G. *On the destruction and overmerging of dark halos in dissipationless N − Body simulations*. ApJ, 457:455, 1996.

Myers, S. T., Jackson, N. J., Browne, I. W. A. et al. *The Cosmic Lens All-Sky Survey - I. Source selection and observations*. MNRAS, 341:1, 2003.

Nakamura, K. and Group, P. D. *Review of particle physics*. Journal of Physics G: Nuclear and Particle Physics, 37(7A):075021, 2010.

Navarro, J. F. and Benz, W. *Dynamics of cooling gas in galactic dark halos*. ApJ, 380:320, 1991.

Navarro, J. F., Frenk, C. S. and White, S. D. M. *The assembly of galaxies in a hierarchically clustering universe*. MNRAS, 275:56, 1995.

Navarro, J. F., Frenk, C. S. and White, S. D. M. *The structure of cold dark matter halos*. ApJ, 462:563, 1996.

Navarro, J. F., Frenk, C. S. and White, S. D. M. *A universal density profile from hierarchical clustering*. ApJ, 490:493, 1997.

Neto, A. F., Gao, L., Bett, P. et al. *The statistics of* $\Lambda$ *CDM halo concentrations*. MNRAS, 381:1450, 2007.

New, K. C. B., Tohline, J. E., Frank, J. et al. *A physical model of warped galaxy disks*. ApJ, 503:632, 1998.

O'Brien, J. C., Freeman, K. C. and van der Kruit, P. C. *The dark matter halo shape of edge-on disk galaxies. IV. UGC 7321*. A&A, 515:A63, 2010.

Oguri, M. *The Mass Distribution of SDSS J1004+4112 Revisited*. PASJ, 62:1017, 2010.

Oguri, M., Lee, J. and Suto, Y. *Arc statistics in triaxial dark matter halos: Testing the collisionless cold dark matter paradigm*. ApJ, 599:7, 2003.

Oh, S., Brook, C., Governato, F. et al. *The central slope of dark matter cores in dwarf galaxies: Simulations vs. THINGS*. ArXiv e-prints, 2010.

Olive, K. A., Steigman, G. and Walker, T. P. *Primordial nucleosynthesis : Theory and observations.* Phys. Rep., 333:389, 2000.

Olling, R. P. *The highly flattened dark matter halo of NGC 4244*. AJ, 112:481, 1996.

Olling, R. P. and Merrifield, M. R. *Two measures of the shape of the dark halo of the Milky Way*. MNRAS, 311:361, 2000.

Ostriker, E. C. and Binney, J. J. *Warped and tilted galactic discs*. MNRAS, 237:785, 1989.

Parkinson, H., Cole, S. and Helly, J. *Generating dark matter halo merger trees*. MNRAS, 383:557, 2008.

Peacock, J. A., Cole, S., Norberg, P. et al. *A measurement of the cosmological mass density from clustering in the 2dF galaxy redshift survey*. Nature, 410:169, 2001.

Peebles, P. J. E. *Origin of the angular momentum of galaxies*. ApJ, 155:393, 1969.

Peebles, P. J. E. *The large-scale structure of the Universe*. 1980.

Peebles, P. J. E. *Principles of physical cosmology*. 1993.

Penzias, A. A. and Wilson, R. W. *A measurement of excess antenna temperature at 4080 Mc/s.* ApJ, 142:419, 1965.

Percival, W. J., Sutherland, W., Peacock, J. A. et al. *Parameter constraints for flat cosmologies from cosmic microwave background and 2dFGRS power spectra*. MNRAS, 337:1068, 2002.

Perlmutter, S., Aldering, G., Goldhaber, G. et al. *Measurements of omega and lambda from 42 High-Redshift supernovae*. ApJ, 517:565, 1999.

Pfenniger, D., Combes, F. and Martinet, L. *Is dark matter in spiral galaxies cold gas? I. Observational constraints and dynamical clues about galaxy evolution*. A&A, 285:79, 1994.

Piontek, F. and Steinmetz, M. *The modelling of feedback processes in cosmological simulations of disc galaxy formation*. MNRAS, 1632, 2010.

Poggianti, B. M. *K and evolutionary corrections from UV to IR*. A&AS, 122:399, 1997.

Power, C., Navarro, J. F., Jenkins, A. et al. *The inner structure of ΛCDM haloes - I. A numerical convergence study*. MNRAS, 338:14, 2003.

Press, W. H. and Schechter, P. *Formation of galaxies and clusters of galaxies by self-similar gravitational condensation*. ApJ, 187:425, 1974.

Rahmati, A. and Jalali, M. A. *New biorthogonal potential-density basis functions*. MNRAS, 393:1459, 2009.

Rees, M. J. *Lyman absorption lines in quasar spectra - Evidence for gravitationally-*

*confined gas in dark minihaloes*. MNRAS, 218:25P, 1986.

Rees, M. J. and Ostriker, J. P. *Cooling, dynamics and fragmentation of massive gas clouds - Clues to the masses and radii of galaxies and clusters*. MNRAS, 179:541, 1977.

Reichardt, C. L., Ade, P. A. R., Bock, J. J. et al. *High-resolution CMB power spectrum from the complete ACBAR data set*. ApJ, 694:1200, 2009.

Riess, A. G., Filippenko, A. V., Challis, P. et al. *Observational evidence from supernovae for an accelerating universe and a cosmological constant*. AJ, 116:1009, 1998.

Riess, A. G., Press, W. H. and Kirshner, R. P. *A precise distance indicator: Type IA supernova multicolor light-curve shapes*. ApJ, 473:88, 1996.

Rix, H. and Zaritsky, D. *Nonaxisymmetric structures in the stellar disks of galaxies*. ApJ, 447:82, 1995.

Rusin, D., Kochanek, C. S., Norbury, M. et al. *B1359+154: A Six-Image lens produced by a z ˜= 1 compact group of galaxies*. ApJ, 557:594, 2001.

Rusin, D., Norbury, M., Biggs, A. D. et al. *High-resolution observations and mass modelling of the CLASS gravitational lens B1152+199*. MNRAS, 330:205, 2002.

Ryden, B. *The intrinsic shapes of elliptical galaxies*. ApJ, 396:445, 1992.

Sackett, P. D. *The shape of dark matter halos*. In D. R. Merritt, M. Valluri, & J. A. Sellwood, editor, *Galaxy Dynamics - A Rutgers Symposium*, volume 182 of *Astronomical Society of the Pacific Conference Series*, 393. 1999.

Sackett, P. D., Rix, H., Jarvis, B. J. et al. *The flattened dark halo of polar-ring galaxy NGC 4650A: A conspiracy of shapes?* ApJ, 436:629, 1994.

Sales, L. V., Navarro, J. F., Lambas, D. G. et al. *Satellite galaxies and fossil groups in the Millennium simulation*. MNRAS, 382:1901, 2007.

Schaye, J. *Star formation thresholds and galaxy edges: Why and where*. ApJ, 609:667, 2004.

Schaye, J. and Dalla Vecchia, C. *On the relation between the Schmidt and Kennicutt-Schmidt star formation laws and its implications for numerical simulations*. MNRAS, 383:1210, 2008.

Schaye, J., Dalla Vecchia, C., Booth, C. M. et al. *The physics driving the cosmic star formation history*. MNRAS, 402:1536, 2010.

Schechter, P. L. and Moore, C. B. *The lensing Galaxy in MG 0414 + 0534*. AJ, 105:1, 1993.

Schneider, P., Kochanek, C. S. and Wambsganss, J. *Gravitational lensing: Strong, weak and micro*. 2006.

Schwarzschild, M. *A numerical model for a triaxial stellar system in dynamical equilibrium*. ApJ, 232:236, 1979.

Sciama, D. W. *On the role of a strongly flattened galactic halo in the decaying dark matter hypothesis*. MNRAS, 244:1P, 1990.

Scoville, N., Abraham, R. G., Aussel, H. et al. *COSMOS: Hubble space telescope observations*. ApJS, 172:38, 2007.

Seljak, U. and Zaldarriaga, M. *A line-of-sight integration approach to cosmic microwave background anisotropies*. ApJ, 469:437, 1996.

Sheth, R. K. and Tormen, G. *On the environmental dependence of halo formation*. MNRAS, 350:1385, 2004.

Shin, E. M. and Evans, N. W. *The effect of satellite galaxies on gravitational lensing flux ratios*. MNRAS, 385:2107, 2008.

Silk, J. *On the fragmentation of cosmic gas clouds. I - The formation of galaxies and the first generation of stars*. ApJ, 211:638, 1977.

Smoot, G. F., Bennett, C. L., Kogut, A. et al. *Structure in the COBE differential microwave radiometer first-year maps*. ApJL, 396:L1, 1992.

Spergel, D. N., Bean, R., Doré, O. et al. *Three-year Wilkinson Microwave Anisotropy Probe (WMAP) observations: Implications for cosmology*. ApJS, 170:377, 2007.

Spergel, D. N., Verde, L., Peiris, H. V. et al. *First-year Wilkinson Microwave Anisotropy Probe (WMAP) observations: determination of cosmological parameters*. ApJS, 148:175, 2003.

Springel, V. *The cosmological simulation code GADGET-2*. MNRAS, 364:1105, 2005.

Springel, V., Di Matteo, T. and Hernquist, L. *Modelling feedback from stars and black holes in galaxy mergers*. MNRAS, 361:776, 2005a.

Springel, V. and Hernquist, L. *Cosmological smoothed particle hydrodynamics simulations: the entropy equation*. MNRAS, 333:649, 2002.

Springel, V. and Hernquist, L. *Cosmological smoothed particle hydrodynamics simulations: a hybrid multiphase model for star formation*. MNRAS, 339:289, 2003.

Springel, V., Wang, J., Vogelsberger, M. et al. *The Aquarius Project: the subhaloes of galactic haloes*. MNRAS, 391:1685, 2008.

Springel, V., White, S. D. M. and Hernquist, L. *The shapes of simulated dark matter halos*. In S. Ryder, D. Pisano, M. Walker, & K. Freeman, editor, *Dark Matter in Galaxies*, volume 220 of *IAU Symposium*, 421. 2004.

Springel, V., White, S. D. M., Jenkins, A. et al. *Simulations of the formation, evolution and clustering of galaxies and quasars*. Nature, 435:629, 2005b.

Springel, V., White, S. D. M., Tormen, G. et al. *Populating a cluster of galaxies - I. Results at z=0*. MNRAS, 328:726, 2001a.

Springel, V., Yoshida, N. and White, S. D. M. *GADGET: A code for collisionless and gasdynamical cosmological simulations*. New Astronomy, 6:79, 2001b.

Stadel, J., Potter, D., Moore, B. et al. *Quantifying the heart of darkness with GHALO - a multibillion particle simulation of a galactic halo*. MNRAS, 398:L21, 2009.

Statler, T. S. *Self-consistent models of perfect triaxial galaxies*. ApJ, 321:113, 1987.

Steiman-Cameron, T. Y., Kormendy, J. and Durisen, R. H. *The remarkable twisted disk of NGC 4753 and the shapes of galactic halos*. AJ, 104:1339, 1992.

Stoehr, F., White, S. D. M., Springel, V. et al. *Dark matter annihilation in the halo of the Milky Way*. MNRAS, 345:1313, 2003.

Sugimoto, D., Chikada, Y., Makino, J. et al. *A special-purpose computer for gravitational many-body problems*. Nature, 345:33, 1990.

Syer, D. and Tremaine, S. *Made-to-measure $N-$ body systems*. MNRAS, 282:223, 1996.

Tegmark, M., Strauss, M. A., Blanton, M. R. et al. *Cosmological parameters from SDSS and WMAP*. Phys. Rev. D, 69(10):103501, 2004.

Thoul, A. A. and Weinberg, D. H. *Hydrodynamic simulations of galaxy formation. II. Photoionization and the formation of low-mass galaxies*. ApJ, 465:608, 1996.

Tinker, J., Kravtsov, A. V., Klypin, A. et al. *Toward a halo mass function for precision cosmology: The limits of universality*. ApJ, 688:709, 2008.

Tissera, P. B. and Dominguez-Tenreiro, R. *Dark matter halo structure in CDM hydrodynamical simulations*. MNRAS, 297:177, 1998.

Toomre, A. *Mergers and some consequences*. In B. M. Tinsley & R. B. Larson, editor, *Evolution of galaxies and stellar populations*, 401. 1977.

Treu, T., Gavazzi, R., Gorecki, A. et al. *The SLACS Survey. VIII. The relation between environment and internal structure of early-type galaxies*. ApJ, 690:670, 2009.

Turner, E. L., Ostriker, J. P. and Gott, J. R., III. *The statistics of gravitational lenses - The distributions of image angular separations and lens redshifts*. ApJ, 284:1, 1984.

Valluri, M., Debattista, V. P., Quinn, T. et al. *The orbital evolution induced by baryonic condensation in triaxial haloes*. MNRAS, 129, 2010.

van der Marel, R. P. *Flattening and kinematics of the galactic halo*. MNRAS, 248:515, 1991.

Van Waerbeke, L., Mellier, Y., Pelló, R. et al. *Likelihood analysis of cosmic shear on simulated and VIRMOS-DESCART data*. A&A, 393:369, 2002.

von Hoerner, S. *Die numerische integration des n-Körper-Problems für Sternhaufen, II.* ZAp, 57:47, 1963.

Wang, J., De Lucia, G., Kitzbichler, M. G. et al. *The dependence of galaxy formation on cosmological parameters: Can we distinguish between the WMAP1 and WMAP3 parameter sets?* MNRAS, 384:1301, 2008.

Wang, L., Li, C., Kauffmann, G. et al. *Modelling galaxy clustering in a high-resolution simulation of structure formation*. MNRAS, 371:537, 2006.

Warren, M. S., Quinn, P. J., Salmon, J. K. et al. *Dark halos formed via dissipationless collapse. I - Shapes and alignment of angular momentum*. ApJ, 399:405, 1992.

Weinberg, S. *Gravitation and Cosmology: Principles and applications of the general theory of relativity*. 1972.

White, S. D. M. *Simulations of merging galaxies*. MNRAS, 184:185, 1978.

White, S. D. M. *Formation and evolution of galaxies*. In R. Schaeffer, J. Silk, M. Spiro, & J. Zinn-Justin, editor, *Cosmology and large scale Structure*, 349. 1996.

White, S. D. M. and Frenk, C. S. *Galaxy formation through hierarchical clustering*. ApJ, 379:52, 1991.

White, S. D. M., Navarro, J. F., Evrard, A. E. et al. *The baryon content of galaxy clusters - a challenge to cosmological orthodoxy*. Nature, 366:429, 1993.

White, S. D. M. and Rees, M. J. *Core condensation in heavy halos - A two-stage theory for galaxy formation and clustering*. MNRAS, 183:341, 1978.

Whitmore, B. C., McElroy, D. B. and Schweizer, F. *The shape of the dark halo in polar-ring galaxies*. ApJ, 314:439, 1987.

Wiersma, R. P. C., Schaye, J. and Smith, B. D. *The effect of photoionization on the cooling rates of enriched, astrophysical plasmas*. MNRAS, 393:99, 2009.

Yadav, J., Bharadwaj, S., Pandey, B. et al. *Testing homogeneity on large scales in the Sloan Digital Sky Survey Data release one*. MNRAS, 364:601, 2005.

York, T., Jackson, N., Browne, I. W. A. et al. *CLASS B0631+519: Last of the cosmic lens all-sky survey lenses*. MNRAS, 361:259, 2005.

Zel'dovich, Y. B. *Gravitational instability: An approximate theory for large density perturbations.* A&A, 5:84, 1970.

Zwicky, F. *On the masses of nebulae and of clusters of nebulae*. ApJ, 86:217, 1937.

*'Begin at the beginning,' the King said, very gravely,*
*'and go on till you come to the end:*
*then stop.'*
*- Lewis Carroll.*